Chemical sensors based on vitreous lead thioarsenates : atomic structure, ionic transport, Pb2+ sensitivity

Bouthayna Alrifai

Thèse de Doctorat

Mention : Chimie
Spécialité : Chimie des matériaux

présentée à ***l'Ecole Doctorale en Sciences Technologie et Santé (ED 585)*** **de l'Université du Littoral Côte d'Opale**
et
à l'Ecole doctorale des Sciences et Technologies (EDST)
de l'Université Libanaise

par

Bouthayna Alrifai

pour obtenir le grade de Docteur de l'Université du Littoral Côte d'Opale

Capteurs chimiques à base de thioarséniates de plomb vitreux : structure atomique, transport ionique et sensibilité aux ions Pb^{2+}

Chemical sensors based on vitreous lead thioarsenates: atomic structure, ionic transport, Pb^{2+} sensitivity

Soutenue le 20 Décembre 2021, après avis des rapporteurs, devant le jury d'examen :

M^me^ Annie Pradel, Directrice de recherche, Montpellier	**Président du jury**
M. Laurent Calvez, Pr., Université de Rennes	**Rapporteur**
M. Grégory Tricot, Dr. (HDR), Université de Lille 1	**Rapporteur**
M. Tayssir Hamieh, Pr., Université Libanaise	**Examinateur**
M. Eugène Bychkov, Pr., Université du Littoral Côte d'Opale	**Directeur de thèse**
M^me^ Joumana Toufaily, Pr., Université Libanaise	**Directeur de thèse**
M. Mohamad Kassem, Dr., Université du Littoral Côte d'Opale	**Co-directeur de thèse**

Acknowledgements

"No road is long with good company."

Writing my thesis feeling that everything has passed so quickly. Thinking of the people I met on my trip and those who have never ever left me. Without them I would not have been granted to finish all this work.

First and foremost, I would like to express my sincere gratitude to Mr. Eugène BYCHKOV and Mrs. Joumana TOUFAILY, my thesis directors, for their confidence and for giving me the opportunity to do my PhD. Without their support this thesis would not have been possible.

Also, I am extremely thankful to my thesis supervisor Mr. Mohamad KASSEM. His patience, his cooperation and his valuable suggestions went into the completion of this research work. It was a great pleasure working with him.

A special thanks to Mrs. Maria BOKOVA for providing me her valuable suggestions during my thesis. She raised many precious points during these years of laboratory work and I hope that I have managed to address them here.

Also, I would like to thank Mr. Marc FOURMENTIN for his help in the Scanning Electron Microscopy measurements and Mr. Christophe POUPIN for the X-ray diffraction measurements.

I would like to express my gratitude to all members in LPCA, especially Mr. Patrick AUGUSTIN for his kind welcoming and for being that nice, positive and helpful person.

I would like also show my appreciation and gratitude to the jury members who have accepted to evaluate my thesis work. Thank you Mrs. Annie PRADEL, research director at Charles Gerhardt Institute at the University of Montpellier, Mr. Laurent CALVEZ, professor at the University of Rennes, Mr. Grégory TRICOT, MCF-HDR at the University of Lille1 and Mr. Tayssir HAMIEH, professor at the Lebanese University.

Getting through this long research trip required more than academic support, and I have many, many people to thank for listening to and, at times, having to tolerate me over the past three years. I cannot begin to express my deepest gratitude for their friendship.

Most importantly, I am grateful for my parents whose constant support and love keep me motivated and confident through this tough journey. My accomplishments and success are because they believed in me. Deepest thanks to my siblings, who keep me grounded, remind me of what is important in life, and are always supportive of my adventures. Finally, I owe my deepest gratitude to my mother and father. I am forever thankful for the unconditional love and support throughout the entire thesis journey and every day of my life.

Table of Contents

General Introduction

Monitoring the quality of water, air and soil has become indispensable in a modern society where environmental monitoring is generally the first pillar of environmental management policies for chronic risks and accidental risks to the environment. Therefore, and in this area of environmental monitoring, monitoring the level of heavy metals (e. g., mercury, cadmium, tellurium, etc.) is very important because there is a direct impact on public health. The fact that heavy metals are not biodegradable makes metal pollution of water, for example, a major problem. In this regards, one of these heavy metals, known to be the most dangerous from an environmental and health point of view, is lead.

The sources of lead emissions vary from country to country. For example, a source of lead emissions in the Dunkirk region is the steel industry, which uses about fifteen ores that are all leaded. In a country like Lebanon (my home country), and as a direct result of burning waste, the concentration of heavy metals such as lead, cadmium, manganese, titanium, chromium and arsenic increased by 98-144% in later years. A report (2016) by the Agricultural Research Institute show the real crisis of water resources in Lebanon, as the water from rivers that flow into the sea contains mercury, lead, copper, arsenic and nitrogen. For these reasons, and for both Dunkirk region and Lebanon, it is imperative to continuously monitor (i) the concentration of lead in the aquatic environment and (ii) the releases of lead into the atmosphere. One of these ways to achieve that, is the development of new sensors that are always more efficient. Hence, the current research work (Ph.D. subject) responds to a real societal demand and is as such co-funded by two universities ULCO (Dunkirk, France) and Lebanese University (Beirut, Lebanon).

In this context, the « Glasses and Sensors » team of the Laboratory of Physico-Chemistry of the Atmosphere (LPCA), located in one of the most industrialized regions of Europe and its Lebanese partners of the Laboratory of Materials, Catalysis, Environment and Analytical Methods (MCEMA) set out to develop potentiometric chemical sensors with chalcogenide glass membranes for the detection of lead in aqueous medium. These glasses are very promising materials as sensitive membranes in ISE (ion selective electrode) application. For this reason, during several years, one of the main activities of our team at LPCA was focused on developing potentiometric chemical sensors with membranes based on chalcogenide glasses to detect heavy metal ions (Hg^{2+}, Cu^{2+}, Cd^{2+} and Tl^{+}, etc.). Therefore, this thesis work represents a scene of an

environmental theme where fundamental research which will be carried out on lead doped chalcogenide glasses is of great scientific interest. The development of new, more efficient sensors, in this case dedicated to lead, requires a determination of the relationships between the composition, the structure, and the ionic and/or electronic transport properties in the solid material. To this end, this thesis is made up of 4 chapters:

- **Chapter I**

In this chapter, we present some generalities on glasses and specifically chalcogenide glasses (history, potential applications, etc.). The synthesis of (i) the quasi-binary PbS-As_2S_3 glass system along with selected crystals of the Pb-As-S crystalline counterpart (dufrénoysite $Pb_2As_2S_5$, baumhauerite $Pb_5As_9S_{18}$ and sartorite $PbAs_2S_4$) and (ii) the pseudo-ternary AgI-PbS-As_2S_3 system (series-A; series-B series-C) has been described. Macroscopic properties including density, mean atomic volume and thermal properties have been presented and discussed.

- **Chapter II**

It is related to the electrical conductivity of the PbS-As_2S_3 system, the Pb-As-S crystals ($Pb_2As_2S_5$, $Pb_5As_9S_{18}$ and $PbAs_2S_4$), the annealed glasses yielding glassy/crystalline alloys and finally the AgI-PbS-As_2S_3 ternary system. These studies were performed using dc conductivity measurements and complex impedance spectroscopy. The results obtained through these measurements are discussed and analyzed in order to make certain hypotheses about the transport mechanisms within these vitreous materials.

- **Chapter III**

This part covers the structural analysis of the PbS-As_2S_3 and AgI-PbS-As_2S_3 glass systems. Raman measurements were employed for both systems. For the primary, DFT modeling of binary Pb-S and ternary As-Pb-S size limited clusters was carried out to allow a reliable interpretation of the observed spectra. High energy X-ray and neutron diffraction measurements were only conducted for the quasi-binary PbS-As_2S_3 system and RMC/AIMD modelling of diffraction data of the equimolar $(PbS)_{0.5}(As_2S_3)_{0.5}$ composition was performed to further clarify the structural aspects at the short- and intermediate-range orders.

- **Chapter IV**

In this final chapter, lead doped chalcogenide glass compositions, in the pseudo-ternary $(AgI)_x(PbS)_y(As_2S_3)_z$, were examined as active membrane materials for the construction of Pb(II)–ISE (ion-selective sensors). For the fabricated sensors, several key analytical parameters were investigated to evaluate the different glass compositions as active membranes in Pb(II)–ISE, including detection limit, sensitivity, linearity, ionic selectivity (in the presence of K^+, Na^+, Ni^{2+}, Ca^{2+}, Cd^{2+}, Cu^{2+} and Hg^{2+} interfering cations), reproducibility and optimal pH-range.

Chapter I:
The quasi-binary PbS-As_2S_3, and the pseudo-ternary AgI-PbS-As_2S_3 systems

I.1 Generalities on glasses

The history of glasses is an old one. It is thought that the earliest man-made glass was obtained about 4000 years ago in ancient Egypt, possibly in a fire for baking earthenware pots. However, in the earliest times of world history, nature has also made glasses, but in violent fury; the volcanic outflow of the molten magma from the bowels of the earth get cooled and formed glasses. For example, obsidian glasses, volcanic alumino-silicate glasses containing oxides of Na, Ca, K, Fe and traces of Mn, are millions of years old and most of them have crystallized during the history of earth's harsh and changing weather [1].

The Scientific understanding of glasses is very new. The studies began with Faraday and others at the beginning of the nineteenth century. Therefore, Glass can be defined as an amorphous solid with no regularity in the arrangement of the atoms in its structure [2], [3] **Figure I.1**. In addition, the American Society for Testing Materials (ASTM) defined the glass as an inorganic product of fusion which has been cooled to a rigid condition without being crystallized. Consequently, it undergoes a second-order transition at the so-called glass transition temperature T_g, **Figure I.2**. This transition temperature corresponds to the accessibility of new configuration energy states; it marks the onset of softening and is accompanied by an increase in the thermal expansion coefficient and the heat capacity. Thereby, its thermal behavior could be described by the fundamental changes in physical properties such as the specific volume, enthalpy and electrical and thermal conductivities.

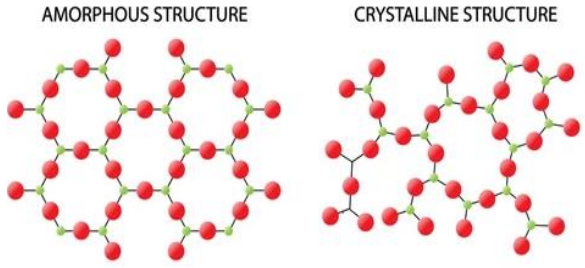

Figure I.1 Comparison of crystalline and amorphous structure of SiO_2.

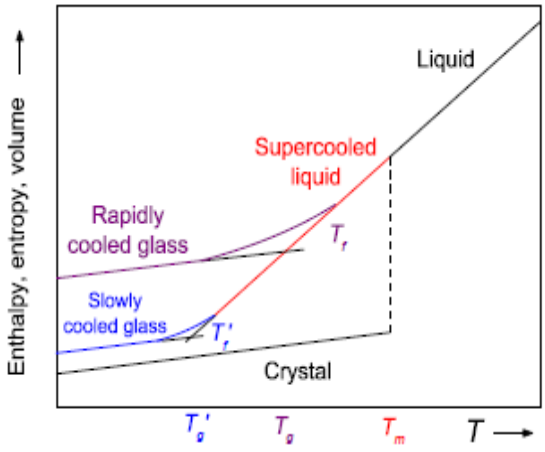

Figure I.2 Plot of specific volume vs. temperature, contrasting the formation of a glass vs. crystals from the melt.

The constituents of glass can be broadly divided into three categories: network formers, network modifiers, intermediate compounds and doping salts [4].

A. Network formers

The network formers are elements that, once cooled, tend to form glasses easily; they form a highly cross-linked network (e.g. mono-, bi- or three-dimensional network) of chemical bonds and constitute the bulk of the glass. Examples of networks formers include oxides or chalcogenides of silicon, boron, phosphorus, germanium or arsenic.

B. Network modifiers

The network modifiers, usually added to glass in small quantities, are used to fine-tune the properties of glasses to suit a number of niche engineering applications. Their incorporation, in the glass network, induces important structural changes that are at the origin of several optical, electric, thermal phenomena, **Figure I.3**. Network modifiers include compounds as alkali, alkaline-earth or metal oxides or chalcogenides e.g. Li_2S, Na_2S, LiO_2, Ag_2S, Cu_2O, MgO, Na_2O, etc,.

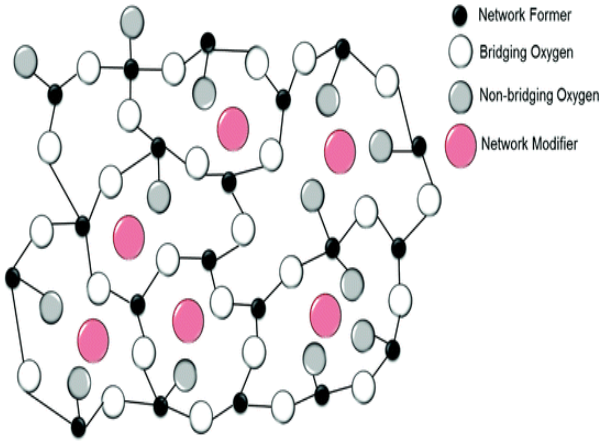

Figure I.3 An example of a glassy network.

C. Intermediate compounds

Depending on the glass composition, intermediates (e.g. titanium, zinc tantalum, or aluminium oxides or chalcogenides) can act behave either as the network formers or the network modifiers. The intermediate compounds are usually oxides or chalcogenides. They are incorporated into the former's network changing, therefore, its structure.

D. Doping Salts

The doping salts comprise compounds such as halides, phosphates, or sulfates with the same cation as the modifier. For these components, the vitreous matrix (network former + network modifier) acts as a solvent. The choice of the doping salts to be added is related to the desired property/application.

I.2 Chalcogenide glasses ChGs

I.2.1 History and generalities

Chalcogenide glasses are the result of the research work related to transparent materials in the infrared region. The first known work on ChGs occurred in the early fifties and focused on glasses containing amorphous selenium, arsenic sulphide and arsenic selenide [5]–[8]. The research in this domain continued and involved elements such as germanium, phosphorus, tellurium and antimony [9]–[11]. Borisova in 1981 published the first review book entirely dedicated to Chalcogenide materials with the title of "Glassy semiconductors" [12].

Chalcogenide glasses, which are among the technologically very important materials, are compounds formed primarily from chalcogen elements of group VIA such as sulphur (S), selenium (Se) or tellurium (Te). They can be mixed with one or more elements from other groups of the periodic table such as elements of group VA {Arsenic (As), Antimony (Sb), Bismuth (Bi) or Phosphorus (P)}, elements of group IVA {Germanium (Ge) or Silicone (Si)}, elements of group IIIA {Indium (In), Gallium (Ga) or Thallium (Tl)}, and/or halogens salts of group VIIA {Fluorine (F), Chlorine (Cl), Bromine (Br) or Iodine (I)}, **Figure I.4**.

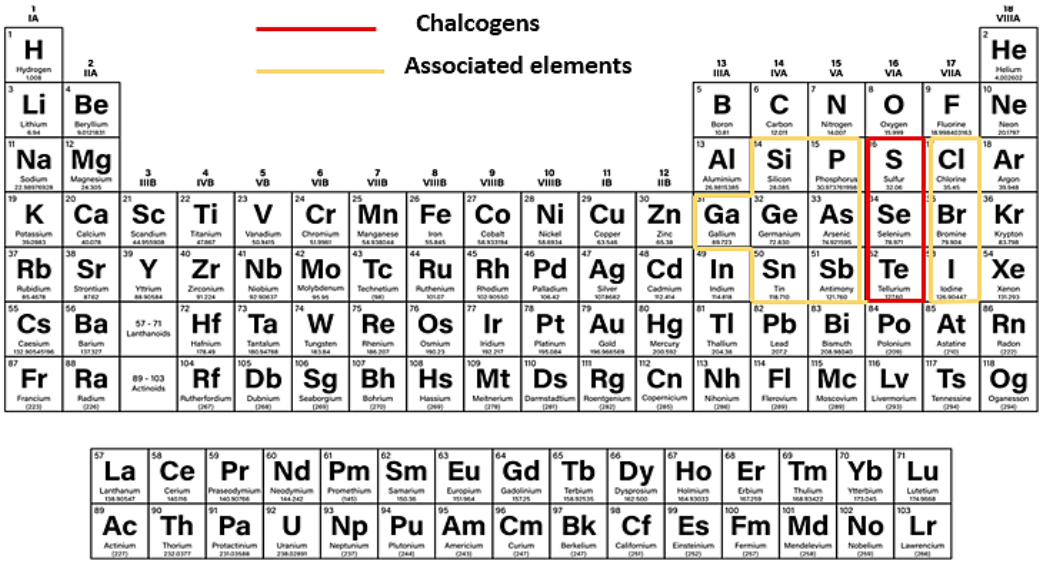

Figure I.4 Periodic table showing the chalcogen elements (red) and the main elements (yellow) that can be associated with them to form chalcogenide glasses.

This considerable glass forming capability with many elements of the Periodic Table makes it possible to vary the composition of chalcogenide glasses over a wide range, resulting in changes in physical and chemical properties. As such, ChGs come in a variety of colours that depend on

their chemical constituents, ranging from partially transparent to completely opaque. In contrast with silica, for example, which is predominantly a passive material, chalcogenides exhibit active properties and are highly nonlinear. In addition, they are glassy semiconductors, which give them interesting electrical properties.

I.2.2 Potential applications

Due to the considerable ability to be doped with a large number of elements of the periodic table, mentioned earlier, chalcogenide glasses are considered as suitable model materials to verify theories of glass formation, network rigidity, ionic and electronic transport in disordered systems, etc. [13]–[15]. They appear to be suitable for various solid-state devices and a large number of advanced applications, **Figure I.5**. Owing to their unique low phonon energy (200–300 cm^{-1}), high transparency in the near- and mid-infrared, high photosensitivity under laser beam, they have been used in many optical applications such as fibers [16], waveguides [17], [18], and solar cells [19]. In addition, the chalcogenide glasses show the largest non-resonant third-order non-linear susceptibility among inorganic glasses [20], [21], therefore they have been extensively investigated for telecommunication applications. They are also used in the field of environmental monitoring and industrial process control as sensible membranes in ion selective electrodes (ISE) for the detection of heavy metal (Cu^{2+}, Pb^{2+}, Cd^{2+}, Zn^{2+}, Ag^{+}) and toxic anions in solution [22]–[28]. The low detection limit and selectivity, long-life time, and fast response of the chalcogenide glasses make them commercially more favorable than the available sensors [29]. In addition, the high ionic conductivity obtained after doping the glasses with lithium or sodium ions permits their use as vitreous electrolytes for all solid-state batteries in rechargeable power systems [30], [31].

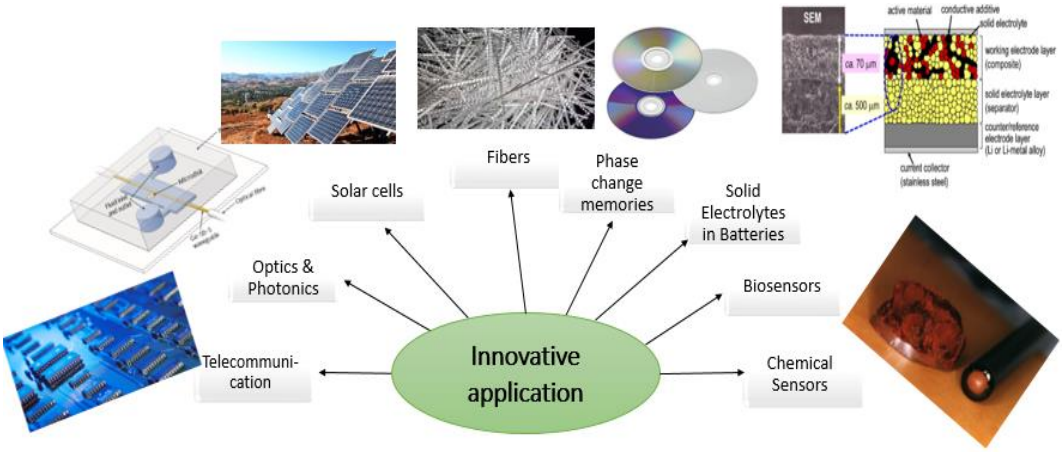

Figure I.5 Some applications of chalcogenide glasses.

I.3 Presentation of the different systems studied

The work of this thesis is mainly focused on the synthesis and characterization of sulfur-based glasses for the application of active membranes in lead (Pb) potentiometric chemical sensors. To achieve our target, we decided to work with two systems: the quasi-binary PbS-As_2S_3 and the pseudo-ternary AgI-PbS-As_2S_3. The basic and electronic properties of the PbS-As_2S_3 glasses were studied in the past [32]–[34], however, the relationship between the glass and crystal characteristics have not been established. Hence, the novelty in this work would be to (1) compare the glass-forming domain in the pseudo-binary system obtained by usual melt-quenching and mechanical milling and (2) analyse the macroscopic and electrical glass properties in comparison with their crystalline counterparts: $PbAs_2S_4$, $Pb_5As_9S_{18}$ and $Pb_2As_2S_5$, and the annealed glasses yielding glassy/crystalline alloys. To our knowledge, the pseudo-ternary AgI-PbS-As_2S_3 is being studied for the first time. Here, our objective would be (1) to synthesize and identify the vitreous domain and (2) to examine the macroscopic, electric and structural characteristics. Furthermore, the mixed lead/silver chalcogenide glasses were examined as active membrane materials for the construction of Pb(II) ion-selective sensors, Pb(II)–ISE. The choice of this later system can be justified by 3 factors: (1) the arsenic sulfide As_2S_3 glasses act as network formers, (2) the silver iodide AgI has excellent ionic conductivity and a good conduction is a necessary condition for a proper functioning of the developed sensors and (3) lead sulfide PbS allows both the integration of Pb^{2+} ions in the vitreous system and the ionic exchange with the aqueous solution.

I.4 Synthesis of chalcogenide glasses

I.4.1 Synthesis techniques

Two different methods were employed in the synthesis of our chalcogenide glasses: (1) the classical melt quenching technique and (2) the mechanical milling technique.

(1) For the classical synthesis technique, the experimental setup used during synthesis is shown in **Figure I.6**. It is composed of different parts:

- A vacuum pump to reach a vacuum of 10^{-5}-10^{-6} mbar.
- An impurities trap cooled with liquid nitrogen to protect the vacuum pump against the fumes produced from the various elements and to avoid the contamination of the ambient atmosphere.

- A well cleaned silica tube to which the high purity starting materials were introduced. The tubes were first cleaned with an aqua regia (a mixture of acids: $^1/_3$ HNO_3 and $^2/_3$ HCl) for several hours, then rinsed with water and alcohol and finally dried in the stove.

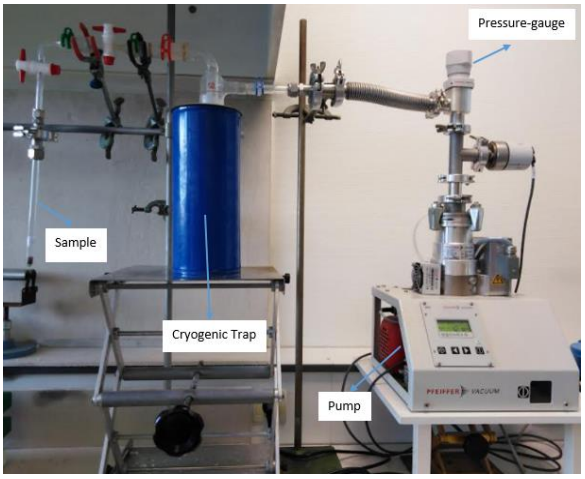

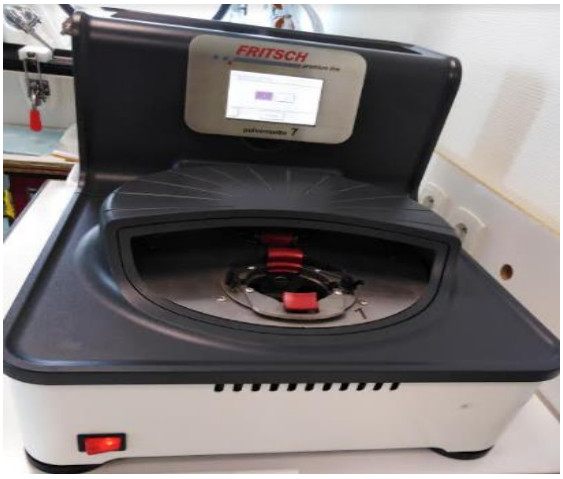

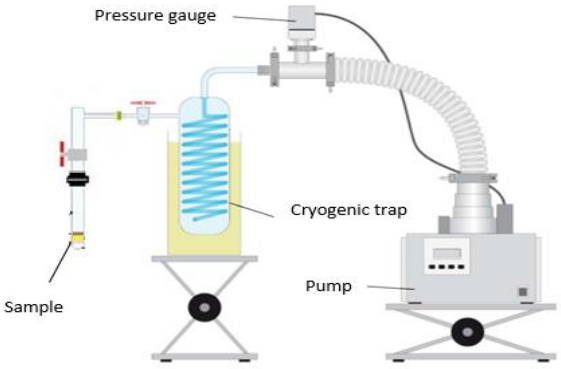

Figure I.6 The experimental setup used for the synthesis of the glasses.

Figure I.7 Pulverisette 7 premium line used in our LPCA laboratory.

(2) For the mechanical milling technique, the glasses were prepared using a planetary micro-mill Pulverisette 7 premium line (Fritsch GmbH, Germany). The starting materials were milled using a zirconia jar and ZrO_2 grinding balls under argon atmosphere (**Figure I.7**).

I.4.2 Glass synthesis: PbS-As_2S_3 and AgI-PbS-As_2S_3 systems

As mentioned before, the melt-quenching method in evacuated silica tubes was employed for the synthesis of bulk lead thioarsenate $(PbS)_x(As_2S_3)_{1-x}$ alloys, $0.0 \leq x \leq 0.7$. To this end, lead sulphide PbS (Sigma-Aldrich 99.9%) and arsenic sulphide As_2S_3 were mixed in appropriate quantities. As_2S_3 was prepared using arsenic pieces (99.9999% pure, Cerac) and sulphur pellets (99.999% pure, Acros Organics) and the obtained melt was air quenched from 650 °C to room

temperature to obtain the red colored glass. The silica ampoules (8 mm ID/10 mm OD) containing the mixture were heated for 24 h at 600–650 °C before being quenched in a cold salt–water mixture, **Figure I.8**. Each sample composition prepared had a mass of 3 g. The same procedure was employed for the synthesis of the pseudo-ternary AgI-PbS-As_2S_3 glasses. The starting materials were silver iodide AgI, PbS and As_2S_3. However, the heat temperature applied for homogenization was 700-750 °C depending of the alloy composition.

The mechanical milling technique (MM) was also employed for the synthesis of MM-$(PbS)_{0.6}(As_2S_3)_{0.4}$ and MM-$(PbS)_{0.7}(As_2S_3)_{0.3}$ samples. In each case, 3 g of starting materials were milled using the planetary micro-mill Pulverisette 7 premium line (Fritsch GmbH, Germany) under argon atmosphere. The mixtures were milled using a zirconia jar (45 mL) and ZrO_2 grinding balls (23 balls with 10 mm in diameter) at a speed of 320 rpm for 50 hours.

I.4.3 Crystal synthesis: Pb-As-S system

Three different crystals were prepared successfully in the Pb-As-S system via the thermal synthesis procedure in cleaned silica tubes sealed under vacuum (10^{-6} mbar). The crystals were dufrénoysite $Pb_2As_2S_5$ (22.22 at.% Pb), baumhauerite $Pb_5As_9S_{18}$ (15.62 at.% Pb) and sartorite $PbAs_2S_4$ (14.28 at.% Pb). We also note that these Pb-As-S compounds belong to the lead-sulphosalts that exist as natural minerals. For $Pb_2As_2S_5$, the two compounds PbS and As_2S_3 were mixed in a ratio 2:1, heated slowly up to 800 °C, homogenized at this temperature for 24h before being cooled down and annealed at 350 °C for 10 days, **Figure I.9**. $Pb_5As_9S_{18}$ was obtained by applying the same procedure for nearly equimolar ratio 5:4.5. Finally, $PbAs_2S_4$ was obtained using the equimolar ratio 1:1 and the annealing temperature was 280 °C for 20 days.

Figure I.8 Image of lead sulfide thioarsenate glasses synthesized via classical quenching method.

Figure I.9 Image of the crystal dufrénoysite $Pb_2As_2S_5$ synthesized in LPCA laboratory.

I.5 Characterization of chalcogenide glasses

In this chapter, the nature of the obtained alloys (amorphous vs. crystalline) as well as their physico-chemical properties (density, mean atomic volume, morphology, thermal temperatures) were studied using different methods such as density measurements, XRD, SEM, DSC.

I.5.1 X-ray diffraction analysis (XRD)

The vitreous/crystalline nature of the synthesized samples was determined from the X-ray diffraction patterns (XRD) obtained using a Bruker D8 Advance diffractometer at room temperature. This latter was equipped with a copper anticathode emitting Kα radiation, a LinxEye detector, a goniometer θ/θ and a rotating sample holder. The scattering intensities were measured over the angular range of $10° \leq 2\theta \leq 80°$ with a step-size of 0.02° and a count time of 2 s per step. The glassy samples were identified from the absence of Bragg peaks in the XRD patterns owing to the lack of long-range order in amorphous materials. Meanwhile, the samples presenting Bragg peaks were considered as crystallized and the crystalline phases were recognized via the comparison of the positions of the Bragg peaks obtained with those of reference compounds in the JCPDS database (Joint Committee on Powder Diffraction Standards) was made.

I.5.2 Density, mean atomic volume and glass packing density

Density is an important macroscopic property since it is related to other physical properties of the material. To obtain the density values *d* of the synthesized samples, a Sartorius YDK 01-OD density kit and a hydrostatic method (toluene as immersion fluid and germanium (5.323 g cm-3) as standard) were used for density *d* measurements. The formula utilized for density calculation is as follows:

$$d = \frac{m_{air}^{sample}}{m_{air}^{sample} - m_{toluene}^{sample}} \times d_{toluene} \qquad \text{(I.1)}$$

where m_{air}^{sample} the mass of the sample weighed in the open air, $m_{toluene}^{sample}$ is the mass of the weighed sample immersion toluene and $d_{toluene}$ is the density of toluene.

Using the density values, both the average glass mean atomic volume V_a and the glass packing density ρ (the ratio between $V_a^0$and V_a) were calculated using the equations (I.2) and (I.3), respectively. We define V_a^0 as the average atomic volume of the glass constituents that is calculated using glass stoichiometry and ionic radii (Eq. I.4). We also define c_i as is the atomic

fraction of the element *i*, M_i the atomic mass, r_i the Shannon ionic radius and N_A the Avogadro constant.

$$V_a = \frac{\sum_i C_i M_i}{d N_A} \quad \text{(I.2)}$$

$$\rho = \frac{V_a^0}{V_a} \quad \text{(I.3)}$$

$$V_a^0 = \sum_i c_i \frac{4\pi}{3} r_i^3 \quad \text{(I.4)}$$

I.5.3 Scanning Electron Microscopy (SEM)

The scanning electron microscopy (SEM) allows investigating the morphology of the synthesized samples and assessing their composition through EDX. It produces images of a sample surface by scanning the surface with a focused beam of electrons. The process is upfront: two-sided carbon tape is fixed to an SEM sample stub and the sample is then set on the surface and examined in an SEM chamber; A carbon coating could be applied or not depending on the conductivity of the sample. SEM images are created following the scanning of the sample surface by an incident electron beam and the detection of the emitted backscattered or the secondary electrons. When a cathode emits electrons under the application of a very high electric field, it is also known as a field emitter-FE- SEM which gives better images. In this work, a JEOL JSM-7100F thermal field emission scanning electron microscope equipped with three EDX Bruker QUANTAX 800 spectrometers (3 x 30 mm^2) was used to check the sample uniformity, **Figure I.10**. This permits both surface observation and elemental analyses.

Figure I.10 The scanning electron microscopy (SEM), available at LPCA, used to examine the morphology of the synthesized samples and estimate their composition through EDX.

I.5.4 Differential Scanning Calorimeter measurements (DSC)

The differential scanning calorimetry (DSC) is an analytical technique that is used to measure the characteristic temperatures and heat flows associated with different thermal phenomena that may occur during the heating or cooling of materials. As such, the glass transition T_g and the crystallization temperatures T_x, for all glassy samples, were obtained via differential scanning calorimetry DSC experiments carried out using a TA Q200 instrument. To obtain the average characteristic temperatures, 3 to 4 tests per sample were performed and the samples mass was 3 to 15 mg. The samples were hermetically sealed in standard aluminium capsules and then heated in the temperature range 20-450 °C under nitrogen flow. The heating rate was 10 K min^{-1} and an empty aluminium pan served as a reference.

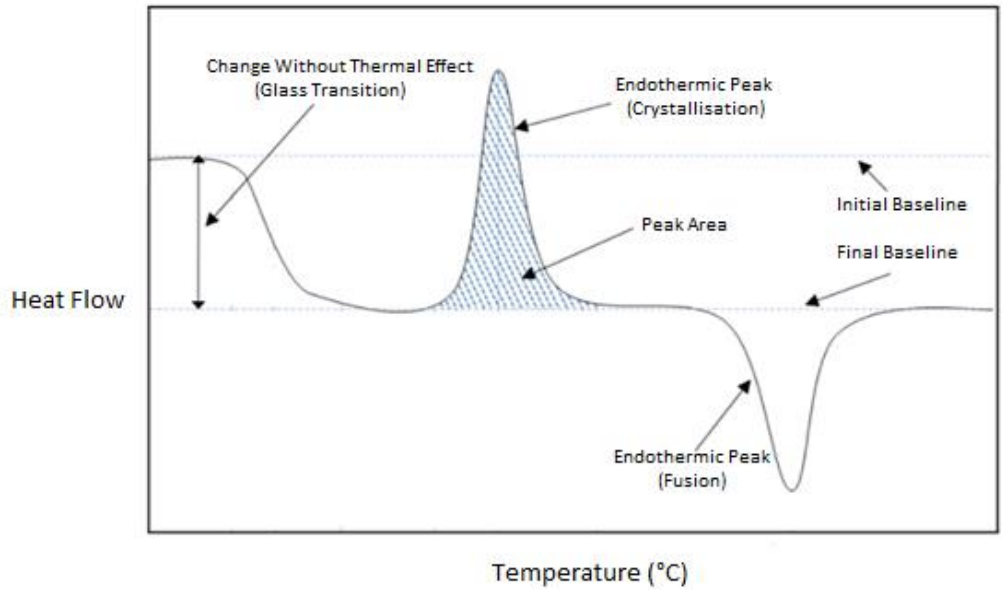

Figure I. 11 Typical DSC curve for a multicomponent chalcogenide glass with characteristic temperatures.

The glass transition temperature is a property of amorphous materials or the amorphous portion of a semi-crystalline materials; it corresponds to an endothermic feature and obtained via the intersection two linear portions [35] adjoining the transition bend of a DSC thermogram. Before this temperature, the glass is in the solid state (infinite viscosity), at T_g, the viscosity is 10^{13} poises and beyond this temperature, the viscosity decreases continuously and gradually with temperature. When the viscosity becomes weak, the high mobility of atoms allows them to re-organize and the atomic structure to re-arrange, this is how crystallization occurs. In thermal analysis, crystallization is characterized by an exothermic peak, **Figure I. 11**. The difference

between these two values, that is the parameter $\Delta T = T_x - T_g$, gives an indication about the stability of the glass facing crystallization. The larger ΔT, the greater is the stability of the glass, and the molding of the material by heating above its glass transition temperature is realizable.

I.6 The vitreous domains of quasi-binary and pseudo-ternary glasses

I.6.1 Quasi-binary $(PbS)_x(As_2S_3)_{1-x}$

I.6.1.1 Glass forming-region and morphology

To verify the amorphous nature of the obtained bulk $(PbS)_x(As_2S_3)_{1-x}$ alloys, $0.0 \leq x \leq 0.7$, both laboratory X-ray and hard X-ray diffraction techniques were employed. **Figure I. 12(a)** shows the X-ray structure factor $S_X(Q)$ for the two x = 0.10 (lead-poor) and x = 0.50 (lead rich) compositions. The absence of Bragg peaks in both cases is a clear indication that these compositions are glasses. The glassy nature of the x = 0.60 and x = 0.70 compositions, synthesized via melt-quenching technique, was analysed using laboratory X-ray diffraction.

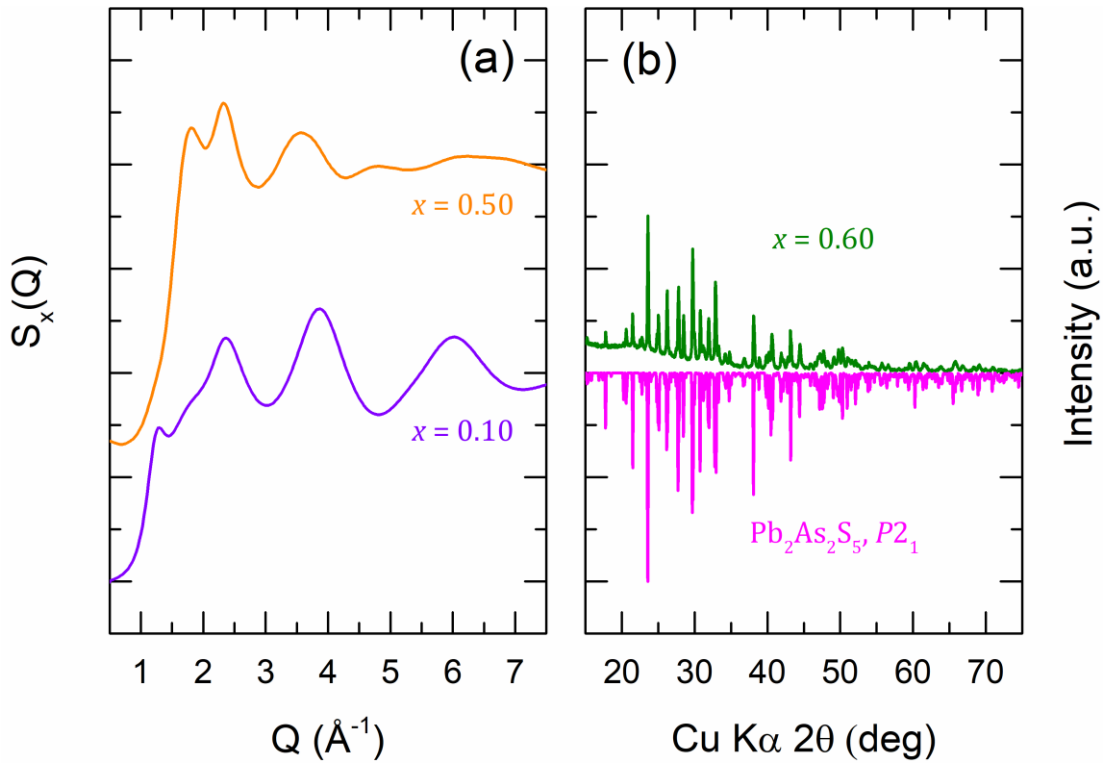

Figure I. 12 (a) X-ray structure factor $S_X(Q)$ for the x = 0.10 and x = 0.50 glass compositions (preliminary high-energy X-ray diffraction results). (b) Diffraction pattern for the x = 0.60 composition prepared by melt-quenching method. The main crystalline phase corresponds to monoclinic dufrénoysite $Pb_2As_2S_5$, space group $P2_1$ [36].

The observed intense Bragg peaks, seen for both x = 0.60 (**Figure I. 12 (b)** and **Figure I. 13**) and x = 0.70 (**Figure I. 13**), correspond to monoclinic $Pb_2As_2S_5$ (dufrénoysite), space group $P2_1$ [36]. Nevertheless, we should note that the x = 0.60 sample contains both vitreous and crystallised parts. Previously, a vitreous domain that extends up to x = 0.62 was reported for $(PbS)_x(As_2S_3)_{1-x}$ alloys [32], [34], [37]. However, it was clearly indicated that for the x = 0.62 composition, it was difficult to obtain glass pieces of sufficient dimensions [37].

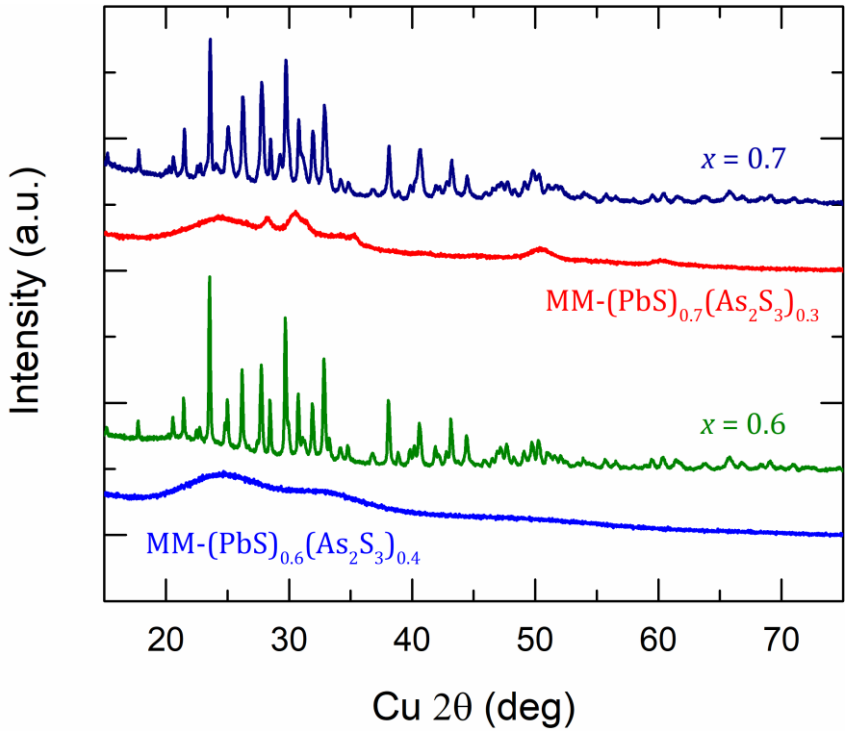

Figure I. 13 Diffraction patterns for the x = 0.60 and x = 0.70 compositions obtained by melt quenching in silica tubes and mechanical milling. In melt-quenched samples, monoclinic $Pb_2As_2S_5$, space group $P2_1$, seems to be the major crystalline species. MM-$(PbS)_{0.6}(As_2S_3)_{0.4}$ appears to be vitreous (blue curve), while MM-$(PbS)_{0.7}(As_2S_3)_{0.3}$ (red curve) seems to remain glassy/crystalline.

The mechanical milling (MM) technique was used to further extend the vitreous domain. **Figure I. 13** shows that MM-$(PbS)_{0.6}(As_2S_3)_{0.4}$ appears to be completely vitreous, the Bragg peaks of crystalline dufrénoysite have completely disappeared (blue curve). In contrast, broad features, reminiscent of Bragg peaks for $Pb_2As_2S_5$, persist in MM-$(PbS)_{0.7}(As_2S_3)_{0.3}$; and this composition can be classified as glass-ceramic (red curve). Hence, according to this work, we can conclude that the vitreous domain for the bulk $(PbS)_x(As_2S_3)_{1-x}$ alloys lies in the range, $0.0 \leq x \leq 0.7$ (**Figure I. 14**).

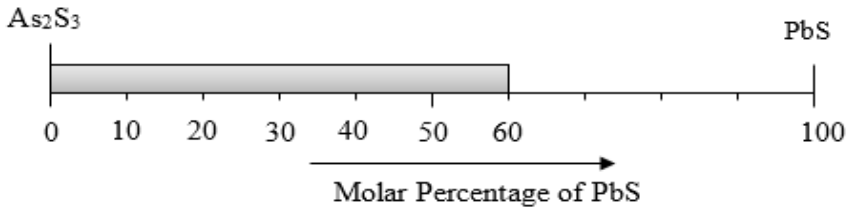

Figure I. 14 The vitreous domain of the quasi-binary system $(PbS)_x(As_2S_3)_{1-x}$.

To highlight possible microstructural changes of the studied $(PbS)_x(As_2S_3)_{1-x}$ alloys, SEM analysis has been performed on few selected compositions. The SEM images are presented in **Figure I. 15** and **Figure I. 16**. It can be clearly seen that the alloys with x = 0.10, 0.30 and 0.60, obtained by melt-quenching, are rather smooth and homogeneous, **Figure I. 15(a-c)**. It should also be noted that for the x = 0.6 sample a vitreous part was chosen for SEM studies. Meanwhile, the morphology of the x = 0.7 composition is quite different; particles of different shapes and sizes are seen, **Figure I. 15(d)**. The size of these particles varies from 1 µm or less up to 15-20 µm. In a similar manner, a SEM micrograph is presented for the powdered glassy MM-$(PbS)_{0.6}(As_2S_3)_{0.4}$ composition, **Figure I. 16(a)**. The observed particles are in the micrometer range. Further analysis, using energy-dispersive X-ray spectroscopy (EDX), shows the morphology and element distribution of the glassy MM-$(PbS)_{0.6}(As_2S_3)_{0.4}$ sample. The constituent elements (Pb, As and S) are evenly and densely distributed over the microparticles of the MM-glass, **Figure I. 16(b-d)**.

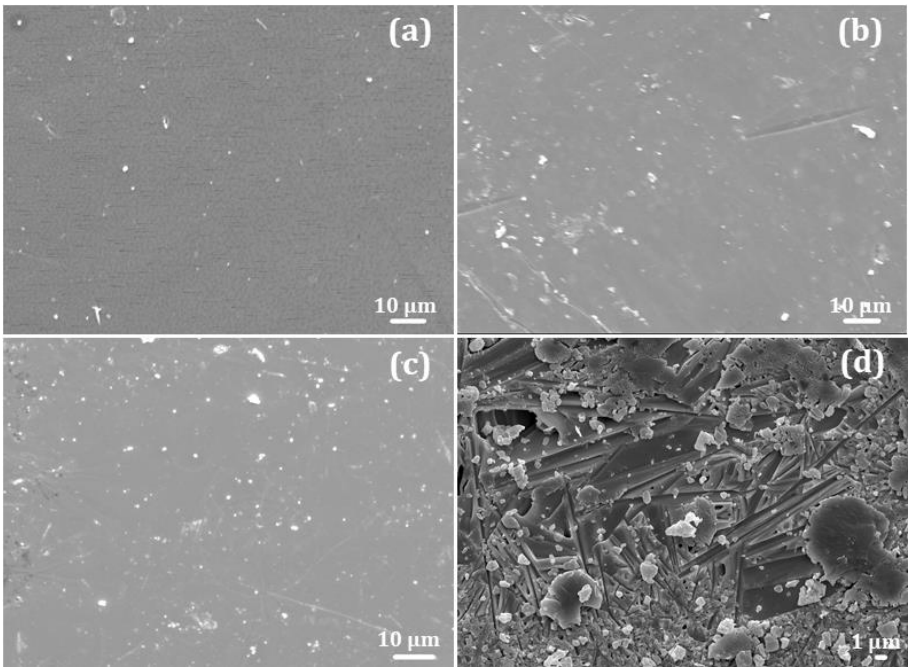

Figure I. 15 SEM micrographs for selected compositions in the $(PbS)_x(As_2S_3)_{1-x}$ system prepared by melt quenching: (a) x = 0.10, (b) x = 0.30, (c) x = 0.60 and (d) x = 0.70.

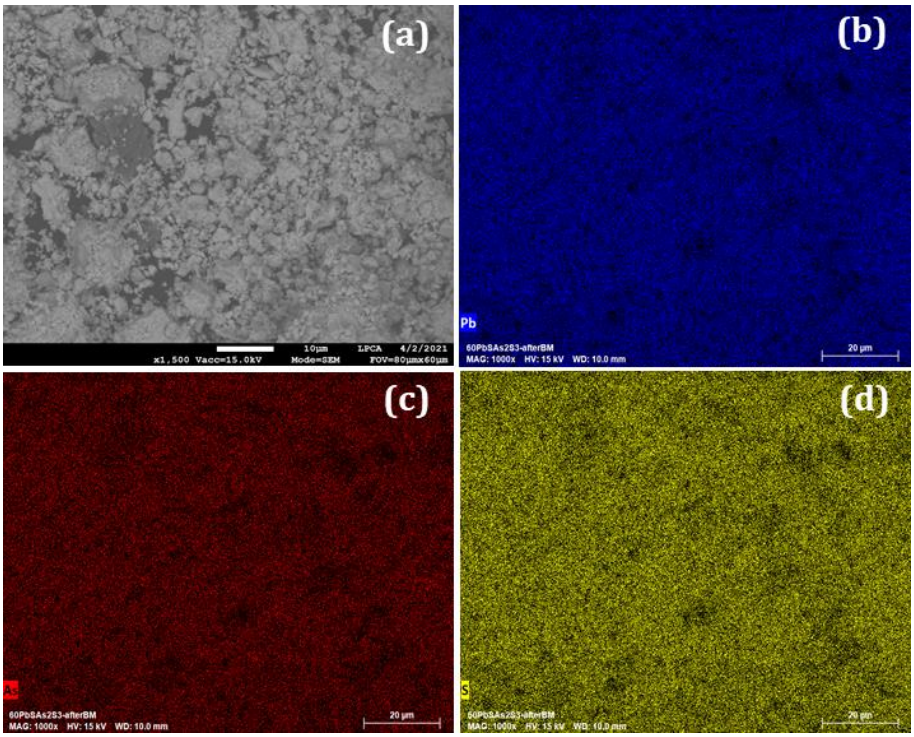

Figure I. 16 (a) SEM micrograph for the glassy MM-$(PbS)_{0.6}(As_2S_3)_{0.4}$ sample and (b-d) corresponding EDX element mapping of Pb (blue), As (dark red) and S (yellow), respectively.

I.6.1.2 Density, mean atomic volume and glass packing density of PbS-As_2S_3 glasses

The obtained density values d of the $(PbS)_x(As_2S_3)_{1-x}$ samples, $0.1 \leq x \leq 0.7$, are presented in **Table I. 1**. The characteristic glass transition and crystallisation temperatures are also present. When possible, both density and thermal temperature values, taken from the corresponding references, are listed in **Table I. 1**. We note that, in literature and for both parameters, data are absent for many compositions in the current quasi-binary PbS-As_2S_3 system.

As mentioned before, using the density values, both the average glass mean atomic volume V_a and the glass packing density ρ {see section I.5.2}. **Figure I. 17** shows the composition dependence of the above three parameters, that is, d, V_a and ρ, as a function of the lead sulphide PbS content x. The density increases monotonically with x (**Figure I. 17(a)**). This trend continues even for the two crystallised compositions x = 0.6 and x = 0.7 obtained by melt-quenching (**Table I. 1**). In fact, the $(PbS)_x(As_2S_3)_{1-x}$ glass density extrapolated to hypothetical PbS glass at x = 1 gives a similar density value to crystalline fcc PbS. Such behaviour makes sense as the density of cubic PbS (d_{PbS} = 7.6 g.cm^{-3} [38]) is much higher than that of the As_2S_3 glassy matrix ($d_{g\text{-}As2S3}$ = 3.19 g.cm^{-3}) or crystalline orpiment As_2S_3 ($d_{c\text{-}As2S3}$ = 3.46 g.cm^{-3} [39]).

Figure I. 17(a) also shows that the obtained density values for melt-quenched $(PbS)_x(As_2S_3)_{1-x}$ are similar to those reported by Katyal et al. [40] (see the dashed black line). On the contrary, the mean atomic volume V_a shows a gradual monotonic decrease from 15.44±0.24 cm^3 mol^{-1} (x = 0.0) to 14.75±0.25 cm^3 mol^{-1} (x = 0.7), **Figure I. 17(b)**. The trend is reversed for the glass packing density ρ increasing with x from 0.62 (x = 0.0) to 0.66 (x = 0.7), **Figure I. 17(c)**.

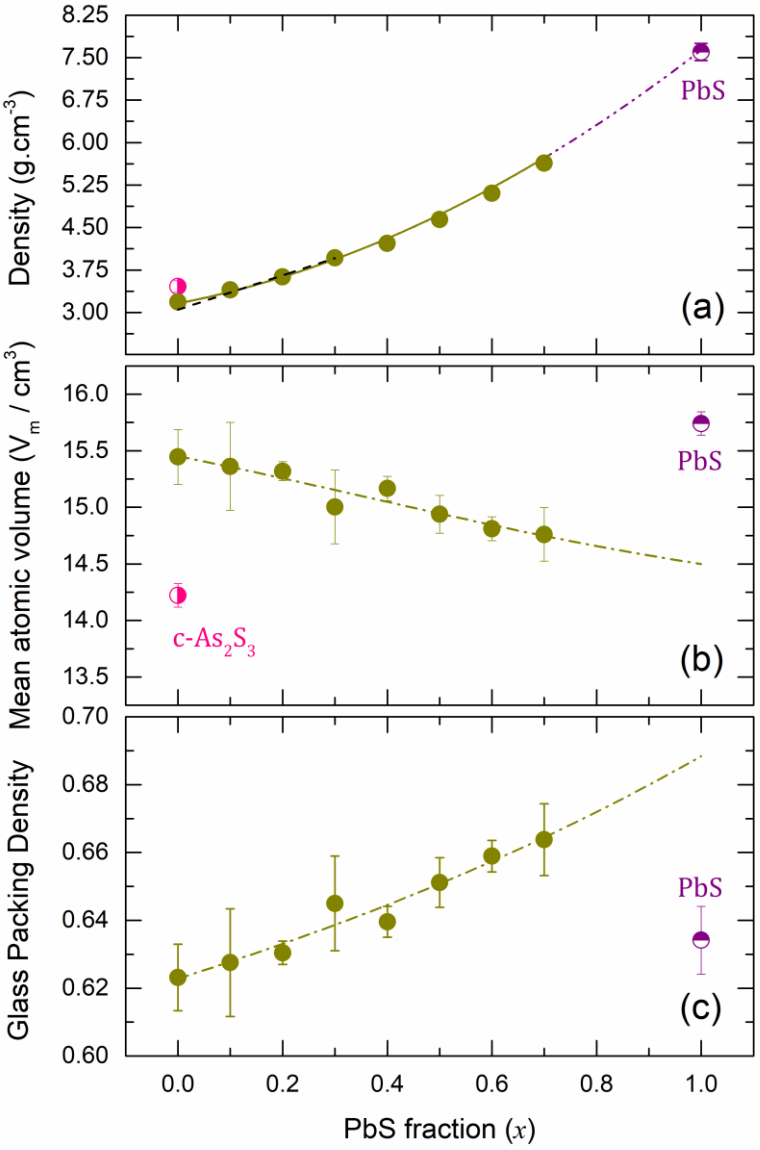

Figure I. 17 (a) Density, (b) mean atomic volume and (c) glass packing density of the $(PbS)_x(As_2S_3)_{1-x}$ alloys plotted as a function of the lead sulphide content. The data corresponding to density and mean atomic volume of orpiment c-As_2S_3 [39] and crystalline lead sulphide PbS [38] are also plotted. The black dashed line seen in Fig.(a) is a reproduction of the density values taken from reference [40].

The extrapolation of the mean atomic volume to a hypothetical PbS glass at x = 1 suggests a denser packing of the latter compared to cubic PbS, **Figure I. 17(b)**. A modifier-like behaviour or chemically-driven densification might account for such decrease as the originally open g-As_2S_3 network structure (44.1% of voids [41]) becomes more compact upon PbS addition. The increasing glass packing density with x is consistent with this hypothesis, as well as the packing density for cubic PbS, ρ_{PbS} = 0.634, **Figure I. 17(c)**.

An alternative approach is related to lower lead coordination number N_{Pb-S} and shorter r_{Pb-S} interatomic distances in glassy lead thioarsenates compared to fcc PbS (N_{Pb-S} = 6, r_{Pb-S} = 2.967 Å) [42]. In fact, our preliminary high-energy X-ray diffraction results (see chapter 3) indicate that r_{Pb-S} = 2.83 Å and $N_{Pb-S} \approx 4$, coherent with denser glass packing.

Table I. 1 Density, glass transition temperature (Tg) and crystallization temperature (Tx) of the binary glass system $(PbS)_x(As_2S_3)_{1-x}$. Glass forming and thermal stability criteria are also given: ΔT =Tx - Tg.

Composition	Density (g.cm^{-3})		T_g (°C) (±3)		T_x (°C) (±3)				ΔT (°C) (±3)	
					T_{x1}		T_{x2}	T_{x3}		
		[33]		[34]		[34]				[34]
0.0	3.19 (5)	3.03	197	185	-	-	-	-	-	-
0.1	3.39 (8)	3.38	184	195	239	235	248	315	55	40
0.2	3.63 (2)	-	183	-	237	-	250	314	54	-
0.3	3.97 (9)	3.95	187	205	238	244	252	314	51	39
0.4	4.22 (3)	-	188	-	238	-	251	314	50	-
0.5	4.64 (5)	-	197	195	238	230	-	309	41	35
0.6*	5.11 (3)	-	196	-	235	-	315	306	31	-
0.7*	5.64 (9)	-	-	-	-	-	-	-	-	-
0.6**	-	-	187	-	271	-	-	315	49	-
0.7**	-	-	174	-	270	-	-	312	60	-

Uncertainties in the last digit(s) of the parameter are given in parentheses.
* Samples obtained by melt quenching
** Samples obtained by mechanical milling

I.6.1.3 Thermal properties

The characteristic glass transition T_g and crystallization temperatures T_x of the pseudo-binary $(PbS)_x(As_2S_3)_{1-x}$ alloys, $0.0 \leq x \leq 0.7$, are listed in **Table I. 1** along with the calculated values

for the ΔT parameter, $\Delta T = T_g - T_{x1}$, where T_{x1} corresponds to the first crystallization peak. In **Table I. 1**, we distinguish between the x = 0.60 and 0.70 compositions obtained by melt quenching* and mechanical milling**. Despite the overall crystalized state of the x = 0.60* sample, a tiny vitreous piece of sufficient dimensions, enough for DSC, was obtained. Typical DSC traces of the glassy lead thioarsenate samples ($0.10 \leq x \leq 0.50$), obtained by classical melt-quenching, are plotted in **Figure I. 18**. The traces show both endothermic and exothermic features corresponding to glass transition and crystallization phenomena, respectively. In contrast, vitreous As_2S_3 shows only a glass transition. All the samples are homogenous in nature as indicates a single T_g feature. The first crystallization peak increases in intensity with x and slightly shifts towards lower temperatures, reflecting diminished glass ability. This trend is also confirmed by decreasing ΔT parameter, **Figure I. 19(c)**.

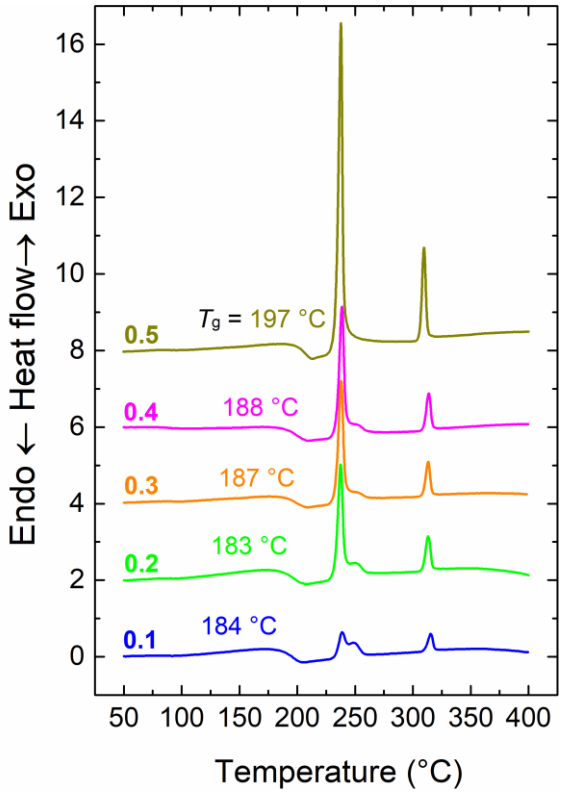

Figure I. 18 DSC traces of $(PbS)_x(As_2S_3)_{1-x}$ glassy samples, $0.1 \leq x \leq 0.5$, obtained by melt quenching.

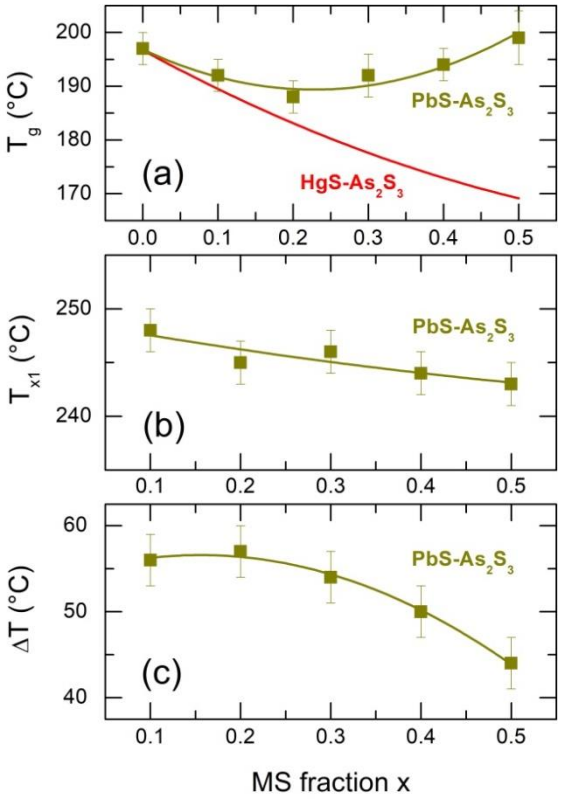

Figure I. 19 (a) Glass transition T_g, (b) first crystallisation T_{x1} temperatures, and (c) the ΔT parameter for $(PbS)_x(As_2S_3)_{1-x}$ glasses, $0.0 \leq x \leq 0.5$. The T_g values for glassy HgS-As_2S_3 [43] are also shown.

Figure I. 19(a) shows a characteristic difference between the two metal thioarsenate glassy systems: HgS-As_2S_3 [43] and PbS-As_2S_3 (this work). Mercury thioarsenate glasses exhibit a

monotonic T_g decrease related to a low mercury local coordination [43], [44], studied by pulsed neutron and high-energy X-ray diffraction. A parabolic shape of the glass transition temperature with a shallow minimum, ΔT_g = -14 °C at x = 0.2, for the PbS-As_2S_3 counterparts is indicative of a different structural organisation confirmed by preliminary diffraction results. The initial T_g decrease seems to be related to a partial fragmentation of a quasi-continuous As_2S_3 glass matrix [41], observed experimentally and confirmed by computer modelling for a number of glassy thioarsenates and thiogermanates [44]–[46]. The increasing T_g at $x > 0.2$ might be related to presumably tetrahedral connectivity of lead species which will be verified by further diffraction analysis and first-principles molecular dynamics. Our DSC results are roughly similar to previously published data [34], [37].

I.6.2 Pseudo-ternary AgI-PbS-As_2S_3

I.6.2.1 Glass forming-region and morphology

The study of the pseudo-ternary AgI-PbS-As_2S_3 system has revealed a very large vitreous domain, **Figure I.20**. In order to confirm the glassy state of our samples, many compositions were analyzed by X-ray diffraction. For the characterized samples with no diffraction peak, only a broad feature characteristic of the glassy state is observed. The glassy samples are represented by circles whereas the crystalline ones are represented by stars, **Figure I.20**. Regarding the diagram, it is clearly seen that the vitreous domain is concentrated in the arsenic sulfide As_2S_3-rich corner and covers an important diagram surface. To detail, the studies of the glass forming region were carried out on the basis of the following three series:

- $(AgI)_x(PbS)_{0.5-x/_2}(As_2S_3)_{0.5-x/_2}$; $(0.0 \leq x \leq 0.6)$
- $(AgI)_{0.3}(PbS)_y(As_2S_3)_{0.7-y}$; $(0.0 \leq y \leq 0.5)$
- $(AgI)_z(PbS)_{0.1}(As_2S_3)_{0.9-z}$; $(0.0 \leq z \leq 0.5)$

The two series A and C represent compositions with increasing AgI content. Meanwhile, for the series B, it is the PbS content that increases.

The XRD patterns of the A-series (**Figure I.21**), corresponding to the formula $(AgI)_x(PbS)_{0.5-x/_2}(As_2S_3)_{0.5-x/_2}$ with $0.0 \leq x \leq 0.8$, exhibits only broad features characteristic of glassy and amorphous materials up to $x \leq 0.6$. Only few low intensity Bragg peaks appear for the x = 0.7 composition; It is mostly glassy as indicated the broad feature which dominates

the XRD pattern. In contrast, for the x = 0.8 composition, the feature characteristic of the glassy nature has completely disappeared and the observed intense Bragg peaks correspond to the silver iodide crystallites (00-001-0502).

For the B-series, corresponding to substitution of As_2S_3 by PbS for a constant content of AgI (x = 0.3), the diffraction pattern is characteristic of vitreous samples up to a PbS content $y \leq 0.5$, whereas well defined Bragg peaks appear for the y = 0.6 composition and, according to JCPDC, are related to Galena, PbS, (00-001-0880).

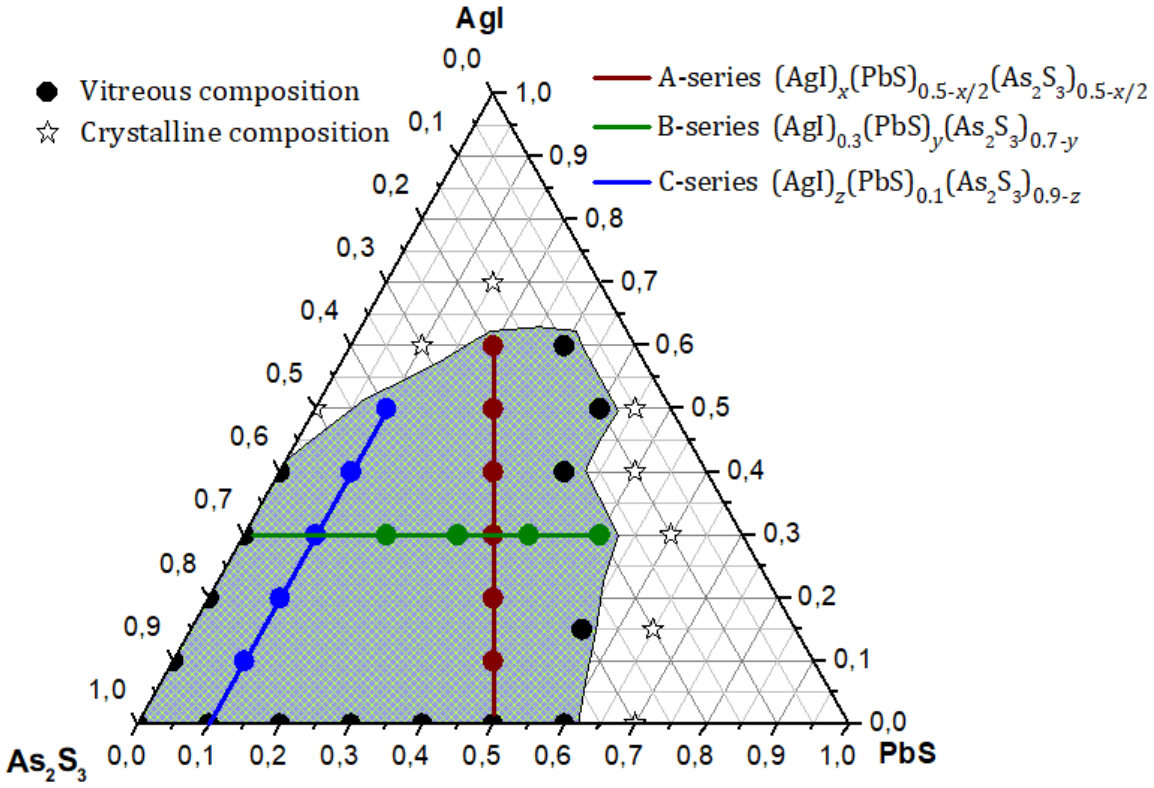

Figure I.20 Glass forming region in the quasi-binary PbS-As2S3 system and the pseudo-ternary AgI-PbS-As_2S_3 system. The axis units are mol.%. A series: $(AgI)_x(PbS)_{0.5-x/2}(As_2S_3)_{0.5-x/2}$, B series: $(AgI)_{0.3}(PbS)_y(As_2S_3)_{0.7-y}$, and C series: $(AgI)_z(PbS)_{0.1}(As_2S_3)_{0.9-z}$.

In case of the C-series, corresponding to substitution of As_2S_3 by AgI for a constant content of PbS (x = 0.1), the diffraction pattern is characteristic of vitreous samples up to an AgI content $z \leq 0.5$, whereas well defined Bragg peaks appear for the z = 0.6 composition and are related to silver iodide AgI (00-001-0502) and gamma AgI (01-009-0399).

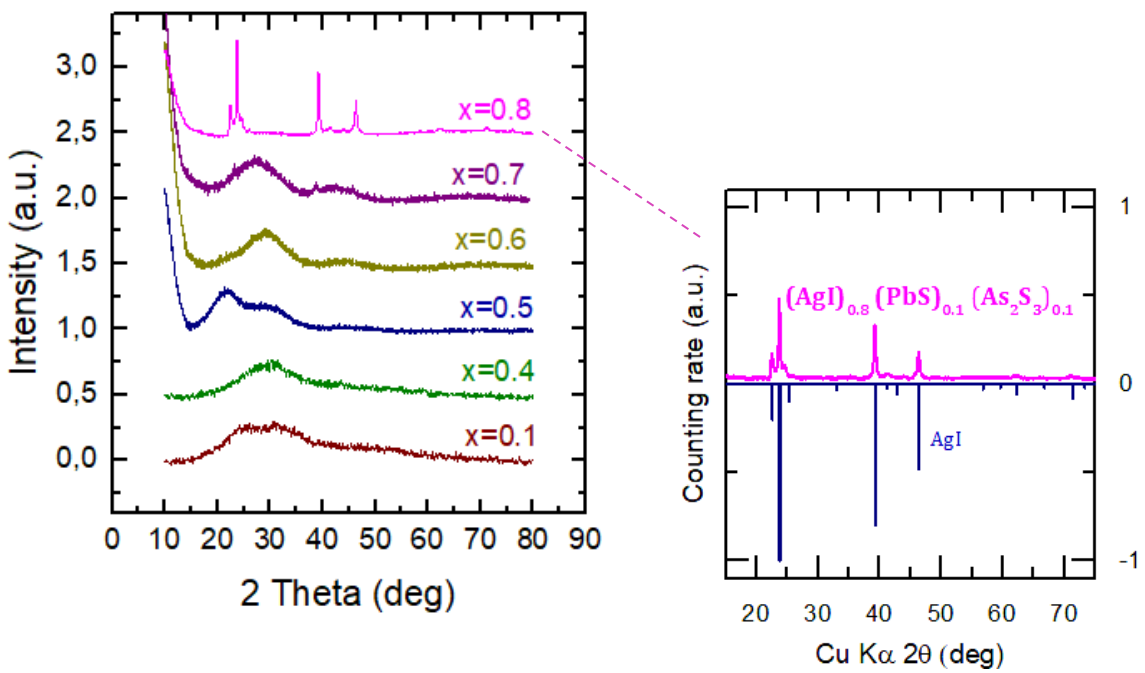

Figure I.21 XRD pattern of the A series: $(AgI)_x(PbS)_{0.5-x/_2}(As_2S_3)_{0.5-x/_2}$ with x = 0.1, 0.4-0.8.

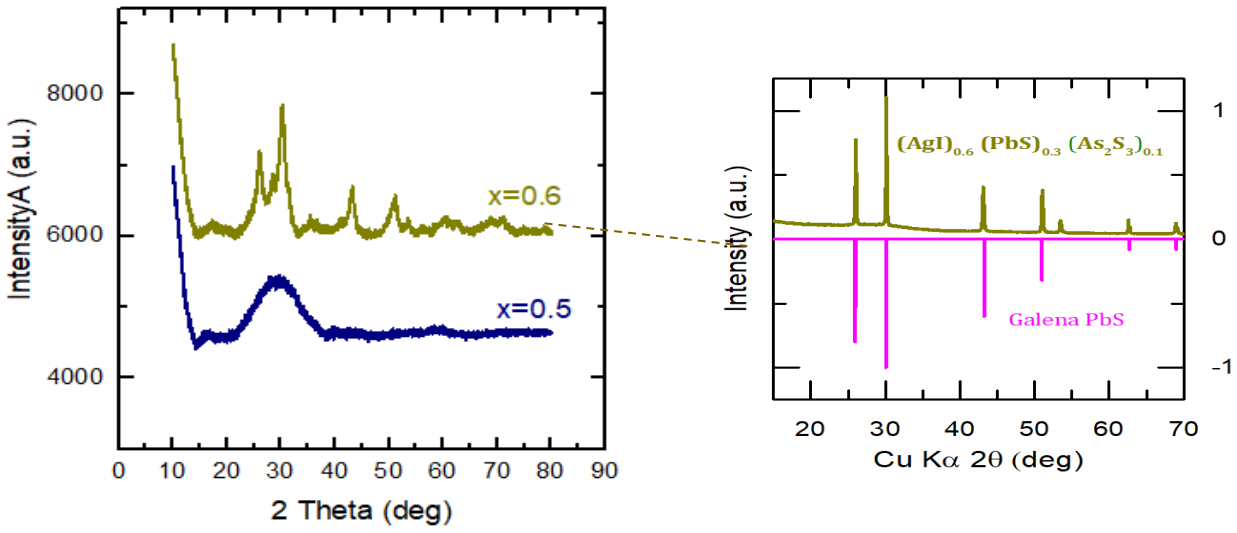

Figure I.22 XRD pattern for the B series: $(AgI)_{0.3}(PbS)_y(As_2S_3)_{0.7-y}$ with y = 0.5, 0.6.

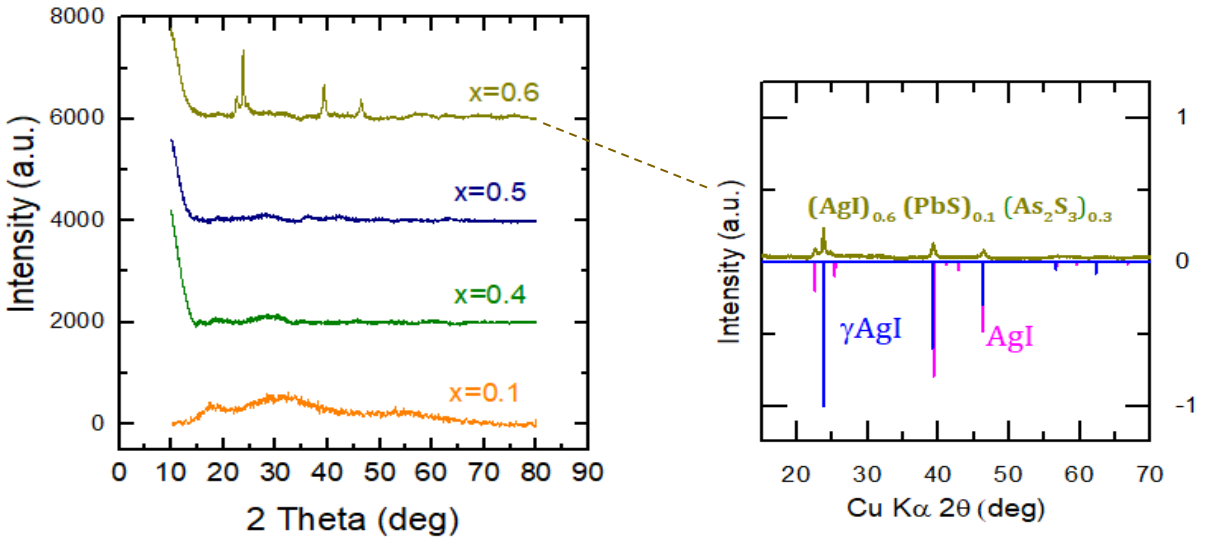

Figure I.23 XRD pattern of the C series: $(AgI)_z(PbS)_{0.1}(As_2S_3)_{0.9-z}$ with z = 0.1, 0.4-0.6.

Table I.2 Comparison between the calculated atomic percentages of the constituent elements of the glasses of A, B and C series and those obtained from X-rays measurements

Atom %	10%		50%		60%	
	SEM (X-rays)	Calculated	SEM (X-rays)	Calculated	SEM (X-rays)	Calculated
A series: $(AgI)_x(PbS)_{0.5-x/2}(As_2S_3)_{0.5-x/2}$						
S	47.71	53.73			23.84	30.76
As	27.79	26.86			15.44	15.38
Pb	17.77	13.43			10.54	7.69
Ag	2.69	2.98			24.18	23.07
I	4.03	2.98			26	23.07
B series : $(AgI)_{0.3}(PbS)_y(As_2S_3)_{0.7-y}$						
S	61.03	50	45.69	46.87		
As	30.01	31.57	25.51	25		
Pb	4.03	2.32	12.71	9.37		
Ag	3.75	7.89	8.27	9.37		
I	1.18	7.89	7.83	9.37		
C series : $(AgI)_z(PbS)_{0.1}(As_2S_3)_{0.9-z}$						
S	54.91	56.81	31.29	40.62		
As	37.26	36.36	27.32	25		
Pb	7.32	2.27	7.25	3.12		
Ag	0.43	2.27	17.4	15.62		
I	0.08	2.27	16.75	15.62		

Similarly to the alloys of the quasi-binary system, scanning electron microscopy analyses were performed on few selected compositions of the ternary system, i.e., series– A, B and C. The SEM images are presented in **Figure I.24** and **Figure I.25**.

As evidenced from the SEM images of the glasses (**Figure I.24**), the introduction of AgI (in the A-series) and PbS (in the B-series) does not show any significant effect on the glass morphology at the micro-meter spatial scale. Similarly to the studied $(PbS)_x(As_2S_3)_{1-x}$ system, one observes that the compositions with x = 0.2 and 0.5 (the A-series) and with z = 0.2 and 0.5(the B-series) are smooth and homogenous in general, **Figure I.24(a-b)** and **Figure I.24(c-d)**, respectively. Also, the distribution of the constituent elements of the glasses obtained from energy-dispersive X-ray spectroscopy (EDX) measurements are listed in **Table I.2**; the atomic percentage of the elements (As, Pb, S, Ag, and I) are comparable with those calculated.

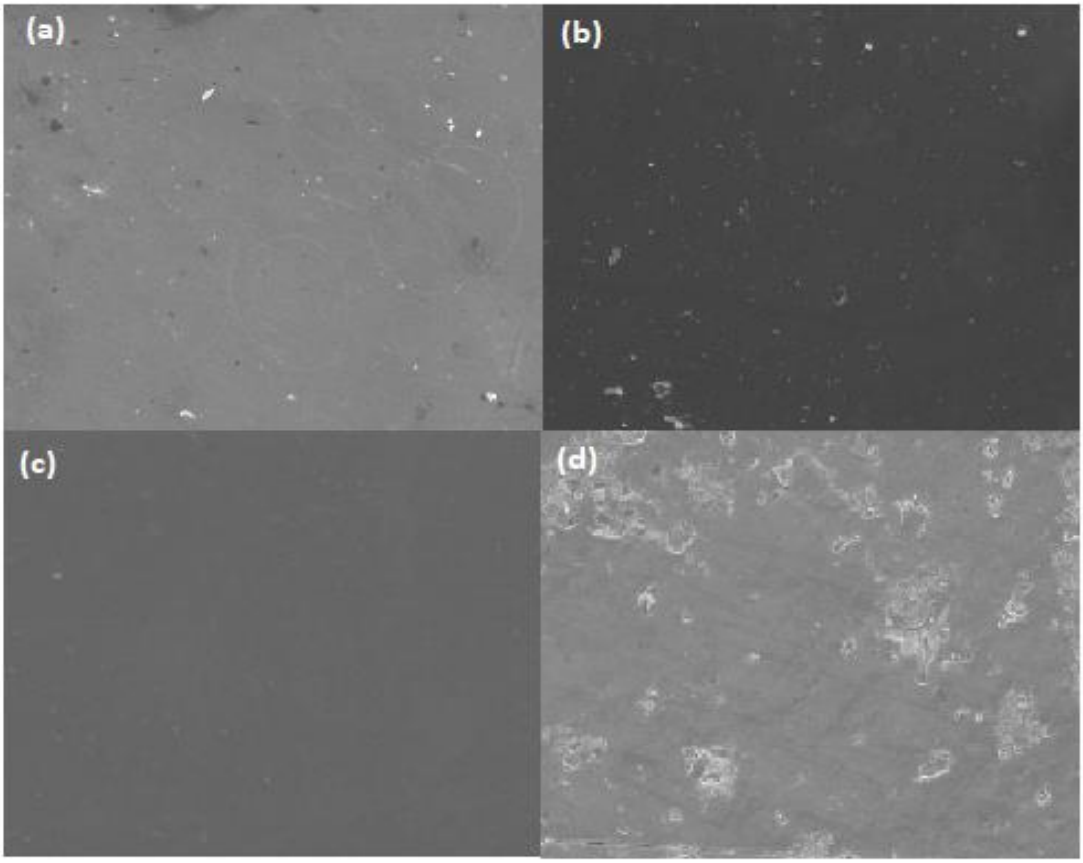

Figure I.24 Scanning electron microscopy images of A-series $(AgI)_x(PbS)_{0.5-x/_2}(As_2S_3)_{0.5-x/_2}$: (a) x = 0.2, (b) x = 0.5 and B-series $(AgI)_{0.3}(PbS)_y(As_2S_3)_{0.7-y}$: (c) y = 0.2, and (d) y = 0.5.

SEM analyses, performed on the z = 0.10, 0.30 and 0.60 of the C-series $(AgI)_z(PbS)_{0.1}(As_2S_3)_{0.9-z}$, show interesting microstructural changes. The glasses appear to be phase-separated throughout the entire composition range. The z = 0.10 composition contains

dark spherical particles compared to the brighter glass matrix, **Figure I.25A(a)**. Those particles are rich in arsenic as evidenced for the EDX elemental mapping, **Figure I.25A(b)**. The other elements (Pb, S, Ag and I) are well distributed within the sample, **Figure I.25A(c-f)**. The non-homogenous character extends for both *z* = 0.30 and 0.60 compositions, **Figure I.25B** and **Figure I.25C**, respectively. In both cases, the separated phases are richer in arsenic, lead and sulfur (**Figure I.25.B, C(b,c,f))** and poorer in silver and iodine, **Figure I.25.B,C(d,e)**.

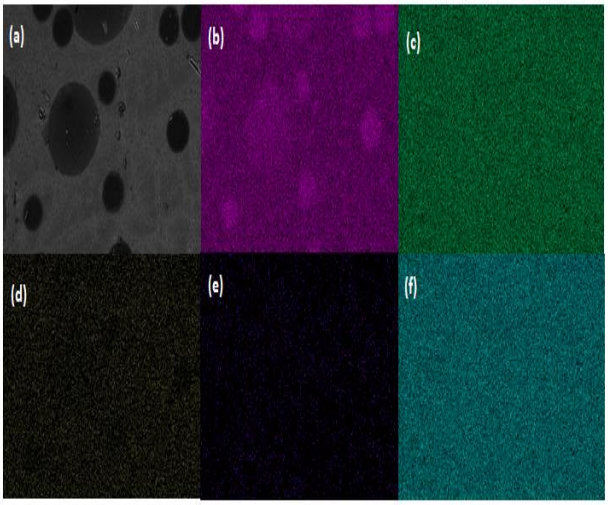

(A)

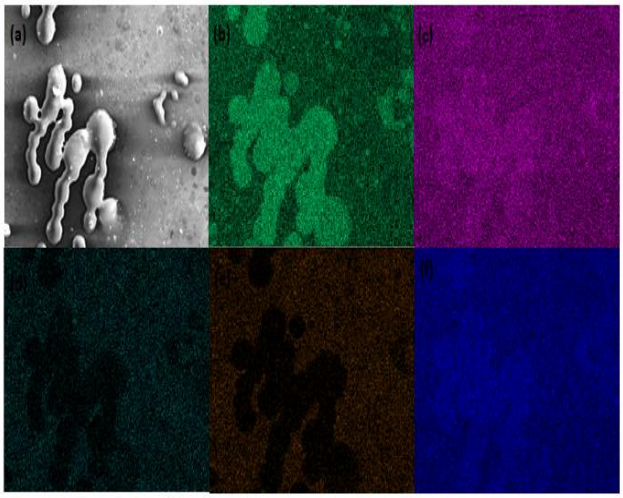

(B)

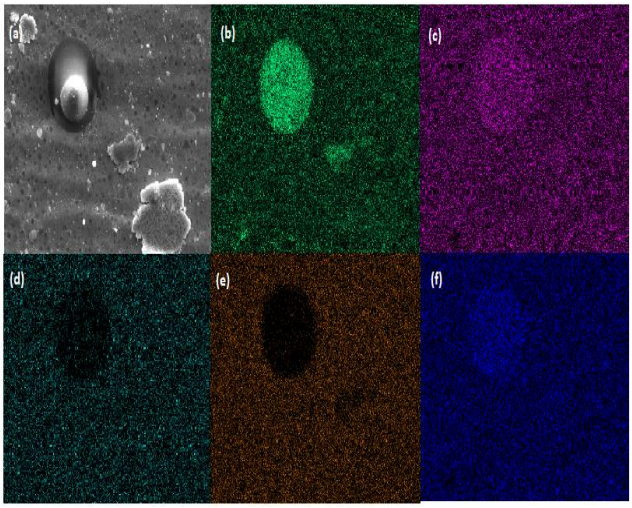

(C)

Figure I.25 SEM images of glass compositions in the C-series $(AgI)_z(PbS)_{0.1}(As_2S_3)_{0.9-z}$, (A) z = 0.1, (B) z = 0.3 and (C) z = 0.5 (b-f) SEM-EDX element mapping of As, Pb, I, Ag and S, respectively.

I.6.2.2 Density and mean atomic volume

The glass density and the mean atomic volume of the A-series: $(AgI)_x(PbS)_{0.5-x/_2}(As_2S_3)_{0.5-x/_2}$ are presented in **Figure I.26** and the values are listed in **Table I.3**. We can clearly see that the density increases monotonically with increasing AgI content from 4.64 g.cm^{-3} (x = 0.0) to 5.53 g.cm^{-3} (x = 0.7), **Figure I.26(a)**. This observed trend is related to silver iodide and is well expected since the density of the two crystalline forms of silver iodide ($d_{\alpha\text{-AgI}}$= 6.12 g.cm^{-3} and $d_{\beta\text{-AgI}}$ =5.68 g.cm^{-3} [47]) is higher than that of the $(PbS)_{0.5}(As_2S_3)_{0.5}$ host glass ($d_{(PbS)0.5(As2S3)0.5}$ = 4.64 g.cm^{-3}). A linear extrapolation up to x = 1 gives a density value which corresponds to that of crystalline α-AgI. Similarly, the mean atomic volume increases monotonically with *x*, **Figure I.26(b)**.

The density of glassy samples of the B-series, $(AgI)_{0.3}(PbS)_y(As_2S_3)_{0.7-y}$, increases monotonically with PbS content *y* while the mean atomic volume remains essentially invariant, **Figure I.27**. The non-monotonic change, as a function of the composition, of the mean atomic volume is more likely to indicate a drastic change in the structure of the glass, which is not observed in the A-series and the B-series of the $(AgI)_x(PbS)_{0.5-x/_2}(As_2S_3)_{0.5-x/_2}$ (this work). The measured density values of the B-series glasses vary between 3.58 g.cm^{-3} (y = 0.0) and 5.67 g.cm^{-3} (y = 0.5). Similarly to its quasi-binary counterpart $(PbS)_x(As_2S_3)_{1-x}$, where the As_2S_3 is being substituted by PbS, the density increase is expected since the crystal form of lead sulfide have significantly higher density (d_{PbS} = 7.5 g cm^{-3}) than that of the $(AgI)_{0.3}(As_2S_3)_{0.7\text{-}y}$ host glass ($d_{(AgI)_{0.3}(As2S3)_{0.7-y}}$ = 3.632 g cm^{-3}). In both cases, i.e., in A-series and B-series, the behavior of both density and mean atomic volume, mimics that seen for the A-series and the B-series of the $(AgI)_x(HgS)_{0.5-x/_2}(As_2S_3)_{0.5-x/_2}$ glass system [48]. The structures of these later glasses, studied using Raman spectroscopy, show that the A- and B-series form a hybrid Hg-S chain/As-S pyramidal network (presence of mixed interconnected $(AgI_{2/2}S_{2/2})_n$ and $(HgS_{2/2})_m$ chains in the glass network). The question arises whether the current ternary lead sulphide system have similar structures. For the time being, we state that, in general, the addition of network-modifier to a chalcogenide network results in breaking the continuous network [49]–[51], transforming part of the bridging sulfur into non-bridging species. As such, each metal cation (Ag, Na or Li) in chalcogenide network will bond to sulfur forming terminal bonds. In contrast, the widely accepted point of view implies that the alloying with metal halides (AgI, AgBr, NaCl, AgCl) leads to an expansion of the glass network.

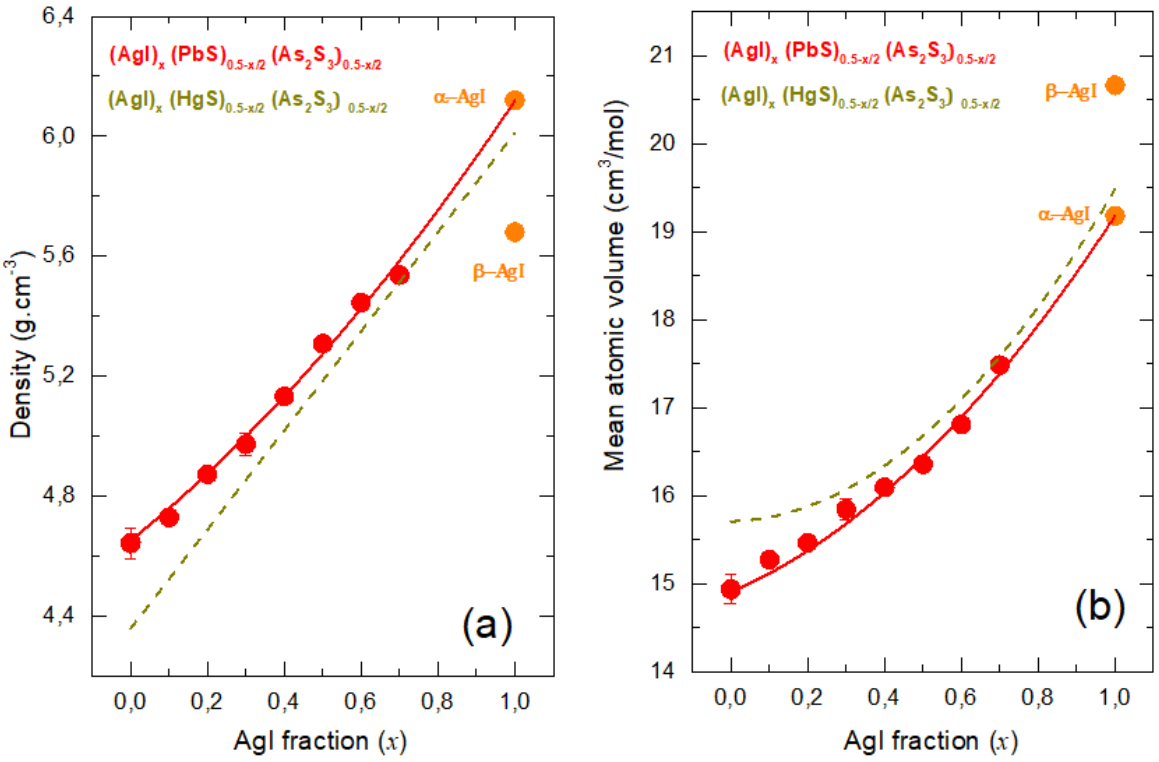

Figure I.26 (a) Density and (b) mean atomic volume of the A-series $(AgI)_x(PbS)_{0.5-x/_2}(As_2S_3)_{0.5-x/_2}$ and $(AgI)_x(HgS)_{0.5-x/_2}(As_2S_3)_{0.5-x/_2}$ alloys as a function of the silver iodide content.

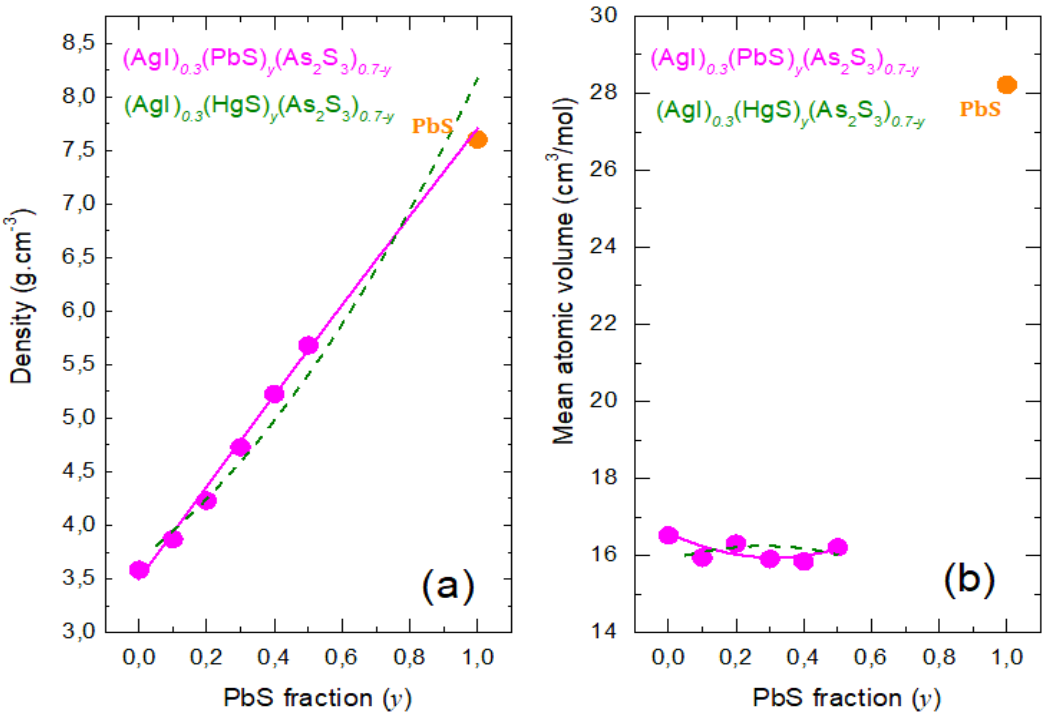

Figure I.27 (a) Density and (b) mean atomic volume of the B-series $(AgI)_{0.3}$ $(PbS)_y$ $(As_2S_3)_{0.7-y}$ and $(AgI)_{0.3}(HgS)_y(As_2S_3)_{0.7-y}$ alloys as a function of the lead sulfide content.

Similarly to the previous two series A and B, the density behavior of glassy samples of the C-series, $(AgI)_z(PbS)_{0.1}(As_2S_3)_{0.9-z}$, is always monotonic. The increase in AgI content *z* leads to increase in density values from 3.39 g.cm^{-3} (z = 0.0) and 4.44 g.cm^{-3} (z = 0.5), **Figure I.28(a)**. Meanwhile, the mean atomic volume shows a monotonic increase but smaller than that seen in the A-series, **Figure I.28(b)**.

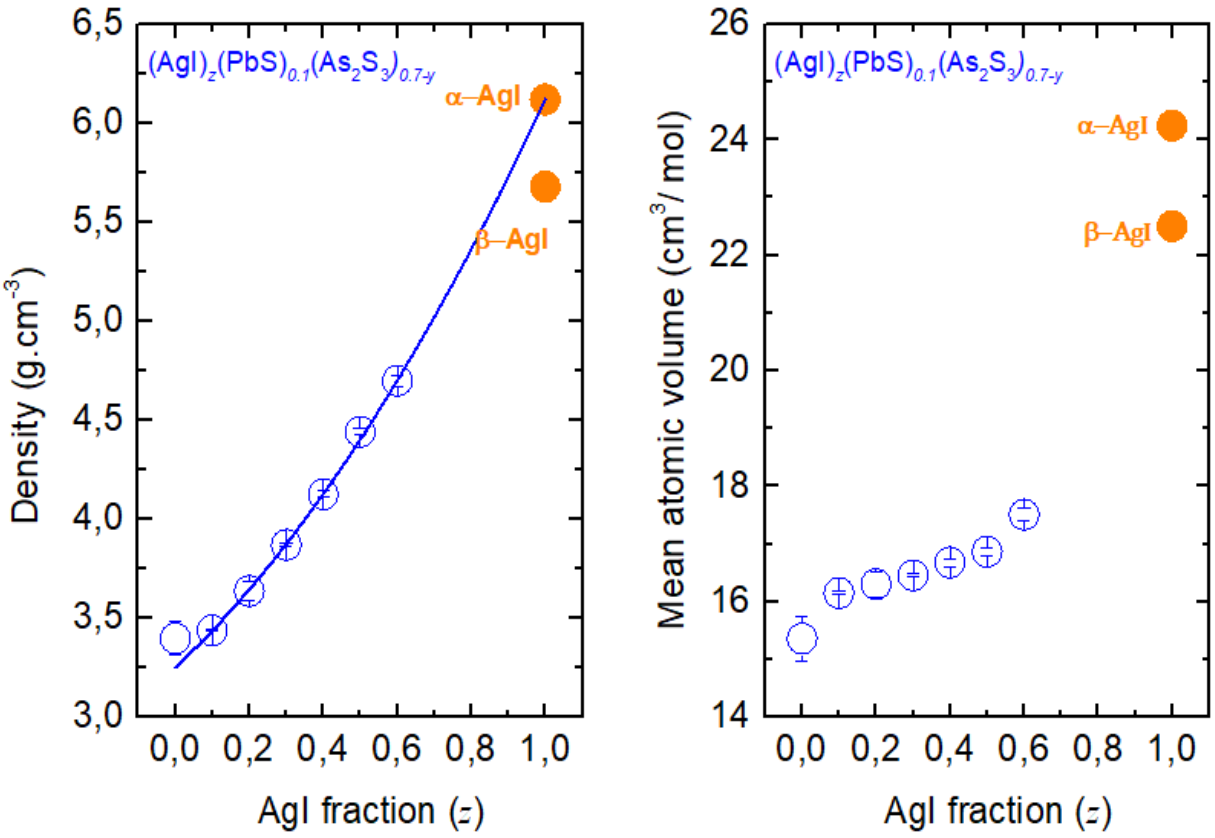

Figure I.28 (a) Density and (b) mean atomic volume of the C series $(AgI)_z(PbS)_{0.1}(As_2S_3)_{0.9-z}$ alloys as a function of the silver iodide content.

I.6.2.3 Thermal properties

Typical DSC curves for the glassy system $(AgI)_x(PbS)_{0.5-x/_2}(As_2S_3)_{0.5-x/_2}$ (series-A) are shown in **Figure I. 29**. All samples show a single endothermic step-like feature corresponding to glass transition. The single glass transition indicates a homogeneous glass nature on both macroscopic and mesoscopic scale. The T_g values of the investigated A-series glasses are plotted, along with those of the mercury sulfide counterpart system [48], as a function of the AgI content (**Figure I.30**). The results are also shown in **Table I.3**.

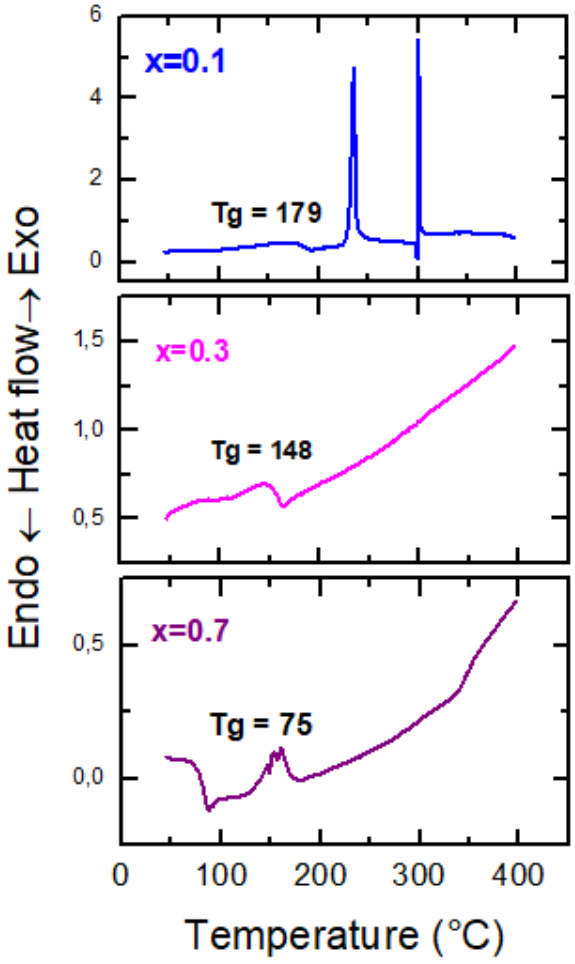

Figure I. 29 DSC traces of the A series $(AgI)_x(PbS)_{0.5-x/_2}(As_2S_3)_{0.5-x/_2}$ glasses with x= 0.1, 0.3 and 0.7, obtained in the temperature range from 30 to 450 °C.

The addition of silver iodide to the $(PbS)_{0.5}(As_2S_3)_{0.5}$ host glass leads to sharp decrease in T_g by 124° C from 199 °C (x = 0) to 75°C (x = 0.7). The decrease in T_g is monotonic in contrast to the mercury sulfide counterpart where the glass transition decreased at two different rates [48]. The changes in glass transition temperatures have already been observed when AgI was added to both Ag_2S-As_2S_3 and Ag_2S-Sb_2S_3 host glasses [52]; the T_g decreases from 144 °C (36 mol% AgI) to 85 °C (70 mol% AgI). The T_g decrease suggests a change in the structural organization of the glass; it can be explained by the fragmentation/ depolymerization of the glass network and hence reducing the network connectivity.

The A-series glasses present, at $x \leq 0.2$, two crystallization features (T_{x1} and T_{x2}) that are comparable to those seen for the quasi-binary PbS-As_2S_3 system. At $x \leq 0.2$, the crystallization temperatures T_{x1} show an overall increase with increasing AgI content; it increases from 238 °C (x = 0.0) to 253 °C (x = 0.2). T_{x1} ended up disappearing beyond this composition and

reappears again for the partially crystalline composition (x = 0.7). Meanwhile, for the compositions below x = 0.7, ΔT increases with increasing AgI content, thus reflecting an improved vitreous formation capacity, **Table I.3**.

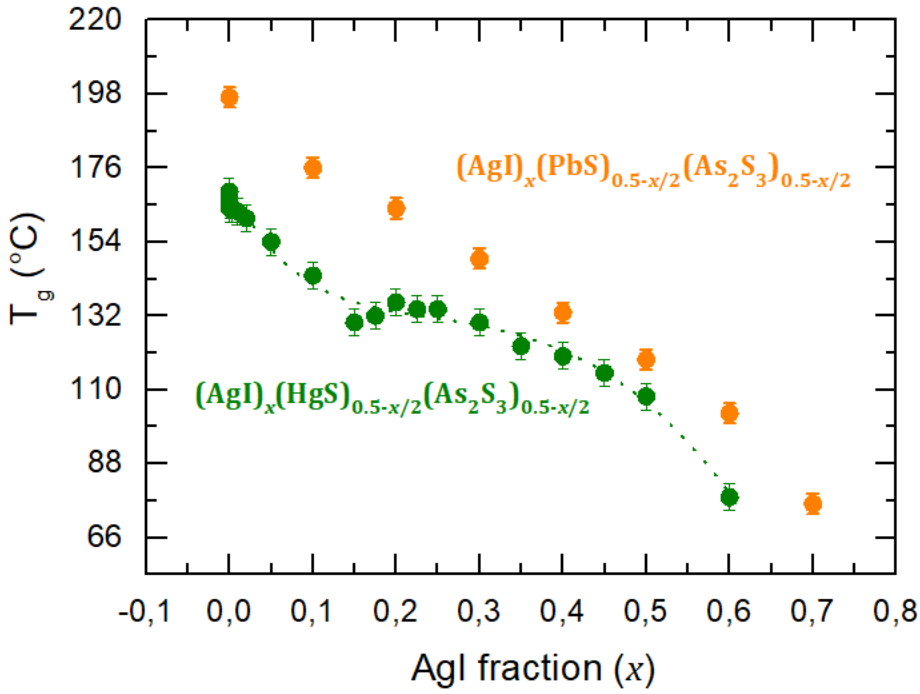

Figure I.30 Variation of the glass transition temperature Tg as a function of AgI content for the A series $(AgI)_x(PbS)_{0.5-x/_2}(As_2S_3)_{0.5-x/_2}$ (orange) and $(AgI)_x(HgS)_{0.5-x/_2}(As_2S_3)_{0.5-x/_2}$ (green).

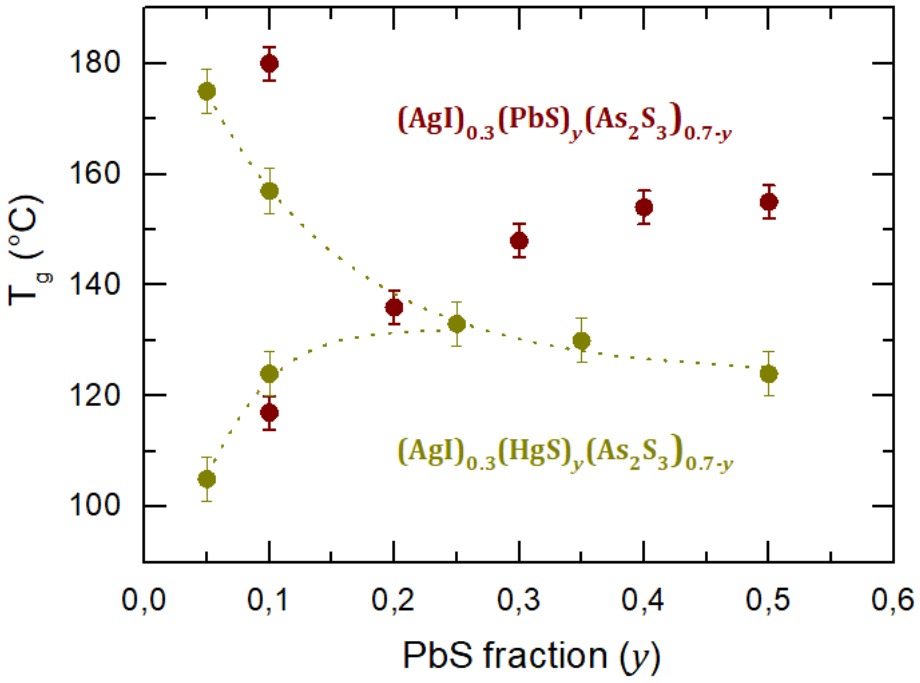

Figure I.31 Variation of the glass transition temperature Tg as a function of PbS content for the B series $(AgI)_{0.3}(PbS)_y(As_2S_3)_{0.7-y}$ (red) and $(AgI)_{0.3}(HgS)_y(As_2S_3)_{0.7-y}$ (green).

Figure I.31 show that the glass transition of the B-series glasses of the lead sulfide, $(AgI)_{0.3}(PbS)_y(As_2S_3)_{0.7-y}$ system, behaves in a similar manner to that of the previously studied mercury sulfide one, i.e., $(AgI)_{0.3}(HgS)_y(As_2S_3)_{0.7-y}$ [52]. The PbS-poor glass (y = 0.1) presents two T_g values (T_{g1} = 117 and T_{g2} = 180 °C) indicating the non-homogenous nature of this composition. This is evident from SEM-EDX graphs of **Figure I.25B**. We note that the y = 0.1 composition of B- series and the z = 0.3 composition of C-series are two different nomenclatures of the same sample (intersection between the green and blue lines in **Figure I.20**. At higher PbS content (y > 0.1), the lead sulfide samples of B-series show a single endothermic step-like feature indicating a homogenous nature. T_g values increase with increasing y ; it increases from 136 °C (y = 0.2) to 155 °C (y = 0.5).

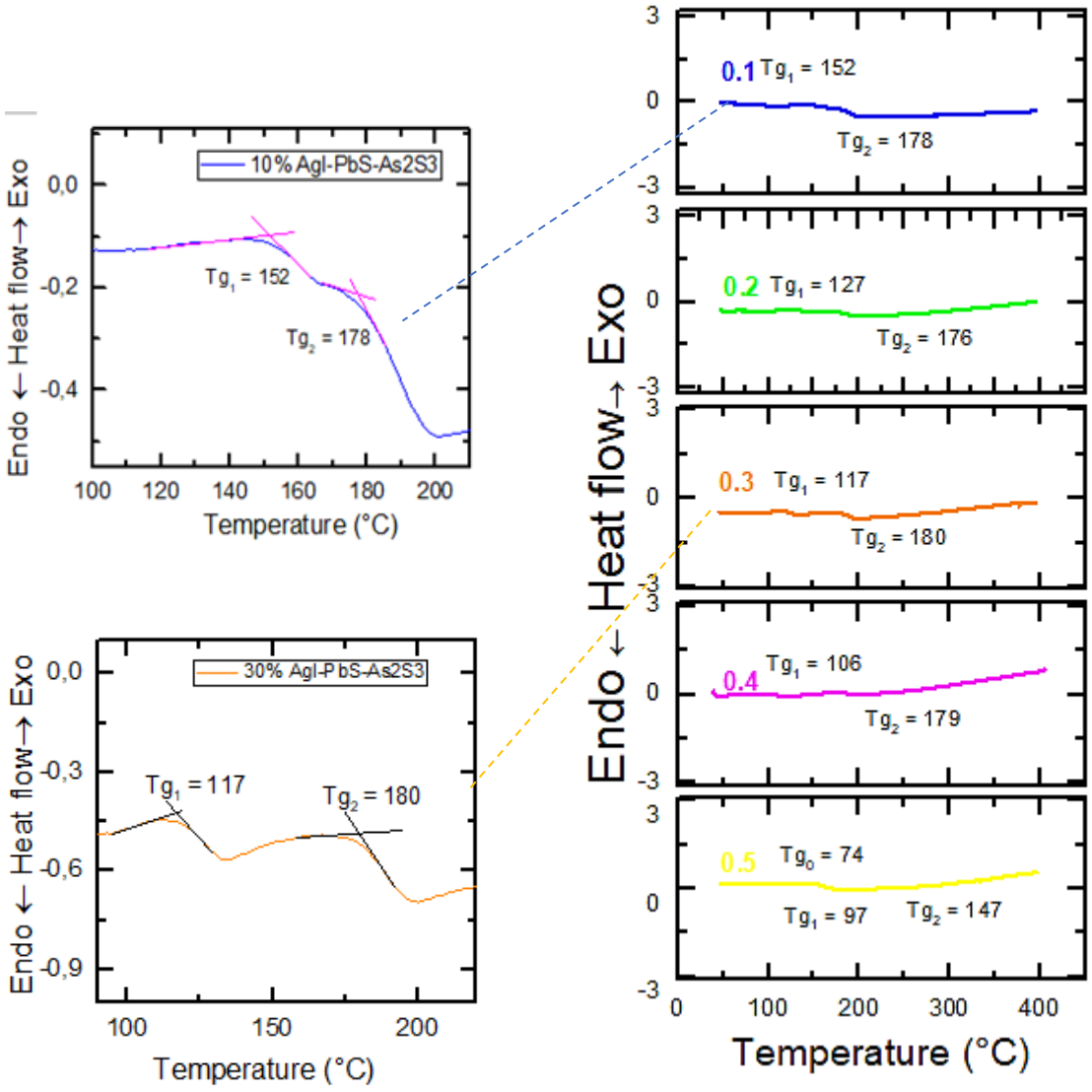

Figure I.32 DSC traces of the C series $(AgI)_z(PbS)_{0.1}(As_2S_3)_{0.9-z}$ glasses, 0.1 ≤ z ≤ 0.5, obtained in the temperature range from 30 to 450 °C.

Figure I.32 shows that all glasses in the C-series, i.e., $(AgI)_z(PbS)_{0.1}(As_2S_3)_{0.9-z}$, exhibit two endothermic step-like features corresponding to glass transition (T_{g1} and T_{g2}) indicating a non-homogeneous glass nature on macroscopic and mesoscopic scale. This inhomogeneity is explained in terms of phase-separation which was evidenced in the SEM previously showed. The evolution of T_g, as a function of the AgI content, for the studied glasses in the C-series, is shown in **Figure I.33** and **Table I.3**.

The continuous addition of AgI to the $(PbS)_{0.1}(As_2S_3)_{0.9}$ host glass lead to a monotonic decrease in T_{g1}values by 87 °C from 184 °C (z = 0.0) to 97 °C (z = 0.5). We note that for the x = 0.5 an additional glass transition appears at lower temperature T_{g0} = 74 °C. The T_{g2}values, on the other hand, remain essentially constant except for the AgI-richest composition (z = 0.5).

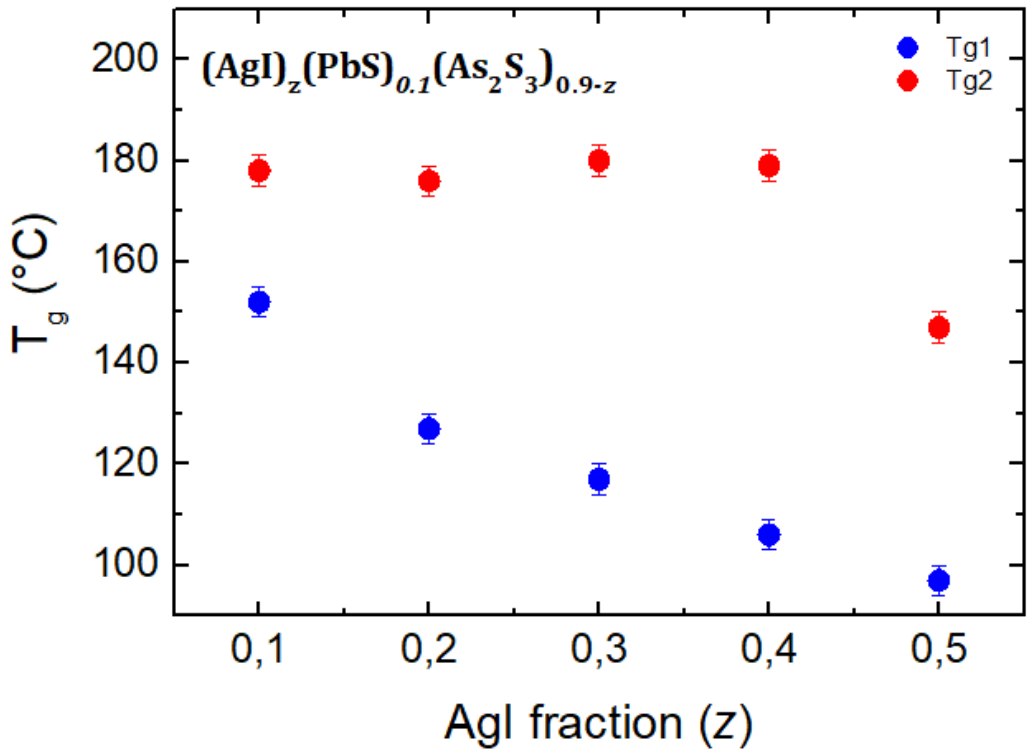

Figure I.33 Variation of the glass transition temperature T_g as a function of AgI content for the C series $(AgI)_z(PbS)_{0.1}(As_2S_3)_{0.9-z}$.

Table I.3 Density, glass transition temperature and the crystallization temperature for the AgI-PbS-As_2S_3 alloys.

Composition	Density ($g.cm^{-3}$)	T_g (°C) (±2)		T_x (°C) (±2)			ΔT (°C)
		T_{g1}	T_{g2}	T_{x1}	T_{x2}	T_{x3}	
A series: $(AgI)_x(PbS)_{0.5-x/2}(As_2S_3)_{0.5-x/2}$							
0.0	4.64 (5)	199	-	238	310	-	39
0.0001	4.64 (1)	201	-	241	317	-	40
0.0003	4.64 (1)	200	-	244	318	-	44
0.001	4.65 (1)	199	-	241	315	-	42
0.003	4.66 (1)	198	-	241	314	-	43
0.01	4.67 (2)	194	-	240	314	-	46
0.02	4.67 (8)	193	-	240	313	-	47
0.05	4.67 (1)	191	-	241	312	-	50
0.1	4.73 (5)	179	-	236	300	-	57
0.2	4.87 (6)	165	-	253	300	-	88
0.3	4.97 (3)	148	-	-	-	-	-
0.4	5.13 (2)	132	-	-	-	-	-
0.5	5.31 (4)	117	-	-	-	-	-
0.6	5.44 (1)	102	-	-	-	-	-
0.7	5.53 (4)	75	-	147	153	161	72
B series : $(AgI)_{0.3}(PbS)_y(As_2S_3)_{0.7-y}$							
0.1	3.87 (5)	117	180	-	-	-	-
0.2	3.99 (4)	136	-	-	-	-	-
0.3	4.72 (2)	148	-	289	327	-	141
0.4	5.22 (2)	154	-	-	-	-	-
0.5	5.67 (1)	155	-	208	234	281	53
C series : $(AgI)_z(PbS)_{0.1}(As_2S_3)_{0.9-z}$							
0.1	3.43 (5)	152	178	-	-	-	-
0.2	3.63 (5)	127	176	-	-	-	-
0.3	3.87 (5)	117	180	-	-	-	-
0.4	4.12 (2)	106	179	-	-	-	-
0.5	4.44 (1)	97	147	-	-	-	-

I.6.3 PbS-As_2S_3 crystal: synthesis and characterization

Earlier, in section I.4.3, we mentioned that lead-arsenic sulphide compounds are naturally occurring minerals and usually referred to as lead-sulfosalts. Examples of those compounds include sartorite, rathite, liveingite, gratonite, seligmannite, bartorite, etc. In this category, a lot of effort was invested in attempting to synthesize few of these Pb-As-S crystal compounds along with the Ag-Pb-As-S crystal which was not an easy task at all (**Table I.4**). Finally, we were able to prepare three different synthetic Pb-As-S crystals: the sartorite $PbAs_2S_4$ [53], the baumhauerite $Pb_5As_9S_{18}$ [54] and the dufrénoysite $Pb_2As_2S_5$ [36]. A period of several months and a lot of unsuccessful essays (**Figure I.34**) were necessary to define the specific conditions leading to the correct synthesis of the desired crystals, **Table I.4**.

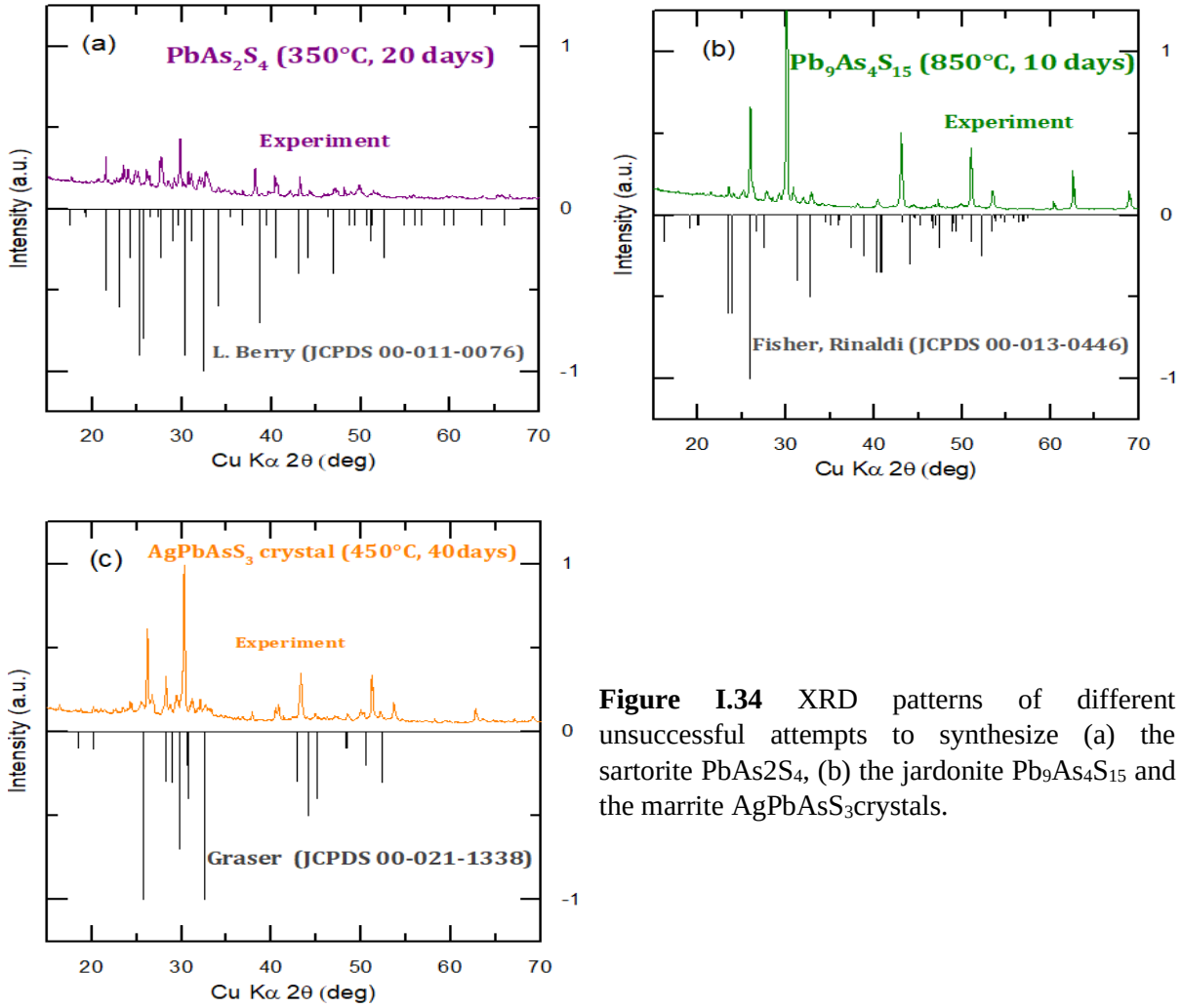

Figure I.34 XRD patterns of different unsuccessful attempts to synthesize (a) the sartorite PbAs2S_4, (b) the jardonite $Pb_9As_4S_{15}$ and the marrite $AgPbAsS_3$crystals.

Table I.4 Table showing the different steps followed to synthesize the desired crystals

Crystals	Melting temperature (°C)	Annealing temperature (°C)	Time (days)	Result
Sartorite $PbAs_2S_4$	800	350	10	×
		350	20	×
		350	30	×
		280	20	✓✓
Dufrénoysite $Pb_2As_2S_5$	800	350	10	×
		350	20	✓✓
Baumhauerite $Pb_5As_9S_{18}$	800	350	10	✓✓
Jardonite $Pb_9As_4S_{15}$	> 1170	850	10	×
		550	20	×
		550	40	×
		350	10	×
Marrite $AgPbAsS_3$	750	350	20	×
		450	10	×
		450	40	×

Figure I.35 shows the XRD diffraction patterns of three crystalline compounds synthesised in the $(PbS)_x(As_2S_3)_{1-x}$ system. The crystallising phases exhibit Bragg peaks corresponding to the reference minerals: sartorite $PbAs_2S_4$ [53], baumhauerite $Pb_5As_9S_{18}$ [54] and dufrénoysite $Pb_2As_2S_5$ [36], respectively.

The surface morphology of the three crystallized samples, obtained from SEM, is depicted in **Figure I.36(a–c)**. The micrographs reveal crystallites with different sizes (varying within 2–50 µm). **Figure I.36(d)** displays a SEM image for the $Pb_5As_9S_{18}$ crystallite (× 3000) as well as its corresponding EDX element (Pb, As, S) mapping. Overall the elements are well distributed but we note the presence of a zone that is rich in arsenic (bright blue), **Figure I.36(f)**, and poor in both lead and sulphur, **Figure I.36(e)** and **Figure I.36(g)**.

Finally, in **Table I.5**, we present the densities of the three synthesized crystals sartorite $PbAs_2S_4$, dufrénoysite $Pb_2As_2S_5$, and the baumhauerite $Pb_5As_9S_{18}$. We can notice from this table that the density values of our synthesized crystals are comparable with those of the naturally occurring minerals.

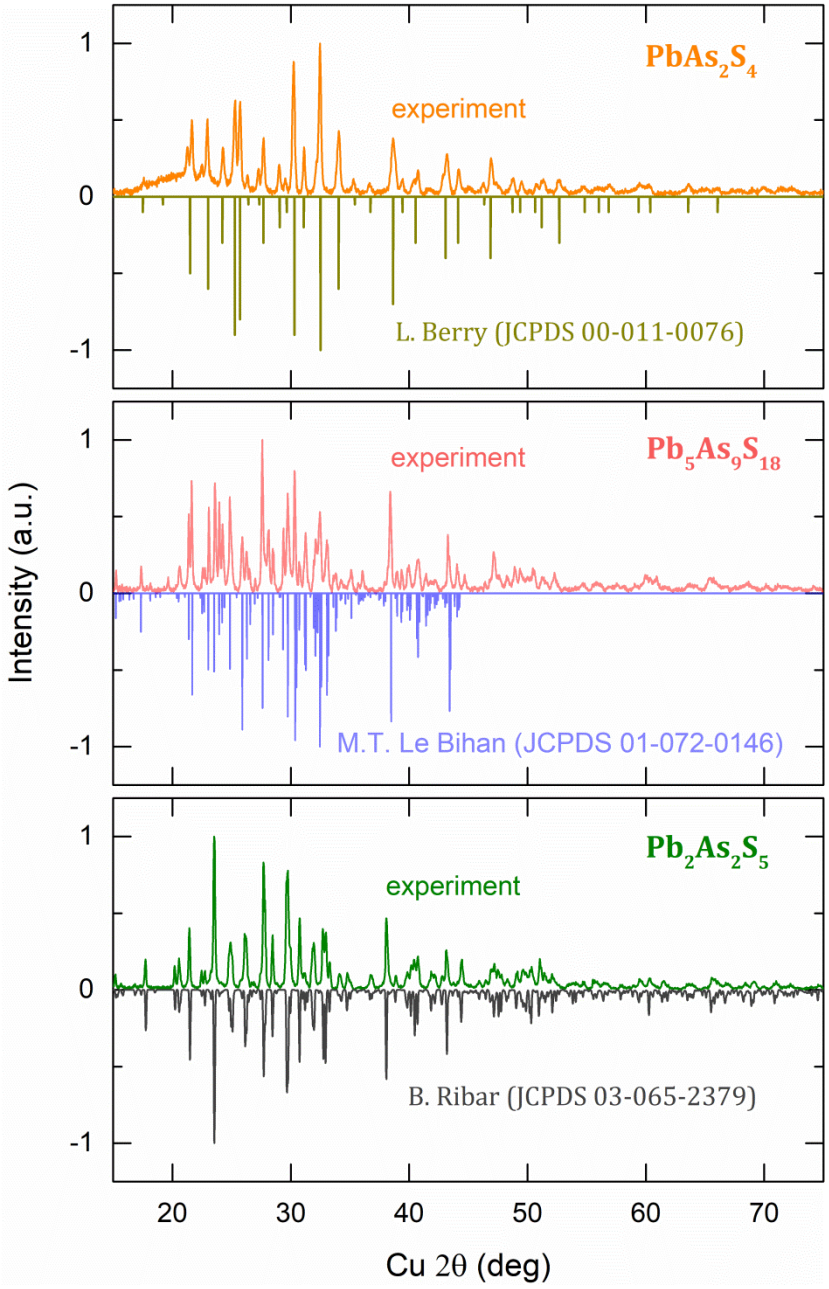

Figure I.35 XRD patterns of the three crystalline compositions synthesized in the PbS-As_2S_3 system (this work): the sartorite $PbAs_2S_4$ structure (Orthorhombic), the baumhauerite $Pb_5As_9S_{18}$ structure (triclinic) and the dufrénoysite $Pb_2As_2S_5$ structure (monoclinic). The XRD patterns of the matched minerals are also presented [36], [38], [39].

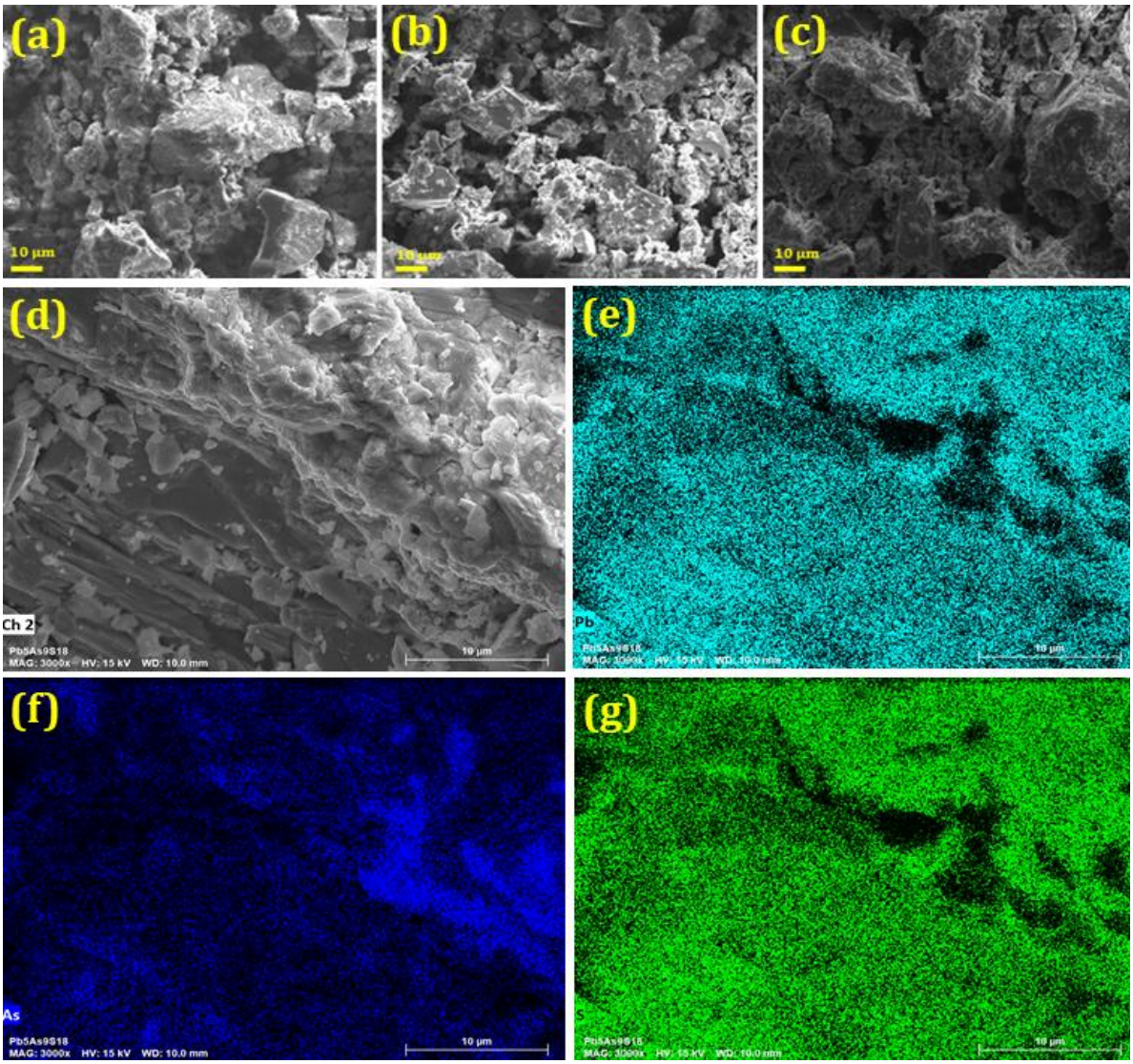

Figure I.36 SEM micrograph for the crystalline compounds (a) $PbAs_2S_4$, (b) $Pb_2As_2S_5$, (c) $Pb_5As_9S_{18}$, (d) $Pb_5As_9S_{18}$ SEM micrograph (× 3000) and its corresponding EDX element mapping of (e) Pb (cyan), (f) As (blue) and (g) S (green).

Table I.5 Comparison between the densities of the synthesized crystals and those in the bibliography.

	$d_{measured}$	$d_{reference}$
Sartorite $PbAs_2S_4$	4.841	5.08-5.12 [55]
Dufrénoysite $Pb_2As_2S_5$	4.935	5.5-5.57 [56]
Baumhauerite $Pb_5As_9S_{18}$	5.182	5.33-5.45 [57]

I.7 Conclusion

In this first chapter, the physical and thermal characteristics of the glassy systems PbS-As_2S_3 and AI-PbS-As_2S_3 have been measured and analyzed. Also, synthetic Pb-As-S crystals were synthesized and characterized.

Two complementary techniques, melt-quenching and mechanical milling, were used to obtain vitreous alloys in the quasi-binary $(PbS)_x(As_2S_3)_{1-x}$ system. Bulk glasses were synthesised over the $0 \leq x \leq 0.5$ composition range; the amorphous MM-alloys at $x < 0.7$. The density and the glass packing increase with increasing x, while the molar volume shrinks and becomes denser in comparison with cubic lead sulphide. Tetrahedral lead local coordination with shorter Pb-S interatomic distances seems to be responsible for this trend, confirmed by preliminary high-energy X-ray diffraction. A single glass transition reveals a shallow minimum at $x \approx 0.2$, ΔT_g = -14 °C, presumably related to a partial fragmentation of a quasi-continuous As-S host network; T_g increase at $x > 0.2$ might be caused by the raising connectivity of glassy lead thioarsenates.

Concerning the pseudo-ternary system, we have carried out a study on novel chalcogenide glasses in the AgI-PbS-As_2S_3 system. A relatively large glass-forming region, located in the As_2S_3-rich corner, was observed. In this category, three series were synthesized (A-, B- and C-series) and characterized. The vitreous domain of the A-series extends up to silver iodide content ($x \leq 0.6$) while that of B-series reaches lead sulfide content ($y \leq 0.5$). Meanwhile, the vitreous domain of the C-series stretches out in the range ($0.0 \leq z \leq 0.5$). For all the A-, B- and C-series glasses, the density increases monotonically with AgI and PbS additions (depending on the dopant in the various series). The thermal studies of the A-series glasses show a monotonic decrease in glass transition with successive AgI addition. Only the PbS-poor glasses of the B-series were nonhomogeneous while the entire glass batch of the C-series were nonhomogeneous (The glasses of C series exhibit two or more T_g values depending on the composition). The inhomogeneity is explained in terms of phase-separation as evidenced the SEM-EDX data.

Finally, three crystals in the Pb-As-S have been synthesized and characterized: (i) the dufrénoysite $Pb_2As_2S_5$, (ii) the baumhauerite $Pb_5As_9S_{18}$ and (iii) the sartorite $PbAs_2S_4$.

I.8 References

[1] W. Shakespeare, “The world of inorganic glasses,” in *Structural chemistry of glasses*, 2002, pp. 1–12.

[2] N. F. Mott and E. A. Davis, *Electronic processes in non-crystalline materials*. Oxford university press, 2012.

[3] C. Cao, Z.-B. Li, X.-L. Wang, X.-B. Zhao, and W. Han, “Recent Advances In Inorganic Solid Electrolytes For Lithium Batteries,” *Front. Energy Res.*, vol. 2, pp. 1–10, Jun. 2014.

[4] J. Souquet and W. Perera, “Thermodynamics applied to ionic transport in glasses,” *Solid State Ion.*, vol. 40–41, pp. 595–604, Aug. 1990.

[5] R. Frerichs, “New optical glasses transparent in the infra-red up to 12-mu.,” *Phys. Rev.*, vol. 78, p. 643, 1950.

[6] R. Frerichs, “New Optical Glasses with Good Transparency in the Infrared*,” *J. Opt. Soc. Am.*, vol. 43, p. 1153, 1953.

[7] W. A. J. Frazer, “Arsenic trisulfide-A new infrared transmitting glass.,” *J. Opt. Soc. Am.*, vol. 43, p. 823, 1953.

[8] G. Dewulf, “Verres Transparents dans l’Infrarouge”(Infrared-Transmitting Glasses).,” *Rev.Opt*, vol. 33, p. 513, 1954.

[9] S. R. Ovshinsky, “Reversible Electrical Switching Phenomena in Disordered Structures,” *Phys. Rev. Lett.*, vol. 21, p. 1450, 1968.

[10] S. R. Ovshinsky, “An introduction to ovonic research,” *J. Non-Cryst. Solids*, vol. 2, p. 99, Jan. 1970.

[11] N. F. Mott and E. A. Davis, “Electronic Processes In Non-crystalline Materials,” Clarendon Press, Oxford, 1979.

[12] Z. Borisova, *Glassy Semiconductors*. Plenum Press, New York, 1981.

[13] C. A. Angell, “Formation of Glasses from Liquids and Biopolymers,” *Science*, vol. 267, no. 5206, pp. 1924–1935, Mar. 1995.

[14] B. Punit, *Insulating And Semiconducting Glasses*. World Scientific, 2000.

[15] E. Bychkov, “Superionic and ion-conducting chalcogenide glasses: Transport regimes and structural features,” *Solid State Ion.*, vol. 180, no. 6, pp. 510–516, May 2009.

[16] J. Sanghera and I. D. Aggarwal, *Infrared Fiber Optics*. CRC Press, 1998.

[17] J.-F. Viens *et al.*, “Fabrication and characterization of integrated optical waveguides in sulfide chalcogenide glasses,” *J. Light. Technol.*, vol. 17, no. 7, pp. 1184–1191, Jul. 1999.

[18] M.-L. Anne *et al.*, “Chalcogenide Glass Optical Waveguides for Infrared Biosensing,” *Sensors*, vol. 9, no. 9, pp. 7398–7411, Sep. 2009.

[19] F. Jiang and M. Okuda, “The Effect of Doping on the Erasure Speed and Stability of Reversible Phase-Change Optical Recording Films,” *Jpn. J. Appl. Phys.*, vol. 30, no. 1R, p. 97, Jan. 1991.

[20] J. Fusong and M. Okuda, “The effect of doping on the erasure speed and stability of reversible phase-change optical recording films,” *Japanese Journal of Applied Physics*, pp. 97–100, Jan. 1991.

[21] H. Nasu, K. Kubodera, M. Kobayashi, M. Nakamura, and K. Kamiya, “Third-Harmonic Generation from Some Chalcogenide Glasses,” *J. Am. Ceram. Soc.*, vol. 73, no. 6, pp. 1794–1796, 1990.

[22] Yu. G. Mourzina *et al.*, “Copper, cadmium and thallium thin film sensors based on chalcogenide glasses,” *Anal. Chim. Acta*, vol. 433, no. 1, pp. 103–110, Apr. 2001.

[23] A. V. Legin, E. A. Bychkov, and Yu. G. Vlasov, “Analytical applications of chalcogenide glass chemical sensors in environmental monitoring and process control,” *Sens. Actuators B Chem.*, vol. 24, no. 1, pp. 309–311, Mar. 1995.

[24] R. Tomova, R. Stoycheva-Topalova, and A. Buroff, “ION-SELECTIVE MEMBRANES BASED ON CHALCOGENIDE GLASSES,” *J. Optoelectron. Adv. Mater.*, vol. 7, no. 3, pp. 1399–1406, Jun. 2005.

[25] Yu. G. Vlasov, E. A. Bychkov, and A. V. Legin, “Lead ion-selective chalcogemde g&s electrodes,” *Zh Anal Khzm*, pp. 1839–1847, 1985.

[26] Yu. G. Vlasov, E. A. Bychkov, and A. M. Medvedev, “Copper ion-selective chalcogenide glass electrodes: Analytical characteristics and sensing mechanism,” *Anal. Chim. Acta*, vol. 185, pp. 137–158, Jan. 1986.

[27] Yu. G. Vlasov, E. A. Bychkov, and B. L. Seleznev, “Silver ion sensors based on Ag-As-Se-Te glasses I. Ionic sensitivity and bulk membrane transport,” *Sens. Actuators B Chem.*, vol. 2, no. 1, pp. 23–31, Mar. 1990.

[28] Y. G. Vlasov and E. A. Bychkov, “Ion-selective chalcogenide glass electrodes,” *Res. Gate*, vol. 9, no. 1, pp. 5–91, Jan. 1987.

[29] M. T. Ramesan and T. Sampreeth, “In situ synthesis of polyaniline/Sm-doped TiO2 nanocomposites: evaluation of structural, morphological, conductivity studies and gas sensing applications,” *J. Mater. Sci. Mater. Electron.*, vol. 29, no. 5, pp. 4301–4311, Mar. 2018.

[30] P. G. Bruce, S. A. Freunberger, L. J. Hardwick, and J.-M. Tarascon, “Li–O 2 and Li–S batteries with high energy storage,” *Nat. Mater.*, vol. 11, no. 1, pp. 19–29, Jan. 2012.

[31] M. Tatsumisago and A. Hayashi, “19 - Chalcogenide glasses as electrolytes for batteries,” in *Chalcogenide Glasses*, J.-L. Adam and X. Zhang, Eds. Woodhead Publishing, 2014, pp. 632–654.

[32] P. K. Bhat and K. L. Bhatia, “Far infrared transmission and Raman scattering in Pb-As-S semiconducting glasses,” *Solid State Commun.*, vol. 22, no. 12, pp. 789–792, Jun. 1977.

[33] S. C. Katyal, K. L. Bhatia, V. C. Padaki, P. K. Bhat, and E. S. R. Gopal, “Elastic properties of PbS-As2S3glasses,” *J. Phys. C Solid State Phys.*, vol. 11, no. 12, pp. L479–L482, Jun. 1978.

[34] K. L. Bhatia, S. C. Katyal, and A. K. Sharma, “On the glass formation tendency in (PbS)x·(M2S3)1−x (M = As, Sb),” *J. Non-Cryst. Solids*, vol. 58, no. 1, pp. 27–34, Oct. 1983.

[35] Y. Onodera, T. Furukawa, S. Hashimoto, T. Usuki, Y. Amo, and Y. Kameda, “Vitrification and transport properties in AgBr-doped chalcogenide systems,” *Solid State Ion.*, vol. 177, no. 26, pp. 2597–2599, Oct. 2006.

[36] B. Ribar, C. Nicca, and W. Nowacki, “Dreidimensionale Verfeinerung der Kristallstruktur von Dufrenoysit, Pb8As8S20,” *Z. Für Krist. - Cryst. Mater.*, vol. 130, no. 1–6, pp. 15–40, Dec. 1969.

[37] P. Bhat and K. L. Bhatia, “Structural properties of As2S3-PbS glasses,” *Phys. Chem. Glas.*, vol. 19, no. 4, pp. 55–59, 1978.

[38] D. R. Lide, *CRC Handbook of Chemistry and Physics, 78th Edition*. CRC Press, 1997.

[39] D. J. E. Mullen and W. Nowacki, “Refinement of the crystal structures of realgar, AsS and orpiment, As2S3,” *Z. Für Krist. - Cryst. Mater.*, vol. 136, no. 1–6, pp. 48–65, Dec. 1972.

[40] S. C. Katyal, K. L. Bhatia, V. C. Padaki, P. K. Bhat, and E. S. R. Gopal, “Elastic properties of PbS-As2S3glasses,” *J. Phys. C Solid State Phys.*, vol. 11, no. 12, pp. 479–482, Jun. 1978.

[41] E. Soignard *et al.*, “Pressure-Driven Chemical Disorder in Glassy As2S3 up to 14.7 GPa, Postdensification Effects, and Applications in Materials Design,” *J. Phys. Chem. B*, vol. 124, no. 2, pp. 430–442, Jan. 2020.

[42] Y. Noda, S. Ohba, S. Sato, and Y. Saito, “Charge distribution and atomic thermal vibration in lead chalcogenide crystals,” *Acta Crystallogr. B*, vol. 39, no. 3, Art. no. 3, Jun. 1983.

[43] M. Kassem, S. Khaoulani, A. Cuisset, D. L. Coq, P. Masselin, and E. Bychkov, “Mercury thioarsenate glasses: a hybrid chain/pyramidal network,” *RSC Adv.*, vol. 4, no. 90, pp. 49236–49246, Oct. 2014.

[44] M. Kassem *et al.*, “Mercury Sulfide Dimorphism in Thioarsenate Glasses,” *J. Phys. Chem. B*, vol. 120, no. 23, pp. 5278–5290, Jun. 2016.

[45] M. Kassem *et al.*, “Chemical and Structural Variety in Sodium Thioarsenate Glasses Studied by Neutron Diffraction and Supported by First-Principles Simulations,” *Inorg. Chem.*, vol. 59, no. 22, pp. 16410–16420, Nov. 2020.

[46] I. Alekseev, D. Fontanari, A. Sokolov, M. Bokova, M. Kassem, and E. Bychkov, “Ionic Conductivity and Tracer Diffusion in Glassy Chalcogenides,” vol. 1, Singapore: World Scientific, 2021, pp. 203–249.

[47] D. J. E. MULLEN and W. NOWACKI, “Refinement of the crystal structures of realgar, AsS and orpiment, As2S3,” *Z. Für Krist. - Cryst. Mater.*, vol. 136, no. 1–6, pp. 48–65, 2015.

[48] S. Khaoulani, M. Kassem, S. Fourmentin, and E. Bychkov, “The AgI-HgS-As2S3 glassy system: Macroscopic properties and Raman scattering studies,” *J. Alloys Compd.*, vol. 685, pp. 752–760, Nov. 2016.

[49] H. Jabraoui, E. M. Achhal, A. Hasnaoui, J.-L. Garden, Y. Vaills, and S. Ouaskit, “Molecular dynamics simulation of thermodynamic and structural properties of silicate glass: Effect of the alkali oxide modifiers,” *J. Non-Cryst. Solids*, vol. 448, pp. 16–26, Sep. 2016.

[50] A. Paraskiva, “Développement de membranes pour les capteurs chimiques potentiométriques spécifiques aux ions Thallium et Sodium,” phdthesis, Université du Littoral Côte d’Opale, 2017. Accessed: May 06, 2021. [Online]. Available: https://tel.archives-ouvertes.fr/tel-01727861

[51] A. Kato, M. Nose, M. Yamamoto, A. Sakuda, A. Hayashi, and M. Tatsumisago, “Mechanical properties of sulfide glasses in all-solid-state batteries,” *J. Ceram. Soc. Jpn.*, vol. 126, no. 9, pp. 719–727, 2018.

[52] J. M. Reau, B. Tanguy, J. J. Videau, J. Portier, and P. Hagenmuller, “Transport properties of rapidly quenched glasses in the Z2S3−Ag2S−AgI (Z=As, Sb) systems,” *Solid State Ion.*, vol. 28–30, pp. 792–798, Sep. 1988.

[53] L. Berry, Queen’s university, Kingston, Ontario, Canada, private communication.

[54] M. T. Le Bihan, “Contribution à l’étude structurale des sulfures d’arsenic et de plomb. Structure de la baumhauerite,” *Acta Crystallogr.*, vol. 14, no. 11, Art. no. 11, Nov. 1961.

[55] “Sartorite.” https://www.mindat.org/min-3537.html (accessed Jul. 15, 2021).
[56] “Dufrénoysite.” https://www.mindat.org/min-1324.html (accessed Jul. 15, 2021).
[57] “Baumhauerite.” https://www.mindat.org/min-572.html (accessed Jul. 15, 2021).

Chapter II:
Conductivity of the glassy systems: PbS-As_2S_3 and AgI-PbS- As_2S_3

II.1 Electrical conductivity: theoretical aspect

II.1.1 Generalities

Total electrical conductivity σ is generated by the movement of electrically charged particles, referred to as charge carriers "j", in response to an electric field. It results from the sum of two different partial conductivities σ_j, i.e., (i) the electronic conductivity σ_e generated by electronic charge carriers (electrons or holes) and (ii) the ionic conductivity σ_i by generated by ionic charge carriers (cations or anions). Equation II.1 regroups the two contributions:

$$\sigma = \sum_j \sigma_j = \sigma_e + \sigma_i \qquad \text{(II. 1)}$$

The partial conductivity σ_j, associated with each charge-carrying species capable of moving within homogeneous and isotropic solid [1], can then be described as the product of the three terms related to the charge carrier "j": its charge (q_j), its concentration (n_j) and its mobility (μ_j). This fundamental statement is correct for electronic conduction in solids; ionic conduction in solids, aqueous fluids, and melts; thus, we may write:

$$\sigma_j = n_j \, q_j \, \mu_j \qquad \text{(II. 2)}$$

In this regards, we mention that it is difficult to separately measure the mobility (μ_j) and the concentration of charge carriers (n_j). Hence, the complication in determining the contribution of each factor alone to the partial conductivity (see section II.1.4.2). Also, we note that the partial conductivity σ_j is related to the electrical conductivity σ via the partial transport number t_j of the charge carrier "j":

$$t_j = \frac{\sigma_j}{\sigma} \qquad \text{(II. 3)}$$

Consequently, combining II.1 and II.3 gives an expression for conductivity as

$$\sigma = \sum_j \sigma_j = \sigma_e + \sigma_i = (t_e + t_i)\sigma \qquad \text{(II. 4)}$$

where t_i is the ionic transport number and t_e is the electronic transport number. The materials are considered to be purely ionic conductors when $t_i > 0.99$ and purely electronic conductors for value of $t_e > 0.99$ [2].

II.1.2 Electronic conductivity

The electronic conductivity, characteristic of metals, semiconductors and superconductors, is explained by the band theory. The bands are regarded as possible energy level for electrons of atoms inside the solid material and depend on atoms' atomic orbitals overlap. The two bands allowed are the valence band and the conduction band, **Figure II. 1**. The valence band **VB**, at a lower energy level than the conduction band in the energy level diagram, is defined as the energy band that comprises of valence electrons present in the outermost shell of an atomic structure. These valence electrons, when provided with sufficient energy, get changed into free electrons and moves to conduction band thereby causing conductivity. The conduction band **CB**, at higher energy state above the fermi level, is is the band of electron orbitals that electrons can jump up into from the valence band when excited. When the electrons are in these orbitals, they have enough energy to move freely in the material (free electrons responsible for conduction).

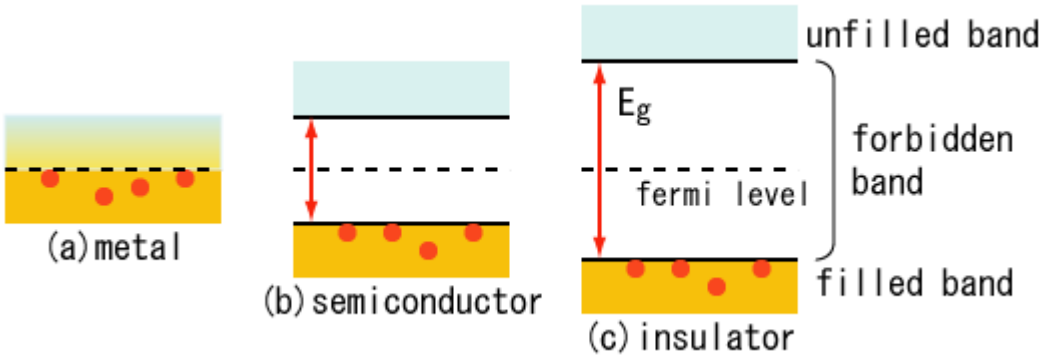

Figure II. 1 A diagram showing the valence and conduction bands of insulators, metals, and semiconductors

These two bands are separated by a forbidden band called **Band-Gap**, i.e., the energy difference between the highest occupied energy state of the valence band and the lowest unoccupied state of the conduction band (the energy value of this separation band defines the electrical properties of the material). Another important parameter in the band theory is the Fermi level. It lies between the valence band and conduction band because, at absolute zero temperature, the electrons are all in the lowest energy state. The fermi level is the highest energy level that an electron can occupy at the absolute zero temperature and it determines the probability of electron occupancy at different energy levels. The closer the Fermi level is to the **CB**, the easier it will be for electrons in the **VB** to transition into the conduction band.

A large band gap means that a lot of energy is required to excite valence electrons to the conduction band. This is the case of insulators, **Figure II. 1(c)**. In semiconductors, the band gap is small enough that an external energy, whether calorific, electromagnetic or light, can move the electrons from the valence band to the conduction band, **Figure II. 1(b)**. Conductors have an overlap between both bands (**VB** and **CB**); the valence electrons are basically free them and hence the high conductivity. Consequently, electronic conductivity of solid materials gives us almost an unambiguous way to classify them. Simply, on the basis of electrical conductivity, they are conductors, semiconductors, or insulators. The range of conductivities of conductors (metals) is quite large, about 10^6 and 10^8 ($S.m^{-1}$) while it is about 10^3 to 10^{-6} for semiconductors, and less than 10^{-6} for insulators.

II.1.3 Electronic conductivity in non-crystalline materials

The rules governing the electronic transport properties of crystalline (ordered) and amorphous (disordered) solids are generally different. In relation to these properties in disordered non-crystalline material, the question arose which of the solid crystalline concepts would be suitable for use in non-crystalline materials. Mott and Davis [3] showed that the concept of electron density of states $N(E)$ is equally valid for the two types of materials. In general, the available evidence suggests that the form (E) in a liquid or non-crystalline solid does not differ much from that of the crystal, except for some details such as states located in the forbidden energy range or the energy gap in semiconductors. (E) quantifies the number of electronic states likely to be occupied and possessing a given energy in a considered material.

Anderson gave a quantitative criterion for the *electron localization*; the localization results in an exponential decrease in the wave function with distance [4]. The localized states therefore exist in terms of potential wells where the electrons remain trapped and cannot move. The variation of the potential of each atom of the lattice is visible on the graph by the depth of the wells; this is generated by the disorder of the crystal lattice, **Figure II. 2**.

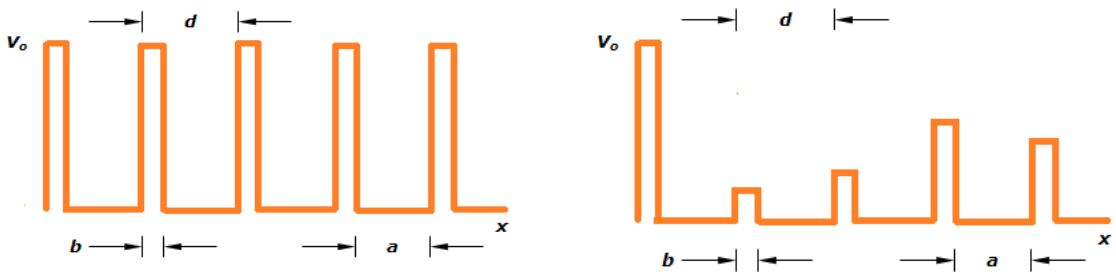

Figure II. 2 (a) Potential wells for a crystalline lattice (b) Potential wells of a non-crystalline lattice.

Banyai [5] suggested that, in most non-crystalline materials, the states are localized near the edges of conduction or valence bands. The concept of localized states is very simple; they are simply "traps" for the injected carriers. Furthermore, at the bottom of a conduction band or on top of a valence band, such localized states must necessarily occur in a disordered material.

In any non-crystalline system, the localized states (low electronic mobility) and the delocalized states (high electronic mobility) cannot coexist with same energy; there exist an energy (E_c) separating the two domains, **Figure II. 3**. This energy was first mentioned by Mott [6] and referred to as mobility edge in reference [7].

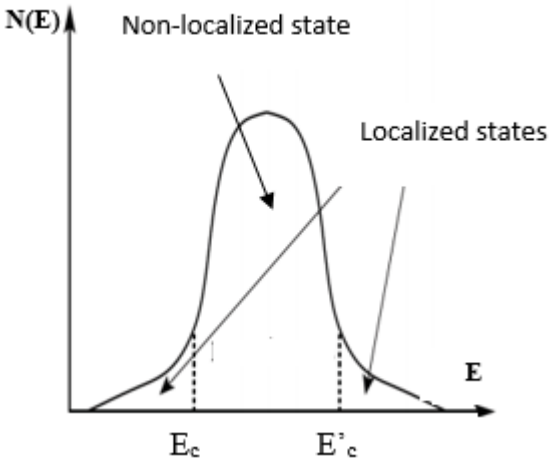

Figure II. 3 Density of electronic states in Anderson's model. E_c and E'_c separate regions of localized and non-localized (extended) states.

For energies below the mobility edge, an electron moves by "hopping" from one localized state to another (a process involving interaction with phonons and with only small activation energy). This mobility disappears at T = 0 K, even if the wave functions of the neighboring states overlap. If the energy E is just above E_c, with E ≅ Ec, the conductivity has a finite value, called "minimum metallic conductivity". For T > 0 K and electron excitation above the mobility limit, the electronic conductivity has an exponential form

$$\sigma = \sigma_{min} \exp[-(Ec - E_F)/kT] \qquad \text{(II.5)}$$

where E_F is the Fermi energy and the minimum metallic conductivity $\sigma_{\min}$ was calculated by Mott [3], $\sigma_{\min} \approx 10^2 - 10^3$ S cm^{-1}.

Figure II.4 presents the two most common models of amorphous semiconductors. The Cohen-Fritzsche-Ovshinsky model [7] suggests a pseudo-gap for non-crystalline materials when the localized states of the conduction band and valence band overlap in the band gap of the semiconductor. In contrast, Mott [6] assumes a real band gap for amorphous semiconductors with $N(E) = 0$ below and above limiting energies E_A and E_B, which corresponds to the lowest electronic states located in the conduction band and at the highest electronic states located in the valence band. The electronic excitation in the localized states at E_A also leads to an exponential dependence of the hopping conductivity on temperature:

$$\sigma = \sigma_{hop} \exp[-(E_A - E_F)/kT] \quad \text{(II.6)}$$

but the pre-exponential factor σ_{hop} is very small compared to $\sigma_{\min,}$ with $\sigma_{hop} / \sigma_{\min}$ ratio of the order of 10^{-2} - 10^{-3} [3].

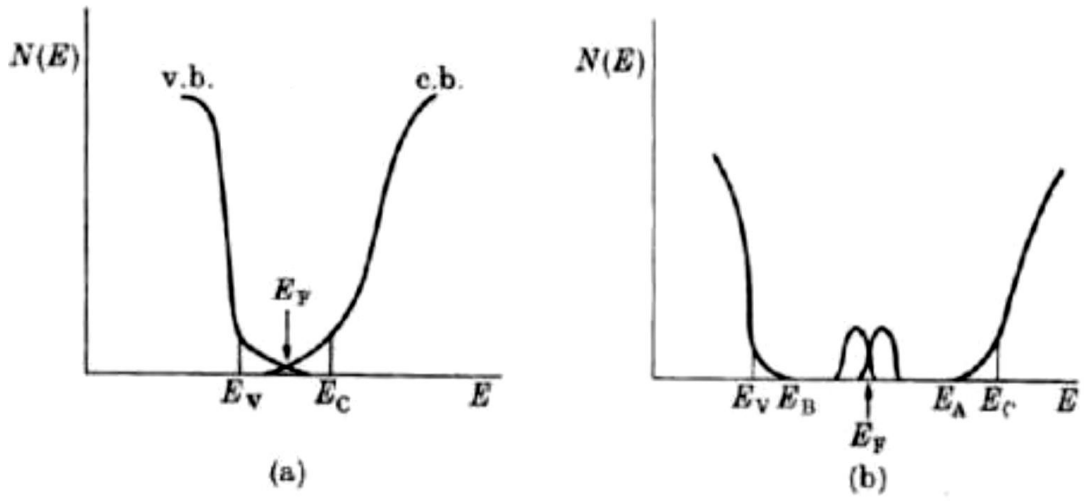

Figure II.4 The density of states in non-crystalline amorphous semiconductors: (a) the Cohen-Fritsche-Ovshinsky model [7], and (b) Mott model [6] with states in the gap bonds pendants acting as deep donors below acceptors; E_V and E_C are the energies separating localized and extended states in the valence and conduction bands, respectively; $\Delta E = E_C - E_A$ and $\Delta E' = E_B - E_V$ are the bandwidths of localized electronic states in the conduction and valence bands.

II.1.4 Ionic conductivity

Ionic conductivity is the electrical conductivity resulting from the motion of ionic charges through the medium network. It was introduced by elementary science as a property of liquid electrolyte solutions [8]. Initially recognized by Faraday, in solid lead fluoride at high temperature [9], it was related to the motion of fluoride anions within the structure. This kind of conductivity in solids is critically important in many electrochemical applications such as battery solid electrolytes, chemical sensors, ionic switches, etc. A brief overview is presented hereafter on ionic conductivity in crystalline and non-crystalline ionic solids.

II.1.4.1 Ionic conductivity in crystalline ionic materials

In an ideal crystal, all constituent ions are arranged in a regular periodic way and are often stacked in a compact form. Thus, there are little spaces for an ion to diffuse into the lattice. However, at any non-zero temperature, some defects might exist in the structure. These defects

could be positional disorders due to deviation from ideal stacking. The degree of such disorder can vary from one material to another or even in the same material can vary from one temperature or pressure to another. The defects can be classified into two categories: (i) intrinsic defects and (ii) extrinsic defects.

In the intrinsic category, two types of defects are important in the context of ion mobility and are 'Frenkel' defect and 'Schottky' defect, **Figure II.5**. Frenkel defect refers to the case where an ion is displaced from its normal lattice point and shifts to a nearby interstice, or space, between atoms in the lattice. Schottky defect refers to the lack of ions of opposite signs in the lattice, resulting in anionic and cationic vacancies, compensating for each other in the network (Since there must be the balance of electric charges). In the extrinsic category, the vacancies are generated following the substitution of one ion by another, the crystalline arrangement is then modified and no longer corresponds to that of the perfect crystal. As such, any ion in the immediate vicinity of vacant sites may jump to one of them. This leaves the previous site of the vacant ion that could now host another ion. The mechanism of diffusion and migration of ions via defects constitute the basic processes of ionic conduction in crystalline ionic solids (conductivity directly depends on the concentration of defects).

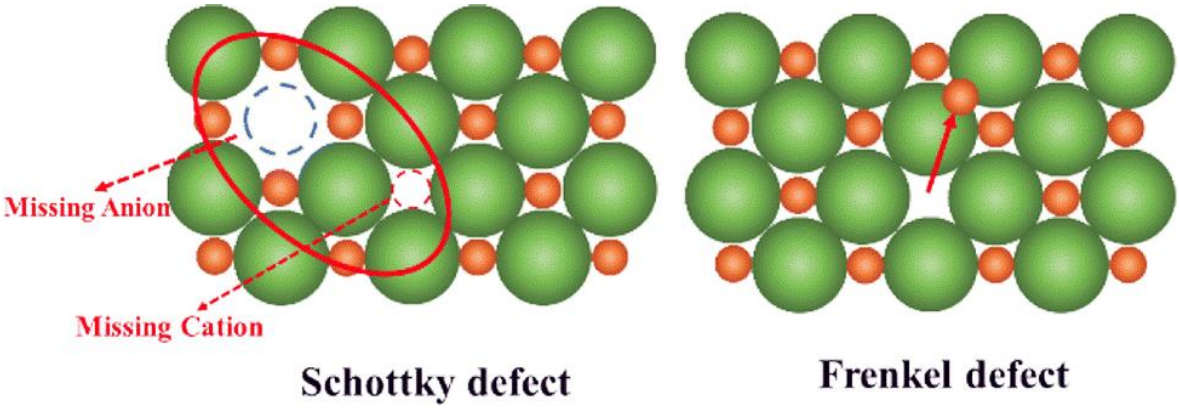

Figure II.5 Schottky's defect (a) and Frenkel's defect (b).

The main mechanisms describing the diffusion of ions in solids were explained in reference [10] which distinguished between six of them, **Figure II.6**:

1. **Direct exchange** occurs when one ion takes the place of the other and vice versa on the same energy level. This mechanism is very unlikely in iono-covalent binary compounds due to the enormous local distortions and repulsions it would cause.

2. **Cycle exchange** is a variant of the previous mechanism. It involves a cooperative movement of several species.

3. **The lacunar mechanism** takes place by the passage of an atom from a normal site to a neighboring vacant site; this movement is done continuously, i.e., the atom will be able to continue its movement when a new gap - or the previous gap - arrives (or returns) to its neighborhood.

4. **The direct interstitial mechanism**, in which an atom moves from one interstitial site in the lattice to another nearby empty interstitial site.

5. **The indirect interstitial mechanism**: the atom in the interstitial position forces a nearby atom of the same nature, located on a normal site, into a free interstitial site.

6. **The cooperative jump mechanisms** proposed to explain the conductivity in certain ionic conductors containing a large concentration of mobile carriers.

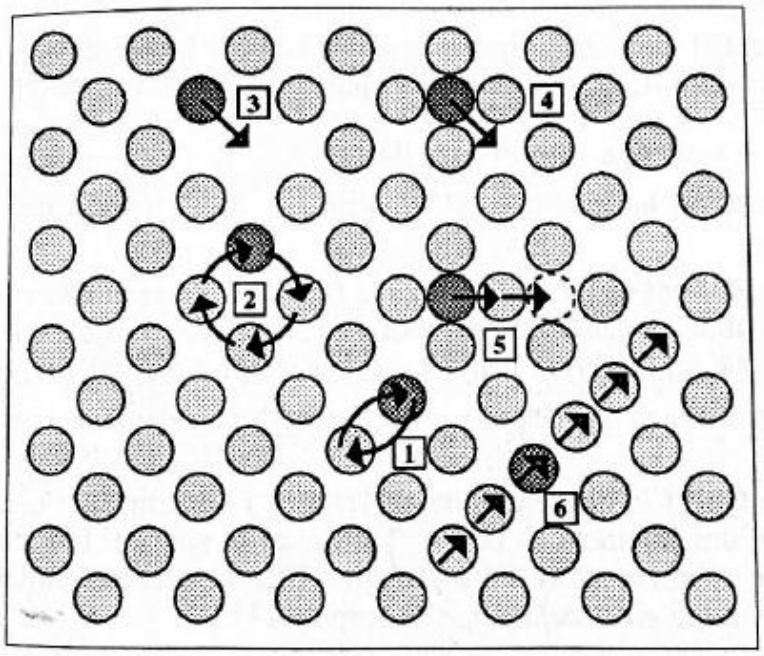

Figure II.6 Diagram of the main diffusion mechanisms taken from reference [10].

II.1.4.2 Ionic conductivity in non-crystalline materials

In the case of non-crystalline materials, the conduction mechanism is associated to the presence of defects in the material, yet not exactly. In contrast to the crystalline ionic materials, the

conductivity does not depend on the concentration of defects which are in excess compared to the number of charge carriers. In fact, it is this excess, which is made possible by the disordered structure of the glass, that ensures ionic conduction. In this category, two main phenomena govern the conductivity: (i) the dissociation of the charge carriers and (2) the migration of charge carriers from one site to another through the vitreous network. It is therefore difficult to interpret ionic conductivity based solely on concepts applied to crystalline materials. In the regards, since it discovery in 1884 [11], the ionic transport in glasses (particularly oxide glasses [12]–[14]) was heavily studied in order to understand the mechanisms governing it.

In general, the conductivity, when only one type of carrier is concerned, is given by the relation (II.2). In addition, the mobility can be obtained from the diffusion coefficient using the Nernst-Einstein equation:

$$\mu kT=qD \qquad \text{(II.7)}$$

For models involving jumps independent carriers, we can write *D* as follows:

$$D = \alpha\lambda^2\nu_0 \exp(-E_m / kT) \qquad \text{(II.8)}$$

where α is the degree of freedom, λ is the average jump distance, ν_0 is the attempt frequency of the ions and E_m is the migration energy.

In addition, the most general expression of the concentration of mobile carriers is written as:

$$n = n_0 \exp(-E_c / kT) \qquad \text{(II.9)}$$

where n_0 is the total number of the modifier cations and E_C the energy related to the creation of mobile carriers.

Hence, the combination of equations (II.2), (II.7), (II.8) and (II.9) gives:

$$\sigma = \frac{q^2\lambda^2 n_0 \nu_0 \alpha}{kT} \exp\left(-\frac{E_c+E_m}{kT}\right) \qquad \text{(II.10)}$$

Most often the conductivity is expressed in the following simplified form:

$$\sigma = \frac{\sigma_0}{T} ex\, p\left(-\frac{E_\sigma}{kT}\right) \qquad \text{(II.11)}$$

Therefore, the measured activation energy E_a is the sum of two terms, the creation energy of mobile carriers E_C, which is directly linked to n and the migration energy of the ions E_m, directly linked to μ.

In the literature, the phenomenon of ionic transport in glasses is explained via numerous models. Among those we mention, the model of the strong electrolyte (Anderson and Stuart model) [15], the model of the weak electrolyte (Ravaine and Souquet) [16], [17], the Monte-Carlo studies by Bunde et al. [18], the power law (Jonscher's law) [19], the Random Free-Energy Barrier Model [20], [21], and the Jump Relaxation Model [22], etc.

II.2 Electrical conductivity in chalcogenide glasses

II.2.1 Overview

Unlike oxide-based systems, which mainly belong to insulators and/or ionic conductors, ion transport in chalcogenide glasses was observed for the first time in the 1970s. The great polarizability of sulfur, selenium or tellurium with respect to oxygen, and the ionic mobility and diffusivity make the chalcogenide glasses suitable candidates for fundamental research and ionic applications in solid state. Pure chalcogenide glasses, i.e. without metal, are electronic conductors [23], [24]. Their conductivity varies with increasing the atomic number of the chalcogen elements present in the glass [25]. In fact, chalcogenide systems having metals in their composition, act as ionic superconductors (where the electronic conductivity is lower than the ionic conductivity of several orders of magnitude). In this case, chalcogenide glasses are characterized by a conductivity that increases significantly with the metal content from 10^{-16}-10^{-14} (insulating materials) to values greater than 10^{-7} S.cm^{-1}. This phenomenon, observed by Tanaka et al. [23], show that the increase in conductivity is due to the metal bonding occurring when passing from sulfur to selenium and then tellurium. The As-S binary system has a very low electronic conductivity at room temperature (298 K) (in the order of 10^{-18} to 10^{-13} S.cm^{-1} depending on the composition). The maximum conductivity value recorded for the As_2S_3 stoichiometric composition was 5×10^{-16} S.cm^{-1}, and it also shows a low activation energy of ≈1.1 eV in [24]. These materials therefore have electrical properties almost identical to those of insulating materials (dielectric materials). **Figure II.7** presents typical conductivities of some chalcogenide glasses. As we can see in the figure, the As_2S_3 glasses have the lowest conductivity value while selenium and tellurium-based glasses exhibit a conductivity that increases up to 8.0×10^{-9} for As_2Se_3 to 2.5×10^{-4} S.cm^{-1} for As_2Te_3 at room temperature, with a change in the activation energy of 0.7 to 0.3 eV respectively [25], [26].

The addition of metallic elements such as thallium (Z = 81) to the glass increases its electronic conductivity [27], except Tl-rich (> 17 at. %) vitreous alloys, showing ionic conductivity [28]–[30]. Meanwhile, the addition of lighter elements such as lithium (Z = 3) [31], silver (Z = 47) [32] or sodium (Z = 23) enhances the ionic conductivity due to the contribution of the mobile ions, hence the ionic transport phenomenon. We can say that the dopants used cause an increase in the ionic conductivity by an increase in the number of mobile carriers and by a redistribution of the negative sites which can be used for the movement of cations. This is the case with the glassy systems AgGeSe, AgGeS and AgGeSeSb which show a sudden change in ionic conductivity with the concentration of Ag^+, so these ions are part of solid electrolytes with high ionic conductivity. The change in conductivity is always linked to the change in concentration (≈ 5 orders of magnitude in Ag concentration) as well as to the percolation transition [33], [34].

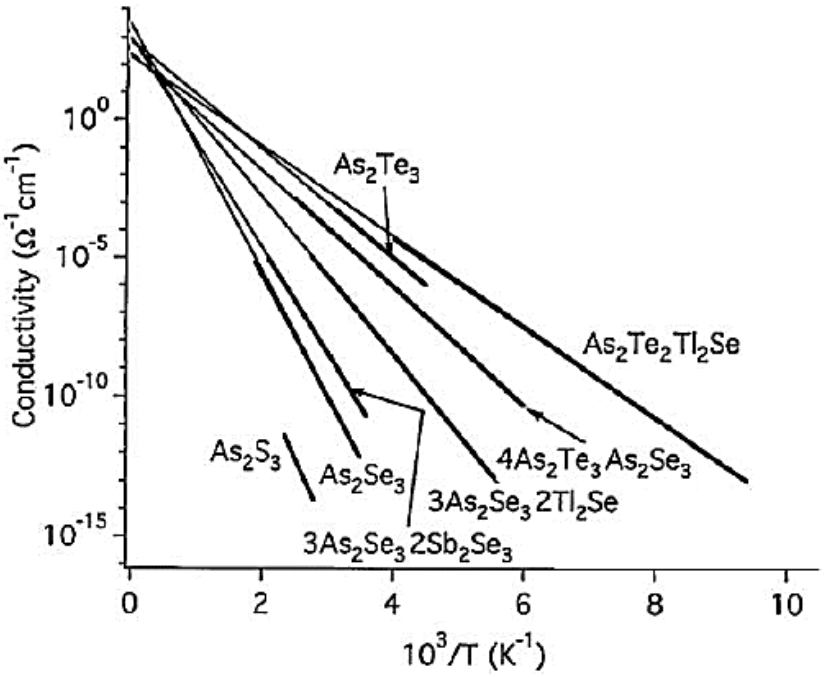

Figure II.7 Conductivity variation as a function of temperature for a set of chalcogenide glasses.

II.2.2 Electrical Measurements

II.2.2.1 Impedance spectroscopy: principle and operating mode

As mentioned earlier in section II.1.1, total electrical conductivity σ results from the combination of two contributions, i.e., ionic and electronic. Impedance spectroscopy is a technique that allows the measurement of these contributions combined. The technique is based

on the variation of the imaginary part of the impedance of the sample and its real part as a function of frequency. By applying an alternating voltage U to a sample, an alternating current I is created and is out of phase with respect to the voltage. Hence the equations:

$$U = U_0 \exp(i\omega t) \quad \text{(II.12)}$$

$$I = I_0 \exp i(\omega t + \varphi) \quad \text{(II.13)}$$

where U_0 and I_0 are the amplitudes of the voltage and current, respectively, ω is the angular frequency and φ is the phase difference between current and voltage.

The ratio between the voltage and the current then makes it possible to define the electrical impedance $Z(\omega)$, characteristic of the sample at a given frequency and thus we can write:

$$Z(\omega) = \frac{U}{I} \quad \text{(II.14)}$$

When the above equations are combined, we get:

$$Z(\omega) = \frac{U_0}{I_0} \exp(i\omega t - i(\omega t + \varphi)) = \frac{U_0}{I_0} \exp(-i\varphi) \quad \text{(II.15)}$$

$$Z(\omega) = |Z| \cos\varphi - i\,|Z| \sin\varphi = Z'(\omega) - i.Z"(\omega) \quad \text{(II.16)}$$

In this regards, the real component of the complex impedance, i.e., $Z'(\omega) = |Z| \cos\varphi$, represents the "effective resistance", while the imaginary component, $Z''(\omega) = |Z| \sin\varphi$, is referred to as the "reactance". **Figure II. 8** illustrates the plot of $Z(\omega)$in the complex plane, with the real part of $Z'(\omega) = |Z| \cos\varphi$ on the abscissa and the imaginary part $Z''(\omega) = |Z| \sin\varphi$ on the ordinate and each measured point corresponds to the impedance at a given frequency ω. If several impedances Z_k are in series, the total impedance Z will be then the sum of these impedances such that: $Z = \Sigma Z_k$.

Before performing the impedance spectroscopy measurements, the quenched samples, if hard, were cut as rectangular plates and polished using silicon carbide SiC powder (9.3 μ grain size). On the contrary, the fragile samples were crushed to transform them into powder which is then strongly compacted and compressed, using a hydraulic pelletizing press, in order to obtain a well compact pellet. In both cases, gold was sputtered on opposite parallel sides of the sample in order to establish the blocking electrodes in the electrochemical cell, Au/glass /Au. The typical thickness of the samples was in the range of 0.5 to 1.5 mm.

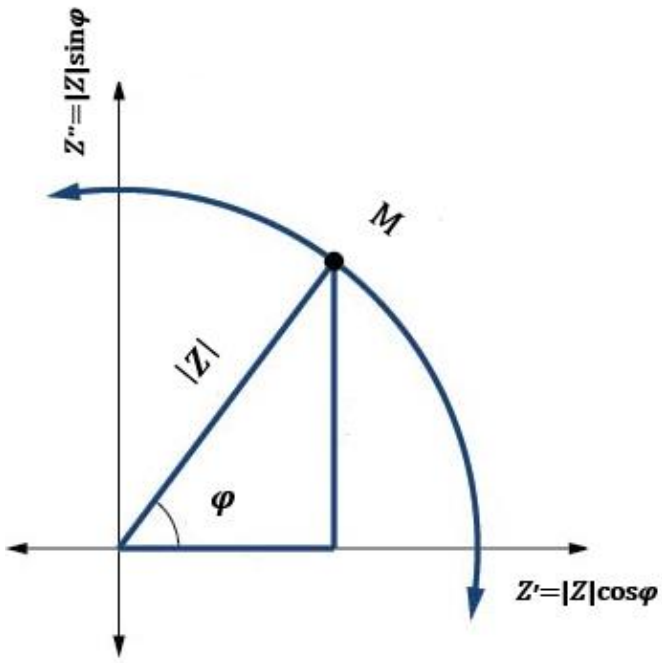

Figure II. 8 The real components $Z'(\omega)$ and the imaginary component $Z'(\omega)$ of the impedance vector in the complex plane.

In this work, an impedance meter ***Hewlett-Packard 4194A*** was employed for the impedance measurements were performed, **Figure II. 9**. The frequency range varies between 100 Hz to 15 MHz. The temperature range extends from room temperatures up to maximum temperatures that are lower than the glass transition temperatures for any given sample. The conductivity cell used is illustrated in **Figure II. 10**. It is air tight and this makes it possible to characterize the samples that are sensitive to humidity under argon. In the cell, the sample is positioned between a conductive rod and a copper plate; both are covered with gold to ensure good electrode/sample/electrode contact. The absence of pressure on the sample avoids the variations in the shape of the sample and therefore the geometric factor when approaching the glass transition temperature. The temperature was measured by a thermocouple placed near the sample with an accuracy of ±1 °C.

Figure II. 9: The Hewlett-Packard 4194A impedance meter used at the LPCA laboratory

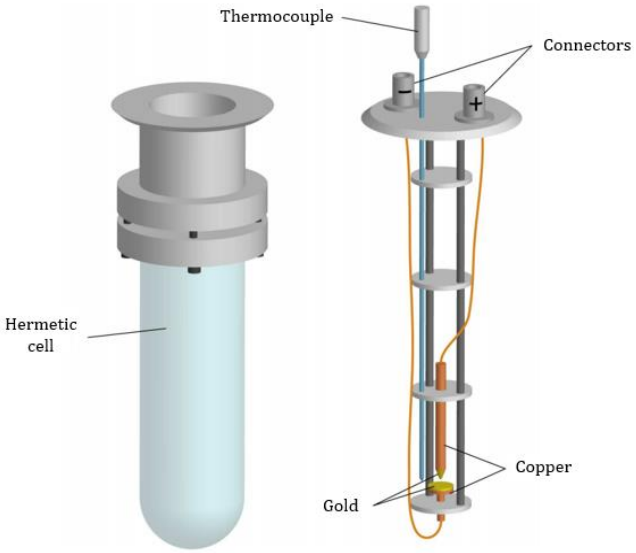

Figure II. 10: Conductivity cell used during electrical measurements.

Figure II. 11: The Hewlett Packard 4339B High Strength Resistivity Meter used at LPCA

At the end of the measurement, we obtain the Cole-Cole diagram plots. **Figure II. 12** represents the plot of the impedance diagrams in the Nyquist plane obtained for a certain sample at different temperatures. Each curve of the figure displays a high frequency arc (semi-circle) accompanied by horizontal arm at low frequencies. The presence of such arm, in the low frequency region, is characteristic of a polarization at the electrolyte/electrode interface; it highlights the phenomenon of diffusion and then accumulation of ions at the interface. In the high frequency domain, the ions do not have time to move sufficiently and the polarization is not observed. In contrast, at low frequencies, the ions travel longer and reach the electrolyte/electrode interface, where they remain blocked. As the phase of the electrolyte is a homogeneous and isotropic glass, it is characterized only by a resistive impedance R. The total solid resistance, corresponding to each temperature, is deduced from the point of intersection

of the arc with the horizontal arm. The total conductivity values σ are then obtained using the relationship (II.17):

$$\sigma = \frac{1}{R} \times \frac{L}{S} \qquad \text{(II.17)}$$

where $\frac{L}{S}$ is the geometrical factor of the sample (L = thickness, S = surface). Finally, the values obtained are plotted according to the function $\ln(\sigma) = f(\frac{1}{T})$.

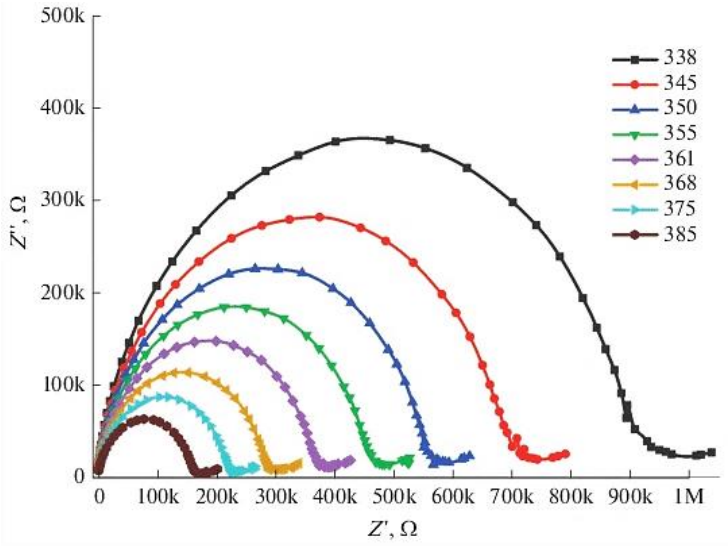

Figure II. 12: Impedance diagrams as a function of temperature.

II.2.2.2 DC conductivity measurements

The conductivity measurements were performed using a ***Hewlett Packard 4339B*** high resistivity meter with a continuous current source (or voltage) and an applied voltage of 100 Volts, **Figure II. 11**. The operating mode related to the electrochemical cell and the sample preparation is similar to the description in the previous section {II.2.2.1}. The DC (direct current) measurements apply Ohm's Law:

$$\sigma = \frac{L}{R \times S} = \frac{I \times L}{U \times S} \qquad \text{(II.18)}$$

With:

L: the length of the sample in centimeters

S : the surface of its cross-section in square centimeter

U : the voltage in volts

I : Intensity of current flowing through the body in Amperes.

II.3 Experimental results

In this chapter, we study the electrical properties of the 2 systems (binary and ternary) of lead-doped chalcogenide glasses that were previously synthesized either with impedance or with direct current as mentioned previously.

II.3.1 Electrical conductivity of glasses and crystals in the quasi-binary PbS-As_2S_3 system

The total electrical conductivity σ, determined from DC measurements, is plotted versus the inverse of absolute temperature (1000/T) for both glasses and crystals synthesised in the PbS-As_2S_3 system, **Figure II. 13**. The results corresponding to the quenched $(PbS)_x(As_2S_3)_{1-x}$ glass compositions ($0.0 \leq x \leq 0.5$) as well as the mechanically milled MM-$(PbS)_{0.6}(As_2S_3)_{0.4}$ and MM-$(PbS)_{0.7}(As_2S_3)_{0.3}$ compositions are presented in **Figure II. 13(a)**. The results of the crystalline compounds $PbAs_2S_4$, $Pb_5As_9S_{18}$ and $Pb_2As_2S_5$ are traced in **Figure II. 13(b).**

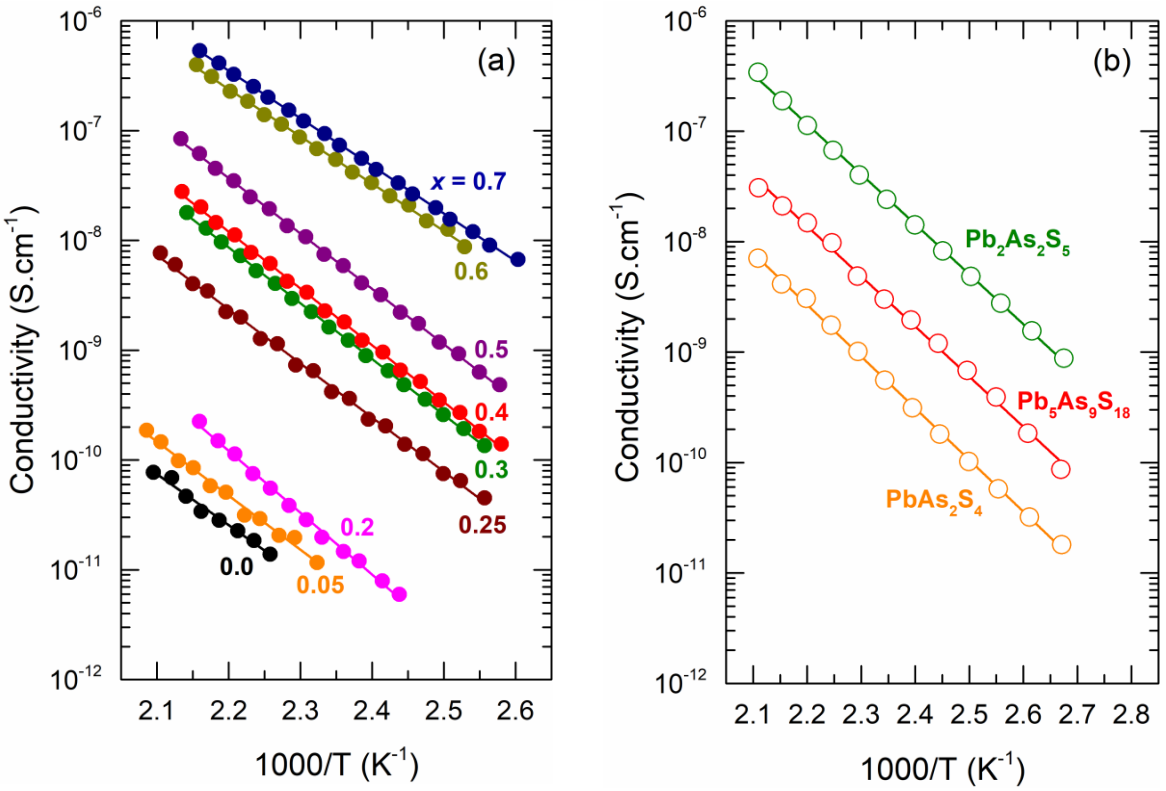

Figure II. 13*:* Total electrical conductivity σ plotted as a function of 1000/T (K) for (a) the $(PbS)_x(As_2S_3)_{1-x}$, $0.0 \leq x \leq 0.5$, glass compositions obtained by melt-quenching and the two composition obtained by mechanical milling MM-$(PbS)_{0.6}(As_2S_3)_{0.4}$ and MM-$(PbS)_{0.7}(As_2S_3)_{0.3}$ and (b) the crystalline compounds $PbAs_2S_4$, $Pb_5As_9S_{18}$ and $Pb_2As_2S_5$. The solid line represents a least-square fit of the data to Eq. (II.19).

The conductivity is temperature dependent and obeys the Arrhenius law for all of our synthesized glassy and crystalline samples:

$$\sigma = \sigma_0 \, exp\left(-\frac{E_\sigma}{kT}\right) \qquad \text{(II.19)}$$

where σ_0 is the pre-exponential factor, E_σ the conductivity activation energy, k the Boltzmann constant, and T the temperature. The room-temperature conductivity σ_{298}, E_σ and σ_0 were calculated from a least-square fit of the data to Eq. (II.19) and the derived parameters summarised in **Table II. 1** and **Figure II. 14**.

Table II. 1: Conductivity parameters of glasses and crystals in the PbS-As_2S_3 system: the room-temperature conductivity σ_{298}, the activation energy E_σ, and the pre-exponential factor σ_0.

Composition		σ_{298} **(S cm^{-1})**	σ_{423} **(*Ref*)**	E_σ **(eV)**	E_σ **(*Ref*)**	σ_0 **(S cm^{-1} K)**	σ_0 **(*Ref*)**	σ_0 **(*Ref*)**	
$(PbS)_x(As_2S_3)_{1-x}$									
X	[Pb] *(at.%)*		[35]		[35]		[36]	[35]	[36]
0.00	0.00	1.0×10^{-16}	–	0.921 (48)	–	0.41	1.20×10^{5}	–	–
0.05	1.03	2.0×10^{-16}	–	0.915 (23)	–	0.63	–	–	–
0.20	4.54	2.0×10^{-16}	–	0.966 (39)	–	4.4	–	–	–
0.25	5.88	4.6×10^{-15}	–	0.978 (10)	–	1.6×10^{2}	–	–	–
0.30	7.32	1.1×10^{-14}	1.8×10^{-10}	1.099 (10)	0.92	1.3×10^{3}	–	12	–
0.40	10.52	1.6×10^{-14}	–	0.994 (10)	–	1.4×10^{3}	3.07×10^{0}	–	3.07
0.50	14.28	5.1×10^{-14}	2.2×10^{-9}	1.002 (09)	0.88	4.6×10^{3}	1.25×10^{5}	30	1.25×10^{5}
0.60	18.75	2.3×10^{-12}	–	0.856 (10)	–	7.2×10^{2}	–	–	–
0.70*	24.14	3.2×10^{-12}	–	0.861 (10)	–	1.2×10^{3}	–	–	–
Pb–As–S crystals									
$PbAs_2S_4$	14.28	9.8×10^{-15}	–	0.930 (10)		5.4×10^{1}	–	–	–
$Pb_5As_9S_{18}$	15.62	5.9×10^{-14}	–	0.926 (20)		2.7×10^{2}	–	–	–
$Pb_2As_2S_5$	22.22	6.4×10^{-13}	–	0.899 (10)		1.1×10^{3}	–	–	–

Uncertainties in the last digit(s) of the parameter are given in parentheses.

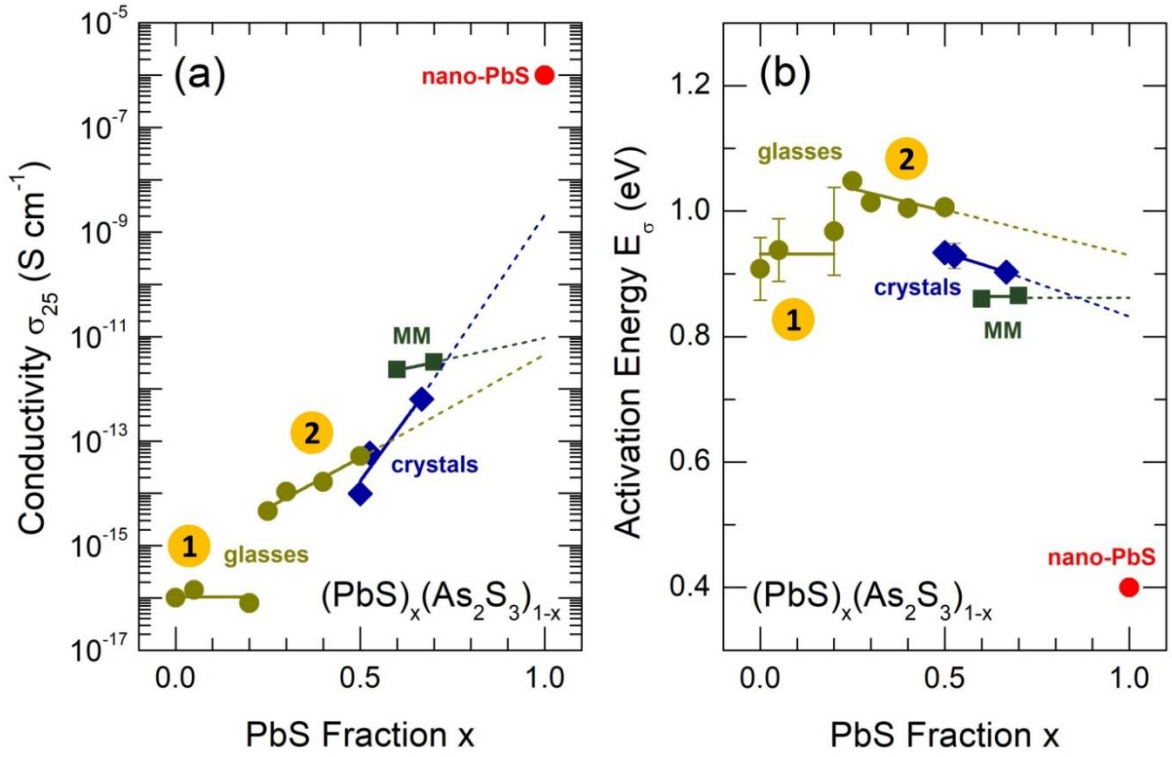

Figure II. 14: Electrical conductivity parameters plotted as a function of lead sulphide fraction x both for pseudo-binary $(PbS)_x(As_2S_3)_{1-x}$ glasses (dark yellow circles), MM-alloys (dark green squares), and the crystalline compounds $PbAs_2S_4$, $Pb_5As_9S_{18}$ and $Pb_2As_2S_5$ (dark blue diamonds): (a) room-temperature conductivity σ_{25}, (b) activation energy E_σ. Reported data for nanocrystalline nano-PbS [37] are also shown (red circle).

The conductivity parameters show complicated composition dependencies, **Figure II. 14**. Basically, the room temperature conductivity for the $(PbS)_x(As_2S_3)_{1-x}$ samples, $0.0 \leq x \leq 0.7$, increases by more than 4 orders of magnitude, from 1.0×10^{-16} S cm^{-1} (x = 0.0) to 3.2×10^{-12} S cm^{-1} (x = 0.7). Nevertheless, two different conductivity domains were observed for melt-quenched glasses: (1) $0.0 \leq x \leq 0.2$ ($\leq$ 4.5 at.% Pb), (2) $0.25 \leq x \leq 0.5$ ($5.8 \leq$ [Pb] ≤ 14.2 at.%), and a separate trend for MM-alloys, $x \geq 0.6$ (18.7 at.% Pb). Domain 1 is characterised by a nearly invariant conductivity, $\approx10^{-16}$ S cm^{-1}, and activation energy, 0.93 ± 0.05 eV, and suggests a certain electrical inactivity of lead sulphide, possibly related to inhomogeneity of the Pb-poor glasses. Then, the conductivity jumps by a factor of $\approx$20, and increases exponentially for glassy Pb-rich alloys (domain 2), accompanied by a monotonic decrease of E_σ. Finally, the MM-alloys exhibit an additional step-like increase by two orders of magnitude with weakly changing conductivity and activation energy.

The observed conductivity increase is reasonable since cubic lead sulphide is a narrow-gap semiconductor with a high electron and hole mobility. Even colloidal PbS nanocrystals exhibit enhanced electronic conductivity, ≈10^{-6} S cm^{-1}, and a moderate band gap $E_g \approx 2E_\sigma$ = 0.8 eV [37]. However, the extrapolated values of $\sigma_{298}^{glass}(1)$ and $E_\sigma^{glass}(1)$ for hypothetical glassy PbS (x = 1) are drastically different from the nanocrystalline parameters; $\sigma_{298}(nano\text{-PbS})/\ \sigma_{298}^{glass}(1) \approx 10^5$, and $E_\sigma(\ nano\text{-PbS})/\ E_\sigma^{glass}(1) \approx 0.44$, **Figure II. 14**. The disordered nature of glassy PbS-As_2S_3 network significantly reduces the carrier mobility while the difference in the lead local environment (tetrahedral vs. octahedral) seems increasing the band gap. The pre-exponential factor, $10 \lesssim \sigma_0 \lesssim 1000$ S cm^{-1}, indicates a conductivity mechanism via the extended electron states [3]. This mechanism appears to be operational for most lead thioarsenate glasses, except probably domain 1. Similar conclusion was reported previously [35], [36].

Likewise, the room temperature conductivity for the ternary crystals, $PbAs_2S_4$ (x = 0.5), $Pb_5As_9S_{18}$ ($x \approx 0.526$) and $Pb_2As_2S_5$ (x = 0.67), increases with increasing lead content, and the activation energy slightly decreases from 0.93 to 0.89 eV. The conductivity parameters for ternary crystals are similar to those of glasses, however, the conductivity extrapolation to x = 1 yields a much higher $\sigma_{298}^{cryst}(1) = 3\times10^{-9}$ S cm^{-1}, presumably related to a higher carrier mobility in the crystalline lattice.

To explore the effect of crystallisation on the structure and properties of lead thioarsenate glasses, thermal treatment of few selected glass samples, x = 0.1, 0.3 and 0.5, has been carried out at 280 °C for 30 days. XRD studies on the annealed samples indicate that sartorite $PbAs_2S_4$ is the only crystal phase being precipitated during the crystallisation, and its formation is independent of the glass composition, **Figure II. 15 (b)**. Broad diffraction patterns characteristic of glassy materials and well-defined Bragg peaks of crystalline $PbAs_2S_4$ indicate the glassy/crystalline nature of the annealed samples. SEM studies of the annealed x = 0.3 composition revealed the existence of interconnected few micron long stick-like particles assumed to be embedded into residual amorphous phase, **Figure II. 15 (a)**. The room temperature conductivity of the annealed samples increases compared to that of the original glasses and monotonically grows with increasing x, **Figure II. 15 (c)**. In addition, the annealed glassy/crystalline samples exhibit a higher conductivity in comparison with the synthesised Pb-As-S ternary compounds and yield $\sigma_{298}^{anneal}(1) = 2\times10^{-8}$ S cm^{-1}, that is, approaching even further the *nano*-PbS value. Similar behaviour is often observed in ion-conducting systems, e.g. in

$Li_7P_3S_{11}$ glass ceramic [38] and its glassy counterpart [39]. More ordered crystalline lattice in the semiconducting $PbAs_2S_4$ phase seems to be the origin of weaker electronic carrier scattering, providing higher electronic mobility and thus conductivity in the annealed samples.

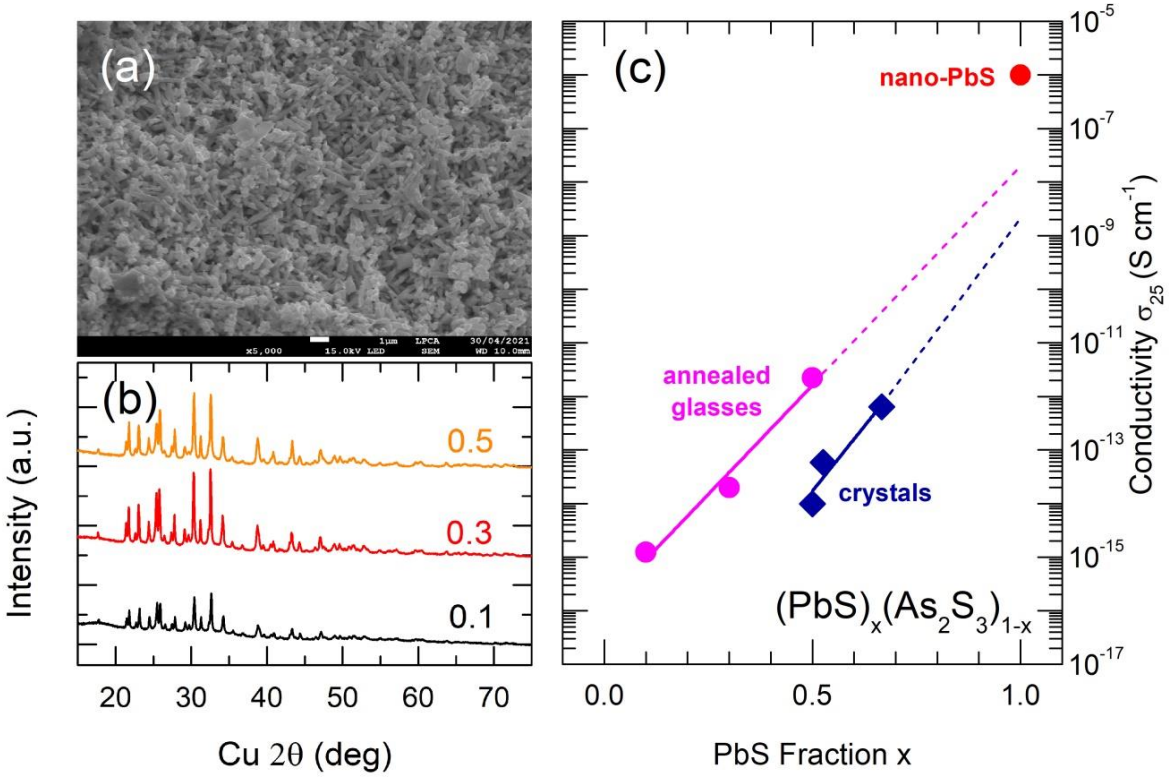

Figure II. 15: Morphology, XRD and conductivity results for annealed glass samples: (a) SEM micrograph for the annealed $x = 0.30$ composition, (b) diffraction patterns for selected $(PbS)_x(As_2S_3)_{1-x}$ compositions, $x = 0.1$, 0.3 and $x = 0.5$, after annealing at 280 °C, (c) room-temperature conductivity σ_{25} of the annealed samples (magenta), and crystalline references (navy).

II.3.1.1 Glassy and crystalline lead thioarsenate

Building on the results obtained in chapters I and II, we can emphasize the following with regards to glassy and crystalline lead thioarsenates, $PbS\text{-}As_2S_3$. The XRD results show a correlation between the $PbS\text{-}As_2S_3$ phase diagram [40] and crystallising phases. In the melt-quenched glasses with $x \leq 0.5$ and annealed at 280 °C, the appearing crystalline compound is orthorhombic $PbAs_2S_4$ ($x = 0.5$), stable below 305 °C [40]. The PbS-rich glasses and MM-alloys, $0.6 \leq x \leq 0.7$, yield a single congruently melting compound in the system, that is, monoclinic $Pb_2As_2S_5$ ($x = 0.67$). Nevertheless, the glass crystallisation results do not mean a similarly between the crystal and glass structure. Both $PbAs_2S_4$ [41] and $Pb_2As_2S_5$ [42] have high lead coordination, $6 \leq N_{Pb-S} \leq 9$ over a wide range of the Pb-S interatomic distances, 2.69

$\leq N_{Pb-S} \leq$ 3.62 Å, in contrast to our high-energy X-ray diffraction results (See chapter III). Another open question remains whether the synthesised glasses and MM-vitreous alloys are homogeneous. From the one side, a single glass transition and systematic changes of thermal properties as a function of composition indicates a glass homogeneity on macroscopic level (chapter I). The SEM images also exhibit rather uniform morphology in contrast to previously reported results [36]. From the other, the electrical conductivity suggests a lead clustering for PbS-poor glasses (domain 1) leading to apparent inactivity of isolated lead sulphide aggregates with a step-like conductivity increase above a critical threshold (chapter II). Similar behaviour was observed for phase-separated silver sulphide glasses [43], [44]. The observed phenomenon assumes a glass heterogeneity on mesoscopic length scale ($\lesssim$ 1000 Å), not visible in SEM. Further studies using small-angle X-ray or neutron scattering are necessary to solve this puzzle.

II.3.2 Electrical conductivity of glasses in the pseudo-ternary AgI-PbS-As_2S_3 system

We remind the lecturer that the first chapter had revealed, for the pseudo-ternary AgI-PbS-As_2S_3 system, the presence of a large vitreous domain. The later was illustrated in **Figure I.20** along with the three series, i.e., (i) the A-series $(AgI)_x(PbS)_{\mathbf{0.5-x/2}}(As_2S_3)_{\mathbf{0.5-x/2}}$, (ii) the B-series $(AgI)_{0.3}(PbS)_y(As_2S_3)_{0.7-y}$ and (iii) the C-series $(AgI)_z(PbS)_{0.1}(As_2S_3)_{0.9-z}$. After having studied the physical, thermal and morphological characteristics of the glasses of the three series, the electrical conductivity measurements of the various synthesized compositions were studied in the current chapter 2. Depending on glass resistivity, the electrical conductivity was determined either by the complex impedance method ($\sigma \geq 10^{-8}$ S.cm^{-1}) or from DC measurements ($\sigma < 10^{-8}$ S.cm^{-1})

II.3.2.1 A-series glasses $(AgI)_x(PbS)_{\mathbf{0.5-x/2}}(As_2S_3)_{\mathbf{0.5-x/2}}$

Typical Cole-Cole impedance plots, at various temperatures (90, 120 and 140°C) and (20, 70, 100 and 110 °C), are displayed for the glass compositions x = 0.3 (**Figure II.16(a)**) and x = 0.5 (**Figure II.16(b)**), respectively. The former is characterized by the presence of deformed demi circles attached to small polarization-tails. The demi-circle, typically related to electronic-conduction in glasses, decreases progressively with increasing temperature due to the decrease of the sample resistance. With increasing silver iodide content x, the demi-circle presents a further decrease ($|Z| \cos \varphi$ axis in the range of k-ohms for x = 0.5 vs. M-ohms for x = 0.3). This is accompanied by an enhancement of the polarization tail at low-frequency, indicating an

enhancement of the ionic character in glass due to the increase of mobile ion concentration. **Figure II.16(b)**.

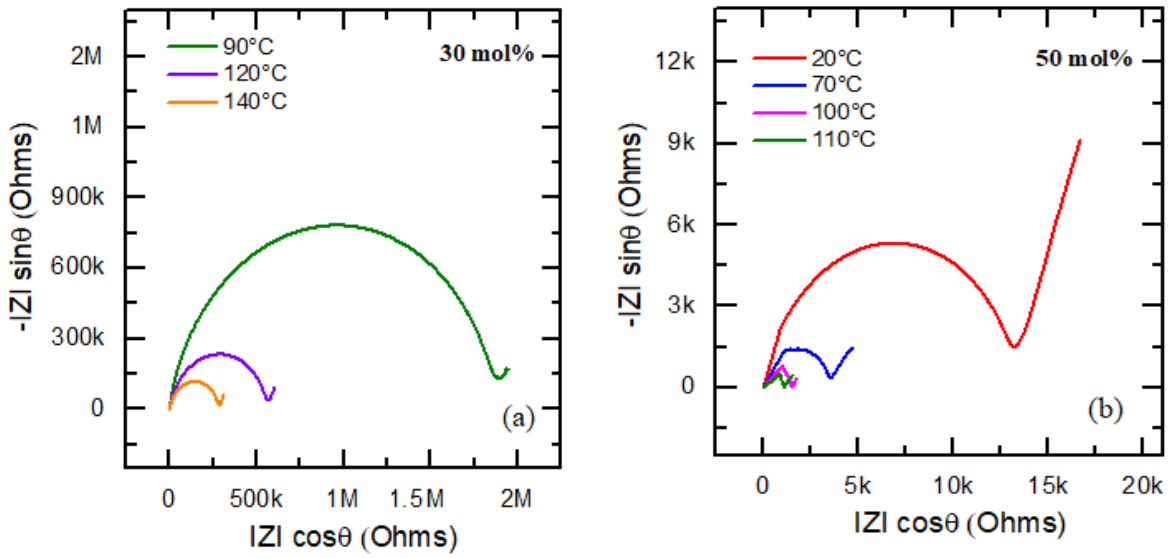

Figure II.16 Nyquist plot of impedance of the (a) x = 0.3 at 90, 120 and 140°C and (b) x = 0.5 at 20, 70, 100 and 110 °C glass compositions in the A-series $(AgI)_x(PbS)_{\mathbf{0.5-x/2}}(As_2S_3)_{\mathbf{0.5-x/2}}$.

Typical conductivity temperature dependencies for the A series glasses, $0.0 \leq x \leq 0.7$, are shown in **Figure II.17**. The total electrical conductivity, σ, does not show any significant hysteresis and obeys the Arrhenius law, equation II.11. The room temperature conductivity σ_{298}, σ_0 and E_σ were calculated from a least-square fit of the data to Eq.(II.11). The results are summarized in **Table II.2**. The later also presents the average interatomic distance between the silver ions in the glasses, $r_{Ag\text{-}Ag}$. The calculations were done assuming a random distribution of Ag^+ cation sites and a spherical approximation:

$$r_{Ag\_Ag} = 2(3.\ V_a\ /4\pi.N_A.C_{Ag})^{1/3} \qquad \text{(II.20)}$$

where V_a is the mean atomic volume, N_A is the number of Avogadro and C_{Ag} is the mobile Ag^+ cation fraction.

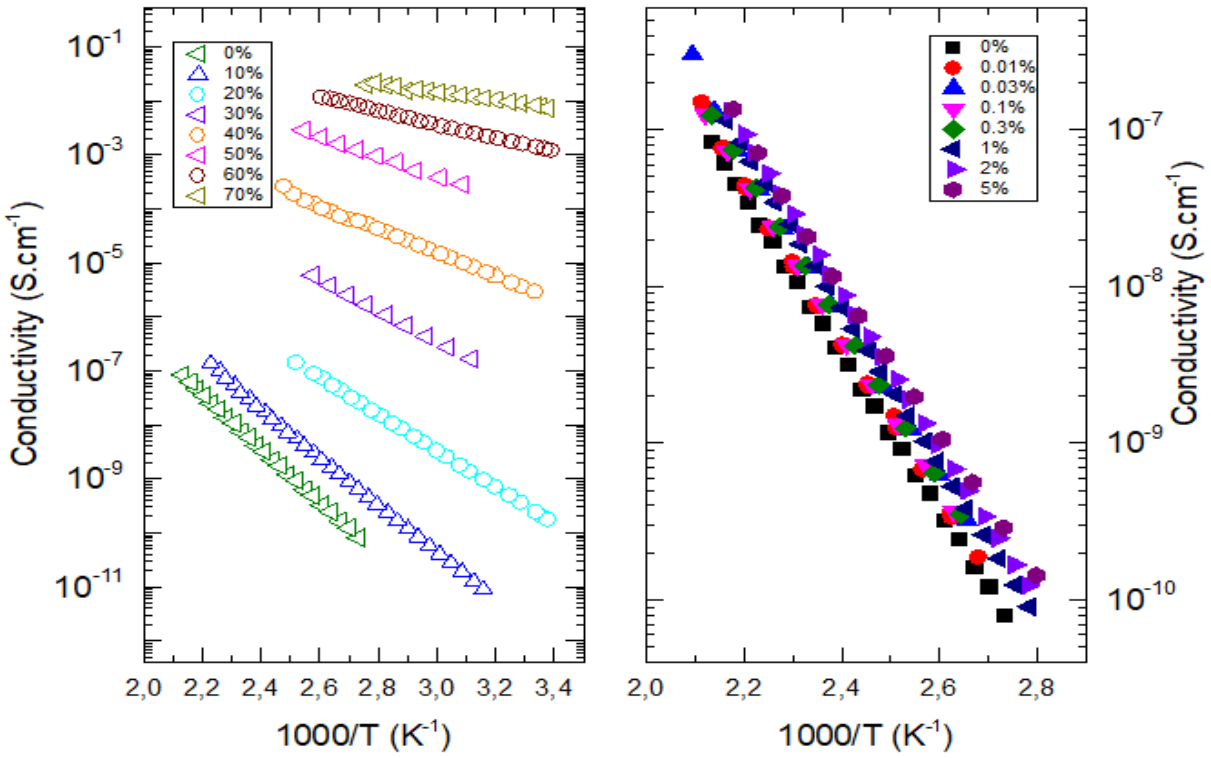

Figure II.17 Temperature dependences of the total electrical conductivity σ for the A series $(AgI)_x(PbS)_{\mathbf{0.5-x/2}}(As_2S_3)_{\mathbf{0.5-x/2}}$ glass system. The right figure presents the results for the host matrix $(PbS)_{0.5}(As_2S_3)_{0.5}$ and the glass compositions (x = 0.1, 0.2, 0.3, 0.4, 0.5, 0.6 and 0.7). The left figure plots the results for the diluted compositions (x < 0.1).

Figure II.18 displays the room-temperature conductivity σ_{298} of the A-series glasses in the current AgI-PbS-As_2S_3 system (blue color), as a function of the silver content x, along with the A-series glasses of the previously obtained AgI-HgS-As_2S_3 system (orange color) [45]. Before presenting the electrical properties of the current leaded system, we summarize the electrical behavior in the previous mercury doped one. The conductivity isotherms of this later present at least three different concentration regions with clearly distinct variation in the electrical conductivity: (a) region-A with diluted silver content (≤ 2-5 at.% Ag), (b) region-B with rich silver content (8 ≤ [Ag] ≤ 18 at.% Ag) and finally (c) region-C with extremely rich silver content (> 18 at.% Ag), **Figure II.18(a)**. In this regards, the observed ionic conductivity evolution in the AgI-HgS-As_2S_3 glasses shows characteristic transport regimes for ion-conducting chalcogenide glasses over a wide composition range: (i) critical percolation regime for diluted glasses (region A), and (ii) modifier-controlled regime for intermediate- and high Ag-rich vitreous alloys (regions B and C). The main difference compared to previously reported conductivity and tracer diffusion results [46], [47] appears to be two sub-regions B and C for

the modifier-controlled domain clearly seen in **Figure II.18(a)** by changing the slope $\partial(\log \sigma)/\partial y$. To clarify, here is a detailed description of the ionic conductivity regimes present.

- **Critical percolation domain A ($y_c < y \leq$ 2–5 at.% Ag)**

The ionic conductivity evolution in region A exhibits all characteristic features of the critical percolation regime [33]. Diluted $(AgI)_x(HgS)_{0.5-x/2}(As_2S_3)_{0.5-x/2}$ chalcogenide glasses show a rapid increase of conductivity (≈ 4.5-5 orders of magnitude) in a limited concentration range, $y \leq$ 2–5 at.% Ag (region A), revealing a power-law composition dependence, **Figure II.18**:

$$\sigma_i(y,T) = \sigma_i\,(1,T).y^{t(T)} \qquad \text{(II.21)}$$

where $\sigma_i(1,T)$ is the ionic conductivity of a hypothetical percolation-controlled phase at the mole fraction $y = 1$, y is the mobile Ag^+ ion content, and $t(T)$ is the temperature-dependant power-law exponent:

$$t(T) = t_0 + T_0/T \qquad \text{(II.22)}$$

where t_0 is the critical exponent at $T = \infty$ and T_0 is the critical fictive temperature which reflects the interconnectivity of an infinite percolation clusters embedded in the host matrix. The conductivity activation energy, E_y, in the critical percolation domain is also depending on T_0:

$$E_y = E_0 - kT_0\ln(y/y_c) \qquad \text{(II.23)}$$

where E_0 is the percolation threshold activation energy needed to induce Ag^+ ion mobility in glass ($y_c \cong$ 30 ppm Ag [33]) and $kT_0\ln(y/y_c)$ is the configuration entropy term related to the infinite percolation cluster(s) frozen below Tg;

The structural hypothesis behind the critical percolation regime suggests a random distribution of silver sites within the glass network [33]. The average Ag–Ag separation distance, calculated using a Wigner–Seitz type relation (Eq. II.20) changes between 80 Å and 10 Å depending on the silver content y. Consequently, the preferential conduction pathways are not yet formed in the critical percolation domain A. The transport properties of the glass in this percolation-controlled domain are governed by the number, interconnections, and topology of the percolation clusters and the backbone of these later is strongly affected by the structural organization of the host matrix. The nature of the mobile cation (e.g. Ag^+, Cu^+, etc.), the chemical form of the dopant (e.g. metal chalcogenide or halide) as well as the chemical form of the host matrix (sulfide or selenide) are irrelevant [45].

- **Modifier-controlled regions B and C**

The ionic conductivity of the $(AgI)_x(HgS)_{0.5-x/2}(As_2S_3)_{0.5-x/2}$ glasses [45] diverges from the power-law behaviour (II.21) in the modifier-controlled domain at higher silver content $y > 3$ at.% Ag ($x > 0.1$), **Figure II.18**. Instead, one observes an exponential increase of conductivity as a function of y:

$$\sigma_i(y) = \sigma_i(0).e^{ay} \qquad \text{(II.24)}$$

where a is a constant. In this region, pulsed neutron and hard X-ray diffraction as well as small-angle neutron scattering experiments reveal a non-random silver distribution in the modifier-controlled domain and formation of preferential conduction pathways formed by direct contacts of corner- and/or edge-sharing silver-related coordination polyhedra [48], [49]. For the $(AgI)_x(HgS)_{0.5-x/2}(As_2S_3)_{0.5-x/2}$ glasses, the change in the slope $\partial \log \sigma/\partial y$ at $x \approx 18$ at.% Ag ($x \approx 0.5$) was attributed to structural changes between regions B and C [45]. In this Modifier-controlled domain, the silver species are distributed non-randomly in the glass network forming preferential conduction pathways and ensuring high Ag^+ ionic mobility.

Similarly to the mercury doped system (orange color), the A-series glasses in the AgI-PbS-As_2S_3 (blue color), show a remarkable increase in room temperature electrical conductivity with increasing silver halide content (≈11 orders of magnitude), **Figure II.18(a)** and **Figure II.18(b)** . In fact, the conductivity of the glasses passes from values that are typical for insulating sulfide glasses (~10^{-14} S cm^{-1}) [24] to those characteristic of superionic vitreous alloys (10^{-3} S cm^{-1}) [50], [51]. The maximum room-temperature conductivity is 7.8×10^{-3} S cm^{-1} for the AgI-rich glasses ($x = 0.7$; 28.57 at.% Ag). The activation energy decreases from ~1.02 ($x = 0.0$) to 0.18 eV ($x = 0.7$), **Figure II.19(a).** In contrast to the pre-exponential factor σ_0 of the mercury containing system (remains essentially invariant;$10^5 \leq \sigma_0(x) \leq 10^6$ S cm^{-1} K), the pre-exponential factor of the lead containing system fluctuates between 10^3 and 10^7 S cm^{-1} K, **Figure II.19(b).**

In case of the current AgI-PbS-As_2S_3, three different conductivity regions are also distinguished: (a) region-A (≤ 3 at.% Ag), (b) region-B (5 ≤ [Ag] ≤ 18 at.% Ag) and (c) region-C (> 18 at.% Ag). To the contrary of its mercury counterpart, the diluted glasses in the AgI-PbS-As_2S_3 (region-A) show a limited percolation-controlled-mechanism, **Figure II.18**. This is evidenced from the log-log scale plot of the conductivity isotherm, **Figure II.18(b)**. The later shows that, at low Ag content, the conductivity changes slightly with silver additions in contrast to the

mercury containing system showing a nearly perfect straight line fit over ~3 orders of magnitude in the concentration. This can be explained by the enhanced electronic conductivity of the $(PbS)_{0.5}(As_2S_3)_{0.5}$ host matrix, $\sigma_{298} \approx 6\times10^{-14}$ S cm^{-1}, masking the ionic transport at low cation content. Another evidence of the enhanced electronic conductivity of the leaded system, in this concentration region-A, could be the higher activation energy E_σ (partially) and the higher pre-exponential factor σ_0 comparing to those of the AgI-HgS-As_2S_3. It was found earlier [52], [53] that the hole conductivity in mixed conducting silver selenide glasses is usually characterised by a higher activation energy and respectively higher σ_0 compared to the Ag^+ ion transport.

Table II.2 Electric properties of the A series glass system $(AgI)_x(PbS)_{0.5-x/2}(As_2S_3)_{0.5-x/2}$

x	[Ag] (at.%)	$r_{Ag\text{-}Ag}$ (Å)	log σ_{298}	E_σ (eV)	log σ_0 (S cm^{-1} K)
0	0	-	-13.21	1.025	6.58
0.0001	0.003	118.3	-13.19	1.039	6.83
0.0003	0.009	82.1	-13.13	1.054	7.16
0.001	0.029	54.9	-13.09	1.023	6.67
0.003	0.086	38.1	-13.04	1.028	6.81
0.01	0.287	25.1	-12.95	1.031	6.94
0.02	0.576	20.2	-12.78	1.018	6.89
0.05	1.460	14.9	-12.67	0.999	6.69
0.1	2.985	11.8	-11.96	0.919	6.04
0.2	6.25	9	-9.69	0.703	4.67
0.3	9.836	8	-7.43	0.577	4.8
0.4	13.793	7.2	-5.58	0.462	4.7
0.5	18.182	6.6	-3.99	0.378	4.86
0.6	23.077	6.1	-2.88	0.281	4.34
0.7	28.571	5.8	-2.11	0.182	3.44

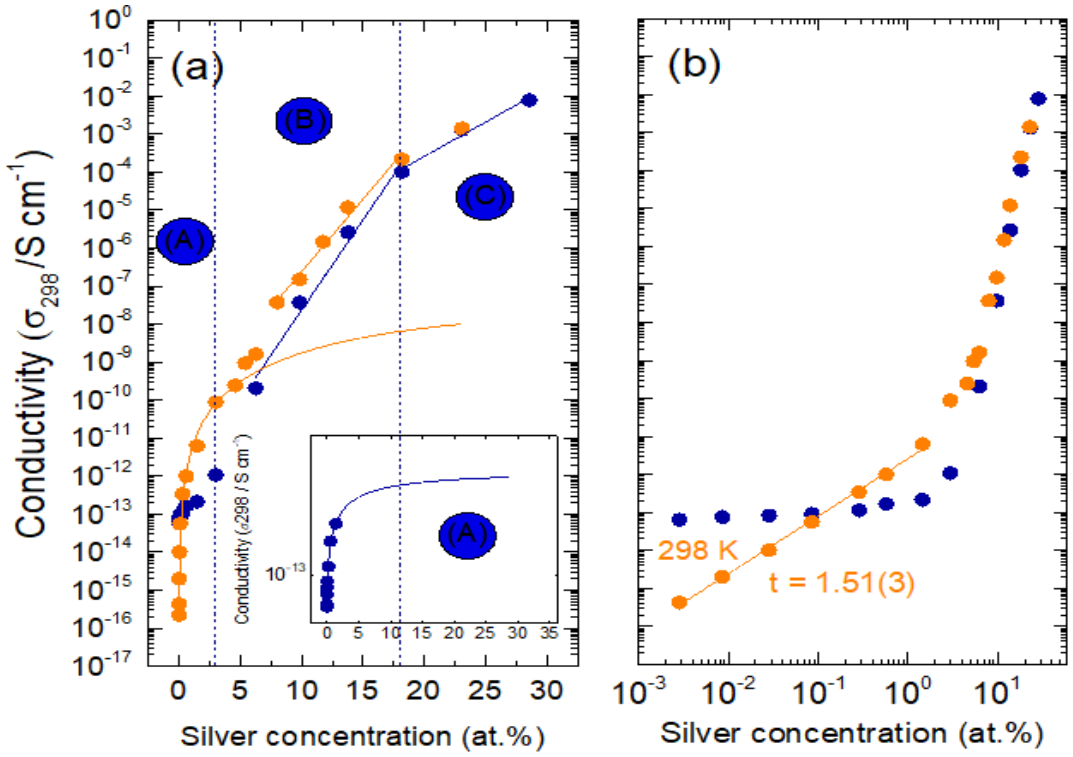

Figure II.18 Conductivity at room temperature σ_{298} for the ternary A series system $(AgI)_x(PbS)_{0.5-x/2}(As_2S_3)_{0.5-x/2}$ (blue color) and $(AgI)_x(HgS)_{0.5-x/2}(As_2S_3)_{0.5-x/2}$ (orange color) (a) semi-logarithmic scale (b) log-log scale.

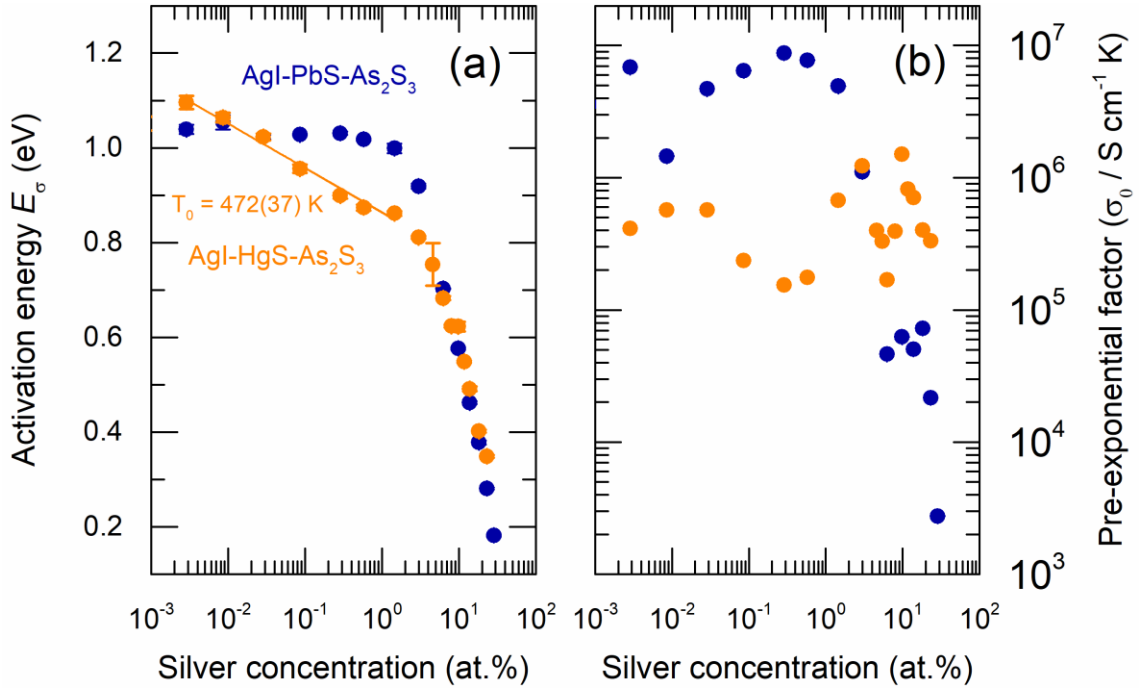

Figure II.19 (a) the activation energy E_σ and (b) the pre-exponential factor σ_0 for the A series ternary systems $(AgI)_x(PbS)_{0.5-x/2}(As_2S_3)_{0.5-x/2}$ (blue color) and $(AgI)_x(HgS)_{0.5-x/2}(As_2S_3)_{0.5-x/2}$ (orange color).

For high silver content (> 5 at.% Ag), the conductivity values of the AgI-PbS-As_2S_3 are typical of the modifier controlled domain. The observed two regions (B and C) are comparable to those in the AgI-HgS-As_2S_3 [45]. Earlier studies show that the transport parameters depend essentially on the modifier content, nature (Ag^+, Cu^+, etc.) and chemical form [33], [43]. In this modifier-controlled domain far above the percolation threshold $y \gg y_c$, the percolation clusters become predominant, cover the whole volume of glass, and form preferential conduction pathways [34]. As for its predecessor in ref [45], we suggest that the high Ag+ ionic mobility of the lead doped system in the modifier controlled domain is probably the results of the interconnected tetrahedral $(AgI_{2/2}S_{2/2})_n$ chains (B domain) or $AgI_{3/3}S_{1/2}$ mixed tetrahedral (C domain) present in the glass network.

II.3.2.2 B-series glasses $(AgI)_{0.3}(PbS)_y(As_2S_3)_{0.7-y}$

Typical temperature dependencies of the AC conductivity for the B-series glasses, $(AgI)_{0.3}(PbS)_y(As_2S_3)_{0.7-y}$ $(0 \leq y \leq 0.5)$, are shown in **Figure II.20**.

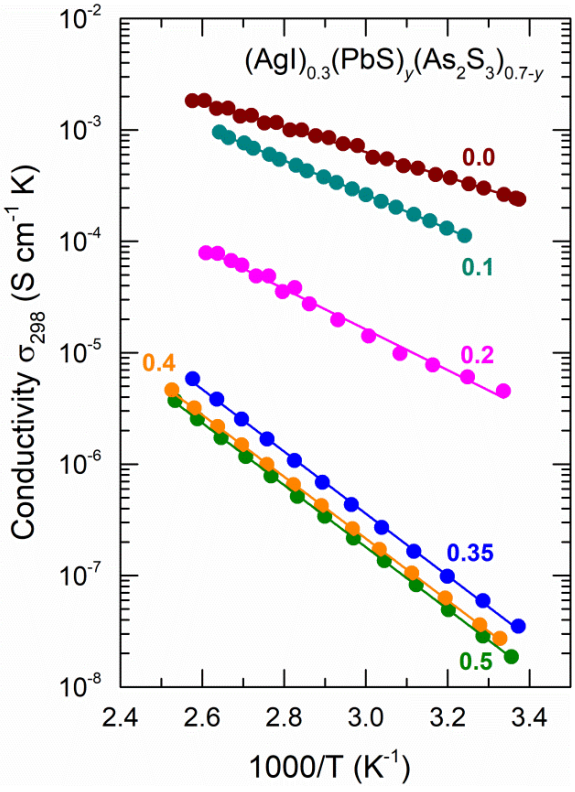

Figure II.20 Total electrical conductivity σ of the ternary system $(AgI)_{0.3}(PbS)_y(As_2S_3)_{0.7-y}$ (B series) as a function of 1000/T.

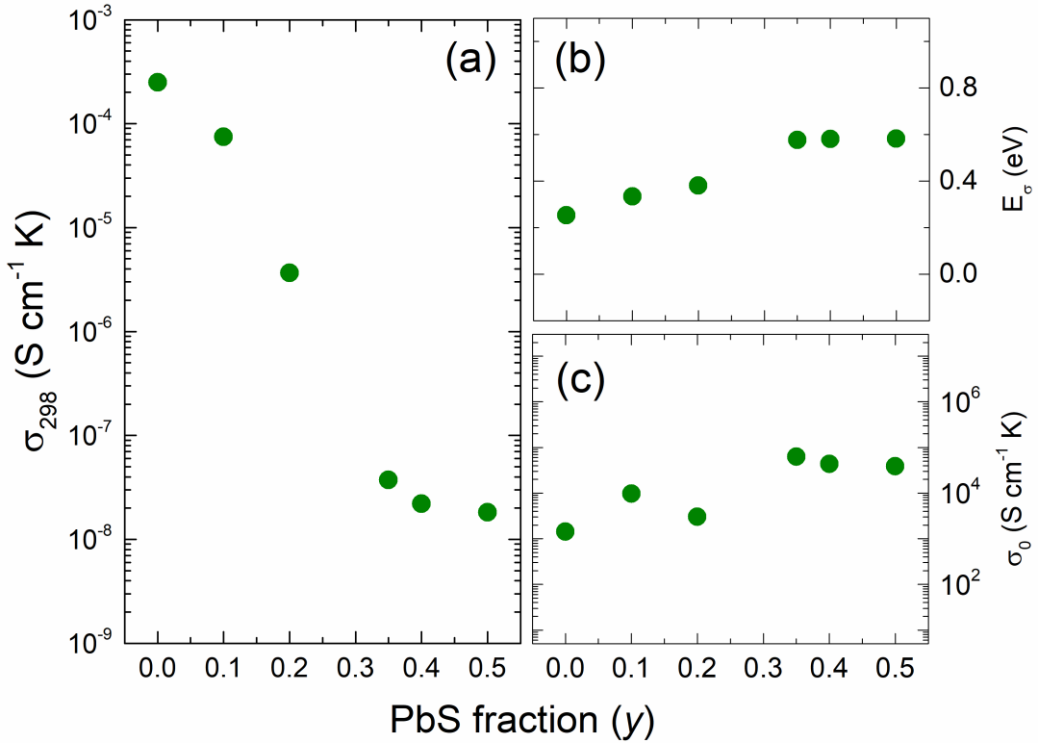

Figure II.21 (a) Room temperature conductivity σ_{298}, (b) the activation energy E_σ, and (c) the pre-exponential factor σ_0 for the ternary system $(AgI)_{0.3}(PbS)_y(As_2S_3)_{0.7-y}$ (B series) as a function of PbS content y.

Table II.3 Electric properties of the B series glass system $(AgI)_{0.3}(PbS)_y(As_2S_3)_{0.7-y}$.

	[Pb] (at.%)	r_{Ag-Ag} (Å)	log σ_{298}	E_σ (eV)	log σ_0 (S cm^{-1} K)
0.0	0	8.9	-3.602	0.253	3.15
0.1	2.6	8.7	-4.128	0.334	3.99
0.2	5.7	8.6	-5.435	0.381	3.48
0.35	9.4	8.1	-7.428	0.577	4.8
0.4	13.8	7.8	-7.658	0.581	4.64
0.5	19.2	7.6	-7.738	0.583	4.59

Similarly to the previous systems, the samples do not show any significant hysteresis effects and obey the Arrhenius law. The parameters σ_{298}, E_σ and σ_0, calculated from the least fit squares of the data using Eq. (II.11), are represented in **Figure II.21** and **Table II.3.** With increasing lead sulfide PbS content, the room temperature conductivity decreases by 4 orders of magnitude from 2.5×10^{-4} S.cm^{-1} (y = 0.0) to 1.83×10^{-8} S.cm^{-1} (y = 0.5), **Figure II.21(a)**. The activation energy increases from ~0.25 eV to ~0.58 eV, **Figure II.21(b).** Meanwhile, the pre-exponential factor σ_0 is quasi constant throughout the composition range, $10^3 \leq \sigma_0(y) \leq 10^5$ S cm^{-1} K (**Figure**

II.21(c)). Rather constant pre-exponential factor is often observed in ion-conducting sulphide glasses even over a wide composition range [54], [55], [56] and was explained by contrasting composition trends of the effective jump distance $l(y)$, decreasing with y, the cation content $C(y)$, increasing with y, the attempt frequency $\nu^0(y)$ and the entropic term $\exp[\Delta S(y)/k]$ giving $\sigma_0(y) \propto l(y)^2 \nu^0(y) C(y) \exp\left(\frac{\Delta S(y)}{k}\right) \approx constant$ [57].

II.3.2.3 C-series glasses $(AgI)_z(PbS)_{0.1}(As_2S_3)_{0.9-z}$

The electrical conductivities of the C-series glasses, $(AgI)_z(PbS)_{0.1}(As_2S_3)_{0.9-z}$, were obtained using AC (alternating current) or DC (direct current) measurements (depending whether the sample is electronic insulator or not). **Figure II.22** displays the typical dependencies of conductivity as a function of temperature. The Arrhenius law is well obeyed and the hysteresis effects are absent. The obtained conductivity parameters σ_{298}, E_σ and σ_0 are summarized in **Table II. 4.**

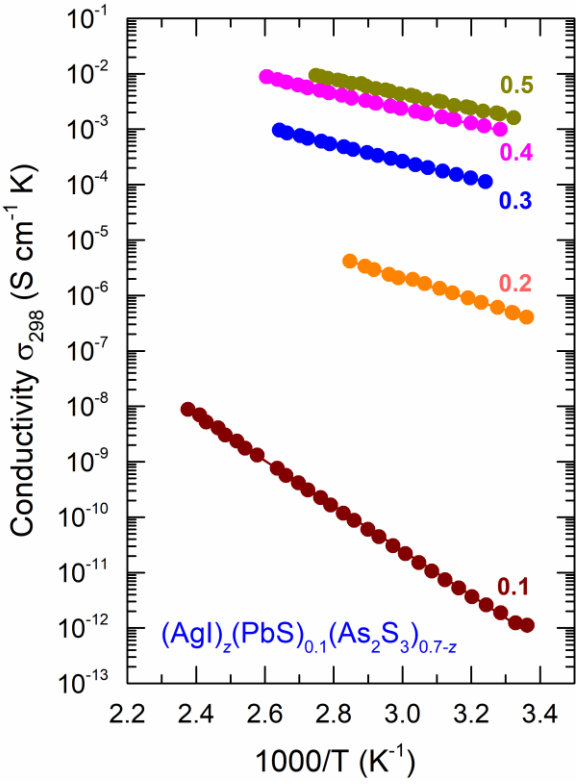

Figure II.22 Total electrical conductivity σ of the C-series glasses, $(AgI)_z(PbS)_{0.1}(As_2S_3)_{0.9-z}$, as a function of 1000/T.

Figure II.22 shows a sharp increase in conductivity (~10 orders of magnitude) with increasing silver iodide content z; the room temperature conductivity of the glasses jumps from 8.9×10^{-13} (z = 0.1) to 1.4×10^{-3} (z = 0.5), **Figure II.23(a)**. This increase is accompanied by a decrease in

activation energy from ~0.83 eV (z = 0.1) to ~0.3 eV (z = 0.5), **Figure II.23(b)**. **Figure II.23(c)** shows that the pre-exponential factor σ_0 fluctuates in the range, $10^3 \leq \sigma_0(z) \leq 10^5$ S cm^{-1} K with a minimum at z = 0.2; σ_0 decreases initially from the glass z = 0.1 to z = 0.2 and increases thereafter with continuous AgI addition. We note that the z = 0.1 glass composition is at the limit of percolation domain for the C-series glasses (similar to A-series glasses).

Table II. 4 Electric properties of the C series glass system $(AgI)_z(PbS)_{0.1}(As_2S_3)_{0.9-z}$.

x	[Ag] (at.%)	r_{Ag-Ag} (Å)	log σ_{298}	E_σ (eV)	log σ_0 (S cm^{-1} K)
0.1	2.27	13.11	-12.046	0.835	4.54
0.2	4.87	10.19	-6.367	0.574	3.09
0.3	7.89	8.71	-4.128	0.413	3.99
0.4	11.42	7.73	-3.136	0.334	4.58
0.5	15.62	6.99	-2.849	0.297	4.65

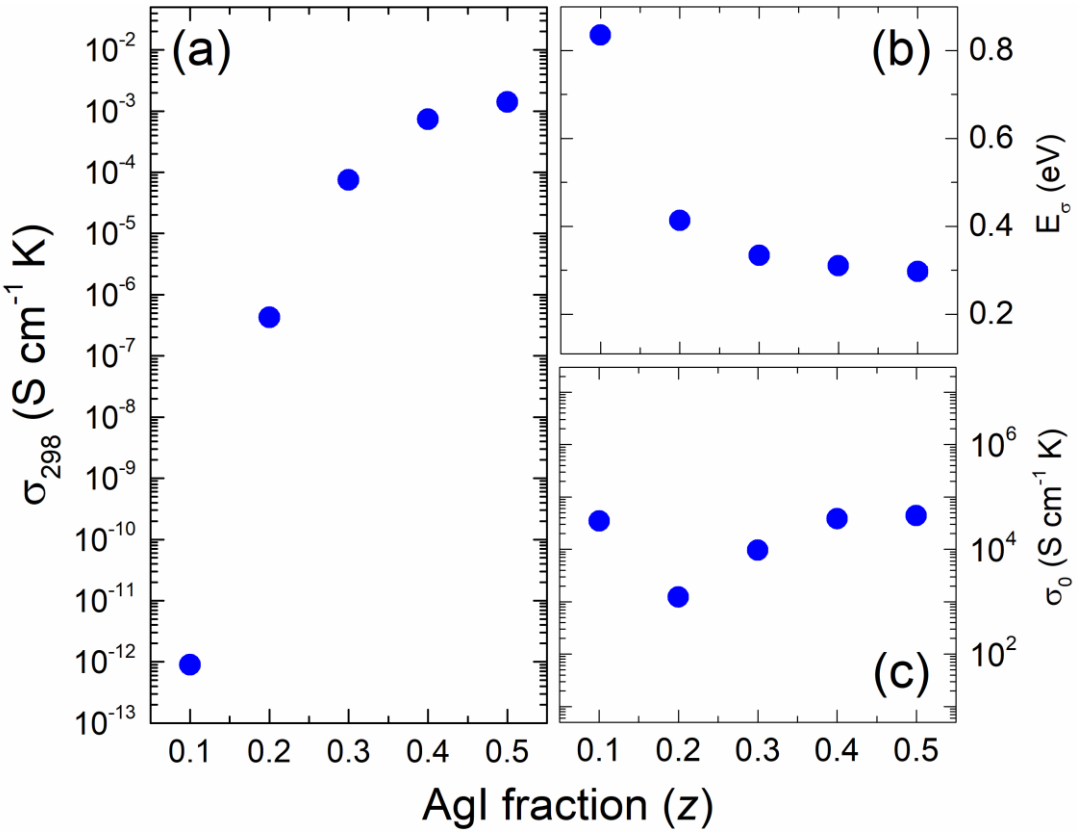

Figure II.23 (a) Conductivity at room temperature σ_{298}, (b) the activation energy E_σ and (c) the pre-exponential factor σ_0 for the C series ternary $(AgI)_z(PbS)_{0.1}(As_2S_3)_{0.9-z}$ system.

II.3.2.4 Ion transport in AgI-PbS-As_2S_3 glasses: role of PbS

It was previously reported [58] that AgY-As_2S_3 glasses (Y = I ou Br) glasses are superionic conductors. Raman spectroscopy, neutron and high-energy X-ray diffraction results combined with preliminary AIMD simulations show that the AgY (Y = I ou Br) molecules interact with the host glass network and mixed silver environment of either 3:1 (3S + 1Y) or 2:2 stoichiometry (2S + 2Y) are formed. **Figure II.24** show that the presence of PbS in the glass leads to an overall decrease in the conductivity. The observed decrease of the electrical (essentially ionic) conductivity with increasing PbS content appears to be reasonable, since the binary AgI–As_2S_3 glasses belong to Ag^+ ion-conducting or superionic materials. Lead sulfide additions reduce the total silver concentration in the ternary system (for both series A and C), thus decreasing the Ag^+ ion transport. However, the electrical conductivity in the binary AgI–As_2S_3 and ternary AgI– PbS–As_2S_3 glasses, plotted as a function of the silver content (**Figure II.24**), shows a difference.

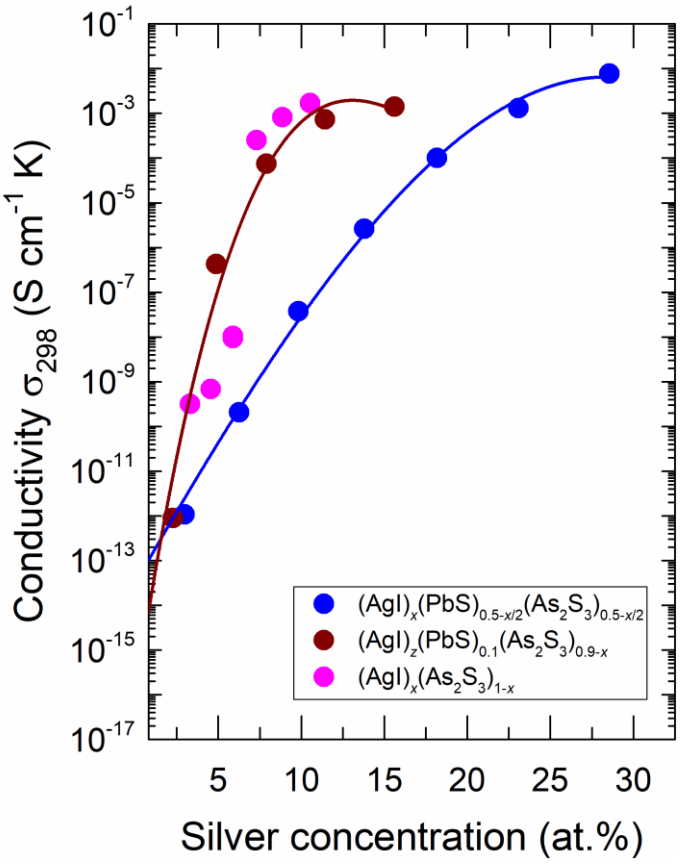

Figure II.24 Room-temperature conductivity σ_{298} for the AgI–As_2S_3 binary glasssystem (magenta colour) and for the two ternary A series $(AgI)_x(PbS)_{0.5-x/2}(As_2S_3)_{0.5-x/2}$ (wine colour) and C series $(AgI)_z(PbS)_{0.1}(As_2S_3)_{0.9-z}$ (blue colour) glass systems plotted as a function of the silver content.

The conductivity of the ternary C-series glasses (PbS-poor; only 10 mol.% PbS) is comparable to that of the binary AgI–As_2S_3. However, the ternary A-series glasses (PbS-rich) with the same Ag concentration exhibit a lower conductivity (up to 4 orders of magnitude) compared to the binary AgI–As_2S_3 and ternary C-series vitreous alloys. The observed difference in σ between the two ternary systems could be attributed to structural changes in the ternary glass and more precisely changes in the preferential conduction pathways topology. Similar phenomena were observed earlier for copper-containing chalcogenide Cu_2Se–Ag_2Se–AsSe [52] and chalcohalide CuI–AgI–As_2Se_3 [59] glasses and were attributed to the mixed cation effect in these glasses. The ionic conductivity and Ag tracer diffusion decreases in the two ternary systems [52], [59] faster than that in the Ag_2Se–AsSe and AgI–As_2Se_3 binaries with decreasing silver concentration. The observed phenomenon is similar to the mixed cation effect with the difference that the guest cation in our glasses is Pb^{2+} (instead of Cu^+ [52], [59]) has a lower ionic mobility compared to Ag^+.

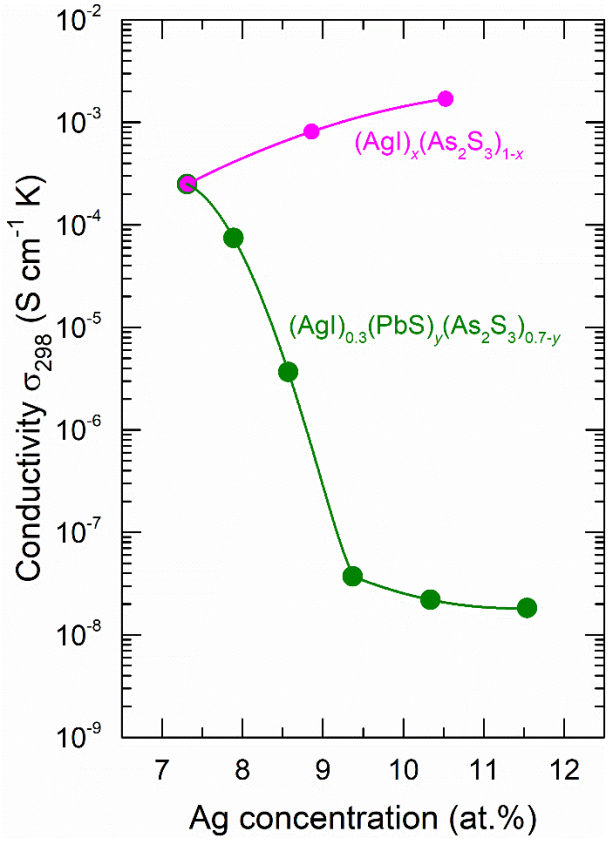

Figure II.25 Room-temperature conductivity σ_{298} for the AgI–As_2S_3 binary (magenta colour) and the ternary B series $(AgI)_{0.3}(PbS)_y(As_2S_3)_{0.7-y}$ (green colour) glass systems plotted as a function of the silver content.

Our structural hypothesis suggests that a non-random mixing of plomb and silver species is taking place and hence a privileged positioning of Pb-related structural units within the preferential conduction pathways formed by Ag-related structural units. Immobile or slow Pb^{2+} ions will affect the Ag^{+} ion dynamics by restricting the number of accessible empty sites thus reducing additionally the ionic conductivity. This is more evident in the case of the B-series glasses; the difference in conductivity rises up to almost 5 orders in magnitude despite the increase of the silver ion fraction in the ternary system; thus, blockage of Ag^{+} preferential conduction pathways by Pb^{2+}, **Figure II.25**.

II.4 Conclusion

The electrical conductivity of $(PbS)_x(As_2S_3)_{1-x}$ alloys increases by four orders of magnitude with x, however, the composition dependence is complicated. The PbS-poor glasses, $x < 0.2$, show nearly invariant conductivity parameters, possibly related to a lead sulphide clustering on mesoscopic length scale, $\lesssim$ 1000 Å. The electronic transport increases monotonically in PbS-rich alloys, both for melt-quenched and mechanically-milled, however, the extrapolated room temperature conductivity for a hypothetical PbS glass, $\sigma_{298}^{\text{glass}}(1)$, is lower by 5 orders of magnitude compared to that in nanocrystalline PbS, $\sigma_{298}(nano\text{-PbS})$. A lower electronic carrier mobility in the disordered glass network and a smaller carrier concentration related to different lead local environment seem to be responsible for the observed effect. Synthesized crystalline lead thioarsenates and the annealed glass samples, becoming glassy/crystalline alloys, reveal similar or higher electronic conductivity. More importantly, the extrapolated $\sigma_{298}^{\text{crystal}}(1)$ and $\sigma_{298}^{\text{anneal}}(1)$ values are approaching $\sigma_{298}(nano\text{-PbS})$ because of higher electronic mobility in the crystalline lattice.

For the vitreous pseudo-ternary AgI-PbS-As_2S_3 system, the conductivity the A-series glasses $(AgI)_x(PbS)_{0.5-x/_2}(As_2S_3)_{0.5-x/_2}$ at room temperature increases by ≈11 orders of magnitude from ~6.8 $\times 10^{-14}$ S.cm^{-1} (x = 0.0) to ~7.8$\times 10^{-3}$ S.cm^{-1} (x = 0.7) while the activation energy decreases from ~1.02 (x = 0.0) to 0.18 eV (x = 0.7). The glasses with a high silver concentration are superionic conductors. A notable superionic transport behaviour is observed in glasses with high silver concentrations (> 17 at.% Ag). The enhanced electronic conductivity of the $(PbS)_{0.5}(As_2S_3)_{0.5}$ host matrix, $\sigma_{298} \approx 6\times 10^{-14}$ S cm^{-1}, masks the ionic transport at low Ag^{+} cation content. Meanwhile, the modifier controlled domain is divided into two distinct regions, indicating thus a difference in the local structure. For the B-series $(AgI)_{0.3}(PbS)_y(As_2S_3)_{0.7-y}$, the conductivity decreases with increasing lead sulfide content. The room temperature conductivity

decreases by 4 orders of magnitude from ~2.5×10^{-4} S.cm^{-1} (y = 0.0) to ~1.8×10^{-8} S.cm^{-1} (y = 0.5). The activation energy increases with y and the pre-exponential factor changes slightly. For the C-series $(AgI)_z(PbS)_{0.1}(As_2S_3)_{0.9-z}$, an expected increase in the conductivity is recorded with increasing silver iodide content z. Indeed, the room temperature conductivity increases by more than 10 orders of magnitude from ~8.9×10^{-13} (z = 0.1) to ~1.4×10^{-3} (z = 0.5) while the activation energy decreases from ~0.83 eV (z = 0.1) to ~0.3 eV (z = 0.5).

II.5 References

[1] A. Helfen, “Elaboration et caractérisation d’un nouvel électrolyte solide pour les piles à combustible : δ-Bi2O3,” phdthesis, Université de Marne la Vallée, Paris, France, 2009. Accessed: Jan. 14, 2020.

[2] M. Filal, “Conductivité ionique de la zircone yttriée : rôle de la microstructure et effet composite,” Université de Picardie, Amiens, France, 1994.

[3] N. F. Mott and E. A. Davis, “Electronic Processes In Non-crystalline Materials,” Clarendon Press, Oxford, 1979.

[4] P. W. Anderson, “Absence of Diffusion in Certain Random Lattices,” *Phys. Rev.*, vol. 109, no. 5, pp. 1492–1505, Mar. 1958.

[5] L. Bányai and A. Aldea, “Theory of the Hall Effect in Disordered Systems: Impurity-Band Conduction,” *Phys. Rev.*, vol. 143, no. 2, pp. 652–656, Mar. 1966.

[6] N. F. Mott, “Electrons in disordered structures,” *Adv. Phys.*, vol. 50, no. 7, pp. 865–945, Nov. 2001.

[7] M. H. Cohen, H. Fritzsche, and S. R. Ovshinsky, “Simple Band Model for Amorphous Semiconducting Alloys,” *Phys. Rev. Lett.*, vol. 22, no. 20, pp. 1065–1068, May 1969.

[8] J. Owen, “Comprehensive Polymer Science and Supplements,” 1989.

[9] M. Faraday, “Philos. Trans. R. Soc. London,” 1831, pp. 299–340.

[10] C. Déportes *et al.*, “Electrochimie des Solides,” *Presses Universitaires de Grenoble*, 1994.

[11] E. Warburg, “Sodium ions migration through glass,” vol. 21, pp. 622–624, 1884.

[12] H. L. Tuller, D. P. Button, and D. R. Uhlmann, “Fast ion transport in oxide glasses,” *J. Non-Cryst. Solids*, vol. 40, no. 1, pp. 93–118, Jul. 1980.

[13] D. P. Button, R. P. Tandon, H. L. Tuller, and D. R. Uhlmann, “Fast Li+ ion conduction in chloro-borate glasses,” *J. Non-Cryst. Solids*, vol. 42, no. 1, pp. 297–306, Oct. 1980.

[14] F. A. Fusco, H. L. Tuller, and D. P. Button, “Lithium, sodium and potassium transport in fast ion conducting glasses: trends and models,” *Mater. Sci. Eng. B*, vol. 13, no. 2, pp. 157–164, Mar. 1992.

[15] O. L. Anderson and D. A. Stuart, “Calculation of Activation Energy of Ionic Conductivity in Silica Glasses by Classical Methods,” *J. Am. Ceram. Soc.*, vol. 37, no. 12, pp. 573–580, 1954.

[16] D. Ravaine and J. L. Souquet, “Thermodynamic approach to ionic conductivity in oxyde glasses. Part 1. Correlation of ionic conductivity with chemical potential of alkali oxide in oxyde glasses.,” *Phys. Chem. Glas.*, vol. 18, no. 2, pp. 27–31, 1977.

[17] D. Ravaine and J. L. Souquet, “A thermodynamic approach to ionic conductivity in oxide glasses—part 2. A statistical model for the variations of the chemical potential of the constituents in binary alkali oxide glasses.",” *Phys. Chem. Glas.*, vol. 19, no. 5, pp. 115–120, 1978.

[18] A. Bunde, M. D. Ingram, and P. Maass, “The dynamic structure model for ion transport in glasses,” *J. Non-Cryst. Solids*, vol. 172–174, pp. 1222–1236, Sep. 1994.

[19] A. K. Jonscher, “The ‘universal’ dielectric response,” *Nature*, vol. 267, no. 5613, pp. 673–679, Jun. 1977.

[20] J. C. Dyre, “The random free-energy barrier model for AC conduction in disordered solids,” *J. Appl. Phys.*, vol. 64, no. 5, pp. 2456–2468, Sep. 1988.

[21] J. C. Dyre and T. B. Schroder, “Universality of ac conduction in disordered solids,” *Rev. Mod. Phys.*, vol. 72, no. 3, pp. 873–892, Jul. 2000.

[22] K. Funke and I. Riess, “Debye-Huckel-type relaxation processes in solid ionic conductors: The model,” *Z. Phys. Chem. N. F.*, vol. 140, no. 2, pp. 217–232, 1984.

[23] K. Tanaka, “Encyclopedia of materials: Science and Technology,” *Elsevier*, vol. 2, pp. 1123–31.

[24] N. F. Mott and E. A. Davis, *Electronic processes in non-crystalline materials*. Oxford university press, 2012.

[25] S. Mahadevan and A. Giridhar, “Silver as a dopant and as a constituent in As-Ag-Te glasses: mean atomic volume and Tg,” *J. Non-Cryst. Solids*, vol. 197, no. 2, pp. 219–227, May 1996.

[26] B. Bilen, Y. Skarlatos, and G. Aktas, “Frequency-dependent conductivity in As2Se3 and As2Te3 thin films,” *J. Non-Cryst. Solids*, vol. 351, no. 27, pp. 2153–2158, Aug. 2005.

[27] M. Kitao, M. Senda, Y. Takano, and S. Yamada, “Effect of Tl additive on conductivity and absorption coefficient in glassy As2Se3,” *J. Non-Cryst. Solids*, vol. 127, no. 1, pp. 36–43, Jan. 1991.

[28] M. Bokova, I. Alekseev, and E. Bychkov, “204Tl tracer diffusion and conductivity in thallium germanium sulphide glasses over a wide composition range,” *J. Electroceramics*, vol. 34, no. 1, pp. 63–68, Feb. 2015.

[29] M. Bokova, I. Alekseev, D. Kalyagin, V. Tsegelnik, Yu. Ermolenko, and E. Bychkov, "204Tl tracer diffusion and conductivity in thallium thiogermanate glasses," *Solid State Ion.*, vol. 253, pp. 101–109, Dec. 2013.

[30] M. Bokova, A. Paraskiva, M. Kassem, I. Alekseev, and E. Bychkov, "Tl2S-GeS-GeS2 system: Glass formation, macroscopic properties, and charge transport," *J. Alloys Compd.*, vol. 777, pp. 902–914, Mar. 2019.

[31] A. Pradel and M. Ribes, "Lithium chalcogenide conductive glasses," *Mater. Chem. Phys.*, vol. 23, no. 1, pp. 121–142, Aug. 1989.

[32] E. Robinel, B. Carette, and M. Ribes, "Silver sulfide based glasses (I). Glass forming regions, structure and ionic conduction of glasses in GeS2-Ag2S and GeS2-Ag2S-AgI systems," *J. Non-Cryst. Solids*, vol. 57, no. 1, pp. 49–58, Aug. 1983.

[33] E. Bychkov, "Superionic and ion-conducting chalcogenide glasses: Transport regimes and structural features," *Solid State Ion.*, vol. 180, no. 6, pp. 510–516, May 2009.

[34] E. Bychkov, D. L. Price, C. J. Benmore, and A. C. Hannon, "Ion transport regimes in chalcogenide and chalcohalide glasses: from the host to the cation-related network connectivity," *Solid State Ion.*, vol. 154–155, pp. 349–359, Dec. 2002.

[35] P. K. Bhat, K. L. Bhatia, and S. C. Katyal, "Electrical conductivity and photoconductivity of As2S3-PbS glasses," *J. Non-Cryst. Solids*, vol. 27, no. 3, pp. 399–409, Mar. 1978.

[36] K. L. Bhatia, M. Singh, and N. Kishore, "Electrical and optical properties of thermally evaporated thin films of (As2S3)1−x(PbS)x," *Thin Solid Films*, vol. 293, no. 1, pp. 303–309, Jan. 1997.

[37] J. P. Clifford, K. W. Johnston, L. Levina, and E. H. Sargent, "Schottky barriers to colloidal quantum dot films," *Appl. Phys. Lett.*, vol. 91, no. 25, p. 253117, Dec. 2007.

[38] Y. Seino, T. Ota, K. Takada, A. Hayashi, and M. Tatsumisago, "A sulphide lithium super ion conductor is superior to liquid ion conductors for use in rechargeable batteries," *Energy Environ. Sci.*, vol. 7, no. 2, pp. 627–631, Jan. 2014.

[39] N. Tanibata, K. Noi, A. Hayashi, N. Kitamura, Y. Idemoto, and M. Tatsumisago, "X-ray Crystal Structure Analysis of Sodium-Ion Conductivity in 94 Na3PS4·6 Na4SiS4 Glass-Ceramic Electrolytes," *ChemElectroChem*, vol. 1, no. 7, pp. 1130–1132, 2014.

[40] F. Tesfaye and P. Taskinen, "Phase Equilibria and Thermodynamics of the System Zn-As-Cu-Pb-S at Temperatures Below 1173 K.," pp. 18–20, 2011.

[41] Y. Iitaka and W. Nowacki, "A refinement of the pseudo crystal structure of scleroclase PbAs2S4," *Acta Crystallogr.*, vol. 14, no. 12, Art. no. 12, Dec. 1961.

[42] B. Ribar, C. Nicca, and W. Nowacki, “Dreidimensionale Verfeinerung der Kristallstruktur von Dufrenoysit, Pb8As8S20,” *Z. Für Krist. - Cryst. Mater.*, vol. 130, no. 1–6, pp. 15–40, Dec. 1969.

[43] E. Bychkov, A. Bychkov, A. Pradel, and M. Ribes, “Percolation transition in Ag-doped chalcogenide glasses: comparison of classical percolation and dynamic structure models,” *Solid State Ion.*, vol. 113–115, pp. 691–695, Dec. 1998.

[44] K. S. Andrikopoulos, J. Arvanitidis, V. Dracopoulos, D. Christofilos, T. Wagner, and S. N. Yannopoulos, “Nanoindentation and Raman studies of phase-separated Ag-As-S glasses,” *Appl. Phys. Lett.*, vol. 99, no. 17, p. 171911, Oct. 2011.

[45] M. Kassem, S. Khaoulani, and E. Bychkov, “Ionic transport in AgI-HgS-As2S3 glasses: Critical percolation and modifier-controlled domains,” *J. Am. Ceram. Soc.*, vol. 101, no. 6, pp. 2287–2296, 2018.

[46] E. Bychkov, V. Tsegelnik, Yu. Vlasov, A. Pradel, and M. Ribes, “Percolation transition in Ag-doped germanium chalcogenide-based glasses: conductivity and silver diffusion results,” *J. Non-Cryst. Solids*, vol. 208, no. 1, pp. 1–20, Nov. 1996.

[47] Y. Drugov, V. Tsegelnik, A. Bolotov, Y. Vlasov, and E. Bychkov, “110Ag tracer diffusion study of percolation transition in Ag2S–As2S3 glasses,” *Solid State Ion.*, vol. 136–137, pp. 1091–1096, Nov. 2000.

[48] E. Bychkov, Y. Tveryanovich, and Y. Vlasov, “Semiconducting Chalcogenide Glass III: Applications of Chalcogenide Glasses,” Elsevier, NewYork, 2004.

[49] E. Bychkov, D. L. Price, and A. Lapp, “Universal trend of the Haven ratio in glasses: origin and structural evidences from neutron diffraction and small-angle neutron scattering,” *J. Non-Cryst. Solids*, vol. 293–295, pp. 211–219, Nov. 2001.

[50] T. Minami, “Fast ion conducting glasses,” *J. Non-Cryst. Solids*, vol. 73, no. 1, pp. 273–284, Aug. 1985.

[51] J. C. Bachman *et al.*, “Inorganic Solid-State Electrolytes for Lithium Batteries: Mechanisms and Properties Governing Ion Conduction,” *Chem. Rev.*, vol. 116, no. 1, pp. 140–162, Jan. 2016.

[52] Yu. G. Vlasov and E. A. Bychkov, “Ionic and electronic conductivity in the copper-silver-arsenic-selenium glasses,” *Solid State Ion.*, vol. 14, no. 4, pp. 329–335, Dec. 1984.

[53] Yu. G. Vlasov, E. A. Bychkov, and B. L. Seleznev, “Compositional dependence of ionic conductivity and diffusion in mixed chalcogen Ag-containing glasses,” *Solid State Ion.*, vol. 24, no. 3, pp. 179–187, Aug. 1987.

[54] B. Barrau, M. Ribes, M. Maurin, A. Kone, and J.-L. Souquet, “Glass formation, structure and ionic conduction in the Na2S-GeS2 system,” *J. Non-Cryst. Solids*, vol. 37, no. 1, pp. 1–14, Mar. 1980.

[55] H. K. Patel and S. Martin, “Fast ionic conduction in Na2S+B2S3 glasses: Compositional contributions to non-exponentiality in conductivity relaxation in the extreme low-alkali-metal limit.,” *Phys Rev B*, vol. 44, pp. 10292–10300, 1992.

[56] A. Paraskiva, M. Bokova, and E. Bychkov, “Na+ ion conducting glasses in the NaCl-Ga2S3-GeS2 system: A critical percolation regime,” *Solid State Ion.*, vol. 299, pp. 2–7, Jan. 2017.

[57] C. Déportes *et al.*, “Grenoble EDP Sciences: Électrochimie des solides,” p. 1994.

[58] R. Zaiter, “Silver and/or mercury doped thioarsenate and thiogermanate glasses : Transport, structure and ionic sensibility,” phdthesis, Université du Littoral Côte d’Opale, 2018. Accessed: Jan. 14, 2020.

[59] A. Bolotov *et al.*, “Degenerated mixed cation effect in CuI–AgI–As2Se3 glasses: 64Cu and 110Ag tracer diffusion studies,” *Solid State Ion.*, vol. 113–115, pp. 697–701, Dec. 1998.

Chapter 3: Structural studies of the PbS-As_2S_3 and AgI-PbS-As_2S_3 systems

III.1 Introduction

In order to have a deep understanding of the relationships between the chemical composition, atomic structure on the local, intermediate and extended range scales, and glass properties that are critical for sensing applications: fast ion transport, long-term stability and reversibility. Structural studies of the synthesized compounds are of great interest. Since in our work, all compounds we are dealing with are chalcogenide glasses. The amorphous nature of these compounds means that they lack symmetry and periodicity and this makes their structural studies via efficient Rietveld-type structural methods unusable. However, these difficulties can be partially solved using indirect spectroscopic methods and/or direct techniques using synchrotron radiation, nuclear reactors or spallation neutron sources. Advanced spectroscopic methods such as EXAFS « Extended X-ray Absorption Fine Structure » [1]–[3], Nuclear Magnetic Resonance (NMR) [4], [5], Nuclear Quadrupole Resonance (NQR) [6], [7], Mössbauer Spectroscopy [8], [9] and Raman spectroscopy [10], [11], have all proved to be effective in solving the local structure of chalcogenide glasses. However, in order to obtain structural information beyond the first coordination sphere, it is advisable to use high-energy X-ray diffraction and/or pulsed neutron diffraction [12]–[15].

In this chapter, we have studied the structure of the systems PbS-As_2S_3 and AgI-PbS-As_2S_3 by means of Raman spectroscopy, then we have completed these studies using neutron scattering and high-energy X-ray diffraction measurements which further provide information on short and medium distance orders.

III.2 Raman spectroscopy

Raman spectroscopy is a molecular spectroscopic technique where scattered light is used to measure the vibrational energy modes of a sample. It is named after the Indian physicist C. V. Raman who, together with his research partner K. S. Krishnan, was the first to observe Raman scattering in 1928 [16]. Raman spectroscopy can provide both chemical and structural information, as well as the identification of substances through their characteristic Raman 'fingerprint'. It extracts this information through the detection of Raman scattering from the sample. **A brief description of the** principle of Raman spectroscopy is given below; a more complete description is given in the McAfee reference book [17].

III.2.1 Principle

When light interacts with a molecule, the oscillating electromagnetic field of a photon induces a polarization of the molecular electron cloud which leaves the molecule in a higher energy state with the energy of the photon transferred to the molecule. This can be considered as the formation of a very short-lived complex between the photon and molecule which is commonly called the virtual state of the molecule. The virtual state is not stable and the photon is re-emitted almost immediately, as scattered light. The vast majority of the photons are dispersed or scattered at the same energy as the incident photon. This is called elastic (energy of scattering particle is conserved) or Rayleigh scattering and is the dominant process (**Figure III.1**). In a much rarer event (a small number of these photons (approximately 1 in 10 million photons) [18] Raman scattering occurs. It is an inelastic scattering process with a transfer of energy between the molecule and scattered photon. Indeed, if the molecule gains energy from the photon during the scattering (excited to a higher vibrational level) then the scattered photon loses energy and its wavelength increases which is called Stokes Raman scattering (after G. G. Stokes) (**Figure III.1**).

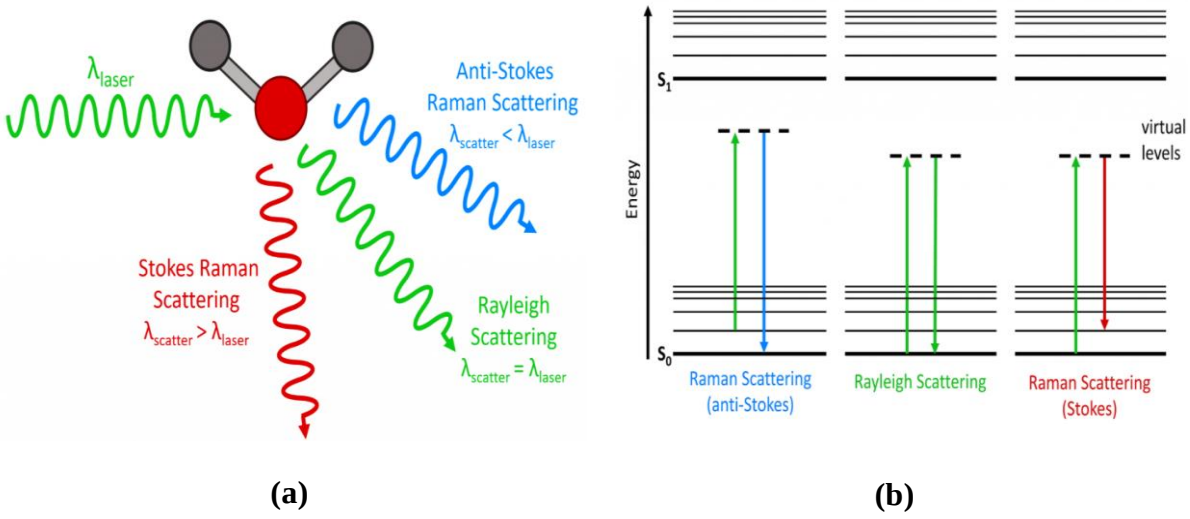

Figure III.1 (a) Three types of scattering processes that can occur when light interacts with a molecule, (b) Jablonski Diagram showing the origin of Rayleigh, Stokes and Anti-Stokes Raman Scatter.

Conversely, if the molecule loses energy by relaxing to a lower vibrational level the scattered photon gains the corresponding energy and its wavelength decreases; which is called Anti-Stokes Raman scattering. Quantum mechanically Stokes and Anti-Stokes are equally likely processes. However, with an ensemble of molecules, the majority of molecules will be in the

ground vibrational level (Boltzmann distribution) and Stokes scatter is the statistically more probable process. Therefore, the Stokes Raman scatter is always more intense than the anti-Stokes and for this reason, it is nearly always the Stokes Raman scatter that is measured in Raman spectroscopy. We note that the position of the Raman scattering bands is directly related to the vibration frequencies of the bond. The equation (III.1), derived from Hooke's law, makes it possible to establish the relation between the frequency of vibration *v*, bond type as well as the nature of the atoms involved:

$$\nu = \frac{1}{2\pi c} \times \sqrt{\frac{k}{\mu}} \qquad \text{(III.1)}$$

where *c* is the speed of light, *k* is the force constant of the bond and μ is the reduced mass of atoms 1 and 2 where

$$\mu = \frac{m1 \times m2}{m1 + m2} \qquad \text{(III.2)}$$

Hence, the frequency of vibration *v* decreases with increasing atomic mass of considered atoms and increases with increasing bond strength.

III.2.2 Instrument

The vibrational properties of lead doped glasses were obtained by using a Raman spectrometer LabRAM HR Evolution in the 80–850 cm^{-1} spectral range [19], [20]. The spectrometer was equipped with a triple monochromator, liquid nitrogen cooled CCD detector and a microscope. The instrument resolution was 1 cm^{-1}, the scattering was excited by a 785 nm solid state laser and the acquisition time was varied between 60 and 300 s. The absence of photo-induced phenomena and the homogeneity of the glass samples were ensured by recording, at different positions and different laser power (between 0.15 and 1.5 mW), of several spectra of the same glass sample. The background subtraction and data analysis were described previously [19].

III.3 Diffraction techniques

The lack of periodicity of amorphous materials hinders significantly the precise determination of their atomic structure. In this regards, using neutron and X-ray diffraction techniques, for structure determination, is extremely helpful as it allows obtaining a mean atomic arrangement around each atomic species. Those two techniques complement one another. This is due to the

fact that (i) the sensitivity of the X-ray diffraction depends on number of electrons in the atom simplistically associated with the size of electronic cloud and (ii) the sensitivity of the neutron diffraction depends on the coherent neutron scattering length schematically shown as a relative size of the atomic nucleus, **Figure III. 2**. Using these two techniques gives us access to a large domain of diffusion vectors, $Q = 4\pi sin\theta/\lambda$, where θ is the scattering angle and λ is the radiation wavelength. In fact, the larger is the range of scattering vector; the better is the resolution in real space. The pulsed neutrons (λ_{min} = 0.05-4 Å) and the hard X-rays ($0.1 \leq \lambda \leq 0.2$ Å) allow to reach Q values up to 50 Å^{-1}, which is very advantageous compared to the ≈10 Å^{-1} obtained with laboratory diffractometers using copper K_α radiation. A brief description of the treatment of theory of scattering of x-rays and neutrons by amorphous materials, and more precisely application to diffraction experiments, is presented below. However, for more details, we refer you to the work of Fischer et al. [21] and references therein.

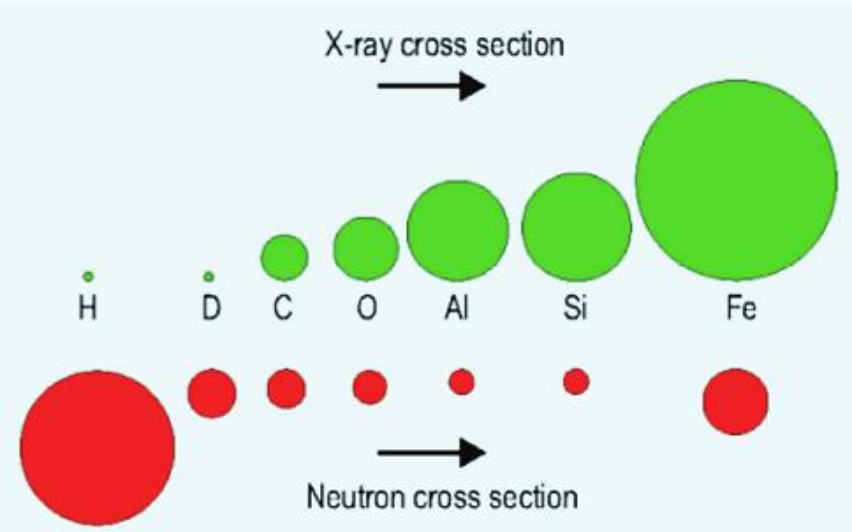

Figure III. 2 Comparison of the sensitivities of some elements to neutrons and X-rays [22].

III.3.1 Structure factor and correlation functions

In his work, Y. Waseda [23] defines 2 indicators to precisely estimate the local order in the material, these are the structure factor $S(Q)$ and the pair correlation function $g(r)$. The correlation function *g(r)* represents a radial distribution function in a system of particles (atoms, molecules, colloids, etc.); it describes the variation in density as a function of the distance from a reference particle. The number of atoms of type *j* in radial distance interval r to r + dr, from an atom of type *i*, is defined by:

$$n_{ij}(r) = 4\pi r^2 c_j \rho g_{ij}(r) dr \quad \text{(III.3)}$$

where ρ is the average atomic number density, c_j is the fraction of atoms of type j present, and the $g_{ij}(r)$ are the partial pair correlation functions. Meanwhile, (Q) corresponds to the sum of the contributions of each of the atoms present, taking into account the phase and the amplitude in reciprocal space.

In the Faber-Ziman formalism [24], the structure factor is related to the scattering intensity $i(Q)$ and we have for neutron scattering and for x-ray scattering the following equation (Eq. III.4) and (Eq. III.5) respectively:

$$i(Q) = \sum_{i}^{M} \sum_{i}^{M} c_i c_j f_i(Q) f_j(Q) \left(S_{ij}(Q) - 1 \right) = i^N(Q) \quad \text{(III.4)}$$

$$i^X(Q) = \frac{i(Q)}{(\sum_i^M c_i f_i(Q))^2} \quad \text{(III.5)}$$

Where M represents the elemental species in the sample, $f_i(Q)$ represents the atomic form factors for x-ray scattering taken from Waasmier and Kirfel [25] or coherent neutron scattering lengths, usually denoted $\bar{b}_i$ and taken from Sears [26]. The overbar represents isotopic averaging over the sample for the i^{th} element. We note that the denominator in Eq. (III.5) acts to 'sharpen' [27] the distinct scattering diffraction pattern by approximately dividing out the form factor dependence. In the neutron scattering, where $\bar{b}_i$ values are independent of Q, such a procedure in not necessary.

For a system containing M elemental species, as it is always the case, the Faber-Ziman theory allows to define the total structure factor $S(Q)$ as the weighted sum of $M(M+1)/2$ of the partial structure factors S_{ij} corresponding to each of the atomic pairs present in the component:

$$S(Q) = \sum_{ij} W_{ij} S_{ij}(Q) \quad \text{(III.6)}$$

Where the W_{ij} factors are the weights of the different partial structure factors and are defined, for both neutron (N) and x-ray (X) as:

$$W_{ij}^N = c_i c_j \bar{b}_i \bar{b}_j \quad \text{(III.7)}$$

$$W_{ij}^X = \frac{c_i c_j f_i(Q) f_j(Q)}{(\sum_i^M c_i f_i(Q))^2} \quad \text{(III.8)}$$

The structure of a sample can be described in real space in terms of its pair correlation function *g(r)*, which is proportional to the probability of finding an atom at a position *r* with respect to a reference atom at the origin. Therefore, the position of the peaks of *g(r)* allows determining the interatomic distances. The function *g(r)* is calculated from the Fourier transform of structure factor *S*(*Q*). we note that, as for the structure factor, the total function *g(r)* is a weighted sum of the partial pair-distribution functions. Equation III.9 relates both reciprocal and real space functions:

$$g(r) = 1 + \frac{1}{2\pi^2\rho}\int_0^{Qmax} q[S(Q) - 1]\frac{\sin Qr}{r}M(Q)dQ \qquad \text{(III.9)}$$

In practice, the Fourier transform of the structure factor is not integrated up to infinity, the finite maximum Q-value that is accessible in diffraction experiments, Q_{max}, leads to peak broadening in real space after Fourier transformation as well as to non-physical oscillations in *g(r)* and in other r-space functions. These truncation oscillations can be avoided via prudent modulation of the experimental *S*(*Q*) by a damping function before Fourier transformation, being equivalent to a coarsening of the r-space resolution; it decreases slowly to 0 at Q_{max}. The commonly used modification function is the Lorch function [28]:

$$M(Q) = \begin{cases} \frac{\sin\left(Q\pi/Q_{max}\right)}{Q\pi/Q_{max}}, Q \le Q_{max} \\ 0, Q \ge Q_{max} \end{cases} \qquad \text{(III.10)}$$

Another equally important real space correlation function and that is usually used is RDF or *N(r)*, i.e., the radial distribution function for the calculation of the coordination. This later has a direct physical interpretation and defined as the number of atoms in a range (r, r + dr) of any given atom [29], [30].

$$N(r) = 4\pi r^2 \rho\, g(r) \qquad \text{(III.11)}$$

RDF can be integrated to obtain the average number of neighboring atoms C in a coordination shell existing between the two distances r_1 and r_2 is thus:

$$C = \int_{r_1}^{r_2} N(r)\, d(r) \qquad \text{(III.12)}$$

In this Ph.D. thesis, we have often used, the real space total correlation function *T(r)*. This function represents a convenient compromise between *g(r)* and *N(r)*. Comparing to *T(r)*, the

former represses high *r* structure and the latter, due to an additional factor of *r*, represses low *r* structure. *T(r)*, for neutron and X-ray diffraction studies of glasses, is thus defined as:

$$T(r) = \frac{\mathrm{N(r)}}{r} = 4\pi r\rho g(r) \qquad \text{(III.13)}$$

Another advantage of *T(r)* is related to the fact that the symmetric distributions of interatomic distances remain symmetric. This allows easier modelling by Gaussian of symmetrical peaks which is important when determining the coordination number C.

III.3.2 Coordination number

The number of atoms of type *j* within a radial distance interval ($\Delta r = r_2 - r_1$) from an atom of type *i* correspond to the coordination number C which is obtained from *T(r)* via equation (III.14):

$$C = \bar{r}_{ij} \int_{r_1}^{r_2} T(r)\, d(r) \qquad \text{(III.14)}$$

where $\bar{r}_{ij}$ is the position of the peak in $T(r)$ and represents the interatomic bond of mean length between atoms of type *i* and *j* in the glass alloy. C^N and C^X denote the neutron and HE-XRD coordination number and are written as follows:

$$C^N = \frac{\bar{r}_{ij} A_{ij}^N}{W_{ij}^N} \qquad \text{(III.15)}$$

$$C^X = \frac{\bar{r}_{ij} A_{ij}^X}{W_{ij}^X} \qquad \text{(III.16)}$$

where A_{ij}^N and A_{ij}^X represent the integrated area of a symmetric Gaussian peak obtained by fitting of a certain peak of *T(r)*.

III.3.3 High Energy X-Ray Scattering

High energy X-ray diffraction measurements (HE-XRD) were conducted at the X-ray Pair Distribution Function XPDF (I15-1) beamline on the Diamond Light Source synchrotron facility, UK (**Figure III. 3**). The beam was monochromated with a Bent-laue monochromator to an energy of 76.7 keV (wavelength ≈ 0.16 Å). This energy provides data at Q values up to 40 $Å^{-1}$. A Perkin Elmer model XRD 1611 CP3 detector was used for the data collection. This

detector has a good signal to noise ratio and very small pixel size (100 µm). The beam size at focus was 700 µm horizontal by 10 µm vertical. We note that the glass sample was held inside 1 mm diameter silica glass capillary (10 µm wall thickness).

Figure III. 3 View inside I15-1 Experimental Hutch.

Due to interference phenomena such as, air scattering, coherent scattering and incoherent scattering, multiple scattering, the coherent intensity is not accessible directly from the scattering intensity. There is therefore a need to make corrective corrections which take into account the above-mentioned contributions and to make a number of absorption corrections due to the sample geometry. In this regards, a software (matlab based) developed in the laboratory can perform all these corrections giving the total X-ray structure factor $S(Q)$ and the pair correlation functions $g(r)$ and $T(r)$. These programs are based on the procedure described by Wagner [31] and according to this method, the scattered intensity is written:

$$I(2\Theta, Q) = I_p \begin{bmatrix} A(2\Theta, E, E')P(2\Theta)I_{coh}(Q) \\ +I_{mult}^{coh}(Q) + \\ A(2\Theta, E, E')P(2\Theta)I_{incoh}(Q') \\ +I_{mult}^{incoh}(Q) \end{bmatrix} \qquad \text{(III.17)}$$

where Ip is the intensity of the primary beam, $I_x(Q)$ is the coherent and incoherent scattering intensity, $A(2\Theta, E)$ is the attenuation coefficient, I_{mult} is the multiple scattering, $P(2\Theta, \mathrm{E})$ is the polarization factor and $E' = E / (1 + 0.00392 E sin^2(\Theta))$. The coefficient $A(2\Theta, E)$ is an attenuation term which depends on the geometry of the sample. It is calculated by integrating

the optical path of the X-ray beam over the irradiated volume of the sample. Air scattering effects, important only at small angles, is recorded during an experiment without sample and subtracted. Multiple scattering is removed using the Warren and Mozzi procedure [32]. The Compton scattering intensity is calculated using the values in the tables of Balyuzi [33].

III.3.4 Neutron diffraction

Neutron diffraction is a method based on the elastic scattering in which the neutrons emerging from the experiment have more or less the same energy as the incident neutrons. The neutron technique is similar to X-ray diffraction technique, but different types of radiation give complementary information. It is a very well suited technique because the scattering power of a given nucleus is independent of the momentum transfer, as consequence of the short range interaction between the neutron and the nucleus [34]. This scattering power is proportional to the square of the scattering lengths. The examined sample is placed in a beam of thermal or cold neutrons and the pattern of intensity around the sample gives information about the structure of the material. In this work, time-of-flight neutron diffraction experiments were carried out on the ISIS spallation source located at the ISIS Facility, Rutherford Appleton Laboratory, UK. Diffraction measurements were made using Sandals diffractometer at room temperature. This instrument has a large number of detectors which cover a large solid angle, and therefore offers high count rates over a large portion of reciprocal space (up to 40 $Å^{-1}$ in reciprocal space. The glass samples were held in thin-walled 6 mm diameter vanadium foil cans inside the evacuated sample tank through which the incident neutron beam passed. The beam cross section was 40 ×15 mm^2, larger than the diameter, but shorter than the height of the cylindrical sample. Data were acquired typically for ∼ 10 to 11 hours of counting time per sample. Measurements were also performed on empty vanadium cans and a 6 mm vanadium rod for normalization purposes and to allow for subtraction of background signals. The neutron diffraction data were corrected for background effects and container scattering, multiple scattering, self-attenuation and inelasticity effects using the GUDRUN [35] software and the Atlas [36] suite of programs in order to obtain the total neutron structure factor $S_N(Q)$.

III.4 DFT (Density Functional Theory)

Currently, due to its possible application to quantum systems of widely varying sizes ranging from a few atoms to several hundred, DFT ((Density Functional Theory)) is considered one of the most widely used methods for "ab initio" calculations of the structure of atoms, molecules,

crystals and surfaces [37]. DFT, in principle, is a method of quantum computation allowing the study of electronic structure. It was mainly developed within the framework of non-relativistic quantum theory (time independent Schrödinger equation) and in the Born-Oppenheimer approximation [38] and was, subsequently, generalized to face many different situations (e.g. free energy at finite temperature, superconductors, relativistic electrons, thermodynamics of classical fluids, molecular dynamics, etc.). Instead of expressing the energy as a functional of its wave function Ψ (Hartree–Fock method), DFT expresses the external potential of nuclei $V_{ext}(r)$ (and through it the total energy of the system) as a unique functional of the electron density (ρ) [39] which is determined from the equations given by Kohn-Sham (KS) [40]:

$$V_{eff}(r) = V_H + V_{XC} + V_{ext} \qquad \text{(III.18)}$$

$$V_{eff}(r) = \frac{\delta E_H}{\delta \rho(r)} + \frac{\delta E_{XC}}{\delta \rho(r)} + \frac{\delta E_{ext}}{\delta \rho(r)} \qquad \text{(III.19)}$$

where $V_{eff}(r)$ is the effective potential, V_H is the classical contribution to the potential energy of particles without interaction and V_{XC} the exchange-correlation potential. All the energy terms and their associated potentials, in KS equations, can be calculated except for this exchange-correlation term E_{XC}. To find an expression of this term, various correlation-exchange functionals have been developed by the researchers: Local density approximation (LDA), generalized gradient approximation (GGA) and (Meta-GGA) and hybrid functionals. In this chapter, we have systematically used the GGA and hybrid functionals.

III.4.1 GGA (generalized gradient approximation)

Contrary to the LDA approximation which states that the electronic density can be considered to be locally constant, the GGA approximation considers the gas of electrons in its real form, i.e. non-uniform and non-local. Thus, the exchange-correlation energy takes into account local variations in (r), through the introduction of the gradient $\vec{\nabla}\rho(r)$ to the LDA equation. Thus:

$$E_{XC}^{GGA}[\rho(r)] = \int \rho(r)\varepsilon_{XC}\,[\rho(r), |\vec{\nabla}\rho(r)|]d^3r \qquad \text{(III.20)}$$

where $\varepsilon_{XC}\,[\rho(r), |\vec{\nabla}\rho(r)|]$ represents the exchange-correlation energy per electron in a system of electrons mutually interacting of non-uniform density. Comparing to LDA, which underestimates the exchange energy by about 10%, overestimates the correlation energy by a value close to 100% and predicts shorter bond lengths than that given by experience in molecules, GGA improves total energies and lengthens and softens bonds and provides a better

description of volumes at equilibrium. Many versions of GGA functionals exist, e.g. PBE (Perdew, Burke, Ernzerhof [41], [42], PW91 (Perdew et Wang [43]) and PBEsol (revised version of the Perdew-Burke-Ernzerhof GGA which improves the equilibrium properties of highly dense solids [44]), etc.

III.4.2 Hybrid functionals

In hybrid functionals, the exchange-correlation separation is reformulated to take into account the long-range correlation effects. To this end, a certain percentage of the true or exact exchange, which is the Hartree-Fock exchange, is added to the expression of the exchange-correlation of the GGA functional. The exact amount of the Hartree-Fock exchange is determined in a semi-empirical fashion. The results obtained with this kind of functional show that the latter are the best in the description of the electronic structures of molecules and of associated properties. Regarding the choice of the calculation method, the differences between the density functionals are generally small for the structural parameters. GGA functionals provide good geometries and are sometimes even better than hybrid functionals, which also tend to be more expensive [45], [46]. Among the most used hybrid functionals, we found B3LYP, B3P86 and B3PW91.

III.4.3 Raman DFT modelling

DFT modeling was carried out using Gaussian 16 software [47]. Structural optimization and harmonic vibrational frequency calculations were performed for size-limited clusters: fcc-PbS, PbS_2 H_2, PbS_3H_3, PbS_4H_4, PbS_6H_6, Pb_2S_2, $Pb_2S_6H_4$, $Pb_2S_7H_6$, Pb_4S_4, Pb_9S_9, $Pb_{14}S_{13}$, $AsPbS_6H_5$, $AsPbS_5H_3$ and $Pb_3As_4S_{10}$. Structural optimization and harmonic vibrational frequency calculations are a compromise between the cost of the calculations and the accuracy of the results. The terminal hydrogens are usually added to the isolated non-molecular clusters to avoid dangling bonds and simulate a continuous network [48]. In this work, the DFT calculations were performed with the Becke [49] three parameters hybrid exchange functional and the Lee-Yang-Parr correlation functional (B3LYP) [50]. The cc-PVTZ basis set was used for Arsenic, sulfur and hydrogen atoms. For Pb atoms, we have applied an external pseudo-potential or Effective Core Potential available in the Environment Molecular Science Library [51]. The small-core relativistic pseudo-potential basis set (cc-pVTZ-PP [52]) was specifically employed. All the structures were optimized using the tight convergence option ensuring adequate convergence and reliability of computed wavenumbers. The B3LYP hybrid functional

is often used in both ab initio molecular dynamics and cluster optimization/vibrational frequency calculations for chalcogenides and pnictides [54], [55], [56].

III.4.4 Preliminary FPMD (First-Principles Molecular Dynamic) simulations of diffraction data

Modelling of the high energy x-ray and neutron diffraction data was carried out using the Born−Oppenheimer molecular dynamics with the CP2K package [56]. The generalized gradient approximation (GGA) with hybrid PBE0 functional [57], [58], combining the exact Hartree-Fock solution and DFT approximation. This approach yields excellent agreement with experimental data for chalcogenide systems [59], [60], however, needs much more HPC (high performance computing) resources compared to classical functionals as PBE or PBEsol [41], [44]. The initial atomic configurations for glassy $(PbS)_{0.5}(As_2S_3)_{0.5}$ were created and optimized using the RMC_POT++ code [61], [62] against the derived x-ray and neutron structure factor of the lead thioarsenate glass to obtain a good agreement with experimental data. The size of the cubic simulation box at room temperature, containing 210 atoms (30 Pb, 60 As, and 120 S atoms), was chosen to match the experimental number density. Further optimization has been carried using density functional theory (DFT), adopting for each atom involved the molecularly optimized correlation consistent polarized triple-ζ valence basis set TZVP [63], [64] along with the Goedecker−Teter−Hutter (GTH) type pseudopotentials [65]. As a preliminary result, at the current stage we have made a DFT optimization at 0 K, and started heating the simulation box. The last available temperature corresponds to supercooled liquid at 600 K. The results for this liquid will be compared with pulsed neutron and hard X-ray diffraction experiments.

III.5 Results and discussions

In this part, we are interested in studying the binary systems $PbS\text{-}As_2S_3$ and the A series of the ternary system, $(AgI)_x\,(PbS)_{0.5-x/2}\,(As_2S_3)_{0.5-x/2}$, using Raman spectroscopy technique which is a predominant tool for the structural study of disordered materials. Therefore, a multi-technique approach combining spectroscopic diffraction techniques was used to better understand these complex microstructural materials. First, we characterized the glassy networks of the quasi-binary $PbS\text{-}As_2S_3$ system and then studied the structural changes induced by the gradual addition of AgI.

III.5.1 Raman Spectroscopy Studies of PbS-As2S3 Glasses

Several Pb-As-S crystalline references were synthesized and studied using Raman spectroscopy in order to compare their Raman spectra with the spectra of our glassy samples.

III.5.1.1 Experimental Raman spectra of PbS-As2S3 glasses

Typical Raman spectra of $(PbS)_x(As_2S_3)_{1-x}$ glasses are shown in **Figure III. 4**. Glassy As_2S_3 shows usual poorly resolved spectral envelope between 300 and 400 cm^{-1}, corresponding to symmetric and asymmetric As-S stretching vibrations [66]–[71]. The low-frequency bending modes are located below 200 cm^{-1}. Two distinct spectroscopic features are visible at 235 and 490 cm^{-1}, related to As-As and S-S stretching [69], [70], [72]–[74] and indicating a small chemical disorder in g-As_2S_3, possibly related to a dissociation in the glass-forming melt: 2 As-S ⇄ As-As + S-S.

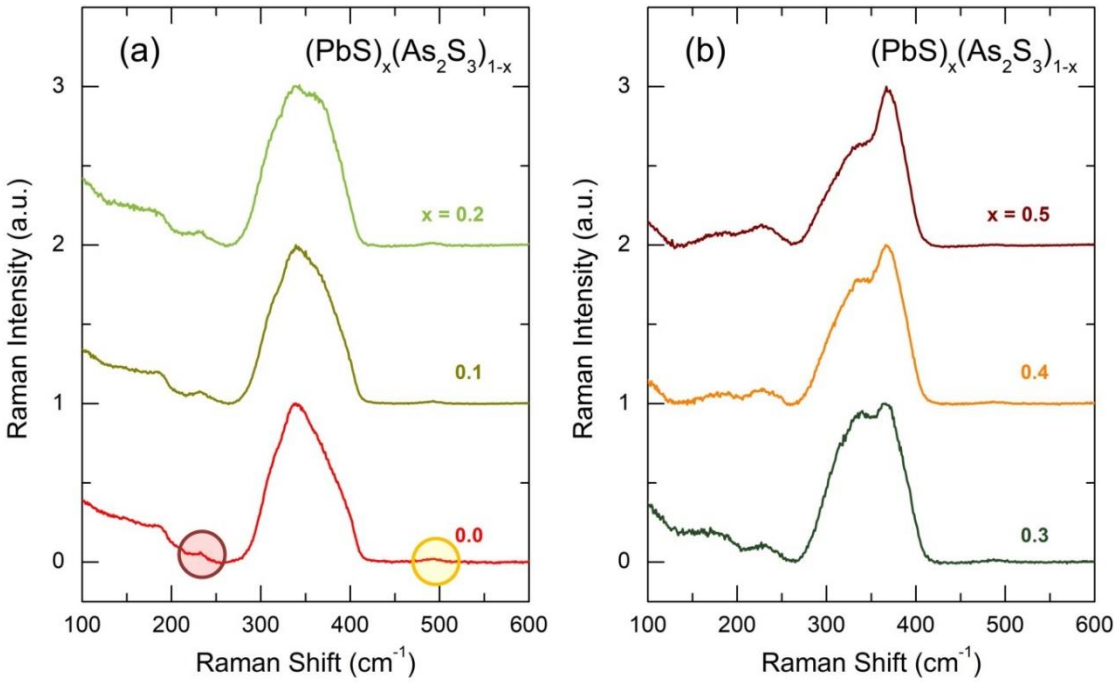

Figure III. 4 Typical Raman spectra of $(PbS)_x(As_2S_3)_{1-x}$ glasses: (a) $0 \leq x \leq 0.2$, (b) $0.3 \leq x \leq 0.5$. The As-As and S-S stretching at 235 and 490 cm^{-1} are highlighted by the brown and yellow circles.

Several characteristic features appear and grow with increasing x. The most visible mode is located at ≈370 cm^{-1} and becomes the most intense peak in the spectra above $x \geq 0.3$. In addition, we can observe a low-frequency broadening of the main spectroscopic feature at 340

cm^{-1} and a clear intensity increase at about ≈230 cm^{-1}. **Figure III. 5(a)** shows the same spectra, normalized to the 340 cm^{-1} mode and plotted together to emphasize changes with increasing lead sulfide content x. We have also used the subtraction of the spectral envelope for glassy As_2S_3 to visualize these changes even more clearly, **Figure III. 5(b)**.

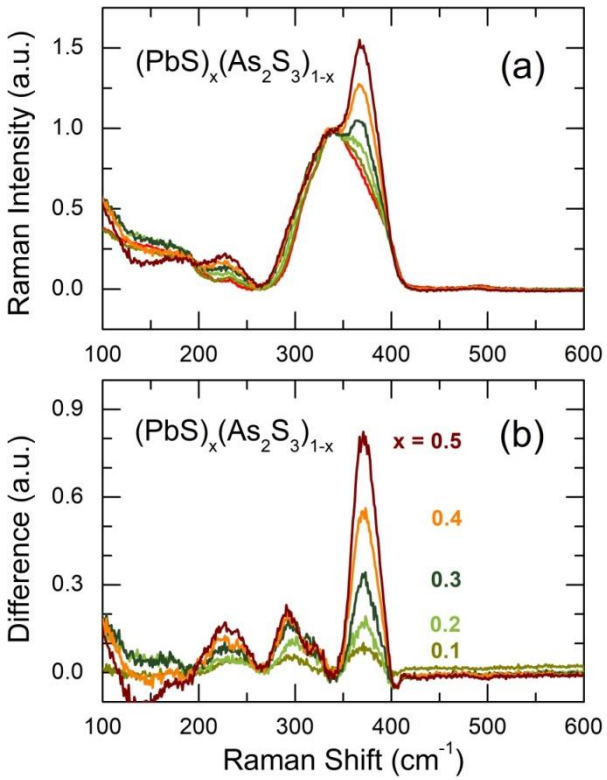

Figure III. 5 (a) Typical Raman spectra of glassy $(PbS)_x(As_2S_3)_{1-x}$, normalized to the 340 cm^{-1} mode, (b) difference Raman spectra of $(PbS)_x(As_2S_3)_{1-x}$ glasses after subtraction of the spectral envelope for glassy As_2S_3.

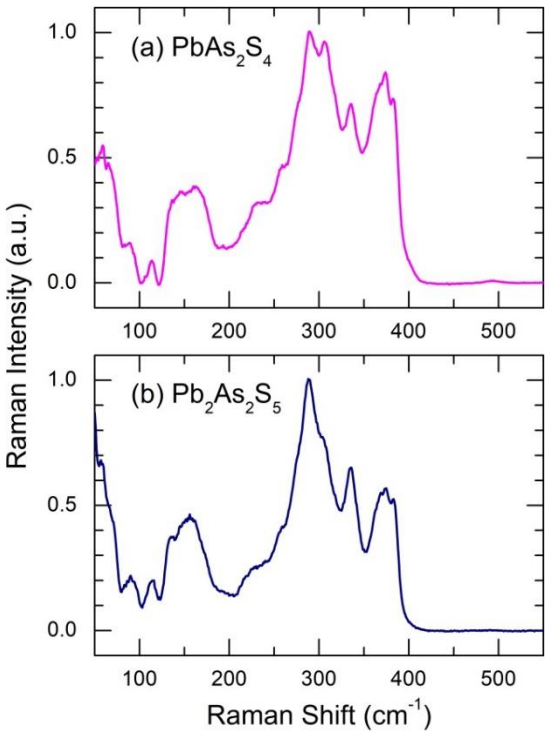

Figure III. 6 Typical Raman spectra of crystalline $(PbS)_x(As_2S_3)_{1-x}$: (a) orthorhombic synthetic sartorite $PbAs_2S_4$ (x = 0.5) and (b) monoclinic synthetic dufrénoysite $Pb_2As_2S_5$ (x = 0.67).

The difference spectra, **Figure III. 5(b)**, have confirmed the above trends and also show a bimodal nature of the ≈300 cm^{-1} feature with a lower frequency component at 290 cm^{-1}, which emerges above $x \geq 0.3$. The origin of these additional modes is two-fold. They could be related either to Pb-S vibrations, or reflect changes in the glassy matrix and, therefore, the As-S stretching frequencies. In order solve this puzzle, we will use the DFT modeling of size limited clusters.

III.5.1.2 Experimental Raman spectra of PbS-As_2S_3 crystals

The Raman spectra of $(PbS)_x(As_2S_3)_{1-x}$ glasses can also be compared with those of PbS-As_2S_3 crystalline compounds. **Figure III. 6** shows typical Raman spectra of orthorhombic synthetic sartorite $PbAs_2S_4$ (x = 0.5) and monoclinic synthetic dufrénoysite $Pb_2As_2S_5$ (x = 0.67). We note both similarities and differences between vitreous and crystalline lead thioarsenates, especially for equimolar composition $(PbS)_{0.5}(As_2S_3)_{0.5}$ = $PbAs_2S_4$, which exists in glassy and crystalline forms. The high frequency (stretching) spectral domain between 200 and 400 cm^{-1} in the two crystals consists of the most intense asymmetric feature at ≈300 cm^{-1} with lower frequency shoulders at ≈230 and ≈260 cm^{-1}. A distinct narrow peak at ≈335 cm^{-1} is followed by unresolved feature at 375 cm^{-1}, presumably containing multiple contributions. At low frequencies, a broad bending feature at ≈150 cm^{-1} is clearly distinguishable accompanied by several less intense peaks. The obtained spectra are rather similar to those reported earlier for sartorite and dufrénoysite minerals [75].

Comparing vitreous $(PbS)_{0.5}(As_2S_3)_{0.5}$ and orthorhombic $PbAs_2S_4$, we note that glassy counterpart exhibits a large fraction of the broad g-As_2S_3 spectral envelope. His Raman profile is also smooth without any narrow peaks characteristic of crystalline lead thioarsenates. Nevertheless, the difference spectra reveal the additional vibration modes emerging at the same frequencies (230, 300, and 370 cm^{-1}) as the distinct spectoscopic features of the crystalline compounds.

The Raman spectra of lead sulfosalt minerals [75] were attributed exclusively to As-S vibrations. The Pb-S stretching and bending modes were not considered. We should however note that despite a widely accepted conclusion that the first order Raman spectra are forbidden for cubic PbS, a combination of resonance Raman spectroscopy and second order Raman results allow to determine that the Pb-S stretching is located between 190 and 240 cm^{-1} [76], [77].

III.5.1.3 DFT Raman spectra of size-limited Pb-S or Pb-As-S clusters

Two types of size-limited clusters were studied: two-component Pb-S and three-component Pb-As-S. After geometry optimization, harmonic frequency calculations have been carried out. The calculated Raman spectra for binary Pb-S clusters are shown in **Figure III. 7**.

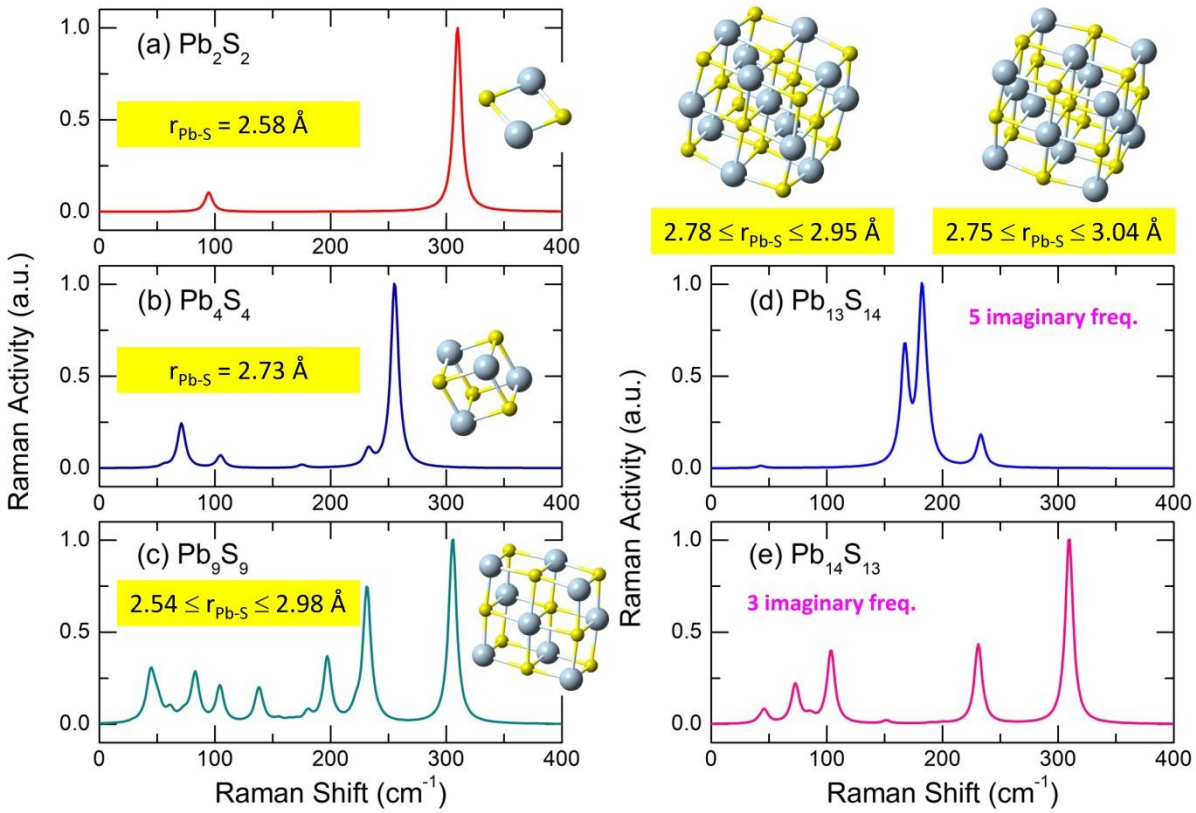

Figure III. 7 DFT Raman spectra for (a) Pb_2S_2, (b) Pb_4S_4, (c) Pb_9S_9, (d) $Pb_{13}S_{14}$, and (e) $Pb_{14}S_{13}$ optimized clusters. The insets show the cluster geometry and interatomic Pb-S separation distances.

The small stoichiometric clusters (Pb_2S_2, Pb_4S_4 and Pb_9S_9) appear to be stable without imaginary frequencies, while the big non-stoichiometric entities ($Pb_{13}S_{14}$ and $Pb_{14}S_{13}$), representing two variants of the fcc elementary cell for cubic PbS, seem to be metastable, revealing 5 and 3 imaginary frequencies, respectively.

All Pb-S clusters, except strongly metastable $Pb_{13}S_{14}$, exhibit clearly distinguishable stretching (180-310 cm^{-1}) and bending (50-150 cm^{-1}) spectral domains. For small stoichiometric clusters, the frequency of the intense A_1 symmetric Pb-S stretching correlates with the Pb-S interatomic distance. For shorter distances, 2.54-2.58 Å, the stretching frequency is maximal, 305-310 cm^{-1}, and *vice versa*. Big metastable clusters are characterized by similar bond distance distributions, 2.76 ± 0.02 Å ≤ r_{Pb-S} ≤ 3.00 ± 0.05 Å, however, drastically different Pb-S stretching frequencies, specifically, for strongly metastable $Pb_{13}S_{14}$ with 5 imaginary frequencies. The DFT results for binary Pb-S clusters suggest that two emerging modes in glassy $(PbS)_x(As_2S_3)_{1-x}$ at ≈230 and ≈300 cm^{-1} may be attributed to asymmetric and

symmetric Pb-S stretching, respectively. However, the most intense feature at ≈370 cm^{-1} is not related to Pb-S vibrations.

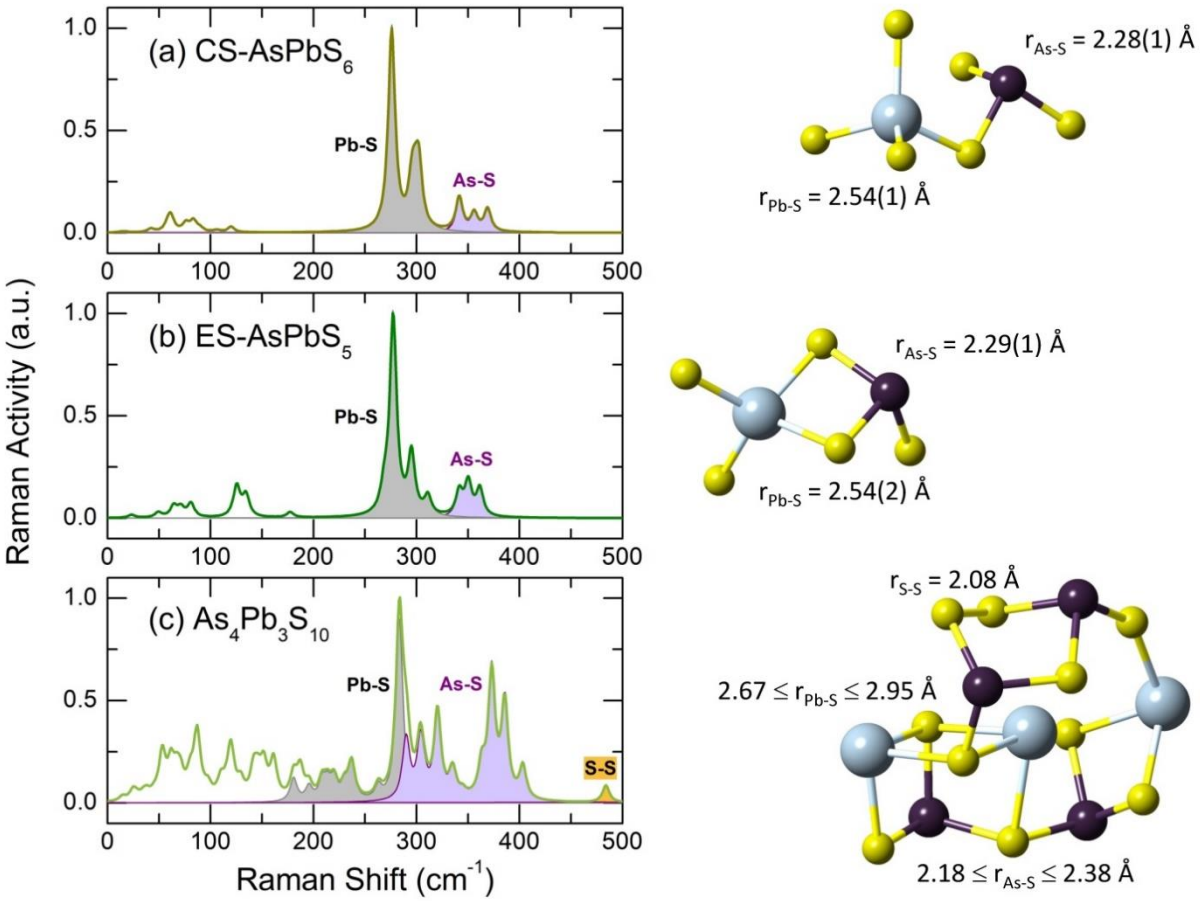

Figure III. 8 DFT Raman spectra of mixed (a) corner-sharing CS-$AsPbS_6H_5$, (b) edge-sharing ES-$AsPbS_5H_3$, and (c) $As_4Pb_4S_{10}$ clusters. The Pb-S stretching is highlighted in light grey; the As-S stretching in light violet; the S-S stretching of the S-S dimer is highlighted in yellow. The optimized geometry of the clusters is shown on the right panel together with typical interatomic distances. The terminal hydrogens are omitted, and the H-related vibrations are removed from the spectra.

The DFT modeling of mixed As-Pb-S clusters enables complementary information on vibrational properties of lead thioarsenates to be gathered. Corner-sharing CS-$AsPbS_6H_5$ and edge-sharing ES-$AsPbS_5H_3$ dimers exhibit strong Pb-S stretching over $270 \leq \omega \leq 310$ cm^{-1} range, distinctly different from the As-S stretching domain, $340 \leq \omega \leq 370$ cm^{-1}, **Figure III. 8.a,b.** The terminal hydrogens, used to avoid bond breaking, are not shown on the right panel representing optimized geometry of the clusters, and the H-related vibrations are subtracted from the spectra. The calculated Pb-S stretching frequencies are similar to those in binary Pb-S clusters, and the As-S vibrations were found to be nearly identical to those in analogous sulfide systems as HgS-As_2S_3 [19]. Low frequency bending vibrations are located below 200

cm^{-1}. Nevertheless, the intensity ratio between Pb-S and As-S vibrations does not correspond to those found experimentally, **Figure III. 4-Figure III. 6**. In order to approach crystalline lead thioarsenates, we have used as a starting configuration for DFT modeling the structural motif of monoclinic sartorite $PbAs_2S_4$ [78].

The crystal structure of $PbAs_2S_4$ consists of infinite chains of corner-sharing pyramids CS-$AsSS_{2/2}$ linking together by lead (**Figure III. 9** [78]).

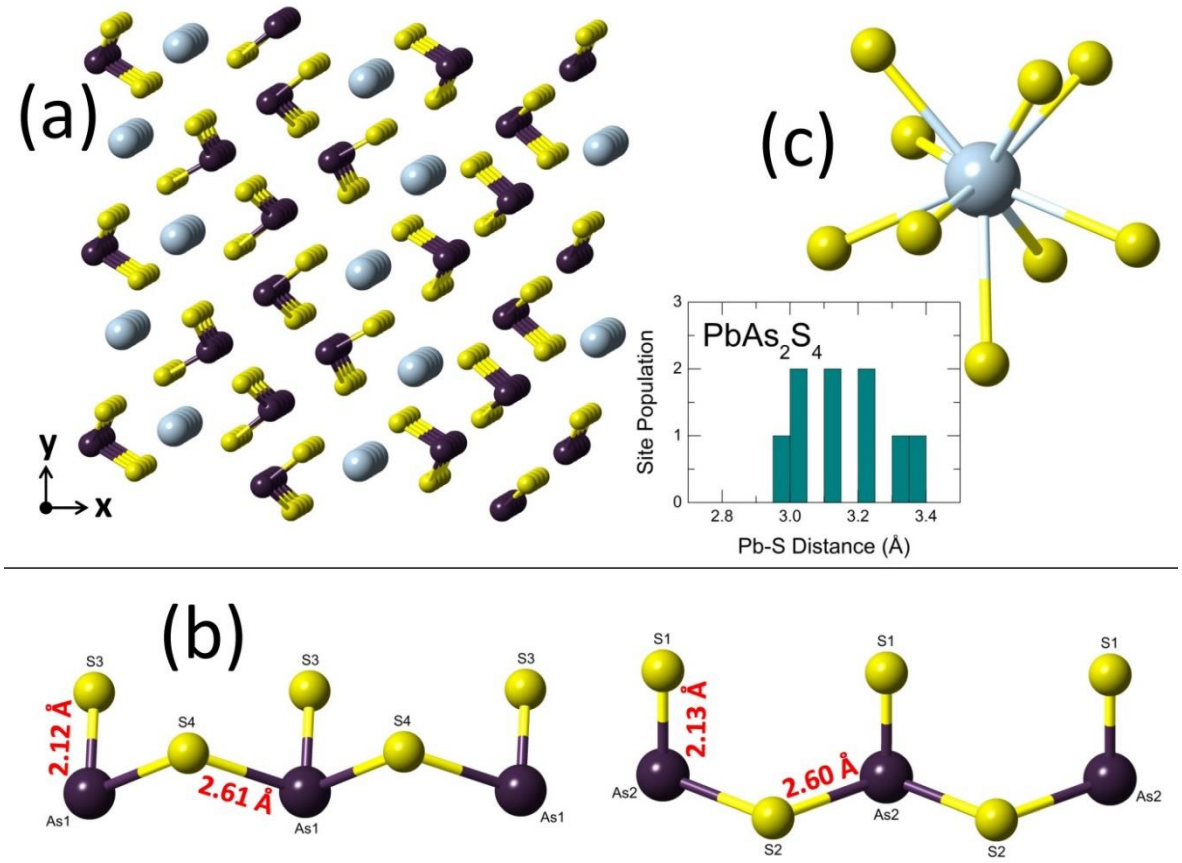

Figure III. 9 Crystal structure of monoclinic $PbAs_2S_4$ [78]: (a) crystal structure nearly parallel to the (001) plane, (b) two types of corner-sharing CS-$AsSS_{2/2}$ chains, (c) local coordination of lead. The insert shows the Pb-S bond distance distribution over the range $0 \leq r_{Pb-S} \leq 4$ Å.

The initial fragment $As_4Pb_3S_{10}$, corresponding to the crystal structure of monoclinic $PbAs_2S_4$, is shown in **Figure III. 10**. However, the cluster stoichiometry appears to be slightly rich in sulfur, $(PbS)_3(As_2S_3)_2(S)_1$, and the DFT optimization has changed the geometry and partially the topology of chemical bonding, forming a S-S dimer, **Figure III. 8(c)**. The calculated DFT Raman spectrum looks rather similar to the both crystalline lead thioarsenates, except the S-S stretching mode at 483 cm^{-1}. The resemblance with synthetic dufrénoysite $Pb_2As_2S_5$ (x = 0.67)

is slightly higher since the PbS/As_2S_3 composition ratio in $As_4Pb_3S_{10}$ (3:2, or $x = 0.6$) is closer to $Pb_2As_2S_5$.

The DFT results for $As_4Pb_3S_{10}$ clearly show that the high-frequency peak at ≈375 cm^{-1} in crystalline and at ≈370 cm^{-1} in vitreous lead thioarsenates is related to the As-S stretching. The blue shift of this stretching mode is caused by shorter $As - S_t$ distances (2.12-2.13 Å in crystalline $PbAs_2S_4$ [78] and 2.18 Å in optimized $As_4Pb_3S_{10}$, **Figure III. 8.c** , where S_t stands for terminal sulfur. In other words, lead is acting rather as a modifier and not as a network former. It should also be noted, that silver and alkali additions to glassy As_2S_3 have led to similar changes in Raman spectra, the appearance of a high frequency peak at ≈375 cm^{-1} with increasing silver or alkali content (**Figure III. 11** [79]).

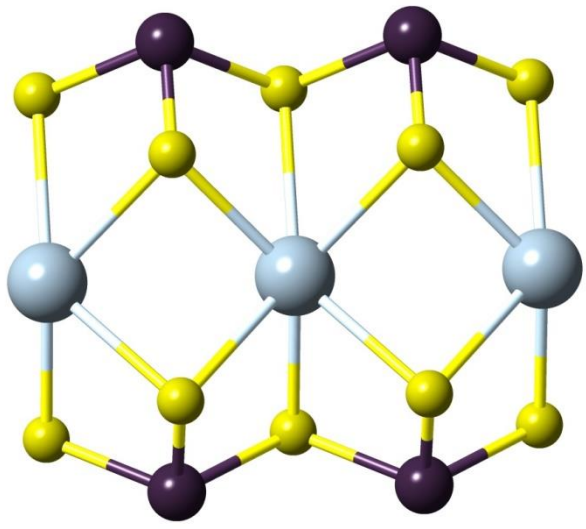

Figure III. 10 Initial fragment $As_4Pb_3S_{10}$, corresponding to the crystal structure of monoclinic $PbAs_2S_4$ [78].

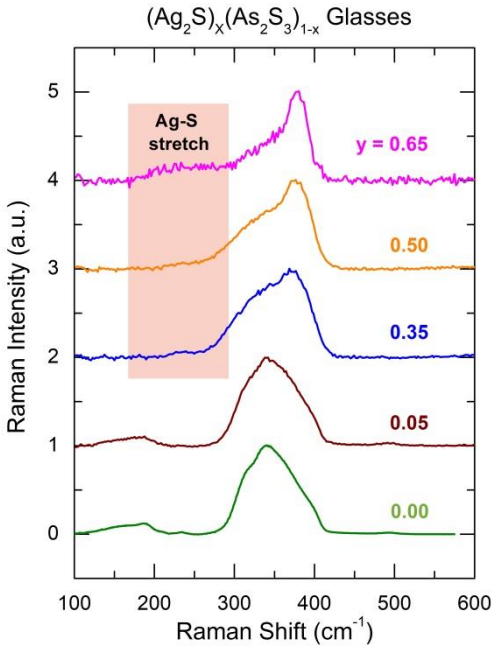

Figure III. 11 Raman spectra of $(Ag_2S)_x(As_2S_3)_{1-x}$ glasses [79].

III.5.2 Raman spectra of $(AgI)_x(PbS)_{0.5-x/2}(As_2S_3)_{0.5-x/2}$ glasses (A-series)

The measured raw Raman spectra of the AgI-PbS-As_2S_3 glasses (A-series) were recorded in the 80-850 cm^{-1} spectral range as was mentioned earlier. As no features were recorded in the high-frequency region above 500 cm^{-1}, we will focus our attention on the 100-500 cm^{-1} domain. As for the previous PbS-As_2S_3 system, this range is appropriate for describing and analysing the majority of bending and deformation modes at low frequencies, ω < 200 cm^{-1}, as well as the

stretching features above 200 cm^{-1}. In order to allow a direct quantitative comparison of the Raman spectra for different glass compositions, a Voigt function was used to fit the spectral background and then subtracted from the experimental data with subsequent normalisation to the As_2S_3 multimodal features centred at ≈340 cm^{-1}.

Typical Raman spectra for A-series glasses, $(AgI)_x(PbS)_{0.5-x/2}(As_2S_3)_{0.5-x/2}$ are presented in **Figure III. 12** for low (a) and high (b) silver iodide content. Similar to the $(PbS)_x(As_2S_3)_{1-x}$ system, the spectra show spectral features mostly related to As-S and Pb-S stretching with some characteristic composition changes. We clearly observe the broad feature centered at 340 cm^{-1} (corresponding to symmetric and asymmetric As-S stretching modes in corner-sharing $AsS_{3/2}$ pyramids) as well as the two peaks at 230 cm^{-1} (As-As stretching) and 490 cm^{-1} (S-S stretching). The 235 cm^{-1} peak is accompanied by another one at around 180 cm^{-1}. The most intense high-frequency peak at 370 cm^{-1}, attributed to $As - S_t$ stretching according to DFT modelling and where S_t stands for terminal sulfur, is always present. Increasing the AgI content from x = 0.0 to x = 0.6 (**Figure III. 12(c)**), the 235 cm^{-1} and 180 cm^{-1} features decrease progressively in intensity in contrast to the peak at 370 cm^{-1} with increased intensity. Furthermore, with continuous AgI addition, a new vibrational mode emerges in the vicinity of 105 cm^{-1} as a shoulder accompanied with a filling up of the feature at ≈260 cm^{-1}.

To visualize these changes even more clearly, the spectral envelope for glassy As_2S_3 was subtracted and the difference spectra is presented in **Figure III. 13(a).** It clearly shows (i) the feature around 230 cm^{-1} (ii) the bimodal nature of the ≈300 cm^{-1} feature with a lower frequency component at 290 cm^{-1}, and (ii) the peak at 370 cm^{-1}, all seen earlier for the binary PbS-As_2S_3 glasses. The new vibrational mode at ≈105 cm^{-1}, increasing with AgI, becomes more pertinent. This peak is probably related to Ag-I stretching. The DFT modelling of AgI monomer reproduces well the AgI stretching frequency at 121 cm^{-1} for the Ag-I interatomic distance of 2.8 Å.

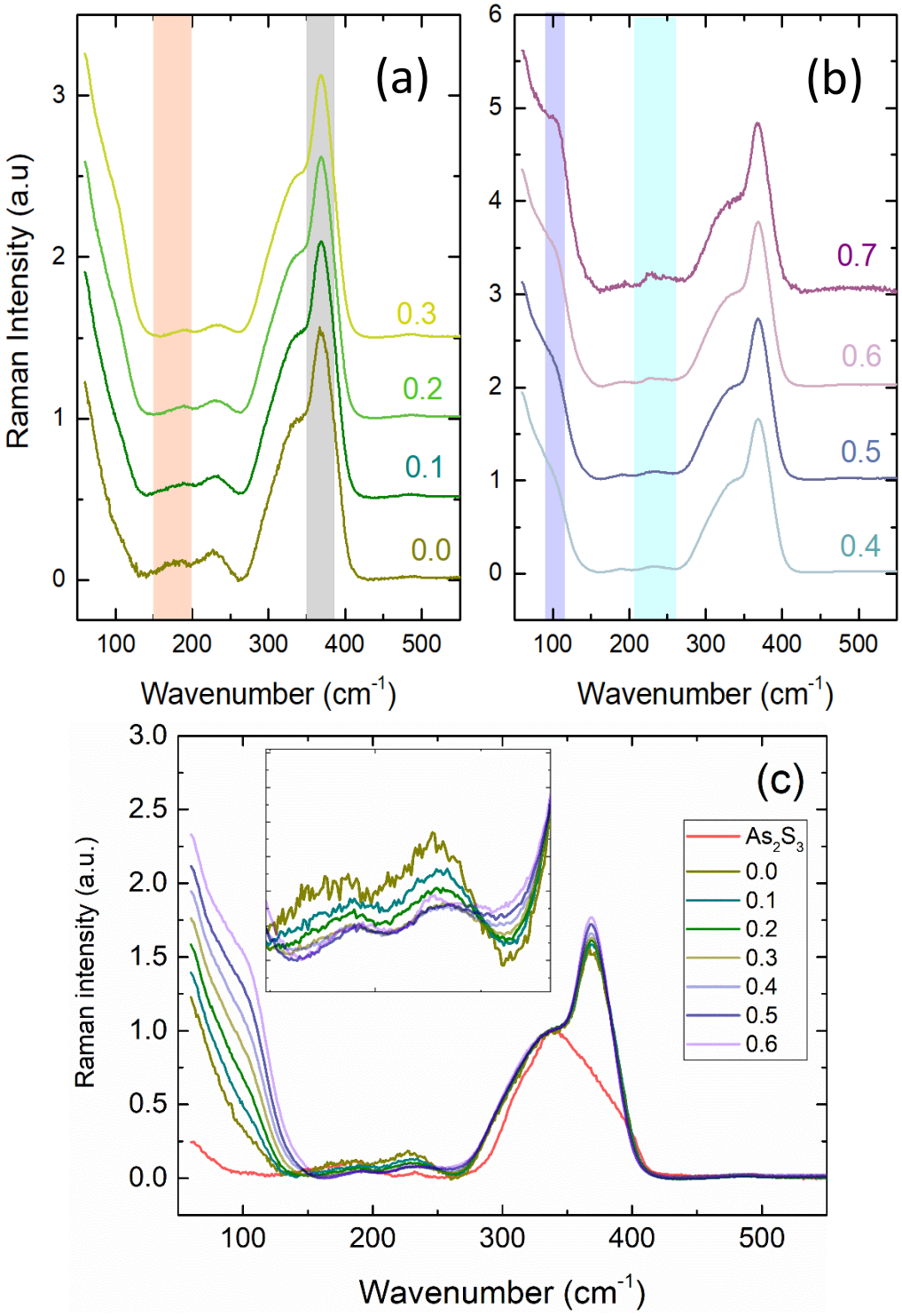

Figure III. 12 Raman spectra for the pseudo-ternary A-series glasses, $(AgI)_x (PbS)_{0.5-x/2} (As_2S_3)_{0.5-x/2}$, with (a) low and (b) high silver iodide content x. (c) Typical Raman spectra of the glassy A-series pseudo-ternary system normalized to the 340 cm^{-1} mode.

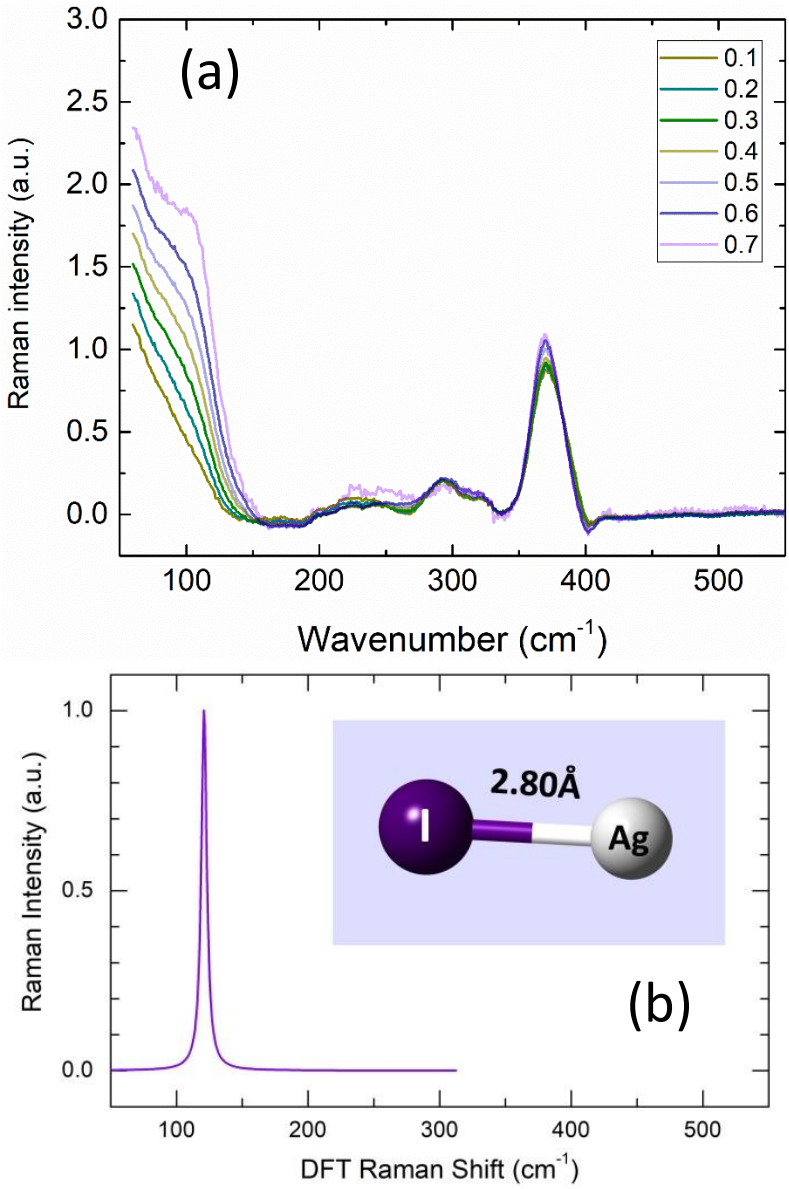

Figure III. 13 (a) difference Raman spectra of $(AgI)_x(PbS)_{0.5-x/2}(As_2S_3)_{0.5-x/2}$ glasses after subtraction of the spectral envelope for glassy As_2S_3. (b) DFT Raman spectra of AgI monomer.

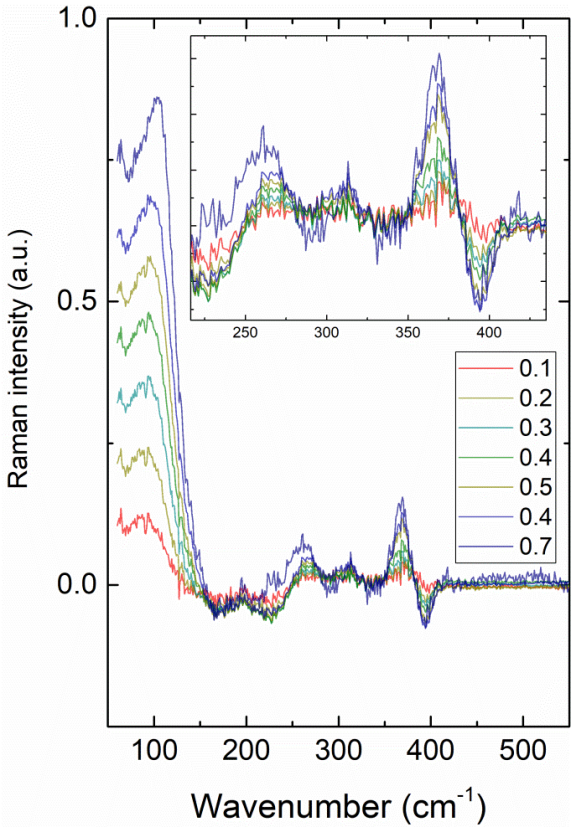

Figure III. 14 The difference Raman spectra obtained by subtraction of the scaled Raman signal for $(PbS)_{0.5}(As_2S_3)_{0.5}$ and normalized to a constant $(PbS)_{0.5}(As_2S_3)_{0.5}$ spectral envelope.

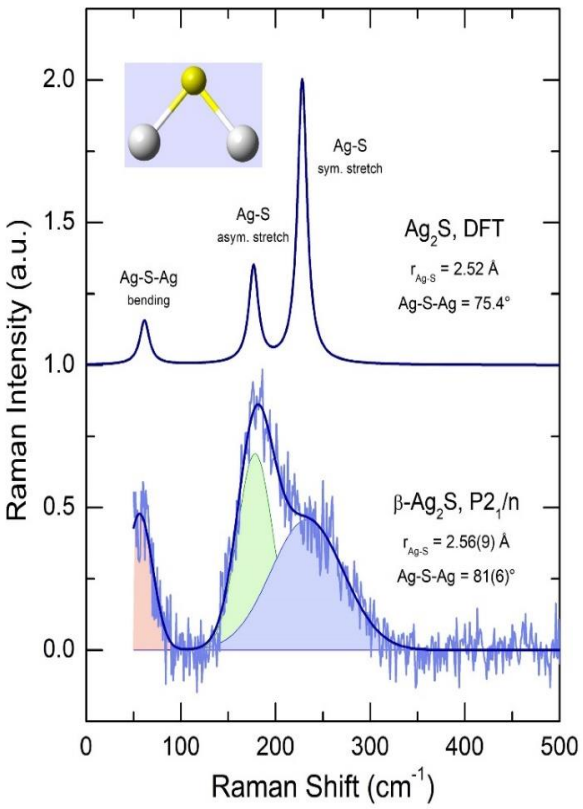

Figure III. 15 DFT Raman spectra of Ag_2S compared to the experimental data for β-Ag_2S.

The difference Raman spectra obtained by subtraction of the scaled Raman spectrum for $(PbS)_{0.5}(As_2S_3)_{0.5}$ is presented in **Figure III. 14**. We should precise that the difference spectra assume the subtraction of PbS- As_2S_3 related vibrations, e.g. As-S and Pb-S stretching modes. The remaining vibrations should be related to AgI-based structural units and vibrational (structural) differences in the subtracted host, $(PbS)_{0.5}(As_2S_3)_{0.5}$, with increasing silver iodide content. Consequently, a monotonic increase of the Ag-I stretching at ≈105 cm^{-1} in the difference spectra, normalized to a constant spectral envelope of the $(PbS)_{0.5}(As_2S_3)_{0.5}$ host, is expected in accordance with the chemical composition of the ternary glasses, $(AgI)_x (PbS)_{0.5-x/2} (As_2S_3)_{0.5-x/2}$. The Ag-I stretching also exhibits a blue shift with increasing *x*. In addition to the 105 cm^{-1} Ag-I stretching, a weak low frequency asymmetric feature at 265 cm^{-1} appears and grows up with AgI content (inset of **Figure III. 14**). The 265 cm^{-1} feature is similar to that found in crystalline Ag_2S **(Figure III. 15)** but shifted to higher frequencies and can be attributed to Ag-S stretching for short Ag-S separations of ≈2.43 Å. Similar peak has been observed in many Ag-rich glasses, increasing with silver content [80], [81]. The above results suggest mixed

silver environment in AgI-PbS-A_2S_3 glasses. An additional analysis is needed to clarify the observed changes.

III.5.3 Neutron and High-Energy X-Ray Diffraction Studies of PbS- A_2S_3 Glasses

III.5.3.1 Q-Space Results

The neutron $S_{\mathrm{N}}(Q)$ and X-ray $S_{\mathrm{X}}(Q)$ structure factors of $(\mathrm{PbS})_x(\mathrm{As_2S_3})_{1-x}$ glasses are shown in **Figure III. 16** and **Figure III. 17**:

$$S_{\mathrm{N}}(Q) = w^{\mathrm{N}}_{\mathrm{AsAs}}S_{\mathrm{AsAs}}(Q) + w^{\mathrm{N}}_{\mathrm{AsS}}S_{\mathrm{AsS}}(Q) + w^{\mathrm{N}}_{\mathrm{SS}}S_{\mathrm{SS}}(Q) + w^{\mathrm{N}}_{\mathrm{PbPb}}S_{\mathrm{PbPb}}(Q) + w^{\mathrm{N}}_{\mathrm{PbS}}S_{\mathrm{PbS}}(Q) + w^{\mathrm{N}}_{\mathrm{PbAs}}S_{\mathrm{PbAs}}(Q), \quad \text{(III.21)}$$

$$S_{\mathrm{X}}(Q) = w^{\mathrm{X}}_{\mathrm{AsAs}}(Q)S_{\mathrm{AsAs}}(Q) + w^{\mathrm{X}}_{\mathrm{AsS}}(Q)S_{\mathrm{AsS}}(Q) + w^{\mathrm{X}}_{\mathrm{SS}}(Q)S_{\mathrm{SS}}(Q) + w^{\mathrm{X}}_{\mathrm{PbPb}}(Q)S_{\mathrm{PbPb}}(Q) + w^{\mathrm{X}}_{\mathrm{PbS}}(Q)S_{\mathrm{PbS}}(Q) + w^{\mathrm{X}}_{\mathrm{PbAs}}(Q)S_{\mathrm{PbAs}}(Q), \quad \text{(III.22)}$$

where $w^{\mathrm{N}}_{\mathrm{ij}}$ are neutron weighting factors, $w^{\mathrm{X}}_{\mathrm{ij}}(Q)$ are Q-dependent X-ray weighting coefficients and $S_{\mathrm{ij}}(Q)$ the Faber-Ziman partial structure factors.

Systematic changes are observed for both $S_{\mathrm{N}}(Q)$ and $S_{\mathrm{X}}(Q)$ with increasing PbS content x. The first sharp diffraction peak FSDP at $Q_0 \approx 1.25$ Å^{-1} decreases dramatically with x and nearly disappears in the X-ray data. An additional peak emerges and grows at $Q_{\mathrm{Pb}} \approx 1.7$ Å^{-1} and his amplitude is higher for $S_{\mathrm{X}}(Q)$s. The first principle peak PP1 slightly increases with x and shifts from $Q_1 \approx 2.4$ Å^{-1} (x = 0) to ≈2.3 Å^{-1} (x = 0.5). In contrast, the amplitude of the second PP2 markedly decreases and exhibits a pronounced shift to lower scattering vectors: $Q_2 \approx 3.9$ Å^{-1} (x = 0) to ≈3.6 Å^{-1} (x = 0.5). The amplitude of high-Q oscillations also systematically decreases with x, and some additional features appear at ≈4.8 Å^{-1} and ≈7 Å^{-1}.The neutron data below $Q \lesssim 0.2$ Å^{-1} exhibit some enhanced small-angle neutron scattering (SANS) except glassy As_2S_3. The SANS intensity is small in the accessible low-Q range, much smaller compared to phase-separated glasses, that is, $\mathrm{As}_y\mathrm{S}_{1-y}$ or $\mathrm{Ge}_y\mathrm{S}_{1-y}$at $y \leq 0.30$ (**Figure III. 18** [66]), however, indicates some inhomogeneity at mesoscopic scale ($\lesssim$ 1000 Å). We should also note that the studied PbS-As_2S_3 glasses show a single glass transition in contrast to phase-separated As-S or Ge-S glasses with strong SANS and two glass transitions.

The X-ray structure factors do not show the enhanced small-angle scattering because the available low-Q domain is limited by $Q_{\min}$ = 0.5 Å^{-1}.

The FSDP and related low-Q features were isolated using the background subtraction reported previously [82], [83]. The results are shown in **Figure III. 19** and **Figure III. 20**. We note that the observed evolution is similar for the two data sets. Nevertheless, different sensitivity of neutrons and hard X-rays causes slightly different quantitative trends.

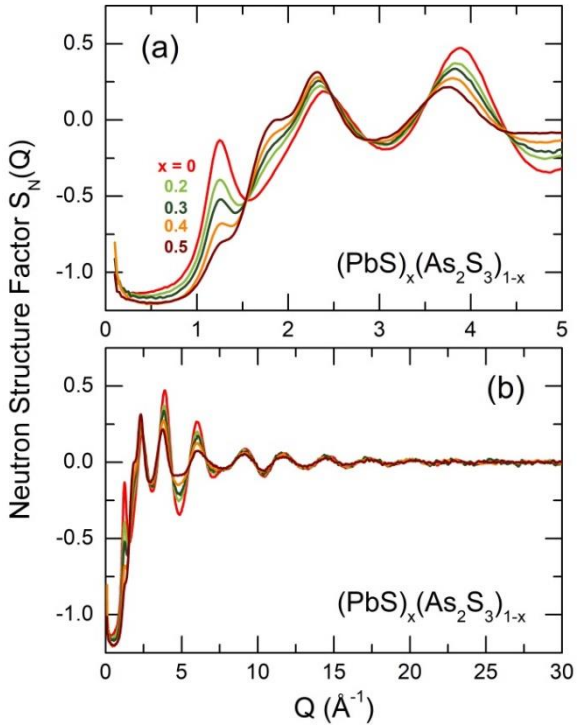

Figure III. 16 Neutron structure factors $S_{\mathrm{N}}(Q)$ of $(\mathrm{PbS})_x(\mathrm{As_2S_3})_{1-x}$ glasses at (a) low scattering vectors Q and (b) over the entire accessible Q-range.

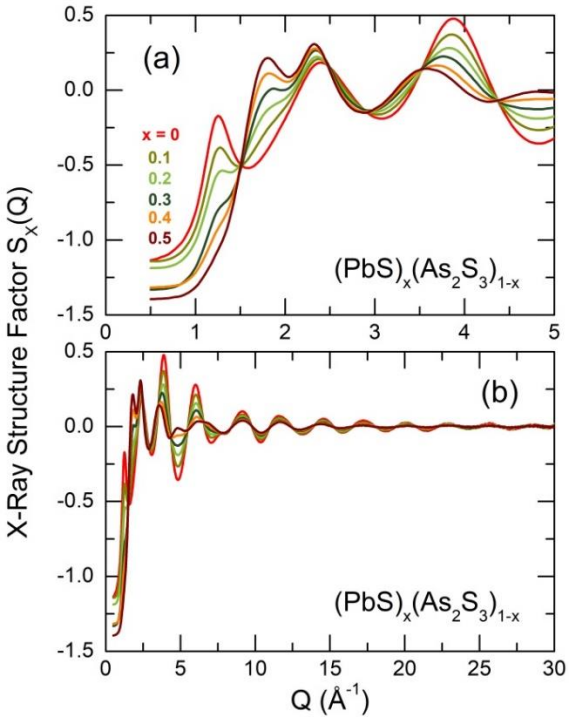

Figure III. 17 X-ray structure factors $S_{\mathrm{X}}(Q)$ of $(\mathrm{PbS})_x(\mathrm{As_2S_3})_{1-x}$ glasses at (a) low scattering vectors Q and (b) over the entire accessible Q-range.

First, we note that the FSDP decreases faster in case of the X-ray structure factors. The origin of the FSDP in thioarsenate glasses is As-As correlations at the intermediate-range scale $L_0 = \frac{2\pi}{Q_0} \approx$ 5-6 Å, verified both experimentally [84] and theoretically [85]–[87]. The neutron As-As weighting factors $w^{\mathrm{N}}_{\mathrm{AsAs}}$ are larger than the X-ray counterparts. For example, for equimolar glass $(\mathrm{PbS})_{0.5}(\mathrm{As_2S_3})_{0.5}$, the ratio $w^{\mathrm{N}}_{\mathrm{AsAs}}/\langle w^{\mathrm{X}}_{\mathrm{AsAs}}(Q)\rangle$ appears to be ≈1.7, where angular brackets for Q-dependent X-ray weightings mean the average value over the accessible Q-range. In other words, neutrons are more sensitive to As-As atomic pairs compared to X-rays,

explaining the observed trend. The decrease of the FSDP amplitude with increasing x also means a fragmentation of the host thioarsenate glass matrix. The origin of the emerging and growing pre-pic at ≈1.7 Å^{-1} and its higher amplitude for X-rays suggests it is related to lead. It was shown earlier for similar HgS-As_2S_3 glassy system, that the origin of the comparable pre-pic is related to Hg-Hg correlations [88]. In case of equimolar composition, $w^{\mathrm{N}}_{\mathrm{PbPb}}/w^{\mathrm{X}}_{\mathrm{PbPb}}(Q = 1.7\text{Å}^{-1})$ is ≈0.5, thus explaining the difference in the Pb pre-pic amplitudes between neutrons and X-rays. Further confirmation will be done by first-principles molecular dynamics (FPMD).

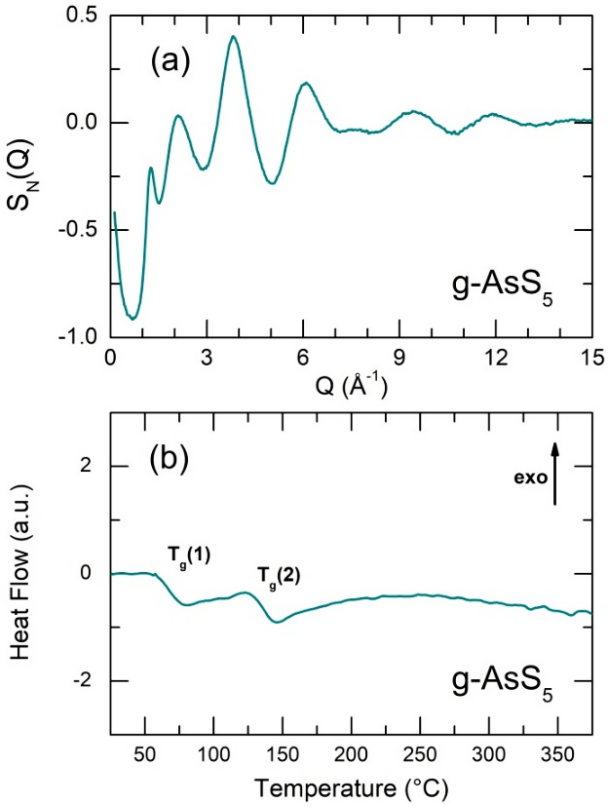

Figure III. 18 (a) Neutron structure factor and (b) DSC trace for phase-separated AsS_5 glass *[66]*.

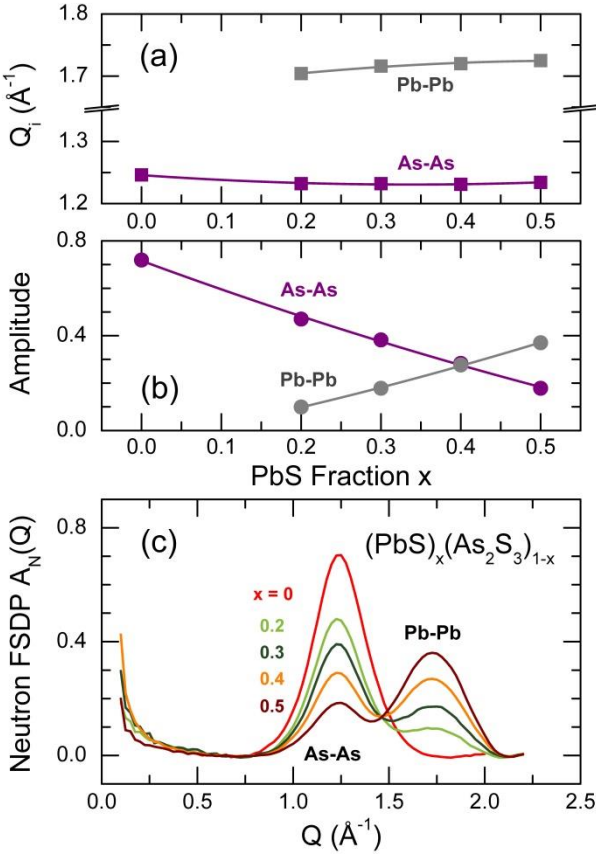

Figure III. 19 Neutron FSDP parameters for PbS-As_2S_3 glasses: (a) FSDP and Pb pre-pic positions, (b) FSDP and Pb pre-pic amplitudes, and (c) isolated low-Q features.

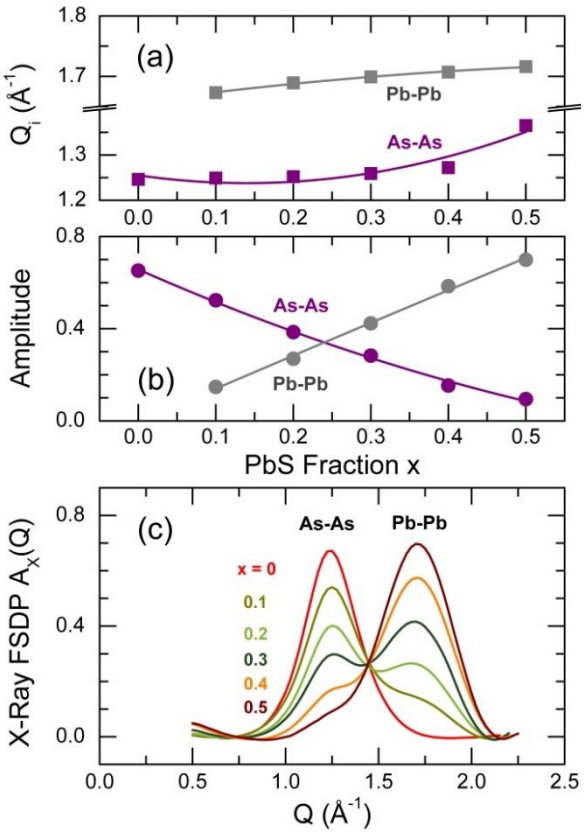

Figure III. 20 X-ray FSDP parameters for PbS-As_2S_3 glasses: (a) FSDP and Pb pre-pic positions, (b) FSDP and Pb pre-pic amplitudes, and (c) isolated low-Q features.

III.5.3.2 r-Space Results

The neutron $T_{\mathrm{N}}(r)$ and X-ray $T_{\mathrm{X}}(r)$ total correlation functions, obtained through the usual Fourier transform, are shown in **Figure III. 21** and **Figure III. 22**:

$$T_{\mathrm{N,X}}(r) = 4\pi\rho_0 r + \frac{2}{\pi}\int_0^{Q_{\max}} Q\left[S_{\mathrm{N,X}}(Q) - 1\right]\sin QrM(Q)\mathrm{d}Q, \qquad \text{(III.23)}$$

where ρ_0 is the experimental number density, $M(Q)$ the Lorch window function, and $Q_{\max}$ = 30 Å^{-1}.

The $T_{\mathrm{N}}(r)$ and $T_{\mathrm{X}}(r)$ functions exhibit the first peak at r_1 = 2.27 Å, corresponding to As-S nearest neighbors (NN). As expected, the amplitude of this peak decreases with x. The second peak at $r_2 \approx$ 2.85 Å emerges and grows with increasing lead sulfide content and seems to be related to Pb-S NN correlations. The amplitude of the second peak is higher for X-rays in accordance with neutron and X-ray weighting coefficients, $w_{\mathrm{PbS}}^{\mathrm{N}}/\langle w_{\mathrm{PbS}}^{\mathrm{X}}(Q)\rangle$ < 1, where the

angle brackets represent the average values over the accessible Q-range. A broad unresolved feature at ≈3.5 Å represent second neighbor correlations. The second neighbor peak decreases with x and shifts to higher r. In addition a new feature appears and increases in intensity at ≈4 Å, also filling the gap between the second neighbor peak and more distant correlations at ≈5.3 Å. The last correlation in glassy As_2S_3 corresponds to center-center distance between AsS_3 pyramids, forming the intermediate-range order in a disordered network consisting of As_pS_q rings. Monoclinic orpiment and triclinic anorpiment As_2S_3 are formed by As_6S_6 rings [89], [90]. These indirect results show that population of As_pS_q rings decreases, and the initial intermediate range order changes, most probably caused by the host network fragmentation, also reflected by the decreasing amplitude of the FSDP (**Figure III. 19** and **Figure III. 20**).

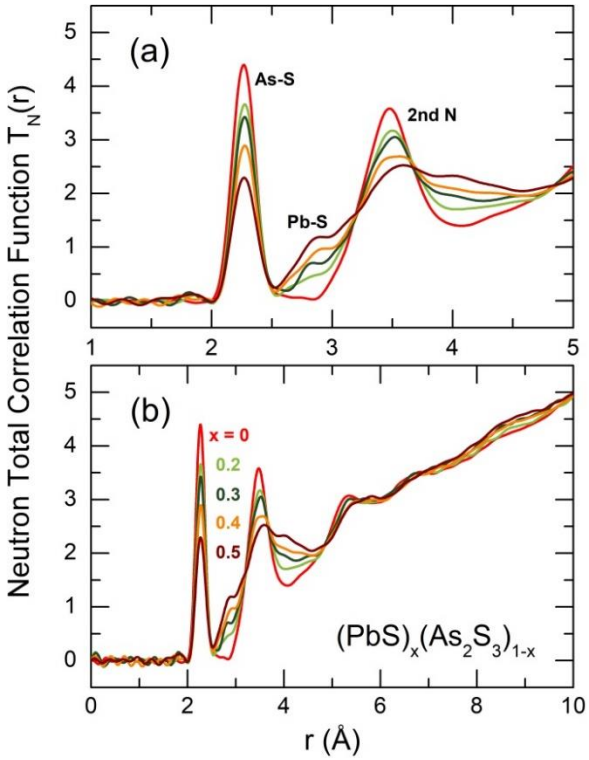

Figure III. 21 Neutron total correlation functions $T_N(r)$ for PbS-As_2S_3 glasses: (a) limited r-range to nearest and second neighbors , (b) extended r-range up to 10 Å.

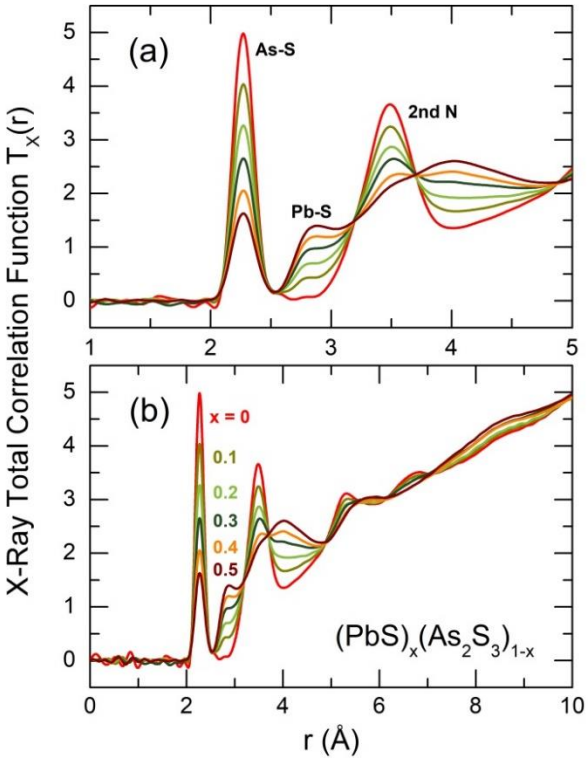

Figure III. 22 X-ray total correlation functions $T_X(r)$ for PbS-As_2S_3 glasses: (a) limited r-range to nearest and second neighbors , (b) extended r-range up to 10 Å.

It is interesting to compare the neutron total correlation functions in glassy equimolar $(PbS)_{0.5}(As_2S_3)_{0.5}$ and monoclinic $PbAs_2S_4$, **Figure III. 23**. The last $T_N(r)$ function was calculated from the cif file [78] using the XTAL code [91]. Similar to Raman results for glassy and crystalline counterparts, one observes both similarities and distinct differences. First,

monoclinic $PbAs_2S_4$ exhibits a large difference in bond lengths involving terminal S_t and bridging S_b sulfur: r_{As-S_t} = 2.125 ± 0.005 Å and r_{As-S_b} = 2.605 ± 0.005 Å, clearly visible in **Figure III. 23**. In the equimolar glass this difference is markedly smaller in accordance with our DFT modeling on $As_4Pb_3S_{10}$ cluster (r_{As-S_t} = 2.21 ± 0.02 Å, r_{As-S_b} = 2.32 ± 0.05 Å), **Figure III. 8**. The large r_{As-S_b} intrachain distance in monoclinic crystal is accompanied by rather short interchain As-S separations (2.87-3.25 Å), hardly existing in the glass as it will show our preliminary FPMD simulations.

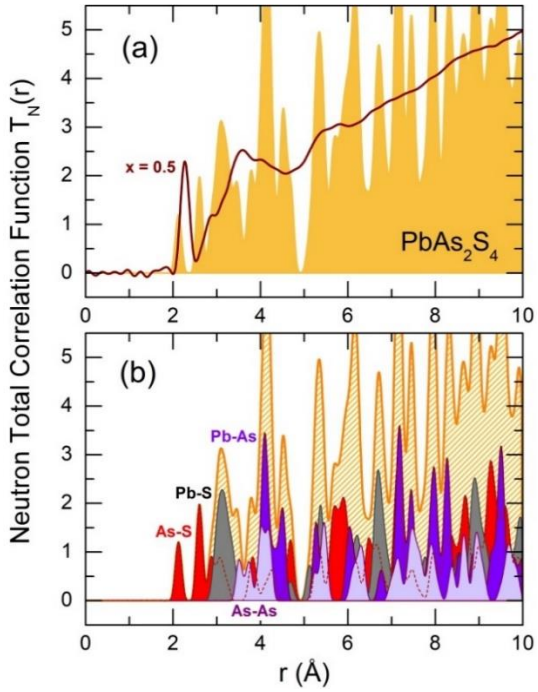

Figure III. 23 (a) Neutron total correlation functions $T_N(r)$ for equimolar $(PbS)_{0.5}(As_2S_3)_{0.5}$ glass and monoclinic $PbAs_2S_4$, obtained using the XTAL code *[91]* from the cif file *[78]*; (b) $T_N(r)$ and selected partial functions $T_{ij}(r)$ for monoclinic $PbAs_2S_4$.

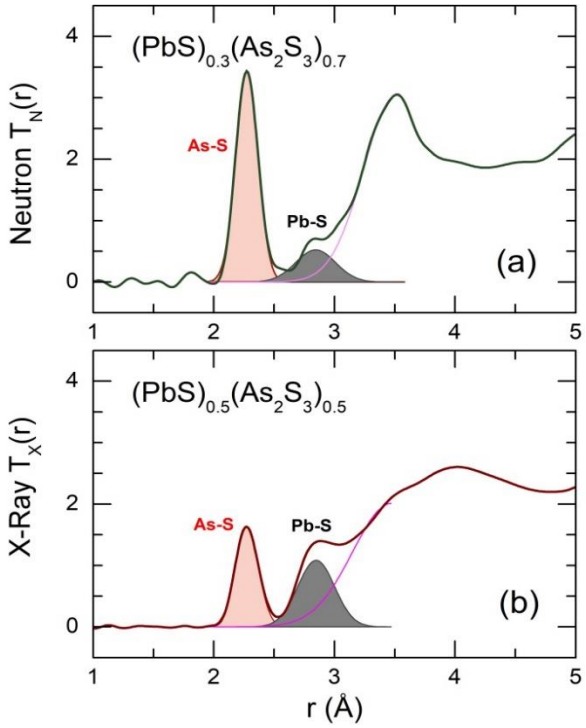

Figure III. 24 A three-peak Gaussian fitting of experimental total correlation functions for selected $PbS-As_2S_3$ glasses: (a) neutron data for $(PbS)_{0.3}(As_2S_3)_{0.7}$, (b) high-energy X-ray data for $(PbS)_{0.5}(As_2S_3)_{0.5}$. The As-S and Pb-S NN correlations are highlighted in light red and gray.

The Pb-S interatomic distances in lead thioarsenate glasses (≈2.85 Å) are shorter than in monoclinic $PbAs_2S_4$ (2.95 Å ≤ r_{Pb-S} ≤ 3.39Å or r_{Pb-S} = 3.17 ± 0.14 Å). The DFT modeling of the $As_4Pb_3S_{10}$ cluster yields r_{Pb-S} = 2.79 ± 0.10 Å, that is, reasonably close to the diffraction results. More distant correlations are rather similar. The emerging feature at ≈4 Å, more intense in the X-ray data and therefore related to lead, most probably corresponds to Pb-As correlations, the Pb-As partial in **Figure III. 23(b)**.

A three-peak Gaussian fitting of the neutron and X-ray diffraction data (the As-S, Pb-S and second neighbor contributions) gives additional information on local coordination of arsenic and lead. Typical fitting results are shown in **Figure III. 24** and the derived interatomic distances and local coordination numbers are summarized in **Table III.1**. The As-S coordination is trigonal. Assuming pure As-S environment, the As-S local coordination number appears to be $N_{\mathrm{As-S}} = 2.9 \pm 0.1$. Small population of As-As and S-S homopolar bonds, observed in Raman results, will not affect the trigonal coordination of arsenic.

The question of local lead environment is more complicated. The three-peak Gaussian fitting with symmetric functions yields $N_{\mathrm{Pb-S}} = 3.5 \pm 0.5$. From one side, the small lead local coordination is consistent with smaller Pb-S interatomic distances. In monoclinic $PbAs_2S_4$, the lead local coordination is $N_{\mathrm{Pb-S}} = 9$ (**Figure III. 9**) and the average Pb-S distance is $r_{\mathrm{Pb-S}} = 3.17 \pm 0.14$ Å [78]. On the other, the Gaussian fitting is using symmetric functions, but we cannot exclude asymmetric bond distance distribution typical for crystalline lead thioarsenates. Consequently, the local Pb-S coordination may be higher. Additional information will be done by our preliminary FPMD modeling.

Table III. 1 Nearest-neighbor interatomic distances r_{ij} and local coordination numbers N_{ij} in PbS-As_2S_3 glasses, calculated from the neutron and high-energy X-ray diffraction results.

x	As-S		Pb-S	
	$r_{\mathrm{As-S}}$ (Å)	$N_{\mathrm{As-S}}$	$r_{\mathrm{Pb-S}}$ (Å)	$N_{\mathrm{Pb-S}}$
Neutron diffraction				
0*	2.27(1)	2.95(10)	–	–
0.2	2.27(1)	2.95(10)	2.84(2)	3.7(2)**
0.3	2.27(1)	2.97(10)	2.84(2)	3.4(2)**
0.4	2.28(1)	2.89(10)	2.85(2)	3.6 (2)**
0.5	2.27(1)	2.89(10)	2.87(2)	3.8(2)**
High energy X-ray diffraction				
0	2.27(1)	3.00(10)	–	–
0.1	2.27(1)	2.95(10)	2.85(2)	4.2(4)**
0.2	2.27(1)	2.92(10)	2.82(2)	3.3(3)**
0.3	2.27(1)	2.91(10)	2.85(2)	3.7(3)**
0.4	2.27(1)	2.88(10)	2.85(2)	3.2(3)**
0.5	2.27(1)	2.91(10)	2.85(2)	3.3(3)**

* Refs. [20], [66]; ** approximate values using a three-peak symmetric Gaussian fitting

III.5.3.3 Preliminary Results of First Principles Molecular Dynamics Modeling of Equimolar Supercooled Liquid $(PbS)_{0.5}(As_2S_3)_{0.5}$

As mentioned earlier {III.4.4}, we are using a 210-atoms box, containing 30 Pb, 60 As and 120 S atoms. The size of the box corresponds to the experimental number density. Typical snapshot of the 600 K simulation box is given in **Figure III. 25**. Even for simulation time at 600 K of 12 ps, we have reasonably good agreement with neutron and high-energy X-ray results, **Figure III. 26** and **Figure III. 27**.

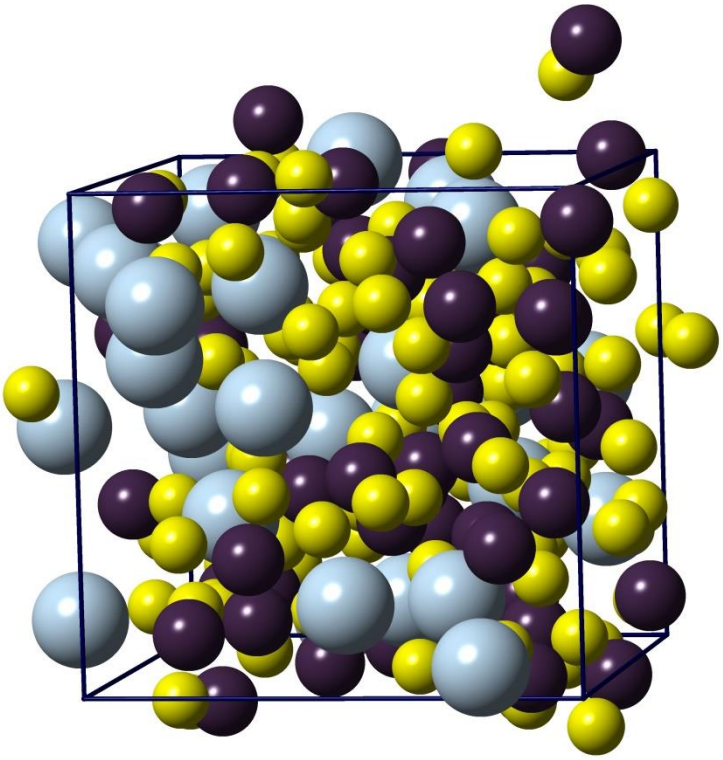

Figure III. 25 Typical snapshot of the 600K FPMD simulation box containing 30 Pb, 60 As and 120 S atoms. This composition corresponds to equimolar $(PbS)_{0.5}(As_2S_3)_{0.5}$. The size of the box was chosen to match the experimental number density.

The GGA/PBE0 neutron $Q[S_{\mathrm{N}}(Q)-1]$ and X-ray $Q[S_{\mathrm{X}}(Q)-1]$ interference functions, **Figure III. 26**, reproduce well both the distant oscillations, and the amplitudes and peak positions at low Q. The calculated neutron $g_{\mathrm{N}}(r)$ and X-ray $g_{\mathrm{X}}(r)$ pair-distribution functions also reflect correctly the atomic distributions in r-space, **Figure III. 27**. Consequently, the 600 K results mimic rather precisely the glass structure at room temperature.

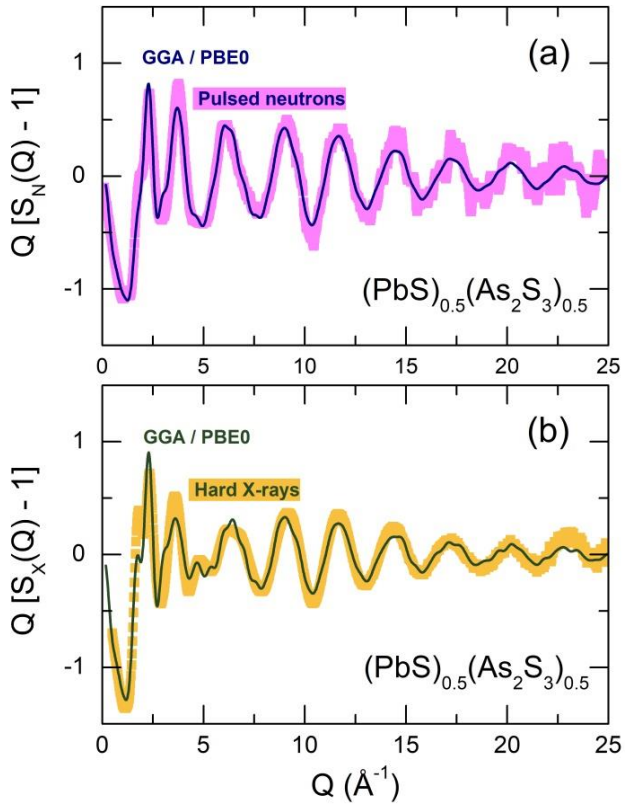

Figure III. 26 Experimental (room temperature) and GGA/PBE0 at 600 K (a) neutron $Q[S_{\mathrm{N}}(Q)-1]$ and (b) X-ray $Q[S_{\mathrm{X}}(Q)-1]$ interference functions for equimolar composition $(PbS)_{0.5}(As_2S_3)_{0.5}$.

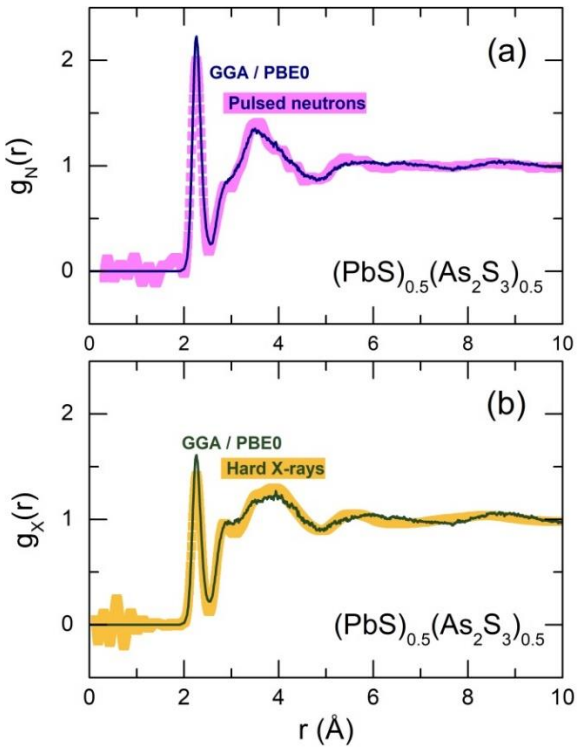

Figure III. 27 Experimental (room temperature) and GGA/PBE0 at 600 K (a) neutron $g_N(r)$ and (b) X-ray $g_{\mathrm{X}}(r)$ pair-distribution functions for equimolar $(PbS)_{0.5}(As_2S_3)_{0.5}$.

The calculated partial structure factors $S_{\mathrm{ij}}(Q)$ for As-S, As-As, Pb-S, Pb-Pb, Pb-As and S-S atomic pairs are summarized in **Figure III. 28**. The $S_{\mathrm{ij}}(Q)$ corresponding to the glassy host (As-S, As-As and S-S) reveal typical trends for vitreous As_2S_3, in particular, a strong FSDP for the As-As and a less intense FSDP for the As-S correlations at 1.15 and 1.28 Å^{-1}, respectively.

The $S_{\mathrm{ij}}(Q)$ partials related to lead (Pb-S, Pb-Pb and Pb-As), **Figure III. 28 (b)**, do not show any strong FSDP except for a week shoulder at ≈0.8 Å^{-1} for $S_{\mathrm{PbPb}}(Q)$. However, strong principle peaks are observed at 1.64 and 1.78 Å^{-1} for Pb-Pb and Pb-As correlations, respectively, corresponding to a low-Q feature at ≈1.7 Å^{-1} in experimental neutron and X-ray results. We also note strong oscillations at high Q for $S_{\mathrm{AsS}}(Q)$, while all Pb-related partials become flat above $Q \gtrsim 8$ Å^{-1}. The observed trend is coherent with enhanced damping at high Q with increasing lead sulfide content x, observed experimentally.

The derived partial pair-distribution functions $g_{ij}(r)$ are collected in **Figure III. 29**. First, we note a distinct chemical disorder observed for glassy matrix. A small S-S NN peak at 2.05 Å and the As-As NN counterpart at 2.47 Å are clearly seen in **Figure III. 29(a)** in accordance with Raman results. The partial S-S and As-As coordination numbers are low, N_{SS} = 0.09 and N_{AsAs} = 0.16, corresponding to the chemical disorder

$$\chi = \frac{N_{AsAs}}{N_{AsAs}+N_{AsS}} \approx \frac{N_{SS}}{N_{SS}+N_{SAs}} = 4.5 \pm 0.5\ \%. \qquad \text{(III.24)}$$

As expected, the arsenic local coordination appears to be trigonal, $N_{AsX} = N_{AsAs} + N_{AsS}$ = 3.03 ± 0.03.

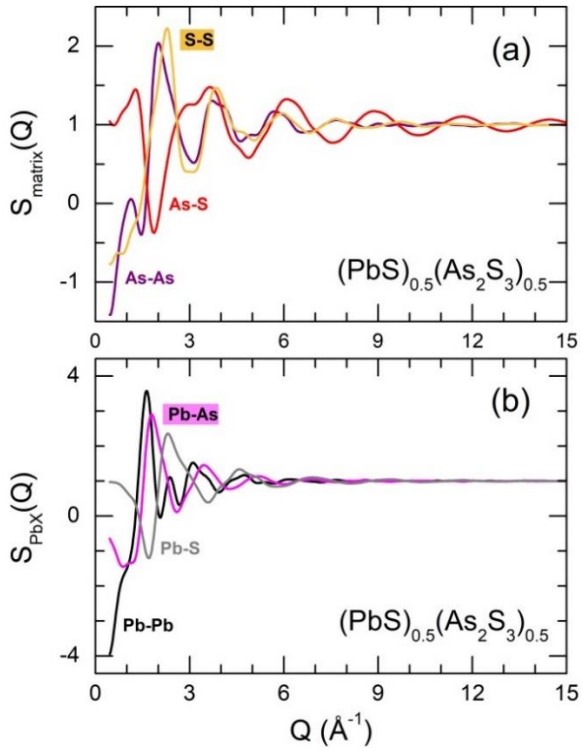

Figure III. 28 GGA/PBE0 partial structure factors $S_{ij}(Q)$ for (a) As-As, As-S and S-S atomic pairs, and (b) Pb-Pb, Pb-S and Pb-As correlations.

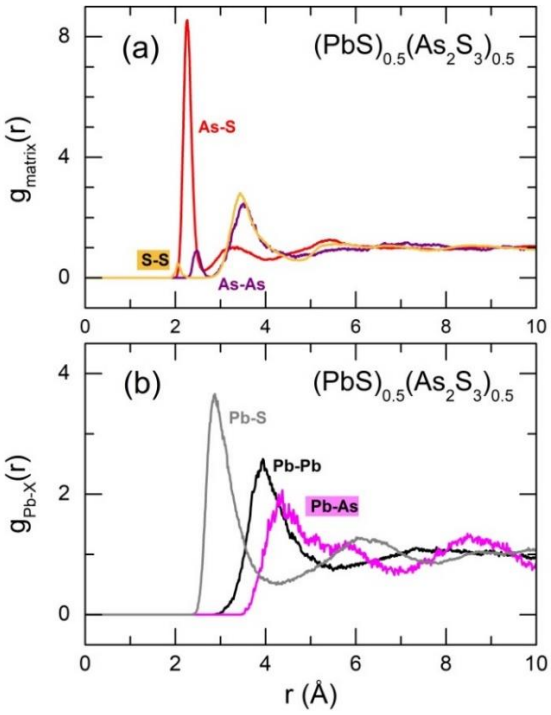

Figure III. 29 GGA/PBE0 partial pair-distribution functions $g_{ij}(r)$ for (a) As-As, As-S and S-S atomic pairs, and (b) Pb-Pb, Pb-S and Pb-As correlations.

The most difficult question is related to lead local coordination. The $g_{PbS}(r)$ partial pair distribution function appears to be broad and highly asymmetric, **Figure III. 29(b)**. The Pb-S peak maximum is centered at 2.87 Å in excellent agreement with neutron and X-ray experimental results, however, its high-r wing extends up to 4.2 Å overlapping with the second neighbor correlations.

Two approaches were used to estimate the Pb-S partial coordination in supercooled equimolar liquid. (i) A three-peak Gaussian fitting was applied to the NN feature of the $T_{\mathrm{PbS}}(r)$ partial correlation function assuming that peak 1 and peak 2 represent shorter and longer NN correlations while peak 3 is related to the short second neighbors. The results are shown in **Figure III. 30** and yield $N_{\mathrm{PbS}} \approx 7$. (ii) We have used integration of $T_{\mathrm{PbS}}(r)$ taking as a cutoff distance r_c = 3.5 Å, roughly corresponding to the maximum Pb-S separation distance in monoclinic $PbAs_2S_4$. The integrated area is shown in **Figure III. 30(b)** together with the $T_{\mathrm{PbS}}(r)$ function for the crystalline reference. The second approach gives N_{PbS} = 6. The two approaches are not unique, thus our estimation of the lead local coordination is $N_{\mathrm{PbS}} = 6 \pm 1$.

Further analysis will follow when the FPMD modeling will be completed.

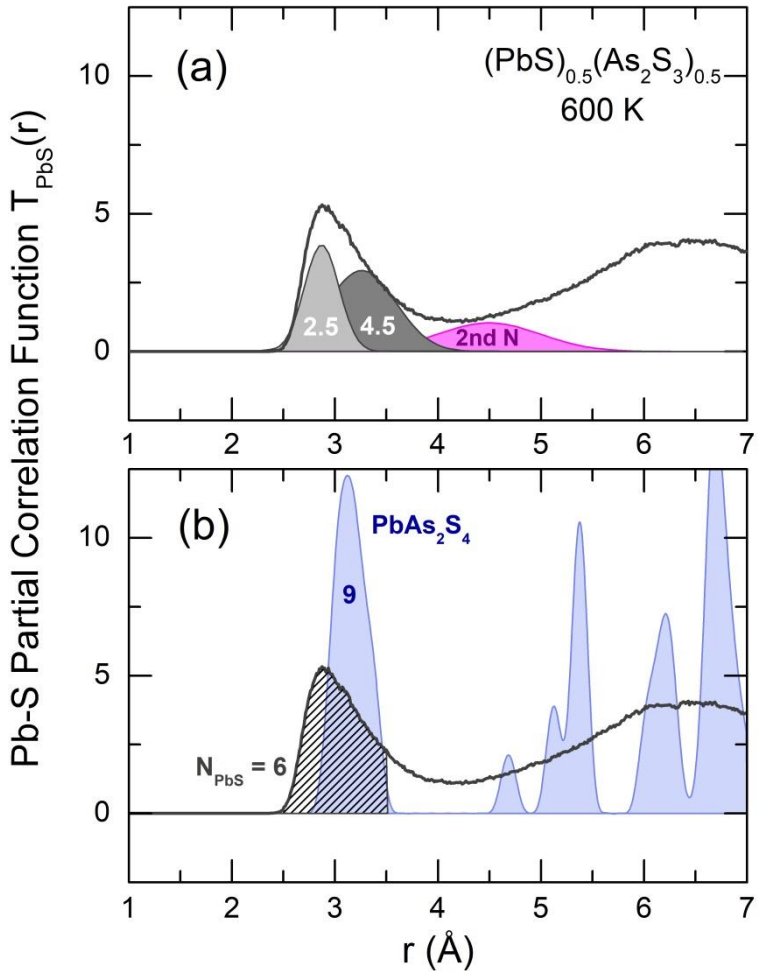

Figure III. 30 Estimation of the Pb-S local coordination number in supercooled equimolar $(PbS)_{0.5}(As_2S_3)_{0.5}$ at 600 K; (a) a three-peak Gaussian fitting of the first $T_{PbS}(r)$ feature; (b) integration of the $T_{PbS}(r)$ function taking the maximum Pb-S interatomic distance in monoclinic $PbAs_2S_4$ as a cutoff. The $T_{PbS}(r)$ partial for monoclinic $PbAs_2S_4$ is also shown. The derived coordination numbers are indicated. The second neighbor peak in (a) is highlighted in magenta.

III.6 Conclusion

Raman spectra of $(PbS)_x(As_2S_3)_{1-x}$ glasses, $0 \leq x \leq 0.5$, and crystalline references, monoclinic synthetic sartorite $PbAs_2S_4$ ($x = 0.5$) and monoclinic synthetic dufrénoysite $Pb_2As_2S_5$ ($x = 0.67$), have been studied at room temperature. The spectra of glasses basically represent a broad unresolved spectral envelope of glassy As_2S_3 with emerging and growing spectral features at 230, 300 and 370 cm^{-1}. The spectra of crystalline $PbAs_2S_4$ and $Pb_2As_2S_5$ do not exhibit the contribution of g-As_2S_3 but show similar Raman features: an asymmetric peak at 290 cm^{-1} with low-frequency shoulders and a high-frequency peak at 375 cm^{-1}.

DFT modeling of binary Pb-S and ternary As-Pb-S size limited clusters allow a reliable interpretation of the observed spectra to be carried out. The features at 230 and 300 cm^{-1} seem to be related to asymmetric and symmetric Pb-S stretching, respectively. The most intense high-frequency peak at 370 cm^{-1} is attributed to $As - S_t$ stretching, where S_t stands for terminal sulfur. The presence of this feature, accompanied by shorter $As - S_t$ bond distances, indicates that lead is acting rather as a network modifier than a network former. Similar spectroscopic high-frequency feature was earlier reported for silver and alkali thioarsenates.

Pulsed neutron and high-energy X-ray diffraction results over a large accessible Q-range with Q_{max} = 30 $Å^{-1}$ was used to study short and intermediate range order in glassy lead thioarsenates $(PbS)_x(As_2S_3)_{1-x}$, $0 \leq x \leq 0.5$. It was found that all studied compositions are fully vitreous without any Bragg peaks even for large neutron samples. Nevertheless, an enhanced small-angle neutron scattering below 0.2 $Å^{-1}$ suggests some mesoscopic inhomogeneity even for glasses with a single glass transition temperature. Lead sulfide additions do not change the trigonal arsenic coordination at a characteristic distance of 2.27 Å, however, seem to cause a host network fragmentation, visible through a systematic decrease of the first diffraction peak at ≈1.25 $Å^{-1}$ and a gradual disappearance and shift of distant correlations in r-space at ≈5.3 Å. The crystal structure of monoclinic $PbAs_2S_4$ and derived structural parameters of equimolar glass $(PbS)_{0.5}(As_2S_3)_{0.5}$ exhibit some similarities and pronounced differences. A big difference between interatomic distances involving terminal and bridging sulfur in monoclinic $PbAs_2S_4$ (r_{As-S_t} ≈ 2.12 Å, r_{As-S_b} ≈ 2.60 Å) is not confirmed for glassy thioarsenates. The high lead local coordination in $PbAs_2S_4$, N_{Pb-S} = 9 at r_{Pb-S} = 3.17 ± 0.14 Å, is not characteristic for glasses either, coherent with smaller Pb-S interatomic distances, 2.85 ± 0.02 Å. However, the

derived lead local coordination in glasses, $N_{\mathrm{Pb-S}}$ = 3.5 ± 0.5, is likely to be underestimated because of the Gaussian fitting with symmetric functions.

Preliminary FPMD modeling of equimolar supercooled $(PbS)_{0.5}(As_2S_3)_{0.5}$ liquid at 600 K has been carried out using GGA/PBE0 hybrid functional. The derived GGA/PBE0 neutron and X-ray structural factors and correlation functions in r-space appear to be in good agreement with experimental results for room-temperature glass suggesting the structural features of supercooled liquid and solid glass are rather similar. The FPMD modeling is consistent with usual conclusion that the FSDP in lead thioarsenate glasses is mostly related to the As-As intermediate range order correlations with additional contribution from the As-S pairs. The emerging new feature at $Q_{\mathrm{Pb}} \approx 1.7$ Å^{-1} is essentially related to the principle peak in $S_{\mathrm{PbPb}}(Q)$ partial with additional contribution from Pb-As correlations. The supercooled $(PbS)_{0.5}(As_2S_3)_{0.5}$ liquid exhibits small chemical disorder χ evidenced by the As-As and S-S homopolar bonds, also visible in Raman spectra of lead thioarsenate glasses. The chemical disorder is small, χ = 4.5 ± 0.5 %. The local arsenic coordination is trigonal, $N_{\mathrm{AsX}} = N_{\mathrm{AsAs}} + N_{\mathrm{AsS}}$ = 3.03 ± 0.03, consistent with known structural studies of sulfide glasses. The lead local environment appears to be strongly asymmetric and rather octahedral, N_{PbS} = 6 ± 1. Nevertheless, a further careful analysis is needed after completing FPMD simulations.

Basically, the derived neutron, X-ray structural as well as the FPMD parameters are rather emphasize a structural role of lead as a modifier than a network former.

III.7 References

[1] A. J. Lowe, S. R. Elliott, and G. N. Greaves, “Extended X-ray absorption fine-structure spectroscopy study of photostructural changes in amorphous arsenic chalcogenides,” *Philos. Mag. B*, vol. 54, no. 6, pp. 483–490, Dec. 1986.

[2] D. A. Baker, M. A. Paesler, G. Lucovsky, and P. C. Taylor, “EXAFS study of amorphous Ge2Sb2Te5,” *J. Non-Cryst. Solids*, vol. 352, no. 9, pp. 1621–1623, Jun. 2006.

[3] T. Usuki, O. Uemura, S. Konno, Y. Kameda, and M. Sakurai, “Structural and physical properties of Ag–As–Te glasses,” *J. Non-Cryst. Solids*, vol. 293–295, pp. 799–805, Nov. 2001.

[4] H. Eckert, J. H. Kennedy, A. Pradel, and M. Ribes, “Structural transformation of thiosilicate glasses: 29Si MAS-NMR evidence for edge-sharing in the system Li2S-SiS2,” *J. Non-Cryst. Solids*, vol. 113, no. 2, pp. 287–293, Dec. 1989.

[5] A. Pradel, G. Taillades, M. Ribes, and H. Eckert, “29Si NMR structural studies of ionically conductive silicon chalcogenide glasses and model compounds,” *J. Non-Cryst. Solids*, vol. 188, no. 1, pp. 75–86, Jul. 1995.

[6] M. Rubinstein and P. C. Taylor, “Nuclear quadrupole resonance in amorphous and crystalline As2S3,” *Phys. Rev. B*, vol. 9, no. 10, pp. 4258–4276, May 1974.

[7] E. Ahn, G. A. Williams, and P. C. Taylor, “Nuclear quadrupole resonance study of local bonding in glassy AsxSe1-x,” *Phys. Rev. B*, vol. 74, no. 17, p. 174206, Nov. 2006.

[8] E. Bychkov and G. Wortmann, “121-Sb Mössbauer study of insulating and ion-conducting antimony chalcogenide-based glasses,” *J. Non-Cryst. Solids*, vol. 159, no. 1, pp. 162–172, Jun. 1993.

[9] E. A. Bychkov, Yu. S. Grushko, and G. Wortmann, “129I-Mössbaurer study of superionic glasses AgI−Sb2S3: Local structure and diffusion effects,” *Hyperfine Interact.*, vol. 69, no. 1, pp. 709–712a, Apr. 1992.

[10] J. Sun *et al.*, “Structural investigation of Te-based chalcogenide glasses using Raman spectroscopy,” *Infrared Phys. Technol.*, vol. 55, no. 4, pp. 316–319, Jul. 2012.

[11] T. S. Kavetskyy, “Radiation-induced structural changes in chalcogenide glasses as revealed from Raman spectroscopy measurements,” 2013, Accessed: Jun. 10, 2021.

[12] G. J. Cuello, A. A. Piarristeguy, A. Fernández-Martínez, M. Fontana, and A. Pradel, “Structure of chalcogenide glasses by neutron diffraction,” *J. Non-Cryst. Solids*, vol. 353, no. 8, pp. 729–732, Apr. 2007.

[13] D. L. Price, S. Susman, and A. C. Wright, “Probing medium-range order in chalcogenide glasses by neutron scattering and optical spectroscopy,” *J. Non-Cryst. Solids*, vol. 97–98, pp. 167–170, Dec. 1987.

[14] S. Sen, S. S. Uzun, C. J. Benmore, and B. G. Aitken, “Structure, topology and chemical order in Ge–As–Te glasses: a high-energy x-ray diffraction study,” *J. Phys. Condens. Matter*, vol. 22, no. 40, p. 405401, Sep. 2010.

[15] S. Neov *et al.*, “Neutron diffraction study on the medium and short-range order of ternary chalcogenide glasses,” *J. Mater. Sci.*, vol. 34, no. 15, pp. 3669–3676, Aug. 1999.

[16] C. V. Raman and K. S. Krishnan, “A New Type of Secondary Radiation,” *Nature*, vol. 121, no. 3048, Art. no. 3048, Mar. 1928.

[17] L. McAfee, “Infrared and Raman spectra of inorganic and coordination compounds. Part A: theory and applications in inorganic chemistry; Part B: application in coordination, organometallic, and bioinorganic chemistry, (Nakamoto, Kazuo).,” *J. Chem. Educ.*, vol. 77, no. 9, p. 1122, 2000.

[18] “Introduction, Basic Theory and Principles,” in *Modern Raman Spectroscopy*, John Wiley & Sons, Ltd, 2019, pp. 1–20.

[19] M. Kassem, S. Khaoulani, A. Cuisset, D. L. Coq, P. Masselin, and E. Bychkov, “Mercury thioarsenate glasses: a hybrid chain/pyramidal network,” *RSC Adv.*, vol. 4, no. 90, pp. 49236–49246, Oct. 2014.

[20] M. Kassem *et al.*, “Bent HgI2 Molecules in the Melt and Sulfide Glasses: Implications for Nonlinear Optics,” *Chem. Mater.*, vol. 31, no. 11, pp. 4103–4112, Jun. 2019.

[21] H. E. Fischer, A. C. Barnes, and P. S. Salmon, “Neutron and x-ray diffraction studies of liquids and glasses,” *Rep. Prog. Phys.*, vol. 69, no. 1, pp. 233–299, 2006.

[22] B. Kamitakahara, “A New Neutron Imaging Facility at BT-6 for the Non-Destructive Analysis of Working Fuel Cells.”

[23] Y. Waseda, “The Structure of Non-Crystalline Materials: liquids and amorphous solids.,” *N. Y. Lond. McGraw-Hill Int. Book Co*, 1980.

[24] T. E. Faber and J. M. Ziman, “A theory of the electrical properties of liquid metals,” *Philos. Mag. J. Theor. Exp. Appl. Phys.*, vol. 11, no. 109, pp. 153–173, Jan. 1965.

[25] D. Waasmaier and A. Kirfel, “New analytical scattering-factor functions for free atoms and ions,” *Acta Crystallogr. A*, vol. 51, no. 3, Art. no. 3, May 1995.

[26] V. F. Sears, “Neutron scattering lengths and cross sections,” *Neutron News*, vol. 3, no. 3, pp. 26–37, Jan. 1992.

[27] C. Finbak, *Acta Chem Scand*, vol. 3, no. 10, pp. 1279–1292, 1949.

[28] E. Lorch, “Neutron diffraction by germania, silica and radiation-damaged silica glasses,” *J. Phys. C: Solid State Phys.*, vol. 2, no. 2, p. 229, Feb. 1969.

[29] S. Susman, K. J. Volin, D. G. Montague, and D. L. Price, “The structure of vitreous and liquid GeSe2: a neutron diffraction study,” *J. Non-Cryst. Solids*, vol. 125, no. 1, pp. 168–180, Nov. 1990.

[30] J. H. Lee, A. P. Owens, A. Pradel, A. C. Hannon, M. Ribes, and S. R. Elliott, “Structure determination of Ag-Ge-S glasses using neutron diffraction,” *Phys. Rev. B*, vol. 54, no. 6, pp. 3895–3909, Aug. 1996.

[31] C. N. J. Wagner, *J Non-Cryst Solids*, vol. 179, 1994.

[32] B. E. Warren and R. L. Mozzi, “Multiple scattering of X-rays by amorphous samples,” *Acta Crystallogr.*, vol. 21, no. 4, Art. no. 4, Oct. 1966.

[33] H. H. M. Balyuzi, “Analytic approximation to incoherently scattered X-ray intensities,” *Acta Crystallogr. A*, vol. 31, no. 5, Art. no. 5, Sep. 1975.

[34] G. L. Squires, *Introduction to the Theory of Thermal Neutron Scattering*. Courier Corporation, 1996.

[35] A. K. Soper, “Rutherford Appleton Laboratory Technical Report.,” RAL-TR-2011-013, Tech.rep, 2011.

[36] A. C. Hannon, W. S. Howells, and A. K. Soper, “ATLAS : A Suite of Programs for the Analysis of Time-of-flight Neutron Diffraction Data from Liquid and Amorphous Samples,” *Inst Phys Conf Ser*, no. 107, pp. 193–211, 1990.

[37] N. Argaman and G. Makov, “Density functional theory: An introduction,” *Am. J. Phys.*, vol. 68, no. 1, pp. 69–79, Jan. 2000.

[38] M. Born and R. Oppenheimer, “Zur Quantentheorie der Molekeln,” *Ann. Phys.*, vol. 389, no. 20, pp. 457–484, 1927.

[39] P. Hohenberg and W. Kohn, “Inhomogeneous Electron Gas,” *Phys. Rev.*, vol. 136, no. 3B, pp. B864–B871, Nov. 1964.

[40] W. Kohn and L. J. Sham, “Self-Consistent Equations Including Exchange and Correlation Effects,” *Phys. Rev.*, vol. 140, no. 4A, pp. A1133–A1138, Nov. 1965.

[41] J. P. Perdew, K. Burke, and M. Ernzerhof, “Generalized Gradient Approximation Made Simple,” *Phys. Rev. Lett.*, vol. 77, no. 18, pp. 3865–3868, Oct. 1996.

[42] J. P. Perdew, K. Burke, and M. Ernzerhof, “Perdew, Burke, and Ernzerhof Reply:,” *Phys. Rev. Lett.*, vol. 80, no. 4, pp. 891–891, Jan. 1998.

[43] J. P. Perdew *et al.*, “Atoms, molecules, solids, and surfaces: Applications of the generalized gradient approximation for exchange and correlation,” *Phys. Rev. B*, vol. 46, no. 11, pp. 6671–6687, Sep. 1992.

[44] J. P. Perdew *et al.*, “Restoring the Density-Gradient Expansion for Exchange in Solids and Surfaces,” *Phys. Rev. Lett.*, vol. 100, no. 13, p. 136406, Apr. 2008.

[45] F. Neese, “A critical evaluation of DFT, including time-dependent DFT, applied to bioinorganic chemistry,” *JBIC J. Biol. Inorg. Chem.*, vol. 11, no. 6, pp. 702–711, Sep. 2006.

[46] M. Orio, D. A. Pantazis, and F. Neese, “Density functional theory,” *Photosynth. Res.*, vol. 102, no. 2, pp. 443–453, Dec. 2009.

[47] M. J. Frisch *et al.*, Gaussian 16, Revision B.01, aussian, Inc., Wallingford CT., 2016.

[48] P. Nachtigall and J. Sauer, “Applications of quantum chemical methods in zeolite science, in Introduction to zeolite science and practice, 3rd edition,” *Elsevier Amst.*, 2007.

[49] A. D. Becke, “Density-functional thermochemistry. III. The role of exact exchange.,” *J. Chem. Phys.*, vol. 98, no. 7, pp. 5648–5653, 1993.

[50] C. Lee, W. Yang, and R. G. Parr, “Development of the Colle-Salvetti correlation-energy formula into a functional of the electron density.,” *Phys Rev B Condens Matter Mater Phys*, vol. 37, pp. 785–789, 1988.

[51] D. Feller, “The role of databases in support of computational chemistry calculations,” *J. Comput. Chem.*, vol. 17, no. 13, pp. 1571–1586, 1996.

[52] K. A. Peterson, D. Figgen, E. Goll, H. Stoll, and M. Dolg, “Systematically convergent basis sets with relativistic pseudopotentials. II. Small-core pseudopotentials and correlation consistent basis sets for the post-d group 16–18 elements,” *J. Chem. Phys.*, vol. 119, no. 21, pp. 11113–11123, Dec. 2003.

[53] M. Celino *et al.*, “First-principles molecular dynamics study of glassy GeS2: Atomic structure and bonding properties,” *Phys. Rev. B*, vol. 88, no. 17, p. 174201, Nov. 2013.

[54] A. Bouzid, C. Massobrio, M. Boero, G. Ori, K. Sykina, and E. Furet, “Role of the van der Waals interactions and impact of the exchange-correlation functional in determining the structure of glassy GeTe4,” *Phys. Rev. B*, vol. 92, no. 13, p. 134208, Oct. 2015.

[55] A. Kyono, “Ab initio quantum chemical investigation of arsenic sulfide molecular diversity from As4S6 and As4,” *Phys. Chem. Miner.*, vol. 40, no. 9, pp. 717–731, Oct. 2013.

[56] J. Hutter, M. Iannuzzi, F. Schiffmann, and J. VandeVondele, “cp2k: atomistic simulations of condensed matter systems,” *WIREs Comput. Mol. Sci.*, vol. 4, no. 1, pp. 15–25, 2014.

[57] J. P. Perdew, M. Ernzerhof, and K. Burke, “Rationale for mixing exact exchange with density functional approximations,” *J. Chem. Phys.*, vol. 105, no. 22, pp. 9982–9985, Dec. 1996.

[58] C. Adamo and V. Barone, “Toward reliable density functional methods without adjustable parameters: The PBE0 model,” *J. Chem. Phys.*, vol. 110, no. 13, pp. 6158–6170, Apr. 1999.

[59] R. Zaiter, “Silver and/or mercury doped thioarsenate and thiogermanate glasses : Transport, structure and ionic sensibility,” phdthesis, Université du Littoral Côte d’Opale, 2018. Accessed: Jan. 14, 2020.

[60] M. Kassem *et al.*, “Chemical and Structural Variety in Sodium Thioarsenate Glasses Studied by Neutron Diffraction and Supported by First-Principles Simulations,” *Inorg. Chem.*, vol. 59, no. 22, pp. 16410–16420, Nov. 2020.

[61] O. Gereben, P. Jovari, L. Temleitner, and L. Pusztai, “A new version of the RMC++ Reverse Monte Carlo programme, aimed at investigating the structure of covalent glasses.,” *J. Optoelectron. Adv. Mater.*, vol. 9, no. 10, pp. 3021–3027, 2007.

[62] O. Gereben and L. Pusztai, “RMC_POT: A computer code for reverse monte carlo modeling the structure of disordered systems containing molecules of arbitrary complexity,” *J. Comput. Chem.*, vol. 33, no. 29, pp. 2285–2291, 2012.

[63] J. VandeVondele and J. Hutter, “Gaussian basis sets for accurate calculations on molecular systems in gas and condensed phases,” *J. Chem. Phys.*, vol. 127, no. 11, p. 114105, Sep. 2007.

[64] F. Weigend and R. Ahlrichs, “Balanced basis sets of split valence, triple zeta valence and quadruple zeta valence quality for H to Rn: Design and assessment of accuracy,” *Phys. Chem. Chem. Phys.*, vol. 7, no. 18, pp. 3297–3305, Aug. 2005.

[65] S. Goedecker, M. Teter, and J. Hutter, “Separable dual-space Gaussian pseudopotentials,” *Phys. Rev. B*, vol. 54, no. 3, pp. 1703–1710, Jul. 1996.

[66] E. Bychkov, M. Miloshova, D. L. Price, C. J. Benmore, and A. Lorriaux, “Short, intermediate and mesoscopic range order in sulfur-rich binary glasses,” *J. Non-Cryst. Solids*, vol. 352, no. 1, pp. 63–70, Jan. 2006.

[67] A. T. Ward, “Raman spectroscopy of sulfur, sulfur-selenium, and sulfur-arsenic mixtures,” *J. Phys. Chem.*, vol. 72, no. 12, pp. 4133–4139, 1968.

[68] E. I. Kamitsos, J. A. Kapoutsis, I. P. Culeac, and M. S. Iovu, “Structure and Bonding in As−Sb−S Chalcogenide Glasses by Infrared Reflectance Spectroscopy,” *J. Phys. Chem. B*, vol. 101, no. 51, pp. 11061–11067, Dec. 1997.

[69] T. Wágner, S. O. Kasap, M. Vlček, A. Sklenář, and A. Stronski, “The structure of AsxS100−x glasses studied by temperature-modulated differential scanning calorimetry and Raman spectroscopy,” *J. Non-Cryst. Solids*, vol. 227–230, pp. 752–756, May 1998.

[70] P. Chen, C. Holbrook, P. Boolchand, D. G. Georgiev, K. A. Jackson, and M. Micoulaut, “Intermediate phase, network demixing, boson and floppy modes, and compositional trends in glass transition temperatures of binary AsxS1−xsystem,” *Phys. Rev. B*, vol. 78, no. 22, p. 224208, Dec. 2008.

[71] G. Lucovsky, “Optic Modes in Amorphous As2S3 and As2 Se3,” *Phys. Rev. B*, vol. 6, no. 4, pp. 1480–1489, Aug. 1972.

[72] M. Frumar, A. P. Firth, and A. E. Owen, “A model for photostructural changes in the amorphous As-S system,” *J. Non-Cryst. Solids*, vol. 59–60, pp. 921–924, Dec. 1983.

[73] K. Shimakawa, A. Kolobov, and S. R. Elliott, “Photoinduced effects and metastability in amorphous semiconductors and insulators,” *Adv. Phys.*, vol. 44, no. 6, pp. 475–588, Dec. 1995.

[74] F. Kyriazis and S. N. Yannopoulos, “Colossal photostructural changes in chalcogenide glasses: Athermal photoinduced polymerization in AsxS100−x bulk glasses revealed by near-bandgap Raman scattering,” *Appl. Phys. Lett.*, vol. 94, no. 10, p. 101901, Mar. 2009.

[75] S. Kharbish, “Micro-Raman spectroscopic investigations of extremely scarce Pb–As sulfosalt minerals: baumhauerite, dufrénoysite, gratonite, sartorite, and seligmannite,” *J. Raman Spectrosc.*, vol. 47, no. 11, pp. 1360–1366, 2016.

[76] G. D. Smith, S. Firth, R. J. H. Clark, and M. Cardona, “First- and second-order Raman spectra of galena (PbS),” *J. Appl. Phys.*, vol. 92, no. 8, pp. 4375–4380, Oct. 2002.

[77] P. G. Etchegoin, M. Cardona, R. Lauck, R. J. H. Clark, J. Serrano, and A. H. Romero, “Temperature-dependent Raman scattering of natural and isotopically substituted PbS,” *Phys. Status Solidi B*, vol. 245, no. 6, pp. 1125–1132, 2008.

[78] Y. Iitaka and W. Nowacki, “A refinement of the pseudo crystal structure of scleroclase PbAs2S4,” *Acta Crystallogr.*, vol. 14, no. 12, Art. no. 12, Dec. 1961.

[79] R. Boidin, “Etude des propriétés de conduction et structurales des verres du système HgI_2-Ag_2S-As_2S_3 : application en tant que capteur chimique,” These de doctorat, Littoral, 2013. Accessed: Jun. 23, 2021.

[80] E. I. Kamitsos, J. A. Kapoutsis, G. D. Chryssikos, G. Taillades, A. Pradel, and M. Ribes, “Structure and Optical Conductivity of Silver Thiogermanate Glasses,” *J. Solid State Chem.*, vol. 112, no. 2, pp. 255–261, Oct. 1994.

[81] C. Rau *et al.*, “Mixed cation effect in chalcogenide glasses Rb2S-Ag2S-GeS2,” *Phys. Rev. B - Condens. Matter Mater. Phys.*, vol. 63, pp. 1842041–1842049, Jan. 2001.

[82] E. Bychkov, C. J. Benmore, and D. L. Price, “Compositional changes of the first sharp diffraction peak in binary selenide glasses,” *Phys. Rev. B*, vol. 72, no. 17, p. 172107, Nov. 2005.

[83] A. Bytchkov, G. J. Cuello, S. Kohara, C. J. Benmore, D. L. Price, and E. Bychkov, “Unraveling the atomic structure of Ge-rich sulfide glasses,” *Phys. Chem. Chem. Phys.*, vol. 15, no. 22, pp. 8487–8494, May 2013.

[84] W. Zhou, D. E. Sayers, M. A. Paesler, B. Bouchet-Fabre, Q. Ma, and D. Raoux, “Structure and photoinduced structural changes in a-As2S3 films: A study by differential anomalous x-ray scattering,” *Phys. Rev. B*, vol. 47, no. 2, pp. 686–694, Jan. 1993.

[85] S. C. Moss and D. L. Price, “Random Packing of Structural Units and the First Sharp Diffraction Peak in Glasses,” in *Physics of Disordered Materials*, D. Adler, H. Fritzsche, and S. R. Ovshinsky, Eds. Boston, MA: Springer US, 1985, pp. 77–95.

[86] S. R. Elliott, “Medium-range structural order in covalent amorphous solids,” *Nature*, vol. 354, no. 6353, pp. 445–452, Dec. 1991.

[87] P. S. Salmon, “Real space manifestation of the first sharp diffraction peak in the structure factor of liquid and glassy materials,” *Proc. R. Soc. Lond. Ser. Math. Phys. Sci.*, vol. 445, no. 1924, pp. 351–365, May 1994.

[88] M. Kassem *et al.*, “Mercury Sulfide Dimorphism in Thioarsenate Glasses,” *J. Phys. Chem. B*, vol. 120, no. 23, pp. 5278–5290, Jun. 2016.

[89] D. J. E. Mullen and W. Nowacki, “Refinement of the crystal structures of realgar, AsS and orpiment, As2S3,” *Z. Für Krist. - Cryst. Mater.*, vol. 136, no. 1–6, pp. 48–65, Dec. 1972.

[90] A. R. Kampf, R. T. Downs, R. M. Housley, R. A. Jenkins, and J. Hyršl, “Anorpiment, As2S3, the triclinic dimorph of orpiment,” *Mineral. Mag.*, vol. 75, no. 6, pp. 2857–2867, Dec. 2011.

[91] A. C. Hannon, *XTAL: a program for calculating interatomic distances and coordination numbers for model structures*. 1993.

Chapter IV: Development of Pb^{2+} chemical sensors based on chalcogenide glasses

IV.1 Introduction

After having studied, in the previous chapter, the macroscopic, transport and structural properties of the lead containing glasses, we conclude with a study of the application of these glasses as ionic membranes in chemical sensors. In our case, the lead sensors are designed to work in an aqueous environment. Therefore, as a first step, it is interesting to understand the chemistry of lead in water as well as the techniques employed in its detection. In this regards, a bibliographic study of the techniques that have been used for the detection and the determination of lead quantity in water is made in order to understand the advantages and disadvantages of each technique. Finally, after some reminders of the principles of the potentiometric methods, we will present (for the fabricated sensors based on selected AgI-PbS-As_2S_3 glasses) the obtained results related to the evaluation of the different glass compositions as active membranes in Pb(II)–ISE, including detection limit, sensitivity, linearity, ionic selectivity (in the presence of K^+, Na^+, Ni^{2+}, Ca^{2+}, Cd^{2+}, Cu^{2+} and Hg^{2+} interfering cations), reproducibility and optimal pH-range.

IV.2 Bibliography

IV.2.1 Chemical and physical properties of lead

Lead is one of more than 100 elements that make up the earth. In fact, it is known by the alchemists to be one of the first elements ever mined. Indeed, the chemical symbol and name of lead originate from the Roman word "*plumbum*" as do the modern words "*plumbing*" and "*plumber*" [1]. Lead, Pb, is a chemical element with the atomic number 82 and a member of group 14 (IV A) of the periodic table. It is a soft, silvery white or grayish heavy metal. Its close-packed face centered cubic structure and high atomic weight result in a relatively high density [2]. Metallic lead is malleable and ductile. It has low tensile strength and is a poor conductor of electricity [3], [4]. It is corrosion resistant. Even in powder form, lead has decreased reactivity by forming a thin protective layer of insoluble compounds, such as oxides, sulfates or oxycarbonates. It is hardened by alloying it with small amounts of arsenic, copper, antimony, or other metals. These alloys are frequently used in the manufacture of various products containing lead [5]. Lead exists in three oxidation states [6]: Pb(0), Pb(II), and Pb(IV). It is rare for lead to occur in nature in its elemental or pure form. The most common lead mineral is the galena (lead sulfide PbS), but sometimes it is found in other mineral forms, which are of lesser

commercial importance, such as anglesite (lead sulfate $PbSO_4$) and cerussite (lead carbonate $PbCO_3$).

Inorganic Pb(II) complexes are known for their low solubility (**Table IV. 1**) [2], [7]. In this regard, for example, lead chloride is considered as moderately soluble while lead nitrate and lead acetate are reasonably soluble [6]. This low solubility has a profound effect on both environmental and biological chemistry of lead. In its native form as ores in the environment, e. g., galena PbS, lead tends to be extremely insoluble. It is interesting to speculate that this insolubility may play an important role in the susceptibility of living organisms to lead poisoning. Although lead is relatively abundant compared to other existing heavy metals, with an average abundance of ~20 ppm in the earth's crust, most naturally occurring lead compounds are highly insoluble that most biological systems (including people) have been exposed to a relatively little amount of lead on an evolutionarily relevant timescale.

Table IV. 1 Solubility of Common Inorganic and Organic Complexes of Pb(II) [6].

Chemical formula	Solubility (g/100 cm^3 of cold H_2O)	Ksp (25°C)
$Pb(C_2H_3O_2)_2$	44.3	
$Pb(NO_3)_2$	37.56	
$PbCl_2$		1.70×10^{-5}
$Pb(SCN)_2$		2.11×10^{-5}
$PbBr_2$		6.6×10^{-6}
$PbSeO_4$		1.37×10^{-7}
PbF_2		3.3×10^{-8}
$PbSO_4$		2.53×10^{-8}
PbI_2		9.8×10^{-9}
PbC_2O_4		8.5×10^{-10}
$PbCrO_4$		2.8×10^{-13}
$Pb(IO_3)_2$		3.69×10^{-13}
$PbCO_3$		7.4×10^{-14}
$Pb(OH)_2$		1.40×10^{-20}
PbS		8.81×10^{-29}
$Pb_3(PO_4)_2$		1×10^{-54}

- **Stability of lead compounds in water**

The potential-pH diagram of lead (also known as the Pourbaix diagram) is presented in **Figure IV. 1** [8]. This diagram shows that metallic lead, usually stable in presence of aqueous solutions free of oxidants, can be dissolved in oxidizing acid solutions with the resulting formation of divalent plumbous ions Pb^{2+}. A very strong oxidizing action may transform these Pb^{2+} ions directly into the brown tetravalent lead peroxide PbO_2 which is insoluble in neutral or moderately acid solutions, slightly soluble in strongly acid solutions with the resulting formation of plumbic ions Pb^{4+}, and very soluble in strongly alkaline solutions with the resulting formation of plumbate ions PbO_3^{2-}. Both PbO and $Pb(OH)_2$ dissolve in acid solutions with formation of Pb^{2+} ion and in alkaline solutions with formation of biplumbite ion $HPbO_2^-$ and, to a lesser extent, plumbite PbO_2^{2-}.

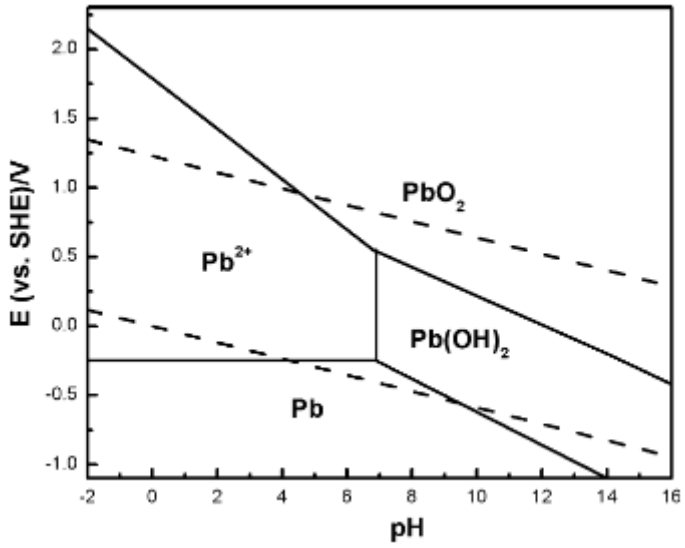

Figure IV. 1 Pourbaix diagram of Pb species.

IV.2.2 Sources and uses of lead throughout history

Although lead contamination occurs naturally due to volcanic eruptions and forest fires, anthropogenic emissions of lead remain the main sources of lead contamination (**Table IV. 2)** [9]. Lead is one of the seven metals of antiquity. It has been used from very early times where it had a very economical value and was produced in high amounts [3], [10]. It was present in all the metal ages and played a significant role in the development of mankind. Because of its softness, low melting temperature (327.5°C), its high density and its relatively low conductivity [11], it was relatively simple for early humans to manipulate lead into a wide variety of objects, ranging from axes to coins to tumblers and figurines. Since it is a major component in alloys

such as bronze (~ 5-30% Pb), it was also figured in the development of the Bronze Age ($\sim 3000 - 1000$ B.C). Consequently, lead emissions increased from 160 tons/year to 10,000 tons/ about 2700 years ago [12]. During the Roman Empire about 2000 years ago, where lead was referred to as the "Roman metal", lead was used in a wide range of applications such as pipes, drinking vessels, coffins, statues and coins [13]. Thus, the production of lead underwent a further increase where it topped out at 50,000-80,000 tons/year [12], [14]. Galena, an essential compound for the production of lead and silver, was used in Egypt as eye paint and in the manufacture of lead glazes and glasses as well as for medicinal purposes in Greece and Rome and as make-up in China [3].

Table IV. 2 Lead emission from natural and anthropogenic sources [9].

	Lead sources	Emission, thousand t/year (%)
Natural	Soil particles transport by wind	0.3-7.5
	Marine aerosols	0-2.8
	Volcanoes	0.5-6.0
	Forest fires	0.1-3.8
	Biogenic processes	0-3.4
	Total	0.9-23.5 (0.3-5.9)
Anthropogenic	Combustion:	
	Coal	1.8-14.6
	Mineral oil	0.9-3.9
	Gasoline	248
	Wood	1.2-3.0
	Metallurgy	30.1-69.6
	Wood industry	5.1-33.8
	Garbage burning	1.6-3.1
	Total	288.7-376.0 (94.1-99.7)

The anthropogenic emissions of lead increased again dramatically during the industrial revolution and have continued to rise in the 20th century. During those times, one of the largest contributions to lead emissions came from the use of the Pb (IV) (e.g., tetraethyllead (TEL)) as an anti-knocking agent in gasoline [15]. In modern times, new and important applications of lead have developed. It was used in batteries, building materials, paint, soldering, wire and

cable insulation and jacketing, ammunitions, as stiffener in candle wicks, in radiation shields and as pigments [6], [16]–[18].

Commercial lead metal is described as being either primary or secondary. Primary lead is produced directly from mined lead ore while secondary lead is produced from scrap lead products which have been recycled. In fact, in addition to the most common lead ore galena, lead bullions contain other elements such as zinc, silver, arsenic, gold, etc., that must be separated in a subsequent refining process [19]. After 20th century mining production has undergone a slow but steady decline, this is due to the fact that recycling has increased and thus, about 50% of the lead produced in the world in 2000 was obtained from recycled scrap lead products [20]. Secondary lead production is now significant in many countries, but mostly in the highly industrialized countries [21]. Indeed, the geographical distribution of lead production has changed worldwide during the past years. It showed a slight decrease in Europe, America, and Africa while it has increased in Asia [22], [23].

Table IV. 3. Trends in uses of lead in selected countries[a] [24], [25].

Use	Percentage of total use in year			
	1985	1990	1996	2001
Batteries	57.7	63.0	72.5	76.7
Cable sheathing	5.6	4.5	2.1	1.4
Rolled and extruded products[b]	7.6	7.7	5.9	6.0
Shot/ammunition	2.8	2.8	2.3	2.1
Alloys	4.2	3.3	3.2	2.5
Pigments and others compounds	14.2	12.8	10.0	8.1
Gasoline additives	3.7	2.1	0.9	0.4
Miscellaneous	4.2	3.8	3.3	2.8

[a] Countries include: Australia, Austria, Belgium, Brazil, Canada, China (Hong Kong Special Administrative Region), China (Province of Taiwan), Denmark, Finland, France, Germany, India, Indonesia, Italy, Japan, Malaysia, Mexico, Netherlands, New Zealand, Norway, Philippines, Republic of Korea, Singapore, South Africa, Spain, Sweden, Switzerland, United Kingdom and USA

[b] Including lead sheet

Table IV. 3 shows the total lead consumption by major use category in selected countries between 1985 and 2001 [24], [25]. By far the world's largest single lead application is in lead-acid batteries. Since 1960 the manufacture of lead–acid batteries had remained the largest single use of lead in almost all countries, representing an ever-increasing percentage of total lead consumption [26]. Extruded lead is also widely used. In fact, the manufacture of lead sheets is

the second most important use of metallic lead after batteries. Most lead sheets are used in buildings and construction industry, where typical applications are flashings and weathering, complete roofing systems and vertical wall cladding. The characteristics of lead sheets, such as durability, recyclable nature, low maintenance and low energy requirement for conversion make this material very useful compared to other more expensive alternatives.

IV.2.3 Toxicities of lead

The toxicity effects of lead were known to the ancients, but only recently, scientists have started to make methodical studies of the overall toxicity of this heavy metal. In **Table IV. 4** the norms concerning certain heavy metals in industrial atmospheric emissions in France and the European Union are presented [27]. Lead is found in the third group and graded among the very toxic elements. Its concentration limit is estimated at 1 $mg.Nm^{-3}$.

Table IV. 4 Heavy metal limit concentrations in industrial air emissions in France and the European Union [27].

Group number	Elements	Flow limit to start the control ($g.h^{-1}$)	Flow limit for in situ control ($g.h^{-1}$)	Concentration limit ($mg.Nm^{-3}$)
1	Cd, Hg, Tl	1	10 (Cd + Hg)	0.05 per metal 0.1 for the whole group 1
2	As, Se, Te	5	50	1
3	Pb	10	100	1
4	Sb, Cr, Co, Cu, Sn, Mn, Ni, V	25	500	5

Since it cannot be degraded by microbial activities, lead is considered as an environmentally persistent toxin, which has accumulated upward the food chain. Once taken into the body, lead can circulate throughout the body in the blood and accumulate in the bones and soft tissues leading to chronic toxicity. Growing evidence supports the premise that there is no threshold for harmful effects from the lead exposure [28], [29]. Depending on the level of exposure, lead can cause neurological [30], [31], renal [32], hepatic [33], hematological, circulatory, immunological, reproductive, developmental [34], [35], auditory [36], gastrointestinal, and cardiovascular pathologies [37]. In general, lead harms children more than adults. Infants and

young children are more sensitive to lower lead levels than adults, they show neurological effects contributing to lowered intelligence quotient (IQ) [38], [29], [39], learning deficits, cognitive deficits [40], [41], lower vocabulary and grammatical-reasoning ability [42], poorer hand-eye coordination [42], longer reaction time, deficits in psychological and classroom performance [43], hyperactivity and behavioral problems [44].

The reason for the high level of lead poisoning in children may be due to the facts that lead is efficiently absorbed and retained and the blood-brain barrier is not fully developed in very young children [45], [46]. High bone lead levels are associated with an increased risk of somatic complaints, social problems, attention problems, anxiety /depression, as well as aggressive and delinquent behaviors among children [47]. In addition, chronic occupational exposure to lead was shown to increase the risk of Parkinson's disease [48]. Chronic exposure to lead can also lead to tooth loss and damages to hard dental tissue [49]. Furthermore, lead can cross the placental barrier, which affects the development of the fetus, especially the developing baby's nervous system. Lead may also cause stillbirths and abortion. Polluted ecosystems cause losses in biodiversity, alteration in community components, decreased pollen germination and seed viability, and reduced growth and reproduction rates in plants and animals [50]–[53].

IV.2.4 Chemical and physio-chemical methods for the analysis of lead

Currently, there are a number of analytical techniques, by which the elemental composition of a heavy metal is determined, based on spectroscopic and colorimetric methods, biosensors and electrochemical analysis. Usually, to detect and determine the trace of heavy metals in water, the water samples are taken on site after a minimum of 6 hours of stagnation and then transported to a certified central laboratory in order to be tested.

The spectroscopic methods

The very often used analytical methods to determine the lead content in aqueous solutions are spectroscopic methods including atomic absorption spectroscopy (AAS), atomic emission spectroscopy (AES), and X-ray fluorescence (XRF), inductively coupled plasma mass spectrometry (ICP-MS).

AAS is based on the atomization of an aqueous sample in a flame or graphite furnace and the absorbance of light by the metal ions in the sample. AAS allows the analysis of only one element at a time and solid samples should be digested in the aqueous solution before analysis. AES uses high temperature plasma, flame or spark to excite elements in an aqueous sample to

an upper particular electronic state and observes the light emitted as it returns to the ground state in order to determine the quantity of an element in a sample. XRF involves using X-rays to cause excitation of inner shell electrons to high energy levels before decaying down and releasing energy in form of fluorescence [54]. ICP-MS is a technique for determining low concentrations (range: parts per billion, ppb) and ultra-low concentrations of elements (range: parts per trillion, ppt). Atomic elements are conducted through a plasma source where they become ionized. Then these ions are sorted according to their mass.

The aforementioned laboratory techniques offer very good sensitivity and limit of detection that can detect lead levels up to part per billion (ppb). However, in addition to the expensive, sophisticated, and bulky instrumentation required, trained personnel are needed to operate the instruments and perform the testing. These techniques are limited to laboratory testing on already prepared samples. Therefore, using these techniques for a large-scale determination of heavy metals can be very costly, time consuming, and labor intensive. Although there are portable XRF instruments, their detection limits are not appropriate for trace-level detection.

The colorimetric methods

A colorimetric method is based on spectrophotometry. It determines the presence and concentration of a chemical element or a chemical compound in a solution using a colored reagent. Depending on the level of precision required, the colorimetric results are analyzed using a spectrophotometer [55]. The main reagents available for the spectrophotometric or colorimetric determination of Pb metal are dithiazone, diethyldithiocarbamate, diphenylcarbazone, and porphyrin compounds. Although each chromogenic system has its advantages and disadvantages with respect to sensitivity, selectivity and stability most of them require extraction using organic solvents, surfactants, or cyanide to increase the sensitivity or selectivity [56]. Recently a renewed interest in detecting heavy metal ions using the colorimetric method has emerged using functionalized metal nanoparticles. Adding nanoparticles such as silica, polystyrene, alumina, gold avoid the aggregation and precipitation of lead sulfide and consequently enables sensitive and reliable detection of lead by using spectrophotometric or colorimetric methods [57]–[60]. This method is based on forming a very stable and dispersible PbS solution by reacting lead with sulfide ions in the presence of stabilizing nanoparticles. A colorimetric method enhanced with non-precious-metal nanoparticles for determining lead ions in water demonstrates that it can accurately measure lead concentration in the range of 0.5-500 ppm [61] where the test produces a visible color change in the solution if the lead sulfide concentration is ≥ 0.5 ppm. Another colorimetric method based on metal induced aggregation

of N-decanoyltromethamine capped gold nanoparticles has been developed [62] shows that the addition of toxic metal Pb^{2+} to NDTM-AuNPs alters the color from pink to violet due to aggregation. The detection limit was found to be at 10 μM by naked eye and 0.35 μM by spectrophotometry.

Biosensors

Biosensors, based on microorganisms, enzymes, microspheres, and nanomaterials, have been developed to detect heavy metals [63], [64]. Sensors with enzymes can detect ppb levels of lead, copper, uranium, zinc, mercury, and cadmium [57], [65].

Electrochemical methods

In response to the fast growing demands of rapid detection and evaluation of contamination by heavy metals, particularly in the field of environmental monitoring, great efforts have been made to develop technologies and methods for in-situ and continuous measurements of heavy metals. The main method of in-situ detection of heavy metals is electrochemical analysis using chemical sensors. Electrochemical methods can be divided in three main categories: potentiometry, coulometry and voltammetry. The earliest voltammetric form was developed by Jaroslav Heyrovsky in the early 1920s, an achievement for which he was awarded the Nobel Prize in Chemistry in 1959 [66]. Since then, many different forms of voltammetry have been developed. Although early voltammetric methods used only two electrodes, a modern voltammetry uses a three-electrodes system consisting of a working electrode, reference electrode, and counter electrode. The auxiliary electrode or the counter electrode is generally a platinum wire and the reference electrode usually is a silver/silver chloride (Ag, AgCl | KCl_{satd}) or the commercial calomel electrode (Hg, Hg_2Cl_2 | KCl_{satd}). This technique is based on applying a time-dependent potential excitation signal to the working electrode changing its potential relative to the fixed potential of the reference electrode and measure the resulting current as a function of that potential providing quantitative and qualitative information about the species involved in the oxidation or reduction reaction. Indeed, the oxidation or reduction of a substance on the surface of the working electrode, at the appropriate applied potential, results in the mass transport of a new material to the surface of the electrode and the generation of a current. The main drawbacks encountered in voltammetric analysis are signal overlapping; when interfering species are present in the sample they can mask the presence of other studied species and the electrode fouling by existing organic matter, such as humic material, which binds with the metal ions and adsorbs on the electrode surface [67].

Regarding potentiometry, chemical sensors have been extensively used for the determination of different types of ions. Particularly, polycrystalline membrane ion-selective electrodes are commercially available. **Table IV. 5** presents the available commercial electrodes and types of membranes. We can notice from the **Table IV. 5** that there are 4 companies producing electrodes for the detection of lead ions (Pb^{2+}). These membranes are based on the mixture of two compounds (PbS and Ag_2S) and all of them fell into the 10^{-6} mol/L detection limit column in the **Table IV. 6**.

Table IV. 5 Available commercial electrodes and types of membranes [68]–[70].

Ions	Radiometer Analytical	Orion	Nico 2000
Hg^{2+}	-	-	HgS / Ag_2S
Pb^{2+}	PbS / Ag_2S	PbS / Ag_2S	PbS / Ag_2S
K^+	PVC	PVC	PVC
S^{2-}	Ag_2S	Ag_2S	Ag_2S

Table IV. 6 Detection limits of some ion-selective electrodes [71]–[73].

	10^{-8} mol/L	10^{-7} mol/L	10^{-6} mol/L	10^{-5} mol/L
Orion	Cu^{2+}, I^-	NH_3, NH_4^+, Cd^{2+}, Ca^{2+}	Br^-, F^-, **Pb^{2+}**, K^+, Na^+	Cl^-
Nico 2000	Cu^{2+}, Ag^+, S^{2-}	Ca^{2+}, Cd^{2+}, I^-	Na^+, Hg^{2+}, **Pb^{2+}**, Br^-, F^-	Cl^-, K^+, NO_2^-
Van London Co.	Cu^{2+}	Cd^{2+}, I^-, Ag^+, S^{2-}	F^-, **Pb^{2+}**, K^+, Na^+	Ca^{2+}, Br^-, NH_4^+, NO_3^-
Radiometer Analytical	-	CN^-, F^-, S^{2-}	Br^-, Ca^{2+}, Cu^{2+}, Cl^-, **Pb^{2+}**, K^+, Na^+ NH_4^+	NH_4^+, Br^-, Ca^{2+}, CN^-, NO_3^-

IV.2.5 Ion-selective electrodes

Ion-selective electrodes (ISEs) are electrochemical sensors that allow the detection of ionic species in aqueous and non-aqueous mediums. They convert the ionic signal into a measurable electronic signal, often electrical potential. The working of ion-selective membranes is provided

by the existence of electrical conductivity that ensures the ion transport and ion-exchange, which explains the working mechanism. ISEs typically require the use of a reference electrode to electrochemically determine the concentration of target ions present in different chemical environments. They have received a worldwide attraction for detecting heavy metal traces because of their very low detection limits, good selectivity, low cost, and portability for in-situ measurements [74], [75]. Many organic, inorganic and composite materials have been studied as electroactive materials for the preparation of ion-selective membrane electrodes. Moreover, the electrochemical detection used by ISE electrodes has short analytical time, low cost, high sensitivity and easy adaptability for in situ measurement. Therefore, electrochemical detection has become one of the most developed methods for the continuous in-situ monitoring of heavy metals.

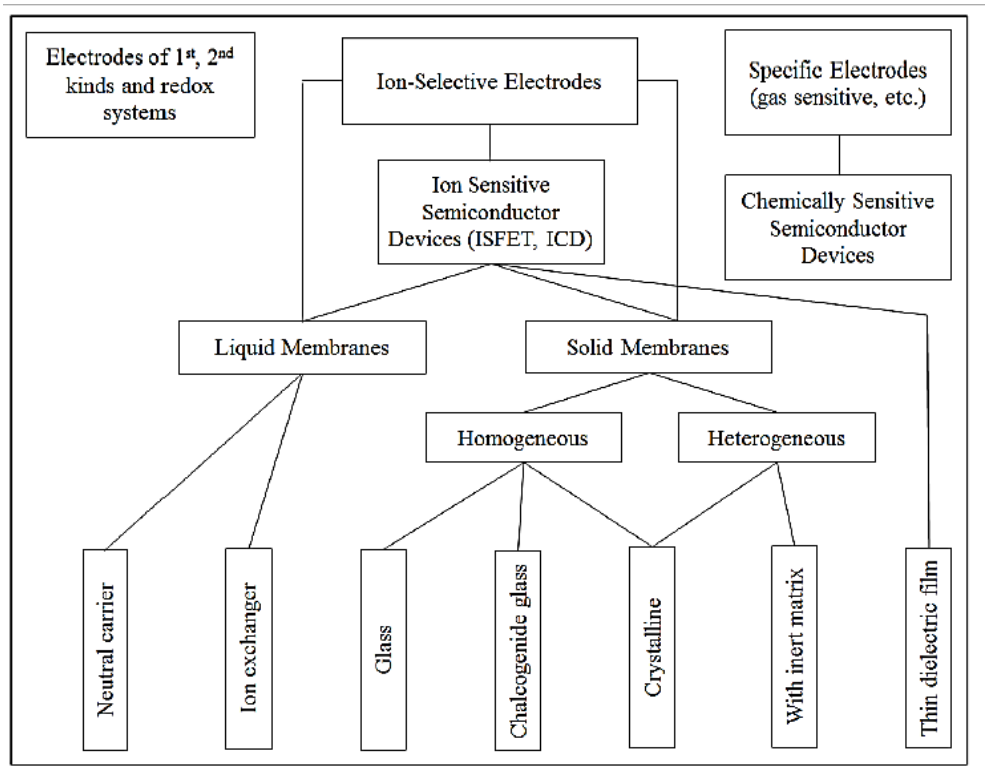

Figure IV. 2 Scheme of the classification of ISEs.

Depending on the type of contact of the internal face of the membranes, ISEs can be divided into two major categories: ISE in liquid contact and ISE in solid contact. Liquid membranes can be neutral carriers and ion-exchangers while solid membranes can be homogeneous and heterogeneous. We can classify silicate glasses, chalcogenide glasses and crystalline in the

group of homogeneous membranes (**Figure IV. 2**). The heterogeneous membranes exist in crystalline or inert matrix form.

The following sections present and discuss the different types of lead selective ISEs developed in liquid contact and solid contact forms.

❖ Liquid membranes

Liquid membrane electrodes are based on active substances, generally some organic compounds which are dissolved in organic solvents and suitable polymers. Sensors with liquid membranes can be divided into two groups depending on the type of active substance:

- ion exchanger and
- neutral carrier.

A common type of conductive sensing membrane is made of a plasticized polymer phase, typically with polyvinylchloride (PVC) as the polymer matrix, and lipophilic ion-exchanger sites. These sensors have some weak points such as insufficiently good selectivity coefficients and having a short lifespan which extends to a maximum of a few months. Most of the work found in the literature [76]–[84] relates to liquid membranes for lead detection made up of an organic molecule embedded in a polymer, generally PVC and are presented in **Table IV. 7**.

❖ Solid membranes

The solid membranes are divided into two main subgroups: homogeneous and heterogeneous membranes. They generally exhibit a little interference with other ions, unlike liquid membranes. In fact, interference can take place only if the interfering ion can interact with the membrane or if a chemical reaction takes place between the membrane and the solution [85].

1-Homogeneous

Silicate glasses

The first ion-selective electrode was the pH electrode based on silicate glass [86]. This composition (72% of SiO_2, 21.3% of Na_2O and 6.4 % CaO) is the basic composition for the pH electrodes. But since it does not work very well in all pH regions, it was changed many times in order to find the best composition for pH greater than 10.

Table IV. 7 Different types of liquid membranes for lead detection and their characteristics.

Chemical composition	Liner Range (mol. L^{-1})	Detection limit (mol. L^{-1})	Sensitivity (mV/décade)	pH	Lifetime
4,7,13,16-tetrathenoyl-1,10-dioxa-4,7,13,16 tetraazacyclooctadecane **[76]**		$10^{-5.7}$	31.9		-
Dithiophenediazacrown ether derivatives **[77]**	10^{-5}-$10^{-2.7}$	$10^{-5.7}$	29.2	-	-
Naphthalene sulfonamide derivative	10^{-7}-10^{-1}	5.62×10^{-8}	29.21	2-7	4 months
2,12-dimethy-l7,17-diphenyltetrapyrazole **[78]**	2.5×10^{-6}-5.0×10^{-2}	$3.2x10^{-4}$	30-32	1.6-6	5 months
Ionophore Pb IV and NaTFPB **[79]**	10^{-8}-10^{-3}	1.20×10^{-9}	23.4	-	Several days
N,N´-bis(2-hydroxy-1-napthalene)-2,6-pyridiamine (BHNPD) **[80]**	3.2 $x10^{-6}$-1.0 x 10^{-1}	2.7 x 10^{-4}	27.4	3.5-7.5	6 months
Calix[4]arenes **[81]**	10^{-6}-10^{-2}	5.01×10^{-6}	24	3-6	6 weeks
4-tert-butylcalix[6]arene **[82]**	1 $x10^{-6}$-1.0 x 10^{-1}	6 × 10^{-7}	30	1.5-6	-
N,N'-bis(5-methyl salicylidene)-p-diphenylene methane diamine **[83]**	5 $x10^{-6}$-1.0 x 10^{-1}	2 $x10^{-6}$	29.4	1.7-6	3 months
N,N-dibenzyl-1,4,10,13-tetraoxa-7,16-diazacyclooctadecane **[84]**	8.2 $x10^{-6}$-1.0 x 10^{-1}	10^{-4}	30	2-6.8	3 months

Glass electrodes have many advantages such as: short response time, simplicity of calibration, reproducibility of the measurements, uses in very small volumes and at high temperature, etc. However, there are some limitations of these electrodes, for example, they cannot be used in a

hydrofluoric acid environment (risk of glass attack) or in a rigorously anhydrous medium (risk of destruction of the hydrated thin ion exchange layer).

Chalcogenide glasses

The detection mechanism of ion-selective electrodes with homogenous membranes made from chalcogenide glasses is mostly the same as for the glass electrodes. A thin layer (5 to 100 nm) is formed on the surface of the glass membrane when it is placed in the solution [87]. The potential difference of the ionic exchange corresponding to the thermodynamic activity of the ion is therefore measured.

Although there is not yet a chemical sensor with chalcogenide glass membrane in commerce, membranes based on chalcogenides and chalcohalides are very promising materials for the detection of heavy metal ions (Pb^{2+}, Hg^{2+}, Cu^{2+}, Cd^{2+}, Tl^{+}, etc...) and toxic anions (CN^{-}, S^{2-}, AsO_4^{3-}) due to several reasons such as: ionic and/or electronic conductivity, good stability, high selectivity coefficient and good chemical durability.

Different chalcogenide glass systems (e.g., PbS-Ag-As_2S_3, PbI_2-Ag_2S-As_2S_3 and $GeSe_2$–PbSe–PbTe) have been investigated as ISE membrane materials (**Table IV. 8**).

Table IV. 8 Sensitivity and detection limit for some silver halide-based sensors for Pb detection found in the literature.

Chemical composition	Detection limit (mol. L^{-1})	Sensitivity (mV/décade)
20PbS-30Ag-50As_2S_3 **[88]**	10^{-5}	26
20Pb-20Ag- 60As_2S_3 **[88]**	10^{-4}	30
40PbI_2-30Ag_2S-30As_2S_3 **[89]**	$1\text{-}3\times10^{-7}$	29
56$GeSe_2$–24PbSe–20PbTe **[90]**	5×10^{-6}	25.8
PbI_2-$AgAsS_2$ **[91]**	10^{-5}	30

The ion-selective membranes developed on the basis of thin evaporated layers of As_2S_3/Ag by Tomova et al. [88] showed high sensitivity towards Ag^{+} and Cu^{2+} ions, respectively down to the concentration range of 10^{-6} mol/L, short response time and good selectivity to interfering ions but poor detection limits (10^{-4} and 10^{-5} M).

Sensors based on glasses from the composition $40PbI_2$-$30Ag_2S$-$30As_2S_3$ show a very good detection limit of $1\text{-}3\times10^{-7}$ M and a slope that coincides with the theoretical one S_0. Vlasov and Bychkov [89] report a very good reproducibility and a pH working range between 2 and 5.5-6. These chalcogenide glass electrodes are highly selective in the presence of alkali and alkali-earth cations, cobalt, nickel, zinc and manganese (II) but are very sensitive to Cu^{2+} and Hg^{2+} ions.

The Pb(II)-ion-selective electrodes (Pb(II)-ISE) of 'coated wire' type developed by Vassilev et al. [90] show linear functions in the concentration range 10^{-5}–10^{-1} mol.L^{-1} with good detection limits in the range $3.5–7.9\times10^{-6}$ M and good selectivity in the presence of Zn^{2+}, Cd^{2+}, Cu^{2+} and Al^{3+} interfering ions but they work reliably only in the acidic pH-region for pH = 2-2.5.

Crystalline

The fluoride ion selective electrode is a well-known ion-selective electrode with a homogeneous solid crystalline membrane. The membrane of the electrode consists of a single crystal of lanthanum fluoride (LaF_3) doped with europium fluoride (EuF_2) which in turn creates gaps that facilitates the ionic transport in the structure of the crystal. This crystal is an ionic conductor specific to fluoride ions whose diffusion involves successive jumps in the created vacancies. A fluoride salt solution is used as a reference solution. In this example, the main interfering ion is the hydroxide ions OH^- because it reacts with the lanthanum to form lanthanum hydroxide. Therefore, these electrodes must be used in the presence of an acidic buffer solution in order to maintain a low concentration of OH^- ions [92].

2- Heterogeneous

Crystalline

Ion-selective electrodes can be based on Ag_2S-MS or Ag_2S-AgX (X = halogen) compositions. They are used for the dosage of M^{2+} ions (for example, M = Pb, Cu, Cd, Hg) or halides. In this case, the membrane is in the form of a polycrystalline heterogeneous pellet. However, an oxidation of these electrodes is observed over time.

Inert matrix

It is possible to make an ion-selective membrane by incorporating small crystals into an inert matrix (polymer, silicon rubber) whose role is to serve as a binder so that the produced heterogeneous membrane can be easily elaborated. In general, the electrodes with heterogeneous membrane have longer response time than homogeneous electrodes.

IV.2.6 Basic principles of the potentiometric methods

Before discussing the properties of the chemical sensors developed within the framework of this project, we will present some generalities about potentiometric chemical sensors.

IV.2.6.1 Electrochemical cell

The measurement system which is simply an electrochemical cell (**Figure IV. 3**) comprises:

a) A reference electrode which has a constant potential E_R regardless of the solution studied;

b) An indicator electrode (or a chemical sensor) whose potential E_M depends on the chemical composition of the medium.

The potential of the indicating electrode (chemical sensor) E_M follows the Nernst's law:

$$E_M = E_0 \pm \frac{R\,T}{Z_i\,F} \ln a_i \qquad \text{(IV.1)}$$

where a_i is the activity of the measured ionic species, E_0 corresponds to the standard potential of the membrane, R is the gas constant (8.314 $J.K^{-1}.mol^{-1}$), T is the absolute temperature in Kelvins, F corresponds to Faraday's constant (96485 Coulomb) and z_i is the charge of the measured ionic species.

By replacing the activity a_i of the ion i by the concentration c_i and the coefficient γ_i ($a_i = c_i\gamma_i$), we obtain:

$$E_M = E_0 \pm 2.303\,\frac{R\,T}{Z_i\,F} \log\,(c_i\gamma_i) \qquad \text{(IV.2)}$$

In reality, the typical electrochemical cell can be represented as follows:

E_{R1} E_{j1} E_{j2} E_M E_{R2}

Ag,AgCl | KCl (satd) || KNO_3 (0.1 M) || $Pb(NO_3)_2$, KNO_3 (0.1 M) | Glass | $Pb(NO_3)_2$ (0.1 M), $AgNO_3$ (0.1 M) | Ag

Reference electrode **Liquid salt bridge** **Analyzed solution** **Lead ion-selective electrode**

The total measured potential E between the two electrodes of the cell is therefore composed from:

$$E = E_{R1} + E_{j1} + E_{j2} + E_M + E_{R2} \qquad \text{(IV.3)}$$

where E_{R1} is the potential at the interface Ag, AgCl | KCl (saturated), E_{R2} is the potential at the interface $Pb(NO_3)_2$, $AgNO_3$ | Ag, E_{j1} is the diffusion potential at the interface between the reference electrode solution and the salt bridge solution, and E_{j2} is the diffusion potential at the interface between the salt bridge electrolyte solution and the analyzed solution and E_M is the potential at the interface of the selective membrane and the analyzed solution.

Assuming that

$$E_{R1} + E_{j1} + E_{j2} + E_{R2} = \text{constant}, \qquad \text{(IV.4)}$$

the overall potential difference becomes identical to that of equation (IV.2). However, it should be remembered that the diffusion potential is not always constant.

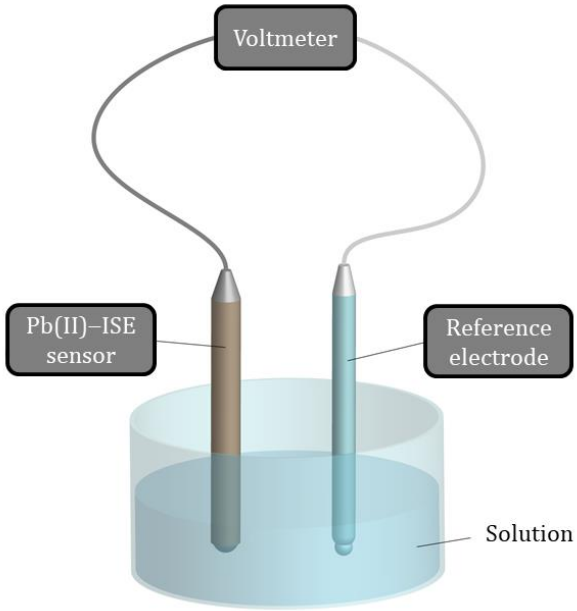

Figure IV. 3 Schema of the simplified electrochemical cell used for potentiometric measurements.

IV.2.6.2 Liquid junction potential

The liquid junction potential results from contact between two liquids with different compositions and concentrations. The mechanism of formation of the liquid junction potential is schematized in **Figure IV. 4**. When ions, in two different zones A_1 and A_2, have different mobilities and the activities a_1 and a_2 of the two zones are different, uncompensated charges are then created at the interface forming a liquid junction potential E_j.

The existence of a liquid junction potential between two electrolytes complicates the experimental measurements, because E_j can have significant and variable values. Therefore, the global potential E is not described precisely by equation (IV.2) but rather by the following

$$E = E_{R1} + E_{j1} + E_{j2} + E_{R2} + E_0 \pm 2.303 \frac{R\,T}{Z_i\,F} \log\,(c_i \gamma_i) \qquad \text{(IV.5)}$$

In order to have direct measurements of the liquid junction potential E_j, we should know the ion coefficient activity. In turn, we must know E_j to measure the ion coefficient activity. This is a thermodynamically indefinite situation. Actually, there are three possible solutions to solve this problem:

(a) using of the appropriate construction and the appropriate solution of the salt bridge in order to minimize the liquid junction potential;

(b) using of a support solution with ionic strength at least ten times higher than the concentration of the measured solution to have a constant liquid junction potential;

(c) using the Henderson equation in order to estimate the liquid junction potential:

$$E_j = -\left(\frac{RT}{F}\right)\int_1^2 \sum \left(\frac{t_i}{z_i}\right) \partial \ln a_i \qquad \text{(IV.6)}$$

where t_i is the transport number of the *i-th* ion, 1 and 2 representing the two solutions forming the junction potential E_j.

In our case, we have chosen the (b) and as a support solution we use the potassium nitrate.

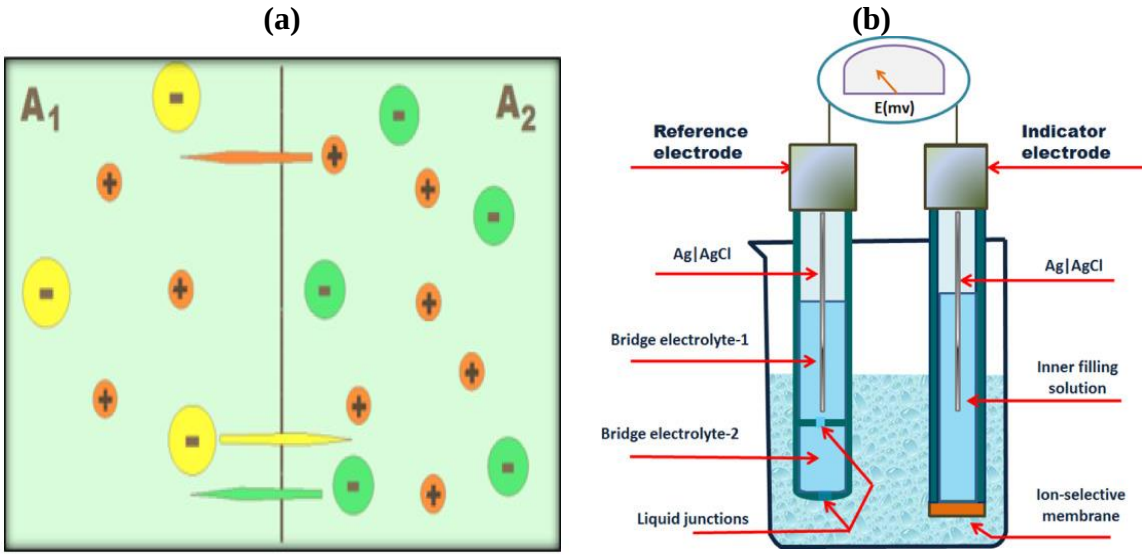

Figure IV. 4 (a) Schematization of the formation of liquid junction potential at the interface between two solutions A_1 and A_2 and (b) Potentiometric cell assembly with a liquid inner contact ion selective membrane electrode as indicator electrode and a double junction reference electrode.

IV.2.6.3 Reference electrode

The main requirements for the reference electrodes are [93]:

- The reference electrodes must be reversible. Their reversibility can be estimated by the value of the ion-exchange current between the reference electrode and the electrolyte, which must be very high.

- The reference electrodes must be reproducible, i.e. their potential must be the same under identical conditions and without hysteresis phenomena.
- The potential of the reference electrodes must be independent of the concentration of ionic species present in the solution to be measured.
- The stability of their potential on the long-term has to be high.

The silver/silver chloride (Ag, AgCl | KCl_{satd}), and the commercial calomel electrode (Hg, Hg_2Cl_2 | KCl_{satd}) correspond perfectly to all these conditions and can therefore be used as reference electrodes.

IV.2.6.4 Indicator electrode

The conditions imposed on the reference electrodes are also valid for the indicator electrodes, except the third requirement. On the contrary, the indicator electrode must be sensitive to the measured ionic species and must obey the Nernst's law. There are several types of chemical sensors as described previously (**Figure IV. 2**). Our sensors possess a selective membrane based on chalcogenide glasses and this type of sensors is presented in **Figure IV. 5** and **Figure IV. 6.**

IV.3 Assembling of chemical sensors

Four different chalcogenide glass compositions were used as active membrane materials in the fabrication of the Pb(II)-ISEs sensors. The chemical compositions of the prepared membranes and the conditions of their synthesis are summarized in **Table IV. 9**. The sensitive membrane is typically 5-6 mm in diameter and has a thickness of the order of 2 to 4 mm. The back sides of the as-prepared glasses were polished with SiC powder (9.3 µ grain size). The ball-shaped membranes were then glued into PVC tubes using an electrical isolator epoxy resin and left to dry for few days under an infrared lamp. After this step, 2 ml of the liquid mixture (1:1) $Pb(NO_3)_2/AgNO_3$ (0.1 M) was added inside the PVC tube; this electrolyte ensures the electrical contact between the glass membrane and the AgCl coated silver wire serving as inner reference electrode.

For each composition, four electrodes were prepared. Thus, the total number of electrodes tested during this study amounts to 16. **Figure IV. 5** and **Figure IV. 6** show a schema of the fabricated

chemical sensor with liquid contact and photos of the actual sensors obtained by the end of fabrication process, respectively.

Table IV. 9 Chemical compositions of the prepared membranes and the conditions of their synthesis.

Chemical composition	Electrode code	T synthesis (°C)	T before quenching(°C)	Quenching
40AgI-10PbS-50As_2S_3	Pb-ISE10	750	600	air
40AgI-30PbS-30As_2S_3	Pb-ISE30	750	600	air
50AgI-25PbS-25As_2S_3	Pb-ISE25	750	600	air
60AgI-20PbS-20As_2S_3	Pb-ISE20	780	600	air

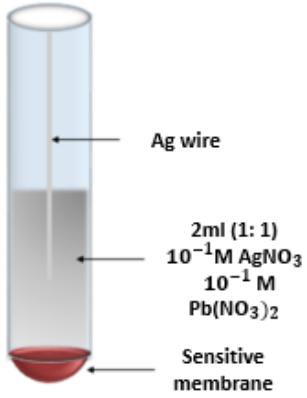

Figure IV. 5 Chemical sensor with liquid contact.

Figure IV. 6 Chemical sensors with a membrane sensitive to lead ions based on chalcogenide glasses.

IV.4 Main characteristics of Pb^{2+} sensors

The assembled lead sensors were diagnosed for a number of parameters related to the calibration functions: detection limit, slope, linear response range, selectivity coefficient in presence of interfering ions ($K_{Pb^{2+},M^{Z+}}$), reproducibility and optimal pH-range.

IV.4.1 Sensitivity and detection limit in standard solutions

The sensitivity and the detection limit are known to be the most important parameters characterizing chemical sensors. They could be found using the calibration curve if we plot the potential as a function of Pb^{2+} concentration in a semi-logarithmic scale (see **Figure IV. 7** for

example). The detection limit corresponds to a limit concentration below which the sensor is no longer sensitive to the ions being measured. It is determined as the intersection of two parts of the calibration curve: the first horizontal part with the constant potential and the second part with the rising potential. The sensitivity is a characteristic that defines the ability of the sensor to respond to a certain ionic species present in a liquid medium. The sensitivity is deduced from the slope (S) of the linear range of the second part of the calibration curve. The Nernst's law (equation IV.1) gives the theoretical value of the slope S_{th} = 29.6 mV/decade for Pb^{2+} ions at 25°C.

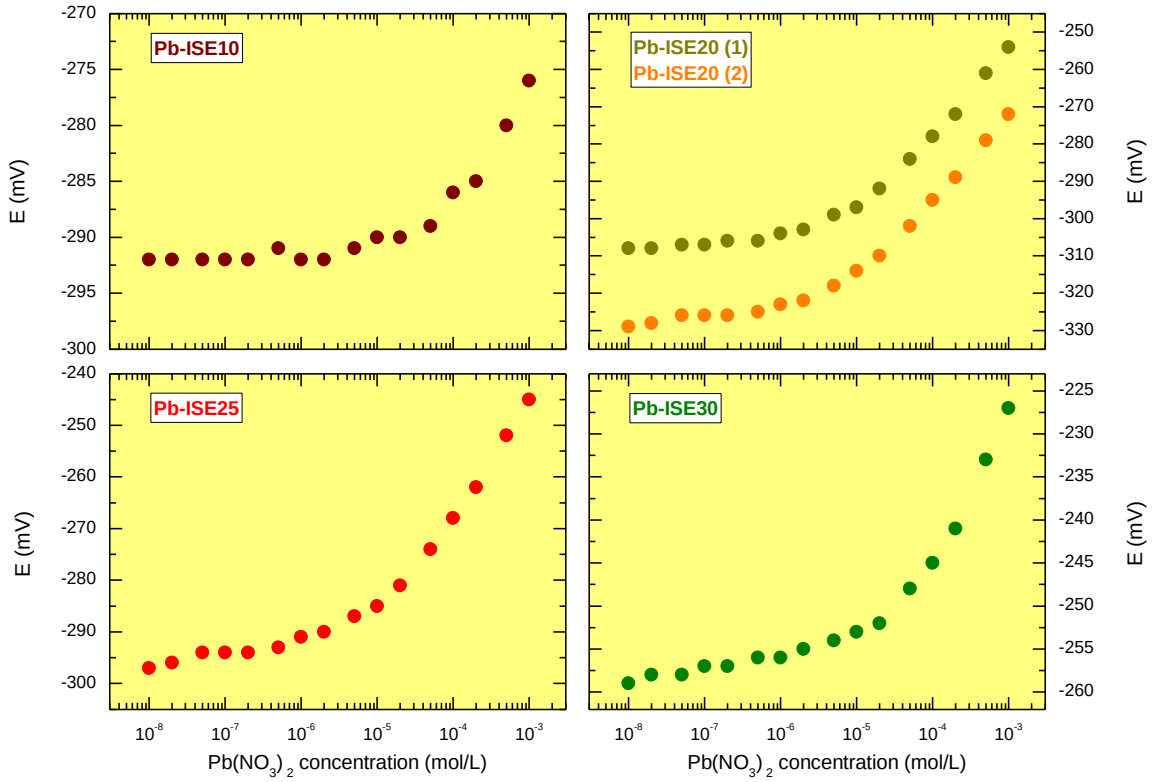

Figure IV. 7 Selected calibration curves for the fabricated Pb^{2+} sensors. In case of the sensor labeled Pb-ISE20, the curves belong to two different sensors.

The sensitivity of the sensors was studied in standard solutions of lead nitrate $Pb(NO_3)_2$ prepared from 1 mol. L^{-1} $Pb(NO_3)_2$ by consecutive dilution with ultrapure water up to 10^{-5} mol. L^{-1}. Calibrations were carried out over a range of concentrations between 10^{-8} mol. L^{-1} and 10^{-3} mol. L^{-1}. All the calibrations were performed using the titration method where Pb $(NO_3)_2$ additions are introduced into 100 ml of potassium nitrate KNO_3 solution with a concentration of 10^{-1} mol. L^{-1} (pH ≈ 7). After having introduced the $Pb(NO_3)_2$ additions, it is necessary to wait to reach the equilibrium potential. The waiting time is normally about 2 minutes and the potential does not change more than ± 2 mV during these 2 minutes.

The support solution of KNO_3 with a constant ionic strength allows us to use the concentration of the ions instead of their activity and therefore we can avoid the calculation of the ion activity coefficients. In addition, it stabilizes the liquid junction potential. In order to avoid contamination of standard solutions by Cl^- ions, a combined reference electrode containing a salt bridge has also been used. In this case we have succeeded in minimizing the potential of liquid junction.

The typical responses of the sensors Pb-ISE10, Pb-ISE30, Pb-ISE25 and Pb-ISE20 as a function of the Pb^{2+} ions concentration are shown in **Figure IV. 7**. **Table IV. 10** summarizes the obtained data of the slope, the linear response range as well as the detection limit for all assembled sensors.

Table IV. 10 Electrochemical parameters of different Pb(II)-ISEs.

	Pb-ISE10	**Pb-ISE20**	**Pb-ISE25**	**Pb-ISE30**
Slope (mV.dec^{-1})	12.9(2)	22.5(4)	21.3(7)	18.3(9)
Linear range (mol.L^{-1})	$2\times10^{-4} - 10^{-3}$	$2\times10^{-5} - 10^{-3}$	$2\times10^{-5} - 10^{-3}$	$10^{-4} - 10^{-3}$
Detection limit (mol.L^{-1})	3.9×10^{-5}	$3.3–5.7\times10^{-6}$	6.1×10^{-6}	1.8×10^{-5}

The membranes Pb-ISE10 and Pb-ISE30 exhibit detection limits in the concentration range $\sim10^{-5}$ M, limited linear responses in the range $\sim10^{-4} – 10^{-3}$ M as well as low slopes of ~12.9 and ~18.3 mV.decade^{-1}, respectively. The calibration parameters improve for the Pb-ISE20 and Pb-ISE25 membranes. The detection limits are in the range around $\sim10^{-6}$ M and the lowest value recorded was 3.3×10^{-6} M for the Pb-ISE20 sensor. The linear range increases by more than one order of magnitude and the calculated slopes are 22.5 and 21.3 mV/decade, respectively. All the sensors present slopes different from the theoretical value (≈29.6 mV/ decade). This confirms that the operating mechanism depends on the composition of the glass and its structure. It is clear that, out of the various membranes tested, the sensors with code Pb-ISE20 present the best results in terms of sensitivity (the highest slope) and detection limit (the lowest). As such, these Pb-ISE20 membranes will be used for further potentiometric characterizations. The 5 months stability of the Pb-ISE20 electrode is shown in **Figure IV. 8.**

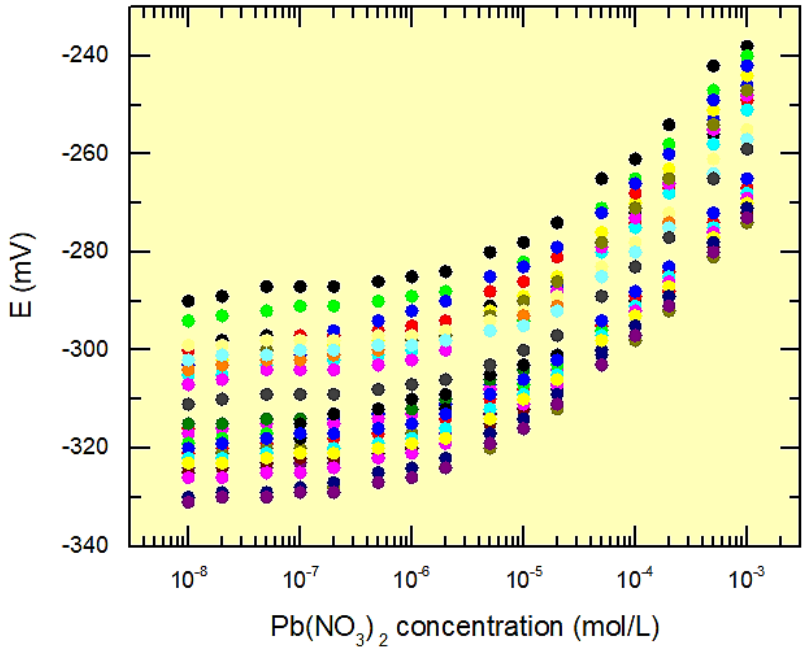

Figure IV. 8 Calibration of Pb-ISE20 electrode from 15/09/2020 to 10/02/2021.

Table IV. 11 shows the sensitivity and detection limit values of the Pb^{2+} sensors presented in the literature. For an easier comparison, the characteristics of our Pb-ISE20 sensor are noted in red. The results of the detection limits of the developed sensors are comparable to those of V. Vassilev et al. [90] and E. Malinowska et al. [81]. Yu .G. Vlasov and E. Bychkov [89], S. Anastasova et al. [79] and A. Kamal [94] reporter sensors with higher detection limits. However, our Pb-ISE20 sensor show a significantly improved detection limit compared to those developed by A.K. Jain et al. [78], V.K. Gupta et al. [80], R. Tomova et al. [88] (≈100 times), X. Yang et al. [76], [77] and C. Bohnke et al. [91] (≈10 times).

In this work, the question arises about the origin of the difference in performance of the different fabricated sensors. We note that optimal sensor performance is a complex function of several parameters. Insufficient ionic sensitivity of the Pb-ISE10 sample is related to low lead sulfide content (10 mol.%) and inhomogeneous glass nature reflected by two glass transition temperatures and SEM studies, chapter 1. The Pb-ISE30 sample has the highest PbS content (30 mol.%) but simultaneously the lowest ionic conductivity (4×10^{-6} S cm^{-1}), chapter 2. Consequently, the ion-exchange current density at the glass/solution interface is lower than for both Pb-ISE25 and Pb-ISE20 membranes and, as a result, the sensor performance is also insufficient. The last two membranes (Pb-ISE25 and Pb-ISE20) are rather close to each other and are characterized by two contrasting trends (an increase in the PbS content is accompanied by a decrease in the ionic conductivity). Glasses with higher silver iodide content are also more

chemically stable; a better performance of Pb-ISE20 seems to be related to higher AgI fraction (60 mol.%).

Table IV. 11 Sensitivity and detection limit of lead sensors presented in the literature.

Chemical composition	Detection limit (mol. L^{-1})	Sensitvity (mV/décade)
4,7,13,16-tetrathenoyl-1,10-dioxa-4,7,13,16-tetraazacyclooctadecane (**X.Yang et al. [76]**)	$10^{-5.7}$	31.9
Dithiophenediazacrown ether derivatives (**X.Yang et al. [77]**)	$10^{-5.7}$	29.2
Naphthalene-sulfonamide derivative (**A. Kamal [94]**)	5.62×10^{-8}	29.21
2,12-dimethy-l7,17-diphenyltetrapyrazole (**A.K. Jain et al. [78]**)	3.2×10^{-4}	30-32
Ionophore Pb IV and NaTFPB (**S. Anastasova et al. [79]**)	1.20×10^{-9}	23.4
N,*N*´-bis(2-hydroxy-1-napthalene)-2,6-pyridiamine (BHNPD) (**V.K. Gupta et al. [80]**)	2.7×10^{-4}	27.4
$40PbI_2$-$30Ag_2S$-$30As_2S_3$ (**Yu .G. Vlasov and E. Bychkov [89]**)	$1\text{-}3 \times 10^{-7}$	29
$GeSe_2$–PbSe–PbTe (**V. Vassilev et al. [90]**)	4×10^{-6}-6.3×10^{-7}	14.3-25.8
Calix[4]arenes (**E. Malinowska et al. [81]**)	5.01×10^{-6}	24
PbI_2-$AgAsS_2$ (**C. Bohnke et al. [91]**)	10^{-5}	30
Pb-Ag- As_2S_3 (**R.Tomova et al. [88]**)	1×10^{-4}	30
PbS-Ag-As_2S_3 (**R.Tomova et al. [88]**)	1×10^{-5}	26
AgI-PbS-As_2S_3 (**B. Alrifai [this work]**)	$(2\text{-}6.8) \times 10^{-6}$	19-26

IV.4.2 Selectivity in the presence of interfering ions in standard solutions

Selectivity is a parameter that shows the possibility of using chemical sensors in the presence of different species in the measured solution. It attests to the utility of the sensor to be used in

real sample measurements. The lower the value of the selectivity coefficient ($K_{Pb^{2+},M^{z+}}$), the more selective the chemical sensor. Theoretically, the selectivity coefficient is given by the Eisenman-Nicolsky equation [95]:

$$E = E_0 + (RT/z_x F)\, ln(a_x + K_{x,y}\, a_y) \qquad \text{(IV.7)}$$

where:

a_x - activity of the primary species *X* detected by the sensor,

a_y - activity of the interfering ion *Y*,

$K_{x,y}$ - selectivity coefficient with respect to species *X* in the presence of *Y* ions,

z_x - charge of the primary ionic species *X*.

In order to determine the selectivity coefficient, we can use the method recommended by IUPAC [96]. This is the mixed solutions method with two versions:

(1) Constant concentration of interfering ions and

(2) Constant concentration of primary ions.

The first method means that we use as a measuring solution a solution containing interfering ions with a constant concentration, whereas the concentration of primary species is variable. In contrast, in the second method, the concentration of the primary ions is fixed while the concentration of the interfering species is variable. This version is generally used when the influence of interfering ions is very strong, in order to avoid possible contamination of the selective membrane by interfering species. Normally, the concentration is chosen according to the interference strength. Typically, when the interference is strong, we work with a low concentration of interfering ions which is generally in the order of 10^{-3} to 10^{-4} mol. L^{-1}.

a. Selectivity to potassium ions K^+

The response of the Pb-ISE20 sensors in the presence of interfering K^+ ions is presented in **Figure IV. 9**. The selectivity coefficient was measured using the mixed solutions method and more precisely its first version (1) with constant concentration of interfering ions. The following equation was applied to calculate the selectivity coefficient:

$$K_{x,y} = \frac{a_x}{a_y} \qquad \text{(IV.8)}$$

with $K_{x,y}$ is the selectivity coefficient, a_x the intersection of the extrapolation of the linear part of the ***E/C*** curve (primary ion) and a_y the concentration of the interfering.

The results are showed in **Table IV. 12**. The selectivity coefficient K_{Pb^{2+},K^+} decreases when the concentration of K^+ ions increases from $K_{Pb^{2+},K^+} = 4 \times 10^{-3}$ in 0.001 mol. L^{-1} KNO_3 to $K_{Pb^{2+},K^+} = 3.5 \times 10^{-5}$ in 0.1 mol. L^{-1} KNO_3. This behavior can be related to the strong decrease in ionic strength when the concentration of KNO_3 decreases by two orders of magnitude. In this case, the influence of the diffusion potential is remarkable.

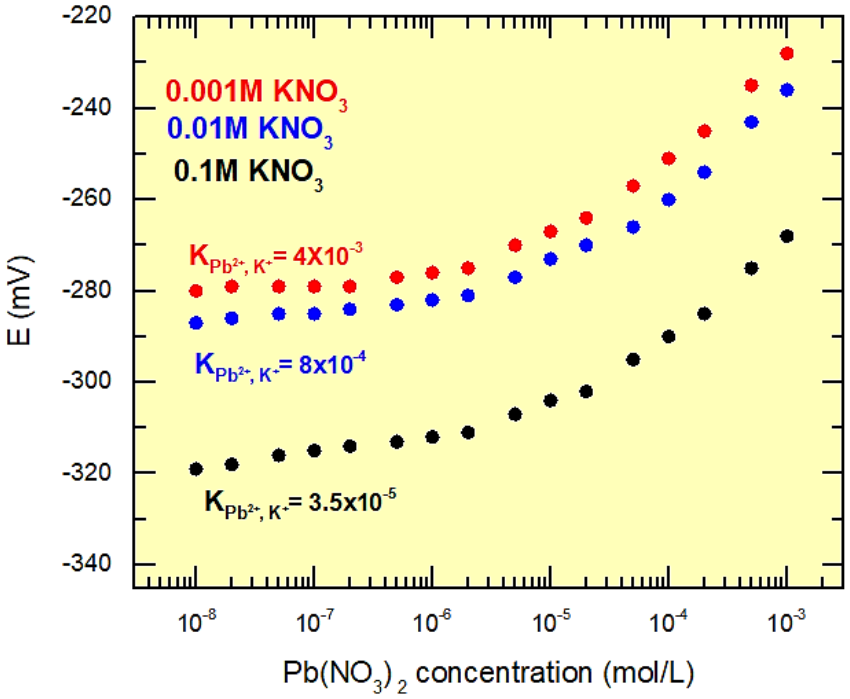

Figure IV. 9 Typical selectivity of a Pb-ISE20 sensor in the presence of K^+ ions.

Table IV. 12 Selectivity coefficient of the Pb-ISE20 sensor in the presence of the interfering ions K^+.

Concentration of the primary ion Pb^{2+} (mol. L^{-1})	**Concentration of the interfering ion K^+ (mol. L^{-1})**	**K_{Pb^{2+},K^+}**
4×10^{-6}	0.001	4×10^{-3}
8×10^{-6}	0.01	8×10^{-4}
3.5×10^{-6}	0.1	3.5×10^{-5}

Table IV. 13. allows us to compare our selectivity coefficients with those detected in the literature. The Pb-ISE20 sensors show the selectivity towards K^+ which is comparable with that found by V.S. Bhat et al. [82] (4-tert-butylcalix[6]arene based sensor), A.K. Jain et al [78]

(2,12-dimethyl-7,17-diphenyltetrapyrazole based sensor) and Yu. G. Vlasov and E. Bychkov [89] (PbS-Ag_2S and PbI_2-Ag_2S-As_2S_3 based sensors). We can see clearly that our sensors show much higher selectivity towards K^+ than the other sensors in the bibliography (by a factor of 10 to 1000) [83], [84].

Table IV. 13 Selectivity coefficient of Pb^{2+} sensors in the presence of the interfering ions K^+ found in the literature.

Chemical composition	K_{Pb^{2+}, K^+}	Concentration of the interfering ion K^+ (mol. L^{-1})
N,*N*-dibenzyl-1,4,10,13-tetraoxa-7,16-diazacyclooctadecane (**V.K. Gupta et al.** [84])	4.2×10^{-2}	0.01
N,*N*'-bis(5-methyl salicylidene)-*p*-diphenylene methane diamine (**M. Mazlum Ardakany et al.** [83])	6.3×10^{-3}	0.1
PbS- Ag_2S (**Yu .G. Vlasov and E. Bychkov** [89])	$10^{-5.7}$	1.0
2,12-dimethyl-7,17-diphenyltetrapyrazole (**A.K. Jain et al.** [78])	2.5×10^{-3}	0.001
40PbI_2-30Ag_2S-30As_2S_3 (**Yu .G. Vlasov and E. Bychkov** [89])	$10^{-5.8}$	1.0
4-tert-butylcalix[6]arene (**V.S. Bhat et al.** [82])	1.27×10^{-1}- 6×10^{-3}	0.001

b. Selectivity to sodium ions Na^+

The selectivity coefficient was measured using the mixed solutions method (1) with constant concentration of interfering ions. The concentration of interfering ions ($NaNO_3$) was 0.1 and 1.0 mol. L^{-1}. Typical response of Pb-ISE20 sensors in the presence of interfering ions Na^+ is presented in **Figure IV. 10**. The results of the selectivity coefficients calculations are given in **Table IV. 14**.

Table IV. 14 Selectivity coefficient of Pb-ISE20 sensors in the presence of Na^+ ions.

Concentration of the primary ion Pb^{2+} (mol. L^{-1})	Concentration of the interfering ion Na^+ (mol. L^{-1})	K_{Pb^{2+}, Na^+}
3×10^{-6}	0.1	3×10^{-5}
8×10^{-5}	1.0	8×10^{-5}

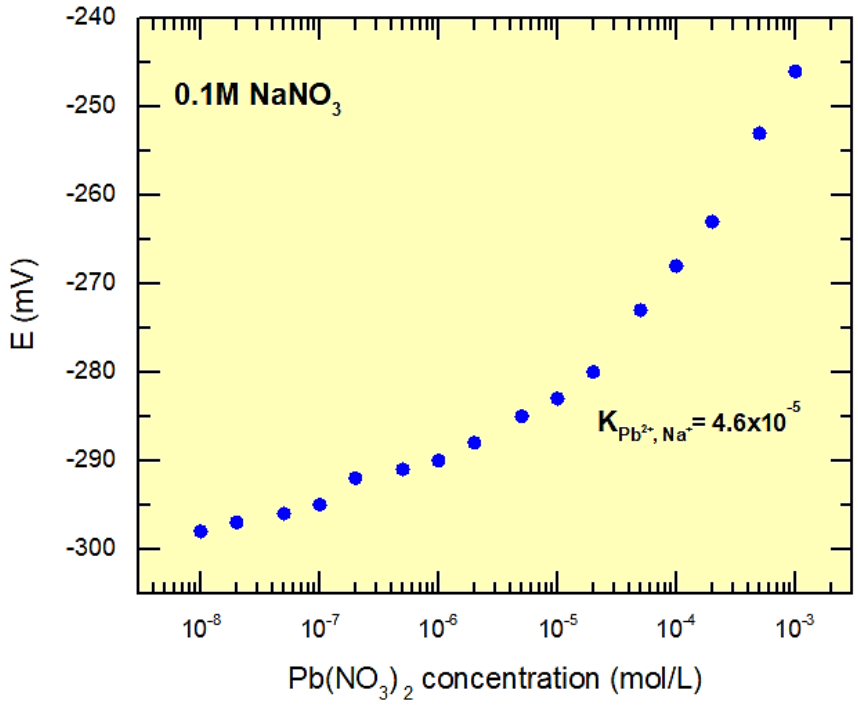

Figure IV. 10 Typical selectivity of a Pb-ISE20 sensor in the presence of interfering ions Na^+.

Table IV. 15 Selectivity coefficient of Pb^{2+} sensors in the presence of the interfering ion Na^+ found in the literature.

Chemical composition	K_{Pb^{2+}, Na^+}	Concentration of the interfering ion Na^+ (mol. L^{-1})
N,*N*'-bis(5-methyl salicylidene)-*p*-diphenylene methane diamine (**M. Mazlum Ardakany at al.** [83])	5.1×10^{-3}	0.1
$40PbI_2$-$30Ag_2S$-$30As_2S_3$ **(Yu. G. Vlasov and E. Bychkov**[89]**)**	$10^{-5.9}$	1.0

In **Table IV. 15** are also given the selectivity coefficients of Pb^{2+} sensors in the presence of Na^{+} ions found in the literature. From this table we can notice that our electrodes clearly show better selectivity coefficients with respect to the Na^{+} ions than the sensor developed by M. Mazlum Ardakany et al. [83] (a factor of 100 is observed) and a comparable coefficient to that of Yu. G. Vlasov and E. Bychkov [89].

c. Selectivity to calcium Ca^{2+} and nickel Ni^{2+} ions

In the case of calcium and nickel, the selectivity coefficients were measured according to the same mixed solutions method with a constant concentration of interfering ions (0.1 mol. L^{-1} of $Ca(NO_3)_2$ and $Ni(NO_3)_2$). Typical responses of Pb-ISE20 sensors in the presence of the interfering Ca^{2+} and Ni^{2+} ions are presented in **Figure IV. 11** and **Figure IV. 12**, respectively. The results of the selectivity coefficients calculations are given in **Table IV. 16.**

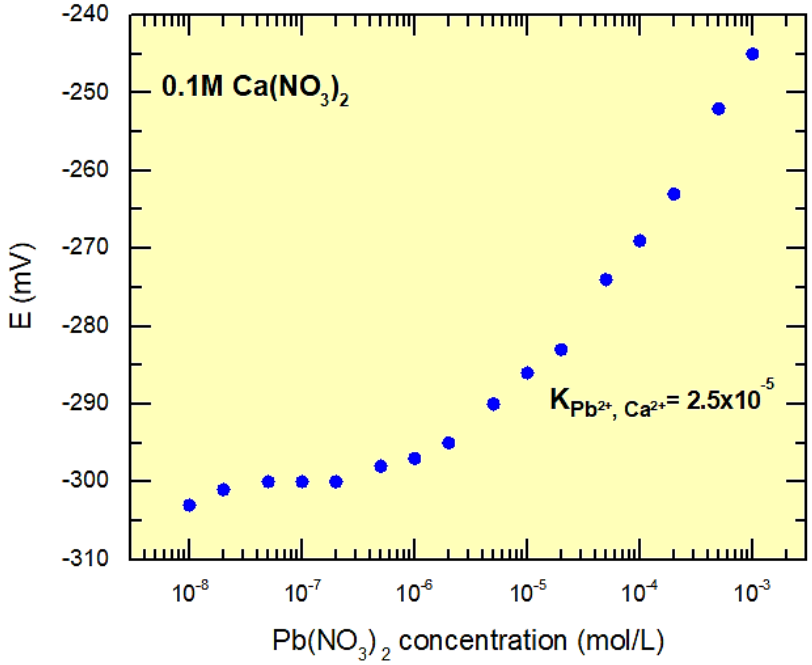

Figure IV. 11 Typical selectivity of a Pb-ISE20 sensor in the presence of interfering ions Ca^{2+}.

Table IV. 16 Selectivity coefficient of Pb-ISE20 sensors in the presence of interfering ions $Ca^{2+}$and Ni^{2+}.

Concentration of the primary ion Pb^{2+} (mol. L^{-1})	**Concentration of the interfering ion M^{2+} = Ca^{2+} or Ni^{2+} (mol. L^{-1})**	**$K_{Pb^{2+}, Me^{2+}}$**
2.5×10^{-6}	0.1	2.5×10^{-5} (Ca^{2+})
4×10^{-6}	0.1	4×10^{-5} (Ni^{2+})

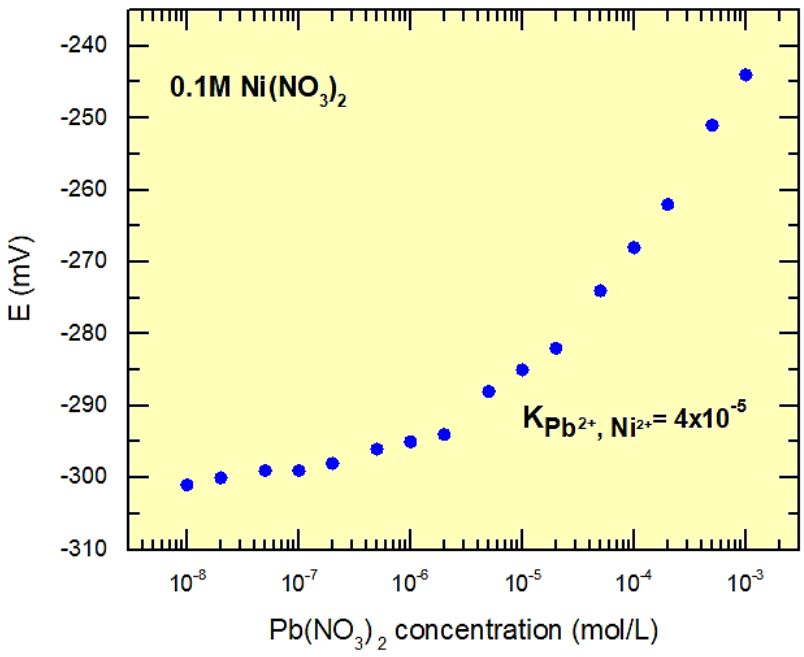

Figure IV. 12 Typical selectivity of a Pb-ISE20 sensor in the presence of interfering ions Ni^{2+}.

In **Table IV. 17** we can also find the bibliographical data for the coefficients of selectivity of lead sensors with respect to the interfering ions of Ca^{2+} and Ni^{2+}. It can be concluded that our developed sensors clearly show comparable to better selectivity coefficients for both cations.

Table IV. 17 Selectivity coefficient of Pb^{2+} sensors in the presence of the interfering ions Ca^{2+} and Ni^{2+} found in the bibliography.

Chemical composition	**Concentration of the interfering ion M^{2+} = Ca^{2+} or Ni^{2+} (mol. L^{-1})**	**$K_{Pb^{2+}, Ca^{2+}}$**	**$K_{Pb^{2+}, Ni^{2+}}$**
N,*N*'-bis(5-methyl salicylidene)-*p*-diphenylene methane diamine (**M. Mazlum Ardakany et al.** [83])	10^{-1}	1.26×10^{-4}	1.2×10^{-3}
$40PbI_2$-$30Ag_2S$-$30As_2S_3$ (**Yu. G. Vlasov and E. Bychkov** [89])	10^{-1}	$10^{-4.3}$	$10^{-4.5}$
2,12-dimethyl-7,17-diphenyltetrapyrazole (**A.K. Jain et al.** [78])	10^{-3}	5.5×10^{-3}	5.1×10^{-3}
PbS- Ag_2S (**Yu.G. Vlasov and E. Bychkov** [89])	10^{-1}	$10^{-3.9}$	10^{-4}
4-tert-butylcalix[6]arene (**V.S. Bhat et al.** [82])	10^{-3}	6.7×10^{-4}-2.02×10^{-5}	1.1×10^{-3}-2.07×10^{-4}

d. Selectivity to cupper Cu^{2+}, mercury Hg^{2+} and cadmium Cd^{2+} ions

The selectivity coefficients in the presence of Cu^{2+}, Hg^{2+} and Cd^{2+} ions were measured using the second mixed solutions method, i.e. with a fixed primary ion concentration and varying interfering ions concentration (2). The following equation was applied to calculate the selectivity coefficient:

$$K_{y,x}=\frac{a_y}{a_x} \qquad \text{(IV.9)}$$

with $K_{y,x}$ the selectivity coefficient, a_x the intersection of the extrapolation of the linear part of the ***E/C*** curve (interfering ion) and a_y the concentration of the primary ion.

This method is usually used when the selectivity of a sensor in the presence of interfering ions is susceptible to cause possible poisoning of the membrane by interfering species. Therefore, it has been assumed that Cu^{2+}, Hg^{2+} and Cd^{2+} ions belong to this category and as such method (2) was used to avoid poisoning of the electrode.

❖ **Selectivity to cupper Cu^{2+} ions**

Figure IV. 13 and **Table IV. 18** show the results of the selectivity measurements of our developed sensors in the presence of Cu^{2+} ions. Meawhile, **Table IV. 19** presents the selectivity coefficients of Pb^{2+} sensors in the presence of Cu^{2+} ions found in the literature.

Table IV. 18 Selectivity coefficient of Pb-ISE20 sensors in the presence of interfering ions Cu^{2+}.

Concentration of the interfering ion Cu^{2+} (mol. L^{-1})	**Concentration of the primary ion Pb^{2+} (mol. L^{-1})**	**$K_{Pb^{2+},Cu^{2+}}$**
1-2 × 10^{-5}	10^{-1}	2–5 × 10^{3}
1-6 × 10^{-5}	10^{-2}	1–1.6 × 10^{3}
2.5-1.6 × 10^{-6}	10^{-3}	4–6 × 10^{2}
1-6 × 10^{-7}	10^{-4}	1–1.6 × 10^{2}

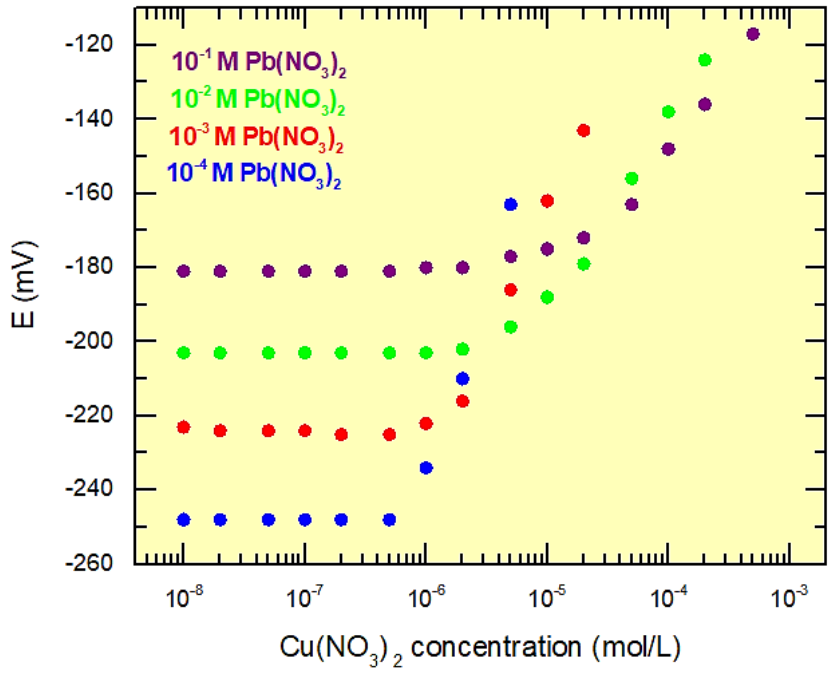

Figure IV. 13 Typical selectivity of a Pb-ISE20 sensor in the presence of interfering ions Cu^{2+}.

Table IV. 19 Selectivity coefficient of Pb^{2+} sensors in the presence of the interfering ions Cu^{2+} found in the bibliography

Chemical composition	Method* for measuring $K_{Pb^{2+}, Cu^{2+}}$	Concentration of the primary ion Pb^{2+} (mol. L^{-1})	$K_{Pb^{2+}, Cu^{2+}}$
N,*N*'-bis(5-methyl salicylidene)-*p*-diphenylene methane diamine **(M. Mazlum Ardakany et al.**[83])	(1)	10^{-1}	1.6×10^{-3}
2,12-dimethyl-7,17-diphenyltetrapyrazole **(A.K. Jain et al.** [78])	(1)	10^{-3}	$2.6\text{-}4.2 \times 10^{-2}$
4-tert-butylcalix[6]arene (**V.S. Bhat et al.** [82])	(1)	10^{-3}	8.13×10^{-5} -1.29×10^{-2}
$GeSe_2$–PbSe–PbTe (**V. Vassilev et al.** [90])	(1)	10^{-3}	7.1×10^{-5} - 3.5×10^{-6}
PbI_2-Ag_2S-As_2S_3 **(Yu .G. Vlasov and E. Bychkov** [89]**)**	(2)	10^{-2}	$10^{3.6}$-$10^{3.9}$
PbS-Ag_2S-As_2S_3 **(Yu .G. Vlasov and E. Bychkov** [89])	(2)	10^{-3}	$10^{2.8}$
PbS- Ag_2S **(Yu .G. Vlasov and E. Bychkov** [89])	(2)	10^{-3}	$10^{3.3}$

*****(1) Constant concentration of interfering ions; (2) Constant concentration of primary ions.

Comparing these results with those of our developed sensors (**Table IV. 19**) we can make the following conclusions:

- Cu^{2+} ions are strongly interfering;
- The selectivity coefficients obtained in this thesis with respect to Cu^{2+} are clearly higher than those published by other authors except the sensor developed by Yu. G. Vlasov and E. Bychkov [89] with the comparable selectivity.
- Finding a way to avoid Cu interference is essential for the use of the sensors.

❖ **Selectivity to mercury Hg^{2+} ions**

The results of the selectivity coefficient measurements in the presence of Hg^{2+} ions are shown in **Figure IV. 14** and **Table IV. 20**. **Table IV. 21** brings together the results of other authors published in the literature. The comparison of the results shows that:

- Hg^{2+} ions are generally more interfering than Cu^{2+} ions;
- The selectivity coefficients in the presence of Hg^{2+} ions are higher than those obtained by other authors except the sensor developed by Yu. G. Vlasov and E. Bychkov [89];
- Direct use of sensors in the presence of Hg^{2+} requires elimination of its influence.

Table IV. 20 Selectivity coefficient of Pb-ISE20 sensors in the presence of interfering ions Hg^{2+}.

Concentration of the interfering ion Hg^{2+} (mol. L^{-1})	**Concentration of the primary ion Pb^{2+} (mol. L^{-1})**	**$K_{Pb^{2+}, Hg^{2+}}$**
1.1×10^{-6}	10^{-1}	9×10^{4}
5×10^{-7}	10^{-3}	2×10^{3}
3.3×10^{-7}	10^{-5}	3×10^{1}
2.5×10^{-7}	10^{-7}	4×10^{-1}

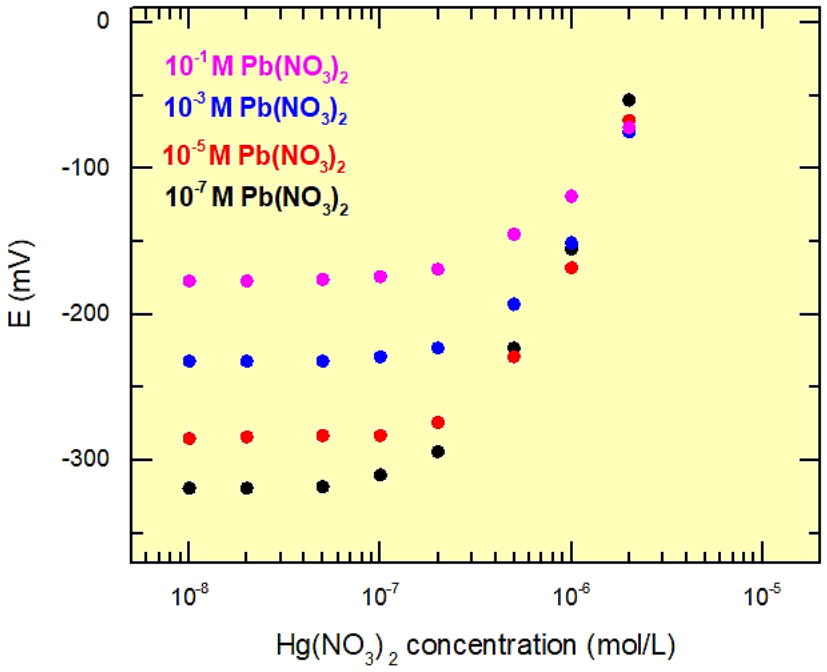

Figure IV. 14 Typical selectivity of a Pb-ISE20 sensor in the presence of interfering ions Hg^{2+}.

Table IV. 21 Selectivity coefficient of Pb^{2+} sensors in the presence of the interfering ions Hg^{2+} found in the bibliography The measurements are carried out using the mixed solutions method with constant concentration of interfering ions (method (1)).

Chemical composition	Concentration of the primary ion Pb^{2+} (mol. L^{-1})	$K_{Pb^{2+}, Hg^{2+}}$
2,12-dimethyl-7,17-diphenyltetrapyrazole (**A.K. Jain et al.** [78])	10^{-3}	9×10^{-3} - 1.1×10^{-2}
4-tert-butylcalix[6]arene (**V.S. Bhat et al.**[82])	10^{-3}	2.9×10^{-2} - 1.47×10^{-1}
PbI_2-Ag_2S-As_2S_3 (**Yu .G. Vlasov and E. Bychkov** [89])	10^{-2}	10^{12}-10^{16}

- **Selectivity to cadmium Cd^{2+} ions**

Figure IV. 15 and **Table IV. 22** present the results of the selectivity measurements towards Cd^{2+} for our developed sensors. **Table IV. 23** allows us to compare our results with those of the bibliography.

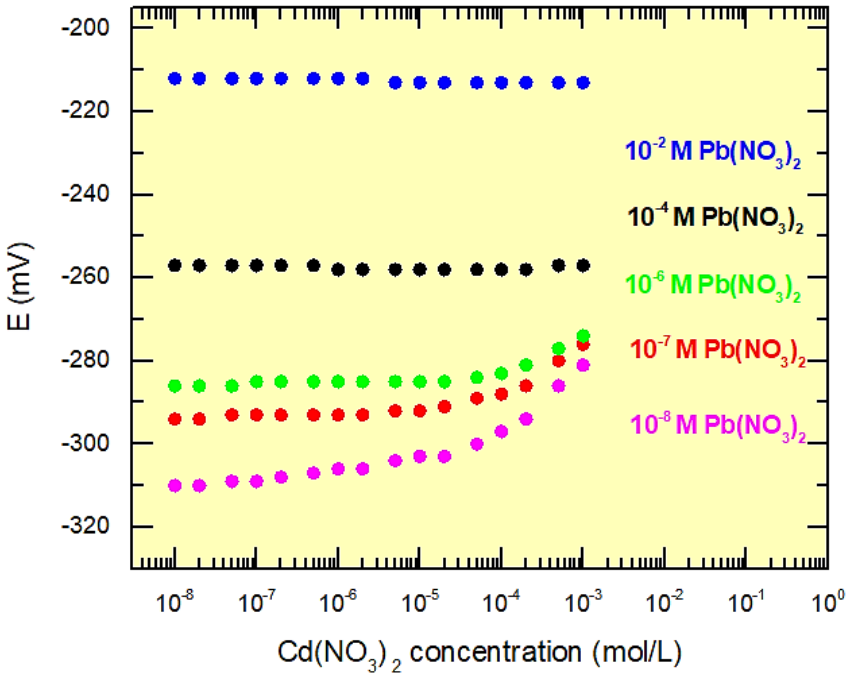

Figure IV. 15 Typical selectivity of a Pb-ISE20 sensor in the presence of interfering ions Cd^{2+}.

Table IV. 22 Selectivity coefficient of Pb-ISE20 sensors in the presence of interfering ions Cd^{2+}.

Concentration of the interfering ion Cd^{2+} (mol. L^{-1})	**Concentration of the primary ion Pb^{2+} (mol. L^{-1})**	**$K_{Pb^{2+}, Cd^{2+}}$**
-	10^{-2}	$<10^{-8}$
-	10^{-4}	$<10^{-8}$
1-7.7 × 10^{-5}	10^{-6}	1-1.3 × 10^{-2}
2-3 × 10^{-5}	10^{-8}	3.3-5× 10^{-4}

The comparison of the data in **Table IV. 22** and in **Table IV. 23** proves that:

- Cd^{2+} ions are generally not interfering Pb^{2+} ions;
- Our sensors exhibit a high selectivity for Pb^{2+} ions over the interfering ions Cd^{2+} and we can notice that the selectivity values are better than the other sensors in the bibliography.

Table IV. 23 Selectivity coefficient of Pb^{2+} sensors in the presence of the interfering ions Cd^{2+} fond in the literature.

Chemical composition	The method* for measuring $K_{Pb^{2+}, Cd^{2+}}$	Concentration of the primary ion Pb^{2+} (mol. L^{-1})	$K_{Pb^{2+}, Cd^{2+}}$
4-tert-butylcalix[6]arene (**V.S. Bhat et al.** [82])	(1)	10^{-3}	7.77×10^{-6} - 1.8×10^{-3}
PbI_2-Ag_2S-As_2S_3 **(Yu .G. Vlasov and E. Bychkov** [89])	(2)	10^{-3}	$10^{-1.6}$
PbS-Ag_2S-As_2S_3 **(Yu .G. Vlasov and E. Bychkov** [89])	(1)	10^{-3}	$10^{-1.6}$
PbS- Ag_2S **(Yu .G. Vlasov and E. Bychkov** [89])	(1)	10^{-3}	$10^{-0.5}$
N,*N*'-bis(5-methyl salicylidene)-*p*-diphenylene methane diamine (**M. Mazlum Ardakany et al.** [83])	(1)	10^{-1}	1.3×10^{-3}

*****(1) Constant concentration of interfering ions; (2) Constant concentration of primary ions.

IV.4.3 Influence of pH in standard solutions

Determining the optimal pH range in which the potential of the lead sensor is invariant for a given concentration of Pb^{2+} is an essential potentiometric measurement. The measurements were performed in the pH range 1 to 8, using constant Pb^{2+} primary cation concentrations and two different concentrations were employed, i.e., 1×10^{-2} M and 1×10^{-5} M $Pb(NO_3)_2$. HCl or NaOH were added to alter the hydrogen ions concentration. The pH value was recorded simultaneously with chemical sensor potentials.

One observes from the **Figure IV. 16** and **Table IV. 24** that the potential is constant in the pH range 2.5–4.8 for the diluted lead concentration (1×10^{-5} M $Pb(NO_3)_2$). The working pH ranges improves slightly with increasing the lead nitrate solution concentration to 1×10^{-2} M and the recorded pH range for which the potential is more or less invariant is 1.9–5. The decrease in the sensor potential values at pH > 5 and pH < 2 is mostly due to the hydrolysis of Pb^{2+} ions on solution and to changes in the liquid junction potential, respectively.

The sensor Pb-ISE20 shows a similar behavior to those developed by Malinowska et al. [81] and Yu. G. Vlasov and E. Bychkov [89], and it presents a wider working pH range in comparison to that developed by V. Vassilev et al. [90] (**Table IV. 25**).

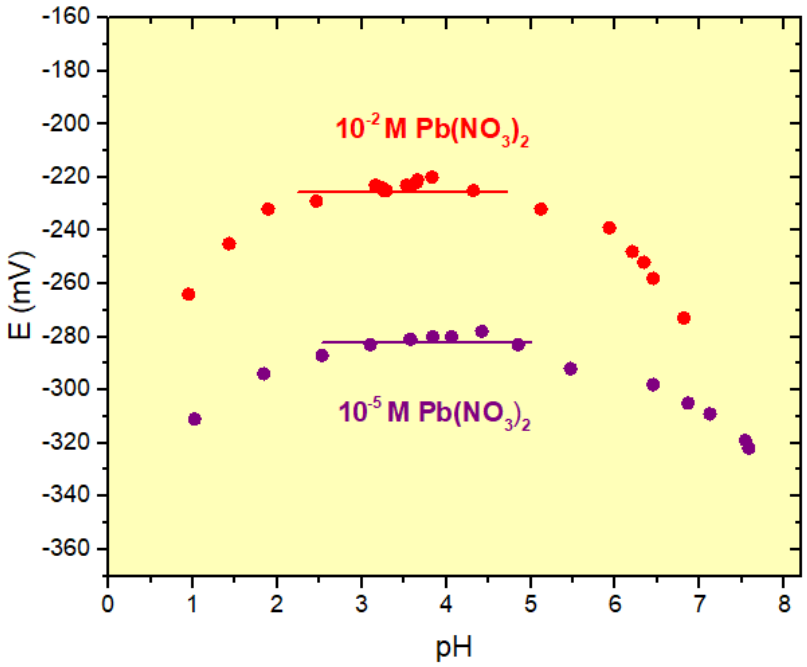

Figure IV. 16 Influence of pH on the response of our Pb-ISE20 sensors.

Table IV. 24 pH range for a given Pb^{2+} concentration where the response of the Pb-ISE20 sensors does not depend on pH

Concentration of the primary ion Pb^{2+} (mol. L^{-1})	**pH**
10^{-2}	$1.9 \leq PH \leq 5$
10^{-5}	$2.5 \leq PH \leq 4.8$

Table IV. 25 pH range where the response of the Pb^{2+} sensors does not depend on pH for membranes found in the literature.

Chemical composition	**Concentration of the primary ion Pb^{2+} (mol. L^{-1})**	**pH**
Calix[4]arenes (**E. Malinowska et al.** [81])	10^{-2}	$3 \leq PH \leq 6$
$GeSe_2$–PbSe–PbTe (**V. Vassilev et al.** [90])	10^{-2}	$1.85\text{-}2 \leq PH \leq 3\text{-}4$
PbI_2-Ag_2S-As_2S_3 **(Yu .G. Vlasov and E. Bychkov** [89])	-	$2 \leq PH \leq 5.5\text{-}6$

IV.4.4 Reproducibility in standard solutions

The reproducibility parameter, primordial for continuous in situ measurements, was investigated using a series of consecutive measurements in standard solutions. The sensor measures, for 2 minutes, the potential of the solution of a given concentration, and is then placed in the open air for another 2 minutes. This procedure is repeated several times for about one hour in order to study the reproducibility of the potential as a function of time. The mean value of the potential and especially the mean square deviation of this value give us a good estimate of the stability and reproducibility of the response of the sensor.

Figure IV. 17 shows the reproducibility of the sensor Pb-ISE20 for six different concentrations of $Pb(NO_3)_2$ solution, i.e., in the concentration domain 10^{-8} – 10^{-3} M. It can be seen from the **Figure IV. 17** that the change in potential during consecutive measurements is small: ± 2-3 mV. The obtained values demonstrate that the reproducibility does not depend on the concentration of the primary Pb^{2+} ions.

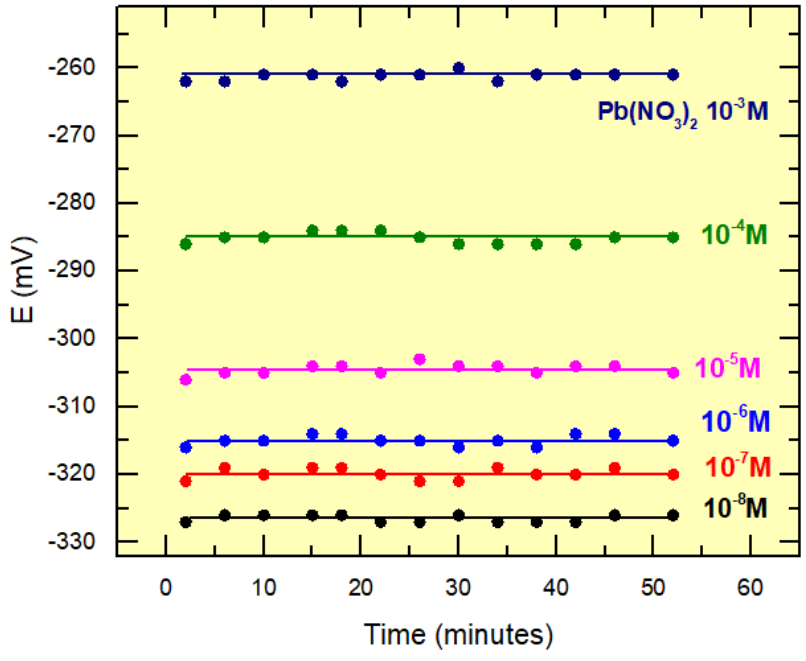

Figure IV. 17 The reproducibility of the sensor Pb-ISE20 in different concentrations of the standard lead nitrate $Pb(NO_3)_2$ solution.

IV.5 Conclusion

The work presented in this last chapter clearly shows that the glasses of the AgI-PbS-As_2S_3 system are promising for synthesizing sensitive membranes of chemical sensors. More specifically, the Pb-ISE20 sensor with the membrane based on 60AgI-20PbS-20As_2S_3 glass shows very satisfactory results in laboratory conditions:

- A good detection limit of $3.3–5.7\times10^{-6}$ mol. L^{-1} or 0.336-0.631 ppm (Pb).
- Good selectivity to Pb^{2+} ions in the presence of K^+, Na^+, Ni^{2+}, Ca^{2+} and Cd^{2+} interfering cations. However, the Pb-ISE20 sensor was sensitive to Cu^{2+} and Hg^{2+} interfering ions.
- Good pH working range (2-5 pH).
- Excellent reproducibility of potentials of the order of ± 2-3 mV.

IV.6 References

[1] N. R. Council, D. on E. and L. Studies, C. on L. Sciences, and C. on M. L. in C. Populations, *Measuring Lead Exposure in Infants, Children, and Other Sensitive Populations*. National Academies Press, 1993.

[2] David. R. Lide, "CRC handbook of chemistry and physics: a ready-reference book of chemical and physical data.," 2005.

[3] J. S. Casas and J. Sordo, *Lead: Chemistry, Analytical Aspects, Environmental Impact and Health Effects*. Elsevier, 2011.

[4] J. Emsley, *Die Elemente*. Walter de Gruyter, 2011.

[5] M. J. Conway, "Chapter Seven. Lead," in *Information Sources in Metallic Materials*, K. G. Saur, 2017, pp. 138–150.

[6] H. Seiler, A. Sigel, and H. Sigel, *Handbook on Metals in Clinical and Analytical Chemistry*. CRC Press, 1994.

[7] D. R. Lide, *CRC Handbook of Chemistry and Physics: A Ready-reference Book of Chemical and Physical Data*. CRC Press, 1995.

[8] H. Li, G. Weng, C. Y. V. Li, and K.-Y. Chan, "Three electrolyte high voltage acid–alkaline hybrid rechargeable battery," *Electrochimica Acta*, vol. 56, no. 25, pp. 9420–9425, Oct. 2011.

[9] T. Pampura, A. Probst, D. Ladonin, and V. Demkin, "Lead content and isotopic composition in submound and recent soils of the Volga Upland," *Eurasian Soil Sci.*, vol. 46, pp. 1059–1075, Nov. 2013.

[10] J. O. Nriagu, "Occupational exposure to lead in ancient times," *Sci. Total Environ.*, vol. 31, no. 2, pp. 105–116, Nov. 1983.

[11] S. Mann, "Biomineralization: the form(id)able part of bioinorganic chemistry! *," *J. Chem. Soc. Dalton Trans.*, no. 21, pp. 3953–3962, 1997.

[12] D. M. Settle and C. C. Patterson, "Lead in albacore: guide to lead pollution in Americans," *Science*, vol. 207, no. 4436, pp. 1167–1176, Mar. 1980.

[13] J. D. C. Boulakia, "Lead in the Roman World," *Am. J. Archaeol.*, vol. 76, no. 2, pp. 139–144, 1972.

[14] S. Hong, J.-P. Candelone, C. C. Patterson, and C. F. Boutron, "Greenland Ice Evidence of Hemispheric Lead Pollution Two Millennia Ago by Greek and Roman Civilizations," *Science*, vol. 265, no. 5180, pp. 1841–1843, Sep. 1994.

[15] A. P. Loeb, “Birth of the Kettering Doctrine: Fordism, Sloanism and the Discovery of Tetraethyl Lead,” *Bus. Econ. Hist.*, vol. 24, no. 1, pp. 72–87, 1995.

[16] A. Trinogga, G. Fritsch, H. Hofer, and O. Krone, “Are lead-free hunting rifle bullets as effective at killing wildlife as conventional lead bullets? A comparison based on wound size and morphology,” *Sci. Total Environ.*, vol. 443, pp. 226–232, Jan. 2013.

[17] M. D. bethesda, *Structural Shielding Design for Medical X-ray Imaging Facilities*. National Council on Radiation Protection and Measurement., 2004.

[18] J. O. Nriagu and M.-J. Kim, “Emissions of lead and zinc from candles with metal-core wicks,” *Sci. Total Environ.*, vol. 250, no. 1, pp. 37–41, Apr. 2000.

[19] IARC Working Group on the Evaluation of Carcinogenic Risks to Humans, *Inorganic and Organic Lead Compounds*, vol. 87. IARC Working Group on the Evaluation of Carcinogenic Risks to Humans, 2006.

[20] J. S. Casas and J. Sordo, *Lead: Chemistry, Analytical Aspects, Environmental Impact and Health Effects*. Elsevier, 2011.

[21] “Lead development association international,” 2003. http://www.ldaint.org (accessed Apr. 20, 2020).

[22] M. J. Scoullos, G. H. Vonkeman, I. Thornton, and Z. Makuch, *Mercury — Cadmium — Lead Handbook for Sustainable Heavy Metals Policy and Regulation*. Springer Science & Business Media, 2012.

[23] “International Lead and Zinc Study Group,” 2004. http://www.ilzsg.org (accessed Jan. 24, 2020).

[24] “International Lead and Zinc Study Group,” 1992. http://www.ilzsg.org (accessed Jan. 24, 2020).

[25] “International Lead and Zinc Study Group,” 2003. https://www.ilzsg.org (accessed Jan. 24, 2020).

[26] “WHO (2017). Recycling used lead-acid batteries: health considerations. Geneva, World Health Organization.” Accessed: Jun. 29, 2021. [Online]. Available: https://apps.who.int/iris/bitstream/handle/10665/259447/9789241512855-eng.pdf?sequence=1&isAllowed=y

[27] “Arrêté du 2 février 1998 relatif aux prélèvements et à la consommation d’eau ainsi qu’aux émissions de toute nature des installations classées pour la protection de l’environnement soumises à autorisation.”

[28] J. Markovac and G. W. Goldstein, “Picomolar concentrations of lead stimulate brain protein kinase C,” *Nature*, vol. 334, no. 6177, pp. 71–73, Jul. 1988.

[29] Lanphear Bruce P. *et al.*, "Low-Level Environmental Lead Exposure and Children's Intellectual Function: An International Pooled Analysis," *Environ. Health Perspect.*, vol. 113, no. 7, pp. 894–899, Jul. 2005.

[30] R. M. Thomson and G. J. Parry, "Neuropathies associated with excessive exposure to lead," *Muscle Nerve*, vol. 33, no. 6, pp. 732–741, 2006.

[31] A. D. Woolf, R. Goldman, and D. C. Bellinger, "Update on the Clinical Management of Childhood Lead Poisoning," *Pediatr. Clin. North Am.*, vol. 54, no. 2, pp. 271–294, Apr. 2007.

[32] S. K. Rastogi, "Renal effects of environmental and occupational lead exposure," *Indian J. Occup. Environ. Med.*, vol. 12, no. 3, pp. 103–106, Dec. 2008.

[33] B. Singh *et al.*, "Impact of lead pollution on the status of other trace metals in blood and alterations in hepatic functions," *Biol. Trace Elem. Res.*, vol. 40, no. 1, p. 21, Jan. 1994.

[34] J. Xuezhi, L. Youxin, and W. Yilan, "Studies of lead exposure on reproductive system: a review of work in China," *Biomed. Environ. Sci. BES*, vol. 5, no. 3, pp. 266–275, Sep. 1992.

[35] N. Batra, B. Nehru, and M. P. Bansal, "Reproductive potential of male Portan rats exposed to various levels of lead with regard to zinc status," *Br. J. Nutr.*, vol. 91, no. 3, pp. 387–391, Mar. 2004.

[36] M. H. Stevens, T. Jacobsen, and A. K. Crofts, "Lead and the deafness of Ludwig van Beethoven," *The Laryngoscope*, vol. 123, no. 11, pp. 2854–2858, 2013.

[37] M. Lustberg and E. Silbergeld, "Blood Lead Levels and Mortality," *Arch. Intern. Med.*, vol. 162, no. 21, pp. 2443–2449, Nov. 2002.

[38] H. L. Needleman and C. A. Gatsonis, "Low-Level Lead Exposure and the IQ of Children: A Meta-analysis of Modern Studies," *JAMA*, vol. 263, no. 5, pp. 673–678, Feb. 1990.

[39] D. C. Bellinger, "Very low lead exposures and children's neurodevelopment," *Curr. Opin. Pediatr.*, vol. 20, no. 2, pp. 172–177, Apr. 2008.

[40] B. P. Lanphear, K. Dietrich, P. Auinger, and C. Cox, "Cognitive deficits associated with blood lead concentrations <10 microg/dL in US children and adolescents.," *Public Health Rep.*, vol. 115, no. 6, pp. 521–529, 2000.

[41] G. A. Mostafa, H. H. El-Shahawi, and A. Mokhtar, "Blood lead levels in Egyptian children from high and low lead-polluted areas: impact on cognitive function," *Acta Neurol. Scand.*, vol. 120, no. 1, pp. 30–37, 2009

[42] H. L. Needleman, A. Schell, D. Bellinger, A. Leviton, and E. N. Allred, “The Long-Term Effects of Exposure to Low Doses of Lead in Childhood,” *N. Engl. J. Med.*, vol. 322, no. 2, pp. 83–88, Jan. 1990.

[43] H. L. Needleman *et al.*, “Deficits in Psychologic and Classroom Performance of Children with Elevated Dentine Lead Levels,” *N. Engl. J. Med.*, vol. 300, no. 13, pp. 689–695, Mar. 1979.

[44] O. David, J. Clark, and K. Voeller, “Lead and hyperactivity,” *The Lancet*, vol. 300, no. 7783, pp. 900–903, Oct. 1972.

[45] E. E. Ziegler, B. B. Edwards, R. L. Jensen, K. R. Mahaffey, and S. J. Fomon, “Absorption and Retention of Lead by Infants,” *Pediatr. Res.*, vol. 12, no. 1, pp. 29–34, Jan. 1978.

[46] W. Yule, R. Lansdown, I. B. Millar, and M.-A. Urbanowicz, “The Relationship between Blood Lead Concentrations, Intelligence and Attainment in a School Population: a Pilot Study,” *Dev. Med. Child Neurol.*, vol. 23, no. 6, pp. 567–576, 1981.

[47] H. L. Needleman, J. A. Riess, M. J. Tobin, G. E. Biesecker, and J. B. Greenhouse, “Bone Lead Levels and Delinquent Behavior,” *JAMA*, vol. 275, no. 5, pp. 363–369, Feb. 1996.

[48] Weisskopf Marc G. *et al.*, “Association of Cumulative Lead Exposure with Parkinson’s Disease,” *Environ. Health Perspect.*, vol. 118, no. 11, pp. 1609–1613, Nov. 2010.

[49] D. Cenić-Milošević *et al.*, “Environmental lead pollution and its possible influence on tooth loss and hard dental tissue lesions,” *Vojnosanit. Pregl.*, vol. 70, no. 8, pp. 751–756, 2013.

[50] J. C. Tjell, M. F. Hovmand, and H. Mosbæk, “Atmospheric lead pollution of grass grown in a background area in Denmark,” *Nature*, vol. 280, no. 5721, pp. 425–426, Aug. 1979.

[51] K. R. Bull *et al.*, “Alkyl lead pollution and bird mortalities on the Mersey Estuary, UK, 1979–1981,” *Environ. Pollut. Ser. Ecol. Biol.*, vol. 31, no. 4, pp. 239–259, Jan. 1983.

[52] M. E. Finkelstein *et al.*, “Lead poisoning and the deceptive recovery of the critically endangered California condor,” *Proc. Natl. Acad. Sci.*, vol. 109, no. 28, pp. 11449–11454, Jul. 2012.

[53] K. Magwedere, J. Shimwino, Y. Hemberger, L. C. Hoffman, E. M. Midzi, and F. Dziva, “Lead and Cadmium Levels in Liver, Kidney and Muscle of Harvested Wild Springbok (Antidorcus marsupialis) Under Extensive Management in Southern and Southeastern Namibia,” *Afr. J. Wildl. Res.*, vol. 43, no. 1, pp. 52–60, Apr. 2013.

[54] G. Gauglitz and D. Moore, “Handbook of spectroscopy,” Apr. 2014. https://onlinelibrary.wiley.com/doi/book/10.1002/9783527654703 (accessed Mar. 17, 2021).

[55] J. Vuković, S. Matsuoka, K. Yoshimura, V. Grdinić, R. J. Grubesić, and O. Zupanić, "Simultaneous determination of traces of heavy metals by solid-phase spectrophotometry," *Talanta*, vol. 71, no. 5, pp. 2085–2091, Mar. 2007.

[56] Z. Li, Z. Zhu, Y. Chen, C.-G. Hsu, and Jiaomai Pan, "Spectrophotometric determination of lead in biological samples with dibromo-p-methyl-methylsulfonazo," *Talanta*, vol. 48, no. 3, pp. 511–516, Mar. 1999.

[57] J. Liu and Y. Lu, "A colorimetric lead biosensor using DNAzyme-directed assembly of gold nanoparticles," *J. Am. Chem. Soc.*, vol. 125, no. 22, pp. 6642–6643, Jun. 2003.

[58] Y.-Y. Chen, H.-T. Chang, Y.-C. Shiang, Y.-L. Hung, C.-K. Chiang, and C.-C. Huang, "Colorimetric Assay for Lead Ions Based on the Leaching of Gold Nanoparticles," *Anal. Chem.*, vol. 81, no. 22, pp. 9433–9439, Nov. 2009.

[59] D. Liu, W. Qu, W. Chen, W. Zhang, Z. Wang, and X. Jiang, "Highly Sensitive, Colorimetric Detection of Mercury(II) in Aqueous Media by Quaternary Ammonium Group-Capped Gold Nanoparticles at Room Temperature," *Anal. Chem.*, vol. 82, no. 23, pp. 9606–9610, Dec. 2010.

[60] S. M. Z. Hossain and J. D. Brennan, "β-Galactosidase-Based Colorimetric Paper Sensor for Determination of Heavy Metals," *Anal. Chem.*, vol. 83, no. 22, pp. 8772–8778, Nov. 2011.

[61] J. Yan and E. M. Indra, "Colorimetric Method for Determining Pb2+ Ions in Water Enhanced with Non-Precious-Metal Nanoparticles," *Anal. Chem.*, vol. 84, no. 14, pp. 6122–6127, Jul. 2012.

[62] M. Sengan, R. K. Kamlekar, and A. Veerappan, "Highly selective rapid colorimetric sensing of Pb2+ ion in water samples and paint based on metal induced aggregation of N-decanoyltromethamine capped gold nanoparticles," *Spectrochim. Acta. A. Mol. Biomol. Spectrosc.*, vol. 239, p. 118485, Oct. 2020.

[63] M. B. Gumpu, S. Sethuraman, U. M. Krishnan, and J. B. B. Rayappan, "A review on detection of heavy metal ions in water – An electrochemical approach," *Sens. Actuators B Chem.*, vol. 213, pp. 515–533, Jul. 2015.

[64] L. Cui, J. Wu, and H. Ju, "Electrochemical sensing of heavy metal ions with inorganic, organic and bio-materials," *Biosens. Bioelectron.*, vol. 63, pp. 276–286, Jan. 2015.

[65] F. Long, A. Zhu, H. Shi, H. Wang, and J. Liu, "Rapid on-site/in-situ detection of heavy metal ions in environmental water using a structure-switching DNA optical biosensor," *Sci. Rep.*, vol. 3, p. 2308, 2013.

[66] J. T. Maloy, “Factors affecting the shape of current-potential curves,” *J. Chem. Educ.*, vol. 60, no. 4, p. 285, Apr. 1983.

[67] O. Abollino, A. Giacomino, and M. Malandrino, “Voltammetry | Stripping Voltammetry☆,” in *Encyclopedia of Analytical Science (Third Edition)*, P. Worsfold, C. Poole, A. Townshend, and M. Miró, Eds. Oxford: Academic Press, 2019, pp. 238–257.

[68] “Orion 9682BNWP Lead Ion Selective Electrode,” *Pulse Instruments - Instruments, Meters and Controls*. http://www.pulseinstruments.net/orion9682bnwpleadionselectiveelectrode.aspx (accessed Mar. 22, 2021).

[69] “Lead Electrode, Lead ISE, Lead Ion Selective Electrode, Lead.” http://www.nico2000.net/analytical/lead.htm (accessed Mar. 22, 2021).

[70] “Radiometer Analytical ISE25Pb-9 Lead Ion Selective Electrode (ISE) (half-cell, screw cap) | Hach USA - Parameter/Reagent - Obsolete.” https://www.hach.com/radiometer-analytical-ise25pb-9-lead-ion-selective-electrode-ise-half-cell-screw-cap/product-parameter-reagent?id=7640595136 (accessed Mar. 22, 2021).

[71] “Nico Scientific - Products.” http://www.nicosensors.com/Level_1/products.htm (accessed Mar. 18, 2021).

[72] “Ion Selective - Van London - pHoenix.” http://www.vl-pc.com/default/index.cfm/custom/ion-selective (accessed Mar. 18, 2021).

[73] “HACH LANGE SENSORS (VAULX-EN-VELIN) Chiffre d’affaires, résultat, bilans sur SOCIETE.COM - 954506002.” https://www.societe.com/societe/hach-lange-sensors-954506002.html (accessed Mar. 18, 2021).

[74] M. D. Tutulea-Anastasiu, D. Wilson, M. del Valle, C. M. Schreiner, and I. Cretescu, “A solid-contact ion selective electrode for copper(II) using a succinimide derivative as ionophore,” *Sensors*, vol. 13, no. 4, pp. 4367–4377, Apr. 2013.

[75] V. K. Gupta, M. R. Ganjali, P. Norouzi, H. Khani, A. Nayak, and S. Agarwal, “Electrochemical Analysis of Some Toxic Metals by Ion-Selective Electrodes,” *Crit. Rev. Anal. Chem.*, vol. 41, no. 4, pp. 282–313, Dec. 2011.

[76] X. Yang, N. Kumar, D. B. Hibbert, and P. W. Alexander, “Lead(II)-Selective Membrane Electrodes Based on 4,7,13,16-Tetrathenoyl-1,10-dioxa-4,7,13,16-tetraazacyclooctadecane,” *Electroanalysis*, vol. 10, no. 12, pp. 827–831, 1998.

[77] X. Yang, N. Kumar, H. Chi, D. B. Hibbert, and P. W. Alexander, “Lead-selective membrane electrodes based on dithiophenediazacrown ether derivatives,” *Electroanalysis*, vol. 9, no. 7, pp. 549–553, 1997.

[78] A. K. Jain, V. K. Gupta, L. P. Singh, and J. R. Raisoni, “A comparative study of Pb2+ selective sensors based on derivatized tetrapyrazole and calix[4]arene receptors,” *Electrochimica Acta*, vol. 51, no. 12, pp. 2547–2553, Feb. 2006.

[79] S. Anastasova *et al.*, “Disposable solid-contact ion-selective electrodes for environmental monitoring of lead with ppb limit-of-detection,” *Electrochimica Acta*, vol. 73, pp. 93–97, Jul. 2012.

[80] V. K. Gupta, A. K. Jain, and G. Maheshwari, “Synthesis, Characterization and Pb(II) Ion Selectivity of N, N´- bis(2-hydroxy-1-napthalene)-2,6-pyridiamine (BHNPD),” *Int. J. Electrochem. Sci.*, vol. 2, pp. 102–112, 2007.

[81] E. Malinowska, Z. Brzózka, K. Kasiura, R. J. M. Egberink, and D. N. Reinhoudt, “Lead selective electrodes based on thioamide functionalized calix[4]arenes as ionophores,” *Anal. Chim. Acta*, vol. 298, no. 2, pp. 253–258, Nov. 1994.

[82] V. S. Bhat, V. S. Ijeri, and A. K. Srivastava, “Coated wire lead(II) selective potentiometric sensor based on 4-tert-butylcalix[6]arene,” *Sens. Actuators B Chem.*, vol. 99, no. 1, pp. 98–105, Apr. 2004.

[83] M. M. Ardakany, A. A. Ensafi, H. Naeimi, A. Dastanpour, and A. Shamlli, “Highly selective lead(II) coated-wire electrode based on a new Schiff base,” *Sens. Actuators B Chem.*, vol. 96, no. 1, pp. 441–445, Nov. 2003.

[84] V. K. Gupta, A. K. Jain, and P. Kumar, “PVC-based membranes of N,N′-dibenzyl-1,4,10,13-tetraoxa-7,16-diazacyclooctadecane as Pb(II)-selective sensor,” *Sens. Actuators B Chem.*, vol. 120, no. 1, pp. 259–265, Dec. 2006.

[85] R. A. Durst, *Ion-selective Electrodes: Proceedings*. U.S. National Bureau of Standards, 1969.

[86] R. G. Bates, “Determination of pH: theory and practice.,” *Determ. PH Theory Pract.*, 1964, Accessed: Mar. 22, 2021.

[87] E. A. Bychkov, M. Bruns, H. Klewe-Nebenius, G. Pfennig, W. Hoffmann, and H. J. Ache, “Cu2+-selective thin films for chemical microsensors based on sputtered copper—arsenic—selenium glass,” *Sens. Actuators B Chem.*, vol. 25, no. 1, pp. 733–736, Apr. 1995.

[88] R. Tomova, R. Stoycheva-Topalova, and A. Buroff, “ION-SELECTIVE MEMBRANES BASED ON CHALCOGENIDE GLASSES,” *J. Optoelectron. Adv. Mater.*, vol. 7, no. 3, pp. 1399–1406, Jun. 2005.

[89] Yu. G. Vlasov and E. Bychkov, “Ion selective chalcogenide glasses,” *Ion-Sel. Electrode Rev*, vol. 9, pp. 5–93, 1987.

[90] V. Vassilev, K. Tomova, and S. Boycheva, “Pb(II)-ion-selective electrodes based on chalcogenide glasses,” *J. Non-Cryst. Solids*, vol. 353, no. 29, pp. 2779–2784, Sep. 2007.

[91] C. Bohnke, J. P. Malugani, A. Saida, and G. Robert, “Conductivite electrique et selectivite ionique des verres AgPO3-MI2 et AgAsS2-MI2 avec M = Pb, Hg,” *Electrochimica Acta*, vol. 26, no. 8, pp. 1137–1142, Aug. 1981.

[92] M. S. Frant and J. W. Ross, “Electrode for Sensing Fluoride Ion Activity in Solution,” *Science*, vol. 154, no. 3756, pp. 1553–1555, Dec. 1966.

[93] G. J. Janz and D. J. G. Ives, “Silver, Silver Chloride Electrodes,” *Ann. N. Y. Acad. Sci.*, vol. 148, no. 1, pp. 210–221, 1968.

[94] A. Kamal, R. Tejpal, V. Bhalla, M. Kumar, and R. K. Mahajan, “Selective and sensitive lead (II) solid-contact potentiometric sensor based on naphthalene-sulfonamide derivative,” *Int. J. Environ. Sci. Technol.*, vol. 12, no. 8, pp. 2567–2578, Aug. 2015.

[95] J. Růžička and C. G. Lamm, “A new type of solid-state ion-selective electrodes with insoluble sulphides or halides,” *Anal. Chim. Acta*, vol. 53, no. 1, pp. 206–208, Jan. 1971.

[96] G. G. Guillbault *et al.*, “Recommendations for nomenclature of ion-selective electrodes.,” *Pure Appl Chem*, vol. 1, no. 48, pp. 127–132, 1976.

General Conclusion

The objective of this thesis was to address the problem of water pollution by heavy metal ions and more precisely Pb^{2+}. The latter is one of the most harmful trace elements for humans. In order to measure the quantities of lead being discharged into the water directly and continuously, we set out to develop a new chemical sensor, the main element of which is a Pb^{2+} ion-selective membrane made of chalcogenide glass.

The development of new, more efficient sensors requires a rigorous methodology making it possible to determine all the relationships between the composition, the structure, and the electric transport properties in the solid material. The improved response of the sensors is ultimately directly correlated with all of these characteristics and properties. Hence, the current work can be devided into two main parts:

(i) a first part devoted to the fundamental research, i.e., the synthesis of the chalcogenide glasses and the characterization of their physicochemical properties (Chapter 1, 2 and 3)

(ii) a second part devoted to application in sensor, i.e., evaluating the potential of the synthesized glasses to be used as sensitive membranes in potentiometric chemical sensors.

In this work, we opted for the complete study of the quasi-binary PbS-As_2S_3 chalcogenide glass system along with selected synthetic Pb-As-S crystals, the dufrénoysite $Pb_2As_2S_5$, the baumhauerite $Pb_5As_9S_{18}$ and the sartorite $PbAs_2S_4$. In addition, three glass series were synthesized in the pseudo-ternary AgI-PbS-As_2S_3 system, i.e., $(AgI)_x(PbS)_{0.5-x/2}(As_2S_3)_{0.5-x/2}$, $(AgI)_{0.3}(PbS)_y(As_2S_3)_{0.7-y}$, and $(AgI)_z(PbS)_{0.1}(As_2S_3)_{0.9-z}$ denoted A, B, and C, respectively. For the PbS-As_2S_3 system, the maximum amount of PbS added to the host glass As_2S_3, using melt-quenching method, was 50 mol.% (x = 0.5). The vitreous domain was extended up (x = 0.6) using the mechanical milling method. For the AgI-PbS-As_2S_3 system, the diagram has revealed a large glass-forming region, located in the As_2S_3-rich corner. In relation to physical and thermal characteristics, the density measurements, for both pseudo-binary and pseudo-ternary systems, show a monotonic increase with PbS and AgI additions. The DSC thermal studies show a single glass transition with a shallow minimum at $x \approx 0.2$ (ΔT_g = -14 °C) for the $(PbS)_x(As_2S_3)_{1-x}$ presumably related to a host network partial fragmentation visible through a systematic decrease of the first diffraction peak (FSDP) at ≈1.25 $Å^{-1}$ and a gradual disappearance and shift of distant correlations in r-space at ≈5.3 Å. However, we note that the

lead sulfide additions do not change the trigonal arsenic coordination at a characteristic distance of 2.27 Å. Meanwhile, with silver iodide addition, the glass transition decrease was monotonic in the A-series glasses. The C-series glasses were non-homogenous as deduced from the two T_g values, indicating a phase separation in the glass evidenced by SEM images. For the B-series glasses, only the PbS-poor glasses of the B-series were nonhomogeneous.

The study of the electronic properties of the $(PbS)_x(As_2S_3)_{1-x}$ shows a four orders of magnitude increase in electrical conductivity with x but the change was non-monotonic. The PbS-poor glasses, $x < 0.2$, show nearly invariant conductivity parameters, possibly related to inhomogeneity of the Pb-poor glasses on mesoscopic length scale ($\lesssim$ 1000 Å) as slightly implied by the enhanced small SANS (small-angle neutron scattering) intensity in the low-Q range ($Q \lesssim 0.2$ Å^{-1}) accessible by $S_N(Q)$ may be an indication of this. Furthermore, with increasing lead content, the electronic transport increases monotonically in both (i) PbS-rich glasses, (ii) ternary Pb-As-S crystals and (iii) annealed glassy/crystalline samples. The observed conductivity increase is reasonable since cubic lead sulphide is a narrow-gap semiconductor with a high electron and hole mobility (e.g. σ_{298}(nano-PbS) $\approx 10^{-6}$ S cm^{-1}). The conductivity extrapolation to $x = 1$ yields the following order: σ_{298}(nano-PbS) > $> \sigma_{298}^{\text{anneal}}(1) > \sigma_{298}^{\text{cryst}}(1) > \sigma_{298}^{\text{glass}}(1)$. This behaviour is explained by the higher carrier mobility in the nano-PbS crystalline lattice. The higher conductivity of the annealed samples compared to synthetic crystal is presumably related to weaker electronic carrier scattering in the latter originating from the more ordered crystalline lattice in the semiconducting $PbAs_2S_4$ phase. The carrier mobility is furthermore reduced by the disordered nature of glassy PbS-As_2S_3 network. In the binary glasses, lead is acting as a network modifier than a network former. This is indicated from the DFT Raman modelling showing the presence of the most intense high-frequency peak at 370 cm^{-1} (attributed to $As - S_t$ stretching) accompanied by shorter $As - S_t$ bond distances. The obtained structural information on lead, obtained from the derived neutron, X-ray and preliminary FPMD modelling structural parameters, assumes that lead is rather acting as a modifier than a network former. Comparing to monoclinic $PbAs_2S_4$, the equimolar glass $(PbS)_{0.5}(As_2S_3)_{0.5}$ exhibits shorter Pb-S interatomic distances, 2.85 ± 0.02 Å vs. 3.17 ± 0.14 Å in the high lead environment crystal (N_{Pb-S} = 9). The shorter distance is coherent with lower lead local coordination in glasses (N_{Pb-S} = 3.5 ± 0.5 via Gaussian fitting of diffraction data or N_{Pb-S} = 6 ± 1 via preliminary FPMD modeling).

Conductivity measurements of the vitreous pseudo-ternary AgI-PbS-As_2S_3 system were also carried. The room temperature conductivity the A-series glasses $(AgI)_x(PbS)_{0.5-x/2}(As_2S_3)_{0.5-x/2}$ increases by ≈11 orders of magnitude divided among three different concentration region. A non-significant percolation-controlled-regime was observed below 3 at.% Ag. This is explained by the enhanced electronic conductivity of the $(PbS)_{0.5}(As_2S_3)_{0.5}$ host matrix, $\sigma_{298} \approx 6\times10^{-14}$ S cm^{-1}, which masks the ionic transport at low Ag^+ cation content. The modifier controlled regime, observed above this silver fraction, is divided into two distinct regions, indicating thus a difference in the local structure (below and above 17 at.% Ag). This is probably related to the existence of different mixed tetraherdra, i.e., interconnected tetrahedral $(AgI_{2/2}S_{2/2})_n$ chains (domain B) or $AgI_{3/3}S_{1/2}$ mixed tetrahedral (domain C), in the glass network. A clue to the mixed silver environment is provided by the blue shifted 265 cm^{-1} Raman feature, increasing with silver iodide addition, attributed to Ag-S stretching as indicated the DFT Raman spectra of Ag_2S. Further HE-XRD and Neutron scattering studies are needed to clarify the observed changes. Similarly, for the C-series $(AgI)_z(PbS)_{0.1}(As_2S_3)_{0.9-z}$, the room temperature conductivity increases by more than 10 orders of magnitude from ~8.9×10^{-13} (z = 0.1) to ~1.4×10^{-3} (z = 0.5) with increasing silver iodide content z. However, a difference in σ (up to 4 orders of magnitude) was observed between the two ternary systems and was attributed to structural changes in the preferential conduction pathways topology of the ternary systems. A non-random mixing of plomb and silver species and hence a privileged positioning of Pb-related structural units within the preferential conduction pathways formed by Ag-related structural units is taking place. Immobile or slow Pb^{2+} ions will affect the Ag^+ ion dynamics by restricting the number of accessible empty sites thus reducing additionally the ionic conductivity. This hypothesis becomes more evident in the case of the B-series glasses, $(AgI)_{0.3}(PbS)_y(As_2S_3)_{0.7-y}$,. In contrast to the binary AgI- As_2S_3, the conductivity of the ternary system is decreasing despite the increase of the silver ion fraction in the later and the difference in conductivity rises up to almost 5 orders in magnitude in favour to binary one for same silver content; thus, blockage of Ag^+ preferential conduction pathways by Pb^{2+}.

Finally, the last part of the work concerns the development of selective sensors for Pb^{2+} ions based on synthesized and characterized glasses. The limit of detection, the selectivity in the presence of several interfering ions, the influence of pH, the reproducibility of response and the long-term stability were studied. Among several glass compositions studied, the Pb-ISE20 membrane $(AgI)_{60}(PbS)_{20}(As_2S_3)_{20}$ exhibits the best detection limit of 3.3-5.7 $\times10^{-6}$ mol. L^{-1}

(0.3-0.6 ppm Pb) in standard solutions. Pb-ISE20 demonstrated also the best results in terms of linearity and slope. It guaranteed an excellent reproducibility, good pH working range and good selectivity and reversibility to Pb^{2+} ions for K^{+}, Na^{+}, Ni^{2+}, Ca^{2+} and Cd^{2+} cations. However, the Pb-ISE20 sensor was sensitive to Cu^{2+} and Hg^{2+} interfering ions.

List of Figures

Chapter I:

Chapter II:

Chapter III:

Chapter IV:

List of Tables

Chapter I :

Chapter II :

Chapter III :

Chapter IV :

Résumé de thèse

Une série notable de développements qui ont mis en évidence l'importance des verres chalcogénures ont été observées au cours des dernières années. Actuellement, la recherche sur ce type de verres est très active en raison de leur grand potentiel d'utilisation pratique. Les propriétés photoconductrices uniques, la transparence infrarouge, la conduction ionique, le phénomène de changement de phase et les propriétés de transport électrique et thermique des verres chalcogénures les rendent très intéressants pour une large gamme d'applications, du stockage de données et d'énergie, mémoires optiques haute densité, photonique, imagerie, dispositifs thermoélectriques, batteries et détection chimique.

En effet, au cours du XXe siècle, les impacts environnementaux et de santé publique liés aux activités anthropiques ont continué à prendre de l'importance tant au niveau du grand public qu'au niveau des instances politiques et de recherche dans lesquelles divers programmes visent à renforcer la recherche et le développement dans le contrôle de la qualité de l'eau, de l'air et du sol. A cet effet, la pollution métallique de l'eau est un problème particulier car les métaux lourds tels que le mercure, le cadmium, le plomb, le tellure, etc… ne sont pas biodégradables. La surveillance du taux de métaux lourds est donc très importante. Parmi ces métaux lourds, celui connu pour être le plus dangereux d'un point de vue environnemental et sanitaire est le plomb. Et c'est la raison pour laquelle nous avons choisi d'étudier de nouveaux verres chalcogénures spécifiquement dédiés à sa détection en solution aqueuse.

De nombreuses techniques sont disponibles sur le marché aujourd'hui qui sont utilisées pour détecter la présence et la quantité de métaux lourds. Parmi ces techniques, seule la potentiométrie permet une mesure in-situ et en continu des teneurs en métaux lourds dans les eaux. Les verres chalcogénures sont des matériaux prometteurs en tant que membranes sensibles pour des électrodes ioniques spécifiques dédiés à la détection du plomb dans l'eau. L'équipe « Verres et Capteurs » du Laboratoire de Physico-Chimie de l'Atmosphère (LPCA) de l'Université du Littoral Côte d'Opale (ULCO), possède une grande expertise dans la réalisation de telles membranes. Pendant plusieurs années, notre équipe s'est concentrée sur le développement de capteurs chimiques potentiométriques à membranes à base de verres chalcogénures pour détecter les ions de métaux lourds (Hg^{2+}, Fe^{3+}, Cu^{2+}, Cd^{2+}, Pb^{2+}, Ag^{+} and Tl^{+}).

Par conséquent, ce travail de thèse représente une scène d'une thématique environnementale où les recherches fondamentales sur les verres chalcogénures à effectuer en amont sont d'un intérêt scientifique particulièrement intéressant. Le développement de nouveaux capteurs plus performants, dédiés au plomb dans ce cas, nécessite une détermination des relations entre la composition, la structure, les propriétés de transport ionique et/ou électronique dans le matériau solide. Au final, cette thèse est composée de 4 chapitres.

Le chapitre I présente quelques généralités sur les verres et plus particulièrement les verres chalcogénures dopés au plomb. La synthèse des systèmes $PbS\text{-}As_2S_3$ et $AgI\text{-}PbS\text{-}As_2S_3$ a été décrite. Les propriétés macroscopiques, y compris la densité, le volume atomique moyen et les propriétés thermiques, ont été présentées et discutées.

Le chapitre II traite la conductivité électrique des systèmes $PbS\text{-}As_2S_3$ et $AgI\text{-}PbS\text{-}As_2S_3$. Ces études ont été réalisées par spectroscopie d'impédance complexe. Les résultats obtenus grâce à ces mesures sont discutés et analysés afin de faire certaines hypothèses sur les mécanismes de transport dans ces matériaux vitreux.

Le chapitre III présente l'analyse structurale des verres $PbS\text{-}As_2S_3$ et $AgI\text{-}PbS\text{-}As_2S_3$. Ces études ont été réalisées par différentes techniques. Dans un premier temps, nous avons utilisé la spectroscopie Raman afin d'avoir une idée sur la structure des verres. Dans un deuxième temps, nous nous sommes intéressés à utiliser la diffraction des rayons X à haute énergie et la diffusion des neutrons pour mieux caractériser la structure des verres.

Le chapitre IV consiste d'une étude préliminaire des capteurs chimiques à base de verres chalcogénures pour la détection des ions Pb^{2+}. Des électrodes avec différentes compositions membranaires ont été testées afin de définir la sensibilité et la limite de détection, les coefficients de sélectivité en présence d'ions interférents, la reproductibilité et l'influence du pH. Ces mesures ont été réalisés afin de mettre en évidence les différences significatives dans le comportement des capteurs.

Chapitre 1

Lors de ce travail, nous avons choisis de synthétiser et de caractériser de verres à base de soufre pour l'application de membranes actives dans des capteurs chimiques potentiométriques au plomb (Pb). Pour atteindre notre objectif, nous avons décidé de travailler avec deux systèmes : le quasi-binaire PbS-As_2S_3 et le pseudo-ternaire AgI- PbS-As_2S_3. Les propriétés de base et électroniques des verres PbS-As_2S_3 ont été étudiées dans le passé, cependant, la relation entre les caractéristiques du verre et du cristal n'a pas été établie. Par conséquent, la nouveauté de ce travail serait de (1) comparer le domaine de formation du verre dans le système pseudo-binaire obtenu par la trempe à l'état fondu habituelle et le broyage mécanique et (2) d'analyser les propriétés macroscopiques et électriques des verres en comparaison avec leurs homologues cristallins : $PbAs_2S_4$, $Pb_5As_9S_{18}$ et $Pb_2As_2S_5$, et les verres recuits donnant des alliages vitreux/cristallins. A notre connaissance, le pseudo-ternaire AgI- PbS-As_2S_3 est étudié pour la première fois. Ici, notre objectif serait (1) de synthétiser et d'identifier le domaine vitreux et (2) d'examiner les caractéristiques macroscopiques, électriques et structurelles. De plus, les verres mixtes de chalcogénure de plomb et d'argent ont été examinés en tant que matériaux membranaires actifs pour la construction de capteurs sélectifs d'ions Pb(II)–ISE. Le choix de ce dernier système peut se justifier par 3 facteurs : (1) les verres de sulfure d'arsenic As_2S_3 agissent comme formateurs de réseaux, (2) l'iodure d'argent AgI a une excellente conductivité ionique et une bonne conduction est une condition nécessaire au bon fonctionnement des capteurs développés et (3) le sulfure de plomb PbS permettent à la fois l'intégration des ions Pb^{2+} dans le système vitreux et l'échange ionique avec la solution aqueuse.

Deux méthodes différentes ont été employées dans la synthèse de nos verres : (1) la technique classique de trempe à l'état fondu et (2) la technique de broyage mécanique.

Alors, du sulfure de plomb PbS (Sigma-Aldrich 99,9 %) et du sulfure d'arsenic As_2S_3 ont été mélangés en quantités appropriées. Les ampoules de silice (8 mm de DI/10 mm de DE) contenant le mélange ont été chauffées pendant 24 h à 600-650 °C avant d'être trempées dans un mélange eau-sel froid. La même procédure a été employée pour la synthèse des verres pseudo-ternaires AgI- PbS-As_2S_3 mais les matériaux de départ ont été chauffées à 700 à 750 °C. La technique de broyage mécanique (MM) a également été utilisée pour la synthèse des échantillons MM-$(PbS)_{0.6}(As_2S_3)_{0.4}$ et MM-$(PbS)_{0.7}(As_2S_3)_{0.3}$ dans lesquels 3 g de matières premières ont été broyés à l'aide d'une jarre en zircone (45 mL) et de billes de broyage ZrO_2 (23 billes de 10 mm de diamètre) à une vitesse de 320 tr/min pendant 50 heures.

Characterization des glasses

Quasi-binaire $(PbS)_x(As_2S_3)_{1-x}$

Pour vérifier la nature amorphe des alliages $(PbS)_x(As_2S_3)_{1-x}$ obtenus, $0.0 \leq x \leq 0.7$, des techniques de diffraction des rayons X et des DRX ont été utilisées. Tous les échantillons synthétisés par la méthode de trempe classique étaient vitreux jusqu'à une teneur en PbS de 50 %, le pic de Bragg apparaît pour $x \geq 0.6$. Les pics de Bragg intenses observés pour x = 0,60 et x = 0,70, correspondent au $Pb_2As_2S_5$ monoclinique (dufrénoysite). Auparavant, un domaine vitreux s'étendant jusqu'à x = 0,62 a été rapporté pour les alliages $(PbS)_x(As_2S_3)_{1-x}$. Cependant, il était clairement indiqué qu'il était difficile d'obtenir des morceaux de verre de dimensions suffisantes pour la composition x = 0,62. La technique de broyage mécanique (MM) a été utilisée pour étendre davantage le domaine vitreux. MM-$(PbS)_{0.6}(As_2S_3)_{0.4}$ était complètement vitreux, les pics de Bragg de la dufrénoysite cristalline ont complètement disparu. En revanche, de larges caractéristiques, rappelant les pics de Bragg pour $Pb_2As_2S_5$, persistent dans MM-$(PbS)_{0.7}(As_2S_3)_{0.3}$, et cette composition peut être classée comme vitrocéramique. Ainsi, nous pouvons conclure que le domaine vitreux pour les alliages $(PbS)_x(As_2S_3)_{1-x}$ se situe dans la plage $0{,}0\ x \leq 0{,}7$.

Pour mettre en évidence les changements microstructuraux possibles des alliages $(PbS)_x(As_2S_3)_{1-x}$ étudiés, une analyse SEM a été réalisée sur quelques compositions sélectionnées. On peut dire que les alliages avec x = 0,10, 0,30 et 0,60, obtenus par fusion-trempe, sont plutôt lisses et homogènes. Notant que la morphologie de la composition x = 0,7 est assez différente ; des particules de différentes formes et tailles sont observées.

la variation de la densité, du volume atomique moyen des échantillons $(PbS)_x(As_2S_3)_{1-x}$, $0.1 \leq x \leq 0.7$ ont été étudiées. La densité augmente de façon monotone avec x. En fait, la densité du verre $(PbS)_x(As_2S_3)_{1-x}$ extrapolée au verre PbS hypothétique à x = 1 donne une valeur de densité similaire au fcc PbS cristallin. Un tel comportement est attendu puisque la densité du PbS cubique (d_{PbS} = 7.6 g.cm^{-3}) est plus élevée que celle de la matrice vitreuse As_2S_3 ($d_{g\text{-}As2S3}$ = 3.19 g.cm^{-3}) ou de l'orpiment cristallin As_2S_3 ($d_{c\text{-}As2S3}$ = 3.46 g.cm^{-3}). Au contraire, le volume atomique moyen V_a montre une diminution monotone progressive 15.44±0.24 cm^3 mol^{-1} (x = 0.0) à 14.75±0.25 cm^3 mol^{-1} (x = 0.7).

Les propriétés thermiques des échantillons ont également été étudiées. Les traces DSC présentent à la fois des caractéristiques endothermiques et exothermiques correspondant

respectivement aux phénomènes de transition vitreuse et de cristallisation. En revanche, l'As_2S_3 vitreux ne montre qu'une transition vitreuse. Tous les échantillons sont de nature homogène comme l'indique une seule caractéristique de T_g. Une forme parabolique de la température de transition vitreuse avec un minimum peu profond, ΔT_g = -14 °C à x = 0,2, pour les homologues PbS-As_2S_3 est indicative d'une organisation structurelle différente confirmée par les résultats préliminaires de diffraction.

Pseudo-ternaire AgI-PbS-As_2S_3

L'étude de ce système a mis en évidence un large domaine vitreux qui est concentré dans le coin riche en sulfure d'arsenic As_2S_3 et couvre une surface de diagramme importante. Pour détailler, les études ont été réalisées sur la base des trois séries suivantes :

- $(AgI)_x(PbS)_{0.5-x/_2}(As_2S_3)_{0.5-x/_2}$; $(0.0 \leq x \leq 0.6)$
- $(AgI)_{0.3}(PbS)_y(As_2S_3)_{0.7-y}$; $(0.0 \leq y \leq 0{,}5)$
- $(AgI)_z(PbS)_{0.1}(As_2S_3)_{0.9-z}$; $(0.0 \leq z \leq 0.5)$

Les deux séries A et C représentent des compositions à teneur croissante en AgI tandis que pour la série B, c'est la teneur en PbS qui augmente.

De même pour les alliages du système quasi-binaire, des analyses par microscopie électronique à balayage ont été effectuées sur quelques compositions sélectionnées du système ternaire, c'est-à-dire les séries A, B et C. L'introduction d'AgI (dans la série A) et de PbS (dans la série B) ne montre aucun effet significatif sur la morphologie du verre au niveau micro- échelle spatiale du mètre. De manière similaire au système $(PbS)_x(As_2S_3)_{1-x}$ étudié, les compositions avec x = 0,2 et 0,5 (la série A) et avec z = 0,2 et 0,5 (la série B) sont lisses et homogènes.

Les analyses SEM, réalisées sur les z = 0,10, 0,30 et 0,60 de la série C $(AgI)_z(PbS)_{0.1}(As_2S_3)_{0.9-z}$, montrent des changements microstructuraux intéressants. Les verres semblent être phase séparées dans toute la plage de composition.

La densité du verre et le volume atomique moyen de la série A : $(AgI)_x(PbS)_{0.5-x/_2}(As_2S_3)_{0.5-x/_2}$ ont été étudiés. Nous pouvons dire que la densité augmente de façon monotone avec l'augmentation de la teneur en AgI de 4.64 g.cm^{-3} (x = 0.0) à 5.53 g.cm^{-3} (x = 0.7). Cette tendance observée est liée à l'iodure d'argent et est bien attendue puisque la densité des deux formes cristallines d'iodure d'argent ($d_{\alpha\text{-AgI}}$= 6.12 g.cm^{-3} and $d_{\beta\text{-AgI}}$ =5.68 g.cm^{-3}) est supérieur à celle du verre d'accueil $(PbS)_{0.5}(As_2S_3)_{0.5}$ ($d_{(PbS)0.5(As2S3)0.5}$ = 4.64 g.cm^{-3}).

La densité des échantillons vitreux de la série B, $(AgI)_{0.3}(PbS)_y(As_2S_3)_{0.7-y}$, augmente d'une façon monotone avec la teneur en PbS y tandis que le volume atomique moyen reste essentiellement invariant. Le changement non monotone, en fonction de la composition, du volume atomique moyen est plus susceptible d'indiquer un changement drastique de la structure du verre, qui n'est pas observé dans la série A et la série B du $(AgI)_x(PbS)_{0.5-x/_2}(As_2S_3)_{0.5-x/_2}$) (ce travail). Dans les deux cas, c'est-à-dire dans les séries A et B, le comportement de la densité et du volume atomique moyen imite celui observé pour les séries A et B du système $(AgI)_x(HgS)_{0.5-x/_2}(As_2S_3)_{0.5-x/_2}$. Comme pour les deux séries précédentes A et B, le comportement en densité des échantillons vitreux de la série C, $(AgI)_z(PbS)_{0.1}(As_2S_3)_{0.9-z}$, est toujours monotone. L'augmentation de la teneur en AgI z entraîne une augmentation des valeurs de densité de 3.39 g.cm^{-3} (z = 0.0) à 4.44 g.cm^{-3} (z = 0.5). D'autre part, le volume atomique moyen montre une augmentation monotone mais inférieure à celle observée dans la série A.

Concernant les propriétés thermiques, pour la série A, l'ajout d'iodure d'argent au verre d'accueil $(PbS)_{0.5}(As_2S_3)_{0.5}$ entraîne une forte diminution de T_g de 124°C de 199°C (x = 0) à 75°C (x = 0,7). La diminution de T_g est monotone contrairement son équivalent du sulfure de mercure où la transition vitreuse a diminué à deux vitesses différentes.

La transition vitreuse des verres de la série B, $(AgI)_{0.3}(PbS)_y(As_2S_3)_{0.7-y}$, se comporte de manière similaire à celle du sulfure de mercure précédemment étudié, $(AgI)_{0.3}(HgS)_y(As_2S_3)_{0.7-y}$. Le verre pauvre en PbS (y = 0,1) présente deux valeurs de T_g (T_{g1} = 117 et T_{g2} = 180 °C) indiquant le caractère non homogène de cette composition. À une teneur plus élevée en PbS (y > 0,1), les échantillons de sulfure de plomb de la série B présentent une seule caractéristique endothermique indiquant une nature homogène des verres. Pour les verres de la série B, $(AgI)_z(PbS)_{0.1}(As_2S_3)_{0.9-z}$, elles présentent deux caractéristiques endothermiques correspondant au transition vitreuse (T_{g1} et T_{g2}), indiquant une nature vitreuse non homogène à l'échelle macroscopique et mésoscopique.

Cristaux de PbS-As_2S_3

Beaucoup d'efforts ont été déployés pour tenter de synthétiser quelques-uns des composés cristallins de Pb-As-S et d'Ag-Pb-As-S, et ce qui n'a pas été une mission facile du tout. Finalement, nous avons pu préparer trois cristaux synthétiques différents de Pb-As-S : la sartorite $PbAs_2S_4$, la baumhauerite $Pb_5As_9S_{18}$ et la dufrénoysite $Pb_2As_2S_5$. Les trois cristaux

différents ont été préparés avec succès dans le système Pb-As-S via la procédure de synthèse thermique dans des tubes de silice nettoyés scellés sous vide. Les cristaux étaient de la dufrénoysite $Pb_2As_2S_5$ (22,22 at.% Pb), de la baumhauerite $Pb_5As_9S_{18}$ (15,62 at.% Pb) et de la sartorite $PbAs_2S_4$ (14,28 at.% Pb). Pour $Pb_2As_2S_5$, les deux composés PbS et As_2S_3 ont été mélangés dans un rapport 2:1, chauffés lentement jusqu'à 800 °C, homogénéisés à cette température pendant 24h avant d'être refroidis et recuits à 350 °C pendant 10 jours . $Pb_5As_9S_{18}$ a été obtenu en appliquant la même procédure pour un rapport presque équimolaire 5:4,5. Enfin, $PbAs_2S_4$ a été obtenu en utilisant le rapport équimolaire 1:1 et la température de recuit était de 280 °C pendant 20 jours.

Chapitre 2

Dans ce chapitre, nous étudions les propriétés électriques des 2 systèmes (binaire et ternaire) de verres chalcogénures dopés au plomb qui ont été précédemment synthétisés soit par des mesures d'impédance soit par DC.

Les échantillons trempés, après ouverture du tube de préparation, sont mis pour les mesures de conductivité de deux manières. Les échantillons durs sont découpés en plaques rectangulaires et polis à l'aide de poudre de carbure de silicium SiC (taille de grain de 9,3 μ). Les côtés de l'échantillon ont été meulés parallèlement et de l'or a été déposé sur les côtés opposés. L'épaisseur typique des échantillons était comprise entre 0,1 et 1,5 mm.

Au contraire, les échantillons fragiles sont broyés pour les transformer en poudre qui est ensuite fortement compactée et comprimée, à l'aide d'une presse à granuler afin de réaliser des granulés d'une épaisseur d'environ 1 mm.

Les conductivités de tous nos échantillons vitreuse et cristallins dépendent de la température et obéissent à la loi d'Arrhenius :

$$\sigma = \sigma_0/T \exp(-E_\sigma/kT)$$

Avec σ_0 est le facteur pré-exponential, E_σ l'énegie d'activation, k la constanre de Boltzmann, et T la température.

Les paramètres de conductivité tracés en fonction du pourcentage atomique de l'ion plomb pour les composés cristallins et vitreux montrent une dépendance claire de la composition. $\sigma_{dc}(x,T)$

et l'isotherme de conductivité $\sigma_{298}(x)$ montrent que les verres de thiorsénate de plomb sont des isolants électroniques. Les paramètres de conductivité présentent des dépendances complexes avec la composition. La conductivité à température ambiante pour les échantillons $(PbS)_x(As_2S_3)_{1-x}$, 0,0 ≤ x ≤ 0,7, augmente de plus de 4 ordres de grandeur, de 1.0×10^{-16} S cm^{-1} (x = 0.0) à 3.2×10^{-12} S cm^{-1} (x = 0.7). Néanmoins, deux domaines de conductivité différents ont été observés pour les verres trempés à l'état fondu : (1) 0,0 ≤ x ≤ 0,2 (≤ 4,5 at.% Pb), (2) 0,25 ≤ x ≤ 0,5 (5,8 ≤ [Pb] ≤ 14,2 at.%), et une tendance distincte pour les alliages MM, x ≥ 0,6 (18,7 at.% Pb). Le domaine 1 est caractérisé par une conductivité quasi invariante $\approx10^{-16}$ S cm^{-1}, et une énergie d'activation, 0,93 0,05 Ev. Ensuite, la conductivité fait une saute d'un facteur 20, et augmente exponentiellement pour les alliages vitreux riches en Pb (domaine 2), accompagné d'une diminution monotone de E. Enfin, les alliages MM présentent une augmentation supplémentaire de deux ordres de grandeur avec un faible changement de la conductivité et de l'énergie d'activation.

Pour explorer l'effet de la cristallisation sur la structure et les propriétés des verres de thioarséniate de plomb, un traitement thermique de quelques échantillons de verre sélectionnés, x = 0,1, 0,3 et 0,5, a été effectué à 280 °C pendant 30 jours. Les études XRD sur les échantillons recuits indiquent que la sartorite $PbAs_2S_4$ est la seule phase cristalline obtenue pendant la cristallisation, et que sa formation est indépendante de la composition du verre.

La conductivité à température ambiante des échantillons recuits augmente par rapport à celle des verres originaux et croît d'une façon monotone avec l'augmentation de x. De plus, les échantillons vitreux/cristallins recuits présentent une conductivité plus élevée par rapport aux composés ternaires Pb-As-S synthétisés et donnent $\sigma_{298}^{\text{anneal}}(1) = 2\times10^{-8}$ S cm^{-1}, c'est-à-dire qu'ils se rapprochent encore plus de la valeur du nano-PbS. Un réseau cristallin plus ordonné dans la phase semi-conductrice $PbAs_2S_4$ semble être l'origine d'une plus faible diffusion des porteurs électroniques, ce qui permet une plus grande mobilité électronique et donc une meilleure conductivité dans les échantillons recuits.

La conductivité électrique des différentes compositions synthétisées dans le système ternaire a également été étudiée :

A series: $(AgI)_x(PbS)_{0.5(1-x)}(As_2S_3)_{0.5(1-x)}$, B series: $(AgI)_{0.3}$ $(PbS)_y$ $(As2S3)_{0.7-y}$ and C series : $(AgI)_z$ $(PbS)_{0.1}$ $(As2S3)_{0.9-z}$.

Pour La série A, la conductivité électrique totale, σ, déterminée soit par la méthode de l'impédance complexe, pour $\sigma \geq 10^{-8}$ S cm^{-1}, soit à partir des mesures de conductivité dc, pour $\sigma < 10^{-8}$ S cm^{-1}, ne présente pas des effets significatives d'hystérésis et obéit à la loi d'Arrhenius.

La conductivité à température ambiante augmente de ≈11 ordres de grandeur avec l'augmentation de la teneur en AgI. En effet, la conductivité des verres passe des valeurs qui sont typiques des verres sulfurés isolants (10^{-14} S cm^{-1}) à celles caractéristiques des alliages vitreux superioniques (10^{-3} S cm^{-1}). La conductivité maximale à température ambiante est de 7.8×10^{-3} S cm^{-1} pour les verres riches en AgI (x = 0,7, x = 28,57 at.% Ag). L'énergie d'activation diminue de ~1,02 à 0,18 eV, tandis que le facteur pré-exponentiel σ_0 varie entre 10^3 et 10^6 S cm^{-1} K. De plus, nous pouvons dire que notre système de verre pseudo-ternaire et de manière similaire au système de sulfure de mercure, possède au moins trois régions de concentration différentes avec une variation clairement distincte de la conductivité électrique :

La région-A, les verres pauvres en AgI (≤ 3 at.% Ag),

Région-B, les verres riches en AgI (3 ≤ [Ag] ≤ 18 at.%Ag),

Région-C, les verres extrêmement riches en AgI (> 18 at.%Ag).

Pour la série B, $(AgI)_{0.3}$ $(PbS)_y$ $(AS_2S_3)_{0.7-y}$, les conductivités de tous les verres ont été mesurées par spectroscopie d'impédance. Nous pouvons dire que tous les échantillons ne présentent pas d'effets d'hystérésis significatifs et obéissent à la loi d'Arrhenius. La conductivité à température ambiante diminue de 4 ordres de grandeur, passant de 2.5×10^{-4} S.cm^{-1} (y = 0.0) à 1.83×10^{-8} S.cm^{-1} (y = 0.5). L'énergie d'activation augmente de ~0,25 eV à 0,58 Ev et les valeurs du facteur pré-exponentiel σ_0 ne changent pas de manière significative, ils varient entre 10^3 and 10^4 S.cm^{-1}. Comme pour les verres des autres séries, les verres de la série C, $(AgI)_z$ $(PbS)_{0.1}$ $(AS_2S_3)_{0.9-z}$, ne présentent pas d'effets d'hystérésis significatifs, obéissent à la loi d'Arrhenius. Les résultats montrent une augmentation très significative de la conductivité lorsque les verres sont enrichis en AgI. En effet, l'augmentation de la teneur en iodure d'argent a permis d'augmenter significativement la conductivité à température ambiante des verres de plus de 10 ordres de grandeur passant de 8.9×10^{-13} (z = 0.1) à 1.4×10^{-3} (z = 0.5). Cette augmentation est accompagnée d'une diminution de l'énergie d'activation de 0,91 eV (z = 0,1) à 0,378 eV (z = 0,5). De plus, le facteur pré-exponentiel σ_0 varie entre 10^3 et 10^4 S cm^{-1} K.

Chapitre 3

Afin de mieux comprendre les relations entre la composition chimique, la structure atomique à l'échelle locale, intermédiaire et étendue, et les propriétés du verre qui sont critiques pour les applications de détection : transport rapide des ions, stabilité à long terme et réversibilité. Les études structurales des composés synthétisés sont d'un grand intérêt. Puisque dans notre travail, tous les composés que nous traitons sont des verres chalcogénures.

Dans ce chapitre, nous avons étudié la structure des systèmes $PbS\text{-}As_2S_3$ et la série A du système ternaire, $(AgI)_x\ (PbS)_{0.5-x/2}\ (As_2S_3)_{\ 0.5-x/2}$, en utilisant la technique de spectroscopie Raman qui est un outil prédominant pour l'étude structurale des matériaux désordonnés. Par conséquent, une approche multi-technique combinant des techniques de diffraction spectroscopique a été utilisée pour mieux comprendre ces matériaux microstructuraux complexes. Dans un premier temps, nous avons caractérisé les réseaux vitreux du système quasi-binaire $PbS\text{-}As_2S_3$ puis étudié les changements structurels induits par l'ajout progressif d'AgI.

Plusieurs références cristallines Pb-As-S ont été synthétisées et étudiées par spectroscopie Raman afin de comparer leurs spectres Raman avec ceux de nos échantillons vitreux.

Les spectres Raman des verres $PbS\text{-}As_2S_3$ et des références cristallines, sartorite $PbAs_2S_4$ (x = 0.5) et dufrénoysite $Pb_2As_2S_5$ (x = 0.67), ont été étudiées à température ambiante. Les spectres des verres représentent essentiellement une large enveloppe spectrale non résolue d'As_2S_3 vitreux avec des caractéristiques spectrales émergentes et croissantes à 230, 300 et 370 cm^{-1}. Les spectres de $PbAs_2S_4$ et $Pb_2As_2S_5$ cristallins ne présentent pas la contribution de g-As_2S_3 mais présentent des caractéristiques Raman similaires : un pic asymétrique à 290 cm^{-1} avec des épaulements basse fréquence et un pic haute fréquence à 375 cm^{-1}.

La modélisation DFT des clustres limités en taille binaire Pb-S et ternaire As-Pb-S permet d'effectuer une interprétation fiable des spectres observés. Les caractéristiques à 230 et 300 cm^{-1} semblent être liées à l'étirement asymétrique et symétrique du Pb-S, respectivement. Le pic à haute fréquence le plus intense à 370 cm^{-1} est attribué à l'étirement As-S_t, où S_t représente le soufre terminal. La présence de cette caractéristique, accompagnée de distances de liaison As-S_t plus courtes, indique que le plomb agit plutôt comme un modificateur de réseau que comme un formateur de réseau. Une caractéristique similaire à haute fréquence spectroscopique a été signalée précédemment pour les thioarséniates d'argent et alcalins.

Les résultats de la diffraction des neutrons pulsés et des rayons X à haute énergie sur une large plage Q accessible avec Q_{max} = 30 $^{-1}$ ont été utilisés pour étudier l'ordre à courte et moyenne distance dans les thioarséniates de plomb vitreux $(PbS)_x(As_2S_3)_{1-x}$, $0 \leq x \leq 0.5$. Il a été constaté que toutes les compositions étudiées sont entièrement vitreuses sans aucun pic de Bragg, même pour de grands échantillons de neutrons. Néanmoins, une diffusion améliorée des neutrons aux petits angles en dessous de 0.2 Å^{-1} suggère une certaine inhomogénéité mésoscopique même pour les verres avec une seule température de transition vitreuse. Les ajouts de sulfure de plomb ne modifient pas la coordination trigonale de l'arsenic à une distance caractéristique de 2,27 Å, cependant, semblent provoquer une fragmentation du réseau hôte, visible à travers une diminution systématique du premier pic de diffraction à ≈1.25 Å^{-1} et une disparition et un décalage progressifs des corrélations distantes dans l'espace r à ≈5.3 Å. La structure cristalline du $PbAs_2S_4$ monoclinique et les paramètres structuraux dérivés du verre équimolaire $(PbS)_{0.5}(As_2S_3)_{0.5}$ présentent certaines similitudes et des différences prononcées. Une grande différence entre les distances interatomiques impliquant le soufre terminal et le soufre de pontage dans le P $PbAs_2S_4$ monoclinique (r_{As-S_t} ≈ 2.12 Å, r_{As-S_b} ≈ 2.60 Å) n'est pas confirmée pour les thioarséniates vitreux. La coordination locale de plomb élevée dans $PbAs_2S_4$, N_{Pb-S} = 9 à r_{Pb-S} = 3.17 ± 0.14 Å, n'est pas non plus caractéristique des verres, cohérente avec des distances interatomiques Pb-S plus petites, 2,85 0,02 Å. Cependant, la coordination locale dérivée du plomb dans les verres, N_{Pb-S} = 3.5 ± 0.5, est susceptible d'être sous-estimée en raison de l'ajustement gaussien avec des fonctions symétriques.

Une modélisation FPMD préliminaire d'un liquide surfondu équimolaire $(PbS)_{0.5}(As_2S_3)_{0.5}$ à 600 K a été réalisée en utilisant la fonctionnelle hybride GGA/PBE0. Les facteurs structuraux dérivés de neutrons et de rayons X GGA/PBE0 et les fonctions de corrélation dans l'espace r semblent être en bon accord avec les résultats expérimentaux pour le verre à température ambiante suggérant que les caractéristiques structurelles du verre liquide et solide surfondu sont assez similaires. La modélisation FPMD est cohérente avec la conclusion habituelle selon laquelle le FSDP dans les verres au thioarséniate de plomb est principalement lié aux corrélations d'ordre de gamme intermédiaire As-As avec une contribution supplémentaire des paires As-S. La nouvelle fonctionnalité émergente à Q_{Pb} ≈ 1.7 Å^{-1} est essentiellement liée au pic principal de $S_{PbPb}(Q)$ partiel avec une contribution supplémentaire des corrélations Pb-As. Le liquide surfondu $(PbS)_{0.5}(As_2S_3)_{0.5}$ présente un petit désordre chimique mis en évidence par les liaisons homopolaires As-As et S-S, également visibles dans les spectres Raman des verres au thioarséniate de plomb. Le désordre chimique est faible, χ = 4,5 0,5 %. La coordination

locale de l'arsenic est trigonale, $N_{\mathrm{AsX}} = N_{\mathrm{AsAs}} + N_{\mathrm{AsS}}$ = 3.03 ± 0.03, en accord avec les études structurales connues des verres sulfurés. L'environnement local principal semble être fortement asymétrique et plutôt octaédrique , N_{PbS} = 6 ± 1. Néanmoins, une analyse plus approfondie est nécessaire après avoir terminé les simulations FPMD.

Fondamentalement, les paramètres neutroniques dérivés, structuraux aux rayons X ainsi que les paramètres FPMD mettent plutôt l'accent sur le rôle structurel du plomb en tant que modificateur que comme formateur de réseau.

Chapitre 4

Après avoir étudié les propriétés macroscopiques des verres et après avoir dévoilé leurs propriétés de transport et de structure, nous pouvons étudier l'application de ces verres comme capteurs chimiques. En effet, le choix des compositions à utiliser dépend des mécanismes de transport ionique mis en jeu. Une fois les compositions à tester choisies, une étude préliminaire des caractéristiques de ces verres en tant que membrane ionique spécifique est réalisée. Les capteurs spécifiques au plomb sont développés pour fonctionner dans un environnement aqueux. C'est pourquoi, dans un premier temps, nous avons pensé qu'il serait intéressant d'étudier la chimie du plomb dans l'eau. Aussi, une étude bibliographique des techniques qui ont été utilisées pour la détection et la détermination de la quantité de plomb dans l'eau est réalisée afin de comprendre les avantages et les inconvénients de chaque technique. Enfin, après quelques rappels de potentiométrie, nous présenterons les travaux réalisés sur l'application des verres du système AgI-PbS-As_2S_3 comme capteurs potentiométriques.

Nos capteurs sont constitués des membranes sensibles qui ont généralement un diamètre de 5-6 mm et une épaisseur de l'ordre de 2 à 4 mm. Les membranes ont ensuite été collées sur le tube PVC à l'aide de la résine époxy. Ensuite, nous avons réalisé le contact liquide en utilisant une électrode d'Ag recouverte d'AgCl dans une solution d'$AgNO_3$ 10^{-1} M pour les membranes contenant de l'argent, et un mélange (1:1) $AgNO_3$ 10^{-1} M et $Pb(NO_3)_2$ 10^{-1} M pour les membranes contenant de l'argent et du plomb.

Principales caractéristiques des capteurs Pb^{2+}

La sensibilité est une caractéristique qui définit la capacité du capteur à répondre à une certaine espèce ionique présente dans un milieu liquide et est connue pour être le paramètre le plus

important caractérisant les capteurs chimiques. La deuxième caractéristique importante est la limite de détection qui correspond à une concentration limite en dessous de laquelle le capteur n'est plus sensible aux ions mesurés. La sensibilité et la limite de détection des capteurs ont été étudiées dans des solutions standards de nitrate de plomb $Pb(NO_3)_2$. Des calibrations ont été effectuées sur une gamme de concentrations entre 10^{-8} mol. L^{-1} et 10^{-3} mol. L^{-1}. Toutes les calibrations ont été effectuées en utilisant la méthode de titrage où les additions sont introduites dans 100 ml de solution de nitrate de potassium KNO_3 avec une concentration de 10^{-1} mol. L^{-1}. Après avoir introduit les additions, il est nécessaire d'attendre pour atteindre le potentiel d'équilibre. Le temps d'attente est normalement d'environ 2 minutes et le potentiel ne varie pas de plus de ± 2 mV pendant ces 2 minutes. Toutes les solutions étalons ont été préparées par la méthode des dilutions successives. La solution de support ayant une force ionique constante était le nitrate de potassium KNO_3 (10^{-1} mol/L, pH≈7). Cette force ionique constante nous permet également d'utiliser la concentration des ions au lieu de leur activité et donc d'éviter le calcul des coefficients d'activité des ions.

La réponse typique du capteur Pb-ISE10, Pb-ISE30, Pb-ISE25 et Pb-ISE20 mesurée pendant quatre semaines a été présenté. On peut dire que la limite de détection et la pente des capteurs dépendent de la composition des membranes. Les changements significatifs de la pente des courbes (S) et du potentiel standard de la membrane (E0) indiquent une instabilité à court terme et une perte de sensibilité des capteurs Pb-ISE10 et Pb-ISE30. Les membranes avec les compositions 50AgI-25PbS-25As_2S_3 (capteur Pb-ISE25) et 60AgI-20PbS-20As_2S_3 (capteur Pb-ISE20) montrent une meilleure limite de détection et une meilleure stabilité comparées à celles des capteurs Pb-ISE10 et Pb-ISE30.

Les résultats des études de limite de détection et de sensibilité pour les capteurs Pb-ISE25 et Pb-ISE20 révèlent que les capteurs Pb-ISE20 avec les membranes basées sur la composition 60AgI-20PbS-20As_2S_3 montrent une meilleure stabilité que le capteur Pb-ISE25. En même temps, tous les capteurs ont une pente différente de la valeur théorique (29 mV / décennie). Par conséquent, il a été décidé de poursuivre les études des paramètres des capteurs utilisant la composition 60AgI-20PbS-20As_2S_3. La stabilité à 6 mois de l'électrode Pb-ISE20.

Afin de déterminer le coefficient de sélectivité, nous pouvons utiliser la méthode recommandée par l'IUPAC. Il s'agit de la méthode des solutions mixtes avec deux versions :

(1) Concentration constante d'ions interférents et (2) Concentration constante d'ions primaires.

La première méthode signifie que nous utilisons comme solution de mesure une solution contenant des ions interférents avec une concentration constante, alors que la concentration des espèces primaires est variable. En revanche, dans la deuxième méthode, la concentration des ions primaires est fixe tandis que la concentration des espèces interférentes est variable. Cette version est généralement utilisée lorsque l'influence des ions interférents est très forte, afin d'éviter une éventuelle contamination de la membrane sélective par les espèces interférentes.

Sélectivité aux ions potassium K^+

Le coefficient de sélectivité a été mesuré en utilisant la méthode des solutions mixtes et plus précisément sa première version avec une concentration constante d'ions interférents. Les résultats montent que le coefficient de sélectivité K_{Pb^{2+},K^+} diminue avec la concentration des ions interférents. Ce comportement est possible à cause de la forte diminution de la force ionique (0.1, 0.01 et 0.001 mol. L^{-1} in KNO_3). Dans ce cas, l'influence du potentiel de diffusion est remarquable. Ces très faibles valeurs du coefficient de sélectivité indiquent que les capteurs peuvent être utilisés dans des environnements où la concentration en potassium est ~10^6 fois plus importante.

Sélectivité aux ions sodium Na^+

Le coefficient de sélectivité a été mesuré en utilisant la méthode des solutions mixtes et plus précisément sa première version avec une concentration constante d'ions interférents. Les additions ont été faites dans la gamme de 10^{-8} to 10^{-3} mol. L^{-1}. La concentration des ions interférents ($NaNO_3$) était de 0.1 mol. L^{-1} et 1 mol. L^{-1}. La réponse typique des capteurs Pb-ISE20 en présence d'ions interférents Na^+ présentent clairement de meilleurs coefficients de sélectivité vis-à-vis des ions Na^+ que le capteur développé par M. Mazlum Ardakany et al. (un facteur de 100 est observé) et un coefficient comparable à celui de Yu. G. Vlasov et E. Bychkov.

Sélectivité aux ions calcium Ca^{2+} et nickel Ni^{2+}

Dans le cas du calcium et du nickel, les coefficients de sélectivité ont été mesurés selon la même méthode des solutions mixtes et plus précisément selon sa première version avec une concentration constante d'ions interférents (0.1 mol. L^{-1} de $Ca(NO_3)_2$ et $Ni(NO_3)_2$). Les additions dosées ont été faites dans la gamme de 10^{-8} à 10^{-3} mol. L^{-1}. Nous pouvons également conclure en comparant nos résultats avec ceux des données bibliographiques que nous capteurs développés ont clairement les meilleurs coefficients de sélectivité.

Sélectivité aux ions cuivre Cu^{2+}, mercure Hg^{2+} et cadmium Cd^{2+}

Les coefficients de sélectivité en présence d'ions Cu^{2+}, Hg^{2+} and Cd^{2+} ont été mesurés en utilisant la deuxième méthode des solutions mixtes, c'est-à-dire avec une concentration fixe d'ions primaires et une concentration variable d'ions interférents.

En comparant Les coefficients de sélectivité des capteurs de Pb^{2+} en présence d'ions Cu^{2+} trouvés dans la littérature avec ceux des capteurs que nous avons développés, nous pouvons tirer les conclusions suivantes :

- Les ions Cu^{2+} sont fortement interférents ;
- Les coefficients de sélectivité obtenus dans cette thèse vis-à-vis de Cu^{2+} sont nettement supérieurs à ceux publiés par d'autres auteurs, à l'exception du capteur développé par Yu. G. Vlasov et E. Bychkov(comparable).
- Trouver un moyen d'éviter l'interférence du Cu est essentiel pour l'utilisation des capteurs.

La comparaison des résultats des capteurs de Pb^{2+} en présence d'ions Hg^{2+} trouvés dans la littérature avec nos résultats montre que :

- Les ions Hg^{2+} sont généralement plus interférents que les ions Cu^{2+} ;
- Les coefficients de sélectivité en présence d'ions Hg^{2+} sont plus élevés que ceux obtenus par d'autres auteurs, à l'exception du capteur développé par Yu. G. Vlasov et E. Bychkov;
- L'utilisation directe des capteurs en présence de Hg^{2+} nécessite l'élimination de son influence.

Et finalement, pour le cadmium, la comparaison de nos résultats avec ceux trouvés dans la littérature on peut conclure que :

- Les ions Cd^{2+} n'interfèrent généralement pas avec les ions Pb^{2+} ;
- Nos capteurs présentent une forte sélectivité pour les ions Pb^{2+} par rapport aux ions Cd^{2+} interférents et les valeurs de sélectivité sont comparables à celles obtenues par V.S. Bhat et al. (pour les concentrations 10-6 et 10^{-8} M).

Influence de pH dans les solutions standards

Déterminer la gamme optimale de pH dans laquelle le potentiel du capteur de plomb est invariable pour une concentration donnée de Pb^{2+} est une mesure potentiométrique essentielle. L'influence du pH a été mesurée à la concentration constante du cation primaire Pb^{2+}, mais en faisant varier le pH de 1 à 8. La valeur du pH a été enregistrée simultanément avec les potentiels des capteurs chimiques. Le changement de la valeur du pH a été effectué en ajoutant un acide ou une base à la solution standard. La réponse typique de nos capteurs Pb-ISE20 en fonction du pH et de la concentration en $Pb(NO_3)_2$ montre plusieurs régions caractéristiques. Le potentiel est constant dans la gamme de pH 2.5–4.8 pour la concentration en plomb dilué (1×10^{-5} M $Pb(NO_3)_2$). Les plages de pH de travail s'améliorent légèrement avec l'augmentation de la concentration de la solution de nitrate de plomb à 1×10^{-2} M et la plage de pH enregistrée pour laquelle le potentiel est plus ou moins invariable est de 1,95. La diminution des valeurs du potentiel du capteur à pH < 2 et pH > 5 est principalement due aux changements dans le potentiel de jonction liquide et à l'hydrolyse des ions Pb^{2+} dans la solution, respectivement.

Reproductibilité dans les solutions standards

Les mesures de reproductibilité ont été effectuées dans le domaine de concentration 10^{-8} -10^{-3} M. La reproductibilité typique pour les capteurs Pb-ISE20 montre un faible changement de potentiel pendant les mesures consécutives, de l’ordre de : 2-3 mV. De plus, on remarque également que la reproductibilité ne dépend pas de la concentration des ions primaires $Pb2^{+}$. En d'autres termes, nous pouvons dire que les capteurs montrent une très bonne reproductibilité dans des conditions de laboratoire.

Abstract

Chalcogenide glasses are very promising for application as active membranes in potentiometric chemical sensors. In the Ph.D. work, we have explored the possibility to use the lead doped chalcogenide glasses for the quantitative analysis of Pb^{2+} ions. We have also studied their physical, thermal, electrical and structural properties.

First, lead thioarsenate chalcogenide glasses ($0 \leq x \leq 0.6$) and crystals ($PbAs_2S_4$, $Pb_5As_9S_{18}$ and $Pb_2As_2S_5$) were synthesized in the quasi-binary $(PbS)_x(As_2S_3)_{1-x}$ system. Two complementary techniques, melt-quenching and mechanical milling, were employed to this end. In addition, three different glass series (A–, B– and C–series) were synthesized in the pseudo-ternary AgI-PbS-As_2S_3 system and the vitreous domain was established. The macroscopic properties of both systems such as the densities and the characteristic temperatures (glass transition and crystallization temperatures) were measured and analyzed according to the glass compositions.

Second, using alternative current ac (complex impedance spectroscopy) and direct current dc conductivity (Resistivity Meter) measurement, the electric properties were studied for all of the above vitreous and crystalline systems and the effects/roles of lead sulfide PbS and silver iodide AgI additions are examined.

Third, to understand the origin of various properties (composition–structure–property relationship), we have conducted structural studies using a set of structural measurement tools (e.g. Raman spectroscopy, neutron and high-energy X-ray diffraction). Thanks to our modeling team at LPCA laboratory, Raman DFT modelling as well as RMC/DFT and FPMD modelling of the diffraction data were performed in the quasi-binary PbS–As_2S_3 glass system.

Finally, the last part of this Ph.D. thesis is fully dedicated to the fabrication and characterization of new chemical sensors based on the lead/silver containing chalcogenide glass membranes for the detection of Pb^{2+} ions in solution. Different compositions are tested in order to define the sensitivity, the detection limit and the selectivity coefficients in the presence of interfering ions. Both reproducibility and the pH influence are also evaluated.

Keywords: chalcogenide glasses, lead thioarsenates, thermal properties, ac and dc conductivity measurements, structure, chemical sensors.

Résumé

Les verres de chalcogénures sont très prometteurs pour les applications en tant que membranes actives dans les capteurs chimiques potentiométriques. Dans le cadre de ces travaux de thèse, nous avons exploré la possibilité d'utiliser les verres de chalcogénures dopés au plomb pour l'analyse quantitative des ions Pb^{2+}. Nous avons également étudié leurs propriétés physiques, thermiques, électriques et structurales.

Tout d'abord, des verres de chalcogénures ($0 \leq x \leq 0.6$) et des cristaux ($PbAs_2S_4$, $Pb_5As_9S_{18}$ and $Pb_2As_2S_5$) de thioarsénate de plomb ont été synthétisés dans le système quasi-binaire $(PbS)_x(As_2S_3)_{1-x}$. Deux techniques complémentaires, la méthode classique de synthèse en tubes silice et le broyage mécanique, ont été employées à cette fin. De plus, trois séries différentes de verre (A–, B– et C–séries) ont été synthétisées dans le système pseudo-ternaire AgI-PbS-As_2S_3 et le domaine vitreux a été établi. Les propriétés macroscopiques des deux systèmes telles que les densités et les températures caractéristiques (températures de transition vitreuse et de cristallisation) ont été mesurées et analysées selon les compositions des verres.

Deuxièmement, à l'aide d'un courant alternatif (spectroscopie d'impédance complexe) et d'une mesure de conductivité en courant continu (résistivité), les propriétés électriques ont été étudiées pour tous les systèmes vitreux et cristallins mentionnées ci-dessus et les effets/rôles des additions de sulfure de plomb PbS et d'iodure d'argent AgI sont examinés.

Troisièmement, pour comprendre l'origine des diverses propriétés (relation composition–structure–propriété), nous avons mené des études structurales à l'aide d'un ensemble d'outils de mesure structurale (par exemple, la spectroscopie Raman, la diffraction de neutrons et de rayons X haute énergie). Grâce à notre équipe de modélisation au sein du laboratoire LPCA, la modélisation DFT des donnéees Raman ainsi que la modélisation RMC/DFT et FPMD des données de diffraction ont été réalisées dans le système quasi-binaire PbS–As_2S_3 vitreux.

Enfin, la dernière partie de ce travail est entièrement dédiée à la fabrication et à la caractérisation de nouveaux capteurs chimiques à base de membranes de verres de chalcogénures contenant du plomb/argent pour la détection des ions Pb^{2+} en solution. Différentes compositions sont testées afin de définir la sensibilité, la limite de détection et les coefficients de sélectivité en présence d'ions interférents. La reproductibilité et l'influence du pH sont également évaluées.

Mots-clés : verres de chalcogénures, thioarsénates de plomb, propriétés thermiques, mesures de conductivité ac et dc, structure, capteurs chimiques.